Image-Based Finite Element Modelling of Fetal Critical Aortic Stenosis with Evolving Hypoplastic Left Heart Syndrome and Fetal Aortic Valvuloplasty Intervention

Laura Elizabeth Green

A dissertation submitted in fulfilment of the requirements for the degree of Doctor of Philosophy of Imperial College London.

Department of Bioengineering

Imperial College London

26th October 2023

Declaration

I (Laura Green) confirm that this thesis contains my own work and does not contain material that has been submitted for the award of any other degree, publication, or presentation, unless stated otherwise and acknowledged in Chapter Sections 1.4-1.5 and in the relevant text. Work done by others is appropriately referenced throughout.

Laura Green

Copyright

Abstract

Fetal critical aortic stenosis with evolving hypoplastic left heart syndrome (CAS-eHLHS) is a mid-gestation cardiac malformation. CAS-eHLHS has a high likelihood of progressing to hypoplastic left heart syndrome (HLHS), where the neonate will require complex surgeries or a heart transplant. Fetal aortic valvuloplasty (FAV) is an in-utero catheter-based intervention, performed on mid-gestation CAS-eHLHS fetal hearts, which aims to widen the stenotic aortic valve, to prevent a HLHS outcome. However, some patients still progress to a HLHS outcome post-FAV, suggesting that it is clinically difficult to predict FAV outcomes. There is also limited understanding of the biomechanical implications of CAS-eHLHS and FAV. Therefore, it was proposed to use finite element (FE) modelling to address such issues.

FE methods were developed to support later work. This included calibrating the fetal lumped parameter model, investigating the effect of helix angle configuration on fetal LV function (helix angle configuration describes the orientation of the LV myofibers relative to the short-axis plane), to support future assignment of the parameter, and developing an optimisation algorithm, for patient specific computational modelling.

FE analysis showed CAS-eHLHS patients to have compromised functionality. Interestingly, peak systolic myofiber stress, output from the computational methods, showed a unique ability in predicting post-FAV outcomes. A simplified equation was derived for real-time estimation of peak systolic myofiber stress, which upheld its predictive capabilities when tested.

Virtual FAV demonstrated how FAV can partially restore several physiological features towards healthy levels, however, the inclusion of aortic valve regurgitation, in the analysis,

compromised LV and left atrium depressurisation but promoted increased stroke volume. Furthermore, patient specific post-FAV modelling enabled analysis of acute FAV outcomes.

Overall, the research improved understanding of the biomechanical implications of CAS-eHLHS and FAV and gave a sense of which cases are more suitable for FAV, which, with future work, could support patient selection.

Acknowledgements

Firstly, I would like to acknowledge and thank my supervisor, Dr Choon Hwai Yap. I am very grateful for Dr Yaps support and guidance throughout my PhD. Dr Yaps vast knowledge, passion for research and dedication to his research group has not gone unnoticed, such traits have been pivotal to my development within the PhD and for that I am forever grateful. I must also acknowledge the financial support I received from the Imperial Start-Up Fund; without such funding I would not have been able to complete this research.

I must thank Dr Andreas Tulzer and Dr Gerald Tulzer, the work they do at Linz Hospital Austria is extraordinary. Their dedication, depth of knowledge and eagerness to collaborate with academia to further the service is admirable. The knowledge and time Dr Andreas Tulzer and Dr Gerald Tulzer gave to myself, and this research, was indispensable and something that I will forever be grateful for.

I would also like to extend a thank you to Dr Wei Xuan Chan. Dr Chan provided fundamental work, support, and training throughout my PhD, he was patient and always eager to engage in debates to foster intellectual growth and advance methodologies. Further to this I would like to thank Meifeng Ren. When I commenced my PhD Meifeng consistently offered a warm presence on Teams, guiding me through the image segmentation techniques. I would also like to extend a thank you to all members of our research group, particularly Gaia Cairelli and Sean Wong who I started the PhD with. I look forward to seeing how everyone's journey unfolds.

Following the defence of my thesis I would like to express my sincere gratitude to Professor Peter Weinberg and Professor Vanessa Diaz, firstly for agreeing to examine my thesis and secondly for their insightful comments and feedback during the defence and afterward.

Last and by no means least, I would like to thank my loving boyfriend, family, and friends. Their encouragement, compassion, and belief in me has been a constant source of strength. I will forever cherish and appreciate their support, where they have celebrated the successes with me and stood by my side during the challenging times.

Contents

List of Figures

List of Tables

List of Abbreviations

2D	2 Dimensional
3D	3 Dimensional
4D	4 Dimensional
AA	Ascending Aorta
AO1	Aortic Arch
AS	Aortic Stenosis
AV	Aortic Valve
AVr	Aortic Valve Regurgitation
BCL	Base Cardiac Length
BPM	Beats Per Minute
BSF	B-Spline of Fourier
BV	Biventricular
CART	Classification and Regression Tree
CAS	Critical Aortic Stenosis
CAS-eHLHS	Critical Aortic Stenosis with Evolving Hypoplastic Left Heart Syndrome
CHD	Congenital Heart Disease

Dil	Balloon Dilation
dMRI	Diffusion Tensor Magnetic Resonance Imaging
EDP	End Diastolic Pressure
EDV	End Diastolic Volume
ER	FE versus Image Strain Error
ESV	End Systolic Volume
EF	Ejection Fraction
FAV	Fetal Aortic Valvuloplasty
FE	Finite Element
FEM	Finite Element Modelling
HLHS	Hypoplastic Left Heart Syndrome
LDRB	Laplace-Dirichlet Rule-Based
LPM	Lumped Parameter Model
LV	Left Ventricle
LVID	Left Ventricle Inner Diameter
LVOT	Left Ventricle Outflow Tract
MVr	Mitral Valve Regurgitation
MV	Mitral Valve

NW	Norwood
PC	Principal Component
PINN	Physics Informed Neural Network
PLI	Polarised Light Imaging
PV	Pressure Volume
PWT	Posterior Wall Thickness
RK	Ross-Kono
RMSE	Root Mean Square Error
ROC	Receiver Operator Curve
RV	Right Ventricle
RWT	Relative Wall Thickness
SSIM	Structural Similarity Index Measure
SV	Stroke Volume
UV	Univentricular
VMTK	Vascular Modelling Toolkit
Wks	Week

List of Symbols

a	Vessel Radius
$A(t)$	Temporal Variation for Pressure Generation
B	Shape of peak isometric tension-sarcomere length relation
b	Time Intercept of Linear Relaxation Duration with Sarcomere Length
b_{ff}	Stiffness Coefficient in Fibre Direction
b_{fx}	Stiffness Coefficient in Shear Direction
b_{xx}	Stiffness Coefficient in Sheet Direction
C	Vessel Compliance (also referred to as Capacitance)
c_1	Zero Mean Translation Constraint
c_2	Zero Mean Rotation Constraint
Co	Passive Stiffness Coefficient
Ca_0	Maximum Intracellular Calcium Concentration
C_{scale}	Capacitance Scaling Coefficient
D	Shunt Dissipative Coefficient
E	Youngs Modulus
$\boldsymbol{F}$	Deformation Gradient Tensor

$\overrightarrow{f_d}$	Unit Vector in Myofiber Direction
K	Valvular Dissipative Coefficient
k	Experimental Coefficient
k_{spring}	Spring Constant Emulating Load Applied by Pericardium
m	Gradient of Linear Relaxation Duration with Sarcomere Length Relaxation
L	Inductance
l	Vessel Length
l_0	Sarcomere Length Under No Active Tension
l_r	Relaxed Sarcomere Length
p	Tissue Incompressibility Parameter
Q	Flowrate
R	Resistance
R_{scale}	Resistance Scaling Coefficient
R_v	Ventricle Resistance
T	Time Duration of a Cardiac Cycle
t_0	Time to Peak Tension
T_{0LV}	Maximum Tension (also known as Myocardial Contractility)
$\boldsymbol{u}$	Displacement Field

U_0	Isovolumetric Pressure Generator Constant
V	Volume
v	Velocity
W	Strain Energy Density Function
w	Vessel Thickness
α	Transverse Angle Coefficient
β	Coefficient for Local Haemodynamics
ΔP	Pressure Gradient
ε	End Systolic Green Lagrange Strain
λ_{min}	Minimum Eigenvalue
μ	Blood Viscosity
μ_{length}	Longitudinal Position Along the LV
μ_x	Mean Signal Intensities in the x Direction
μ_y	Mean Signal Intensities in the y Direction
ρ	Density
σ	Standard Deviation
$\boldsymbol{\sigma}$	Stress Tensor
$\bar{\tau}$	Transmural Averaged Angle

τ_{diff}	Epicardial to Endocardial Transmural Angle Difference
φ	Linear Transmural Myocardial Distance
ω	Cardiac Cycle Time Variation

Chapter 1: Introduction

A brief chapter to introduce the research rationale, state the aim and specific aims, describe the research structure, and declare any publications or presentations given as a product of this research.

1.1 Research Rationale

Critical aortic stenosis (CAS) in mid-gestation fetal hearts is an obstructive lesion, which promotes abnormal intracardiac blood flow and blood pressure (Arzt et al. 2011). In selected cases, CAS can progress to critical aortic stenosis with evolving hypoplastic left heart syndrome (CAS-eHLHS), which results in further morphological and physiological aberrations, where approximately 73% of CAS-eHLHS patients progress to the fatal hypoplastic left heart syndrome (HLHS) by birth (Mäkikallio et al. 2006).

Fetal aortic valvuloplasty (FAV) is an in-utero catheter-based intervention, which aims to widen the stenotic aortic valve (AV) to promote healthier development in gestation. FAV has shown promise (Friedman et al. 2018), reducing the likelihood of progression to HLHS from 73% (Mäkikallio et al. 2006) to 24-41% (Friedman et al. 2018; Galindo et al. 2017; Tulzer et al. 2022a; Tulzer et al. 2021b). However, this success is not without risks, as experienced FAV intervention centres have reported an approximate 4-10% procedural related loss (Arzt et al. 2011; McElhinney et al. 2009; Pickard et al. 2020; Tulzer et al. 2022b). In addition to the inherent procedural risks, a substantial number of patients continue to the unfavourable HLHS outcome, suggesting that the ability to predict FAV outcomes remains limited, thus compromising current patient selection capabilities. Furthermore, there is limited understanding of how CAS-eHLHS modifies fetal biomechanics and the impact FAV intervention has on cardiac functionality. To address these challenges, the development of fetal finite element (FE) methods would be required, to then be able to characterise the behaviour of the CAS-eHLHS myocardium.

Therefore, there is motivation and scope to study CAS-eHLHS patients and FAV intervention, to better understand the biomechanical implications of both the disease and

intervention. Furthermore, improved understanding of the biomechanics of CAS-eHLHS LVs could elucidate patient characteristics that are related to FAV outcomes, which in turn could inform future patient selection, surgical planning, and parental counselling.

1.2 Overall Aim and Specific Aims

Overall Aim: To develop methods for FE modelling of fetal healthy and CAS-eHLHS LVs to then gain understanding of the biomechanical environment of CAS-eHLHS, pre- and post-FAV intervention and determine whether pre-FAV biomechanics are indicative of post-FAV outcomes.

The following specific aims are designed to fulfil the overall aim, and are:

Specific Aim 1: To develop fetal lumped parameter model (LPM) and FE methods to enable patient specific modelling of healthy and CAS-eHLHS fetal LVs.

Through developing the LPM and FE methods, Specific Aim 1 will directly support Specific Aims 2 and 3 and the fulfilment of the Overall Aim. Specifically, the LPM will be calibrated to the latest literature measurements. Subsequently, the effect of helix angle configuration on LV functionality will be studied. The helix angle configuration delineates the orientation of the myofibers away from the short axis plane, throughout the LV, thereby informing LV contraction dynamics, therefore, studying the interplay between helix angle configuration and LV functionality could help inform the assignment of helix angle configuration in future studies. Finally, an optimisation algorithm will be developed, to incorporate further patient specificity into the modelling methods and facilitate inverse computation of biomechanics characteristics.

Specific Aim 2: To characterise the biomechanical environment of CAS-eHLHS LVs and determine whether pre-FAV biomechanics characteristics' can predict FAV outcomes.

Specific Aim 2 assesses a range of CAS-eHLHS fetal heart morphometrics from echocardiographic images and computational biomechanics parameters derived from patient specific FE modelling, to understand how CAS-eHLHS LVs differ from healthy fetal LVs and assess each parameter's ability to predict FAV intervention outcomes. The aim is a pilot study, which could support patient selection and parental counselling, by providing insights into fetal biomechanical functionality that are currently clinically unavailable.

Specific Aim 3: Understanding the Biomechanical Effects of FAV Intervention.

Through virtual FAV intervention methods Specific Aim 3 works to comprehend the range of possible FAV intervention outcomes, to generate a wide-angle view of how LV functionality varies as a product of FAV intervention. Further to this, patient specific post-FAV models are analysed and compared to the corresponding pre-FAV data from Specific Aim 2, to analyse the actual biomechanical response to intervention.

In summary, Specific Aim 1 was designed to develop methodologies and provide insights that support the fulfilment of Specific Aims 2 and 3. Then Specific Aims 2 and 3 investigate the biomechanics of the CAS-eHLHS fetal LV pre- and post-FAV, to fulfil the Overall Aim.

1.3 Chapter Overview

The thesis consists of 6 further chapters. A brief description of each following chapter is provided below.

Chapter 2 first provides details of fetal cardiac development and fetal LV functionality. The chapter also provides a review of current HLHS and CAS-eHLHS disease characteristics, and intervention options and outcomes.

Chapter 3 provides details of the fundamental computational methods utilised in this research. Specifically, the methods for image segmentation and cardiac motion estimation are provided, alongside a description of an existing fetal LPM and the FE methods utilised in this thesis.

Chapter 4 develops the LPM and FE methods. Firstly, the LPM which describes the fetal circulatory system was calibrated. Secondly, the effect of helix angle configuration on LV biomechanics and the impact LV morphology has on the relationship between helix angle configuration and LV biomechanics was studied, using patient specific and idealised LV geometries combined with volume constrained FE techniques. The research showed that helix angle configuration impacts LV functionality, and a configuration was recommended that was close to the optimal values in minimising LV work done, maximising peak systolic myofiber stress, minimising the deformational burden of the myocardial tissue, and reducing error in image-based and computed myocardial strains. The research also showed that size scaling of the LV did not impact cardiac biomechanics, suggesting conclusions made in the chapter are applicable to the adult LV also. Finally, an optimisation algorithm was developed to incorporate further patient specificity into the LPM+FE methods, particularly for CAS-eHLHS cases, enabling back-computation of biomechanical parameters.

Chapter 5 evaluates the impact of CAS-eHLHS on fetal heart biomechanics, compared to healthy fetal hearts. An output from the research was the identification that one biomechanics

characteristic, peak systolic myofiber stress, was a pre-FAV intervention parameter that was able to distinguish how fetal hearts would respond to intervention, in the cohort studied. A simple empirical equation was derived to calculate peak systolic myofiber stress using clinical parameters. Said equation's ability to predict intervention outcome was then tested on a retrospective cohort, where it upheld its predictive capabilities.

Chapter 6 evaluates how the biomechanics of CAS-eHLHS LVs alter post intervention. Virtual FAV intervention is performed on the pre-FAV hearts, optimised for in Chapter 5, to isolate the mechanistic nature of FAV intervention. Such models demonstrated how FAV intervention can partially restore several physiological features, and how aortic valve regurgitation (AVr), a biproduct of the intervention, can impede LV and left atrium depressurisation, but promote greater stroke volume (SV). Patient specific post-FAV models were developed and analysed showing great patient variability and highlighting the need for such detailed models to determine acute post-FAV outcomes.

Chapter 7 summarises the preceding chapters' results, evaluates the impact of the work and proposes future work.

1.4 Publications

Some results in this thesis have been documented in the publications listed below. Where appropriate collaborators contributions are acknowledged in the thesis.

Green, L., Chan, W. X., Ren, M., Mattar, C., Lee, L. C., Yap, C. H., The Dependency of Fetal Left Ventricular Biomechanics Function on Myocardium Helix Angle Configuration. Biomech. Model. Mechanobiol., 2022;22, 629-43. https://doi.org/10.1007/s10237-022-01669-z

Ren, M., Chan, W. X., Green, L., Armstrong, A., Tulzer, A., Tulzer, G., Buist, M., Yap, C. H., Contribution of Ventricular Motion and Sampling Location to Discrepancies in Two-Dimensional Versus Three-Dimensional Fetal Ventricular Strain Measures. JASE, 2023;36(5), 543-52. https://doi.org/10.1016/j.echo.2022.12.024

Green, L., Chan, W. X., Prakash, I., Tulzer, A., Tulzer, G., Yap, C. H., Pre-Intervention Myocardial Stress is a Good Predictor of Aortic Valvuloplasty Outcome for Fetal Critical Aortic Stenosis with Evolving HLHS. J. Physiol., 2024;602(4), 663-81. **https://doi.org/10.1113/JP285475**

1.4.1 Publications Under Review

Ren, M., Chan, W. X., Green, L., Buist, M., Yap, C. H., Biventricular Finite Element Modelling of the Fetal Heart in Health and During Aortic Stenosis. Biomech. Model. Mechanobiol.,.

Green, L., Chan, W. X., Tulzer, A., Tulzer, G., Yap, C. H., Myocardial Biomechanical Effects of Fetal Aortic Valvuloplasty. Biomech. Model. Mechanobiol.,.

1.5 Conferences

Some of the results within this thesis have been presented at conferences. Unless stated otherwise, I (Laura Green), presented the research at said conference.

1.5.1 Podium Presentations

Green, L., Chan, W. X., Tulzer, A., Tulzer, G., Yap, C. H., Using the Digital Twin of Human Fetal Heart to Predict Outcomes of a Fetal Heart Intervention. European Society of Biomechanics Congress (Porto, Portugal), 2022.

Green, L., Chan, W. X., Ren, M., Mattar, C., Lee, L. C., Yap, C. H., The Dependency of Fetal Left Ventricular Biomechanics Function on Myocardium Helix Angle Configuration and Morphology. World Congress of Biomechanics (Taipei, Taiwan), 2022.

Green, L., Chan, W. X., Tulzer, A., Tulzer, G., Yap, C. H., Biomechanics of Fetal Aortic Stenosis and Fetal Aortic Valvuloplasty. BioMedEng (London, UK), 2022.

Chan, W. X., Green, L., Ren, M., Wong, H., Yap, C. H., Biomechanics of Fetal Aortic Stenosis with Evolving HLHS and Fetal Aortic Valvuloplasty. 15th World Congress on Computational Mechanics and 8th Asian Pacific Congress on Computational Mechanics (Yokohama, Japan), 2022. [Presented by Dr Yap]

Green, L., Chan, W. X., Tulzer, A., Tulzer, G., Yap, C. H., Biomechanical Modelling of Fetal Heart with Aortic Stenosis to Predict Intervention Effectiveness. 18th International Symposium on Computer Methods in Biomechanics and Biomedical Engineering (Paris, France), 2023.

Ren, M., Chan, W. X., Green, L., Armstrong, A., Tulzer, A., Tulzer, G., Buist, M. L., Yap, C. H., The Reasons for Differences Between 2D and 3D Echocardiography Strain Measurements. European Society of Biomechanics Congress (Maastricht, Netherlands), 2023. [Presented by Meifeng Ren].

1.5.2 Poster Presentations

Green, L., Chan, W. X., Tulzer, A., Tulzer, G., Yap, C. H., Biomechanics Parameter Predicts Successful Fetal Heart Intervention Outcome Better than Clinical Scans. European Society of Biomechanics Congress (Maastricht, Netherlands), 2023.

1.5.3 Conference Awards

I was awarded the 2023 Poster Award at the European Society of Biomechanics, held in Maastricht, Netherlands. The poster was presenting *'Biomechanics Parameter Predicts Successful Fetal Heart Intervention Outcome Better than Clinical Scans'.*

Chapter 2: Background

Firstly, Chapter 2 covers fundamental knowledge of fetal heart cardiac development, specific structural and functional properties of the fetal LV related to this research and specific morphological and physiological adaptations to the fetal cardiovascular system to sustain intrauterine life. Following this, the topic of fetal cardiovascular disease is introduced, with a specific focus on CAS-eHLHS. Current pre- and post-natal intervention options for HLHS and CAS-eHLHS are described, alongside current research evaluating their success and proposing ways to improve patient outcomes.

2.1 Cardiac Development

Congenital heart disease (CHD) has been stated to be a product of abnormal cardiogenesis (Rufaihah et al. 2021). So first the topic of cardiogenesis and further cardiac development in-utero must be introduced. Briefly, the heart develops from cardiac progenitor cells, via cell proliferation (hyperplasia), into two lateral endocardial linear tubes (Harris and Black 2010; Tan and Lewandowski 2019). At around 21 days gestation, the heart tubes begin to merge (Tan and Lewandowski 2019). The merged cardiac tubes begin forming the following regions: the truncus arteriosus, the bulbus cordis, the primitive ventricle, and the primitive atrium (Tan and Lewandowski 2019). Following the formation of these regions and the sinus venosus, the heart begins to pump, with blood flowing into the sinus venosus and up to the truncus arteriosus. The tube then begins to loop ('cardiac looping') and form the distinct LV, right ventricle (RV), left atrium and right atrium (RA) chambers by 28 days gestation (Tan and Lewandowski 2019). At approximately 49 days gestation, the distinct chambers that are observed in the mature heart begin to form and the cardiac valves have developed (Tan and Lewandowski 2019). For the remainder of gestation, continued maturation and refinement of the cardiac structure and function occurs (Rufaihah et al. 2021; Tan and Lewandowski 2019).

2.1.1 Fetal Specific Cardiac Adaptations

Intrauterine fetal development is dependent on the mother's placenta to sustain life and grow, within the isolated and hypoxemic uterus (Cavaliere 2016). Therefore, to facilitate development in-utero, the fetus must have morphological and physiological differences from extrauterine life. Specific intrauterine adaptations include the presence of three shunts. Firstly, a shunt named the ductus arteriosus, which connects the pulmonary artery to the aorta. The ductus arteriosus redirects deoxygenated, or oxygen poor blood, to the lower half of the fetal body to

exit through the umbilical arteries and be reoxygenated via the placenta. The ductus arteriosus ensures the deflated lungs are not overloaded during gestation. Secondly, the ductus venosus shunts oxygenated blood from the umbilical cord to the inferior vena cava, bypassing the liver. Thirdly, once oxygenated blood is received by the right atrium it is shunted via the foramen ovale to the LA. After birth, the ductus arteriosus functionally closes in the following three days, the ductus venosus ceases function once the umbilical cord is cut and the foramen ovale functionally closes soon after birth but may take up to 3 months to anatomically close (Cavaliere 2016). Also, as the lungs are not perfused until birth, they remain deflated throughout gestation, which increases fetal cardiovascular resistance and results in the RV having similar function to the LV. This similarity in fetal ventricular function leads to both ventricles having similar pressure and, therefore, in gestation the LV generally has an asymmetric geometry, with a straighter septal wall, mirroring that of the RV. Postnatally the LV will have greater intracardiac pressure compared to the RV, therefore, being the more dominant cardiac structure and more "prolate" in shape.

2.2 Fetal LV Structure and Mechanics

2.2.1 Myocardial Tissue Architecture

The LV wall is comprised of three layers: endocardium, myocardium, and epicardium (Figure 2.1). The endocardium is the inner most layer of the ventricular wall, formed from endothelial cells (Harris and Black 2010), which are critical for cardiac valve development. The epicardium is the outer most layer of the ventricular wall, formed from mesothelial cells (Harris and Black 2010). The epicardium plays an important role in cardiac development, as it is a supplier of paracrine cues, which perform cellular communication (Quijada et al. 2020). This

ability of the epicardium becomes dormant at birth, however, may reactivate due to trauma later in life (Quijada et al. 2020).

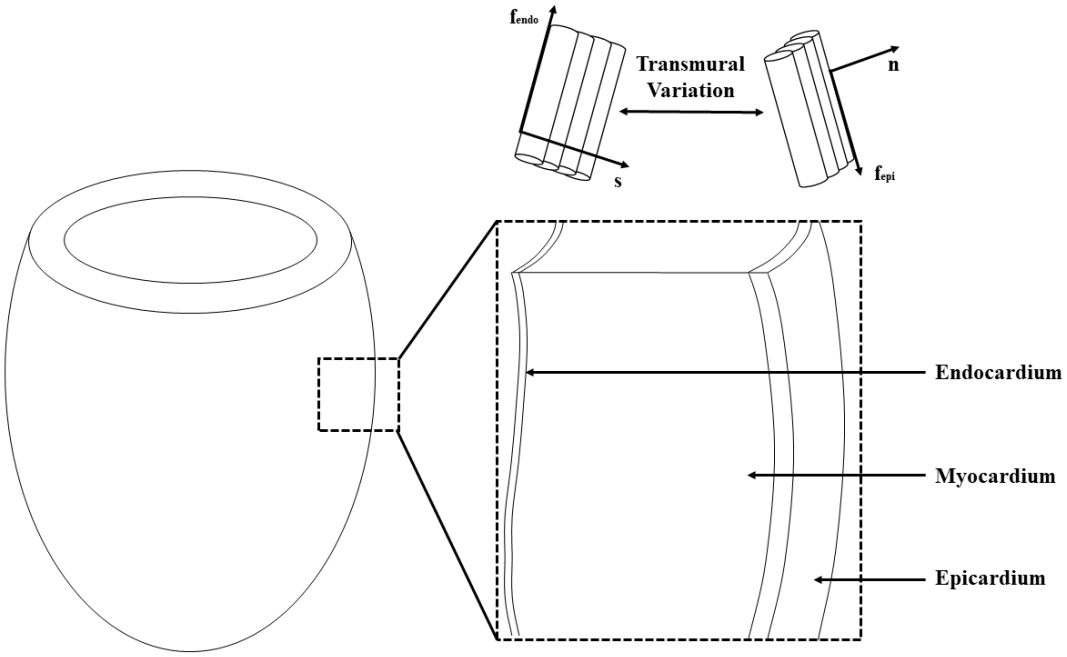

Figure 2.1. *Idealised LV schematic, with hashed box enlarged on the right-hand side to show the details of the layers, from the outer most layer being the epicardium, then the bulk material and middle layer being the myocardium, and the inner, thinnest layer, being the endocardium. Above the enlarged hashed box, details of the myocardial fibrous bundles, that are formed into sheet-like structures, are shown. The sheets rotate throughout the transmural depth of the LV wall, where their directions can be defined by the sheetlet direction (s), normal sheetlet direction (n) and fibre angle which is shown at the endocardium (f_{endo}) and at the epicardium (f_{epi}) in this instance.*

The myocardium consists of an interconnected network of cardiomyocytes, which are generally organised into sheet like structures (Nielles-Vallespin et al. 2017). The helix angle of cardiomyocytes, within these sheet-like structures, have different orientations dependent on

many factors, including, ventricular location, age, and the presence of disease. An example of how the cardiomyocyte structure varies across the LV wall is included in Figure 2.1. Cardiomyocytes are formed from fibrous bundles of myofibrils, where one myofibril is known as a unit of muscle cell. Myofibrils are bundles of proteins, including myosin, actin and titin, which laterally repeat to form sarcomeres. Sarcomeres are the primary contractile unit of the myocardium, aiding the translation of electrical stimuli into mechanical motion, through transmural thickening and apical-basal shortening via the sliding of the myosin and actin filaments (Guan et al. 2020; Yang et al. 2018). The description of the myofiber direction at the endocardium (f_{endo}) and at the epicardium (f_{epi}) are often referred to as helix angle configuration in this thesis, and require assigning in the LV FE modelling methods, along with the sarcomere length, as they help describe the way in which the LV contracts.

Cardiomyocytes are reported to develop from a disordered configuration towards an anisotropic state between 14-20 weeks gestation (Mekkaoui et al. 2013; Pervolaraki et al. 2017). From 20 weeks gestation the LV fibres follow a helical structure with a positive (right-handed) orientation at the sub endocardium and a negative (left-handed) orientation at the sub epicardium (Nishitani et al. 2020). The transmural variation of the LV fibres results in near circumferential alignment of mid-wall fibres.

Imaging modalities have been used to quantify the variations observed in fetal LV helix angle configuration. Through polarised light imaging (PLI), Ohayon et al., reported fetal endo-to-epi helix angle configuration of 55 to -55° (Ohayon et al. 1999), whilst Yang et al. reported endo-to-epi helix angle configuration of 60 to -60° for human neonatal LVs, (Yang et al. 2018). Furthermore, through diffusion tensor magnetic resonance imaging (dMRI), Garcia-Canadilla et al. found mid-wall helix angle configuration to be greater than 0° in the fetal LV and Nishitani et

al. measured the transmural fibre angle to vary from 80 to 120° in 20 fetal cases ranging from 8 to 24 weeks gestation (Garcia-Canadilla et al. 2018; Nishitani et al. 2020).

Differences in quantifications of helix angle configurations could be due to natural variability among fetal hearts or because of the limitations credited to differing image modalities. For example, methodological variation occurs as histological and PLI techniques use *ex vivo* matter, which can result in distortion of matter, whilst dMRI can be conducted *in vivo.* However, dMRI is limited due to resolution constraints, which can only infer helix angle configuration based on global structure (Yang et al. 2018).

2.2.2 Passive Myocardial Stiffness

LV passive myocardial stiffness defines the rigidity of the heart muscle. Titin, a protein present in the sarcomeres, is an exponent of passive myocardial stiffness, with its presence and level of expression regulating the degree of passive stiffness (Lahmers et al. 2004). The value for fetal passive myocardial stiffness is hard to quantify, due to the limited data available. Ren et al., performed biventricular (BV) biaxial mechanical testing of fetal porcine myocardial tissue, to evaluate the variance of passive stiffness across samples, finding passive stiffness to be independent of porcine late fetal and neonatal time points and there to be no appreciable difference in passive stiffness between the LV and RV (Ren et al. 2022).

Passive stiffness is important in the definition of ventricular diastolic function and requires describing when modelling the behaviour of the fetal LV myocardium. Frequently in FE formulation of the LV, the Fung type transversely isotropic hyperelastic constitutive model is applied to define the passive stiffness of LV (Lee et al. 2016; Ong et al. 2020; Shavik et al. 2018). The model is applicable for biological tissues, such as the myocardium, and defines the

tissues as transversely isotropic, such that the material has mechanical properties that are dependent on direction (for example, in the direction of the helix angle), enabling the mathematical description of tissues with aligned fibres (Guccione et al. 1991). Furthermore, the model describes the material as hyperelastic, such that the material experiences a non-linear stress-strain relationship, that is derived from the strain energy density function. Finally, the model is constitutive, meaning that it refers to the description of the mechanical properties of the tissue via mathematical formulation. The complete mathematical formulation of the Fung type transversely isotropic hyperelastic constitutive model, assigned in this thesis, is disclosed in Section 3.3.

2.2.3 Myocardial Active Tension

Myocardial active tension, also referred to as myocardial contractility, is the ability of the myocardium to generate force, which is essential for efficient cardiac pumping. Racca et al., measured the myocardial contractility of healthy fetal tissue samples at 130- and 134-days gestation and found the myocardial contractility to be 49.9 ± 9.3 kPa and 36.0 ± 12.1 kPa respectively (Racca et al. 2016). Whereas, many studies have quantified adult myocardial contractility, with reports varying between 88 – 144 kPa (Asner et al. 2016; Gao et al. 2017; Genet et al. 2014; Land et al. 2017; Wang et al. 2013). Based on the Frank-Starling Law, in healthy hearts, you would expect contractility to increase as SV increases, due to increased myocyte stretch, because of increased ventricular volume (Kirkpatrick et al. 1976; Schwinger et al. 1994). Therefore, although there is limited data on fetal myocardial contractility some interpolation could be performed between the available fetal and adult data, to estimate the myocardial contractility of healthy fetal hearts. The mathematical formulation of myocardial contractility, applied in this thesis, is presented in Section 3.3.

2.2.4 Electrical Activation of the LV

Normal cardiac function involves systematic electrical activation, contraction, and relaxation (Sengupta et al. 2006a). During cardiac contraction the LV longitudinal axis shortens, and the LV wall thickens and twists due to the depolarisation of cardiomyocytes via the electrical signal emitted from the sinoatrial node, which is translated through the heart and distributed through the LV myocardium via the Purkinje fibres. The fibrous architecture of the LV wall is therefore vital to the translation of electrical stimuli to mechanical work, and therefore cardiac function (Buckberg et al. 2008). The mathematical formulation describing the temporal variation of electrical activation, contraction and relaxation of the LV is discussed and recorded in Section 3.3.

2.3 Disease Development

2.3.1 Precedence of CHD

The most common congenital disorder among newborns is CHD (Teun Van Der Bom et al. 2011). In this thesis CHD is defined in accordance with a previous published definition, as "a gross structural abnormality of the heart or intrathoracic great vessels that is actually or possibly of functional significance" (Mitchell et al. 1971). It is reported that moderate to severe forms of CHD affect 0.6-2% of live births (Hoffman and Kaplan 2002). Examples of moderate and severe CHD were collated and documented by Teun Van Der Bom et al., where moderate examples include AVr, right ventricular outflow tract obstruction and mitral disease (Teun Van Der Bom et al. 2011). Severe CHD examples include mitral atresia, which is also referred to as the closure of the mitral valve (MV), and Fontan procedure patients, who are patients undergoing a treatment pathway typically due to having a UV physiology (Teun Van Der Bom et al. 2011).

Information regarding the Fontan procedure (Fontan surgeries) will be elaborated upon in Section 2.4.1, as it is a treatment pathway for patients diagnosed with HLHS.

2.3.2 Pathophysiology of CAS

Aortic stenosis is the narrowing of the AV, where the degree of narrowing can range from mild to severe (NICE 2018). Severe aortic stenosis is also known as CAS, which in this research will only be studied and discussed in relation to the fetal heart.

It is reported that less than 10% of neonates with CAS, that are BV at birth, are identified prenatally (Freud et al. 2015). However, during the time in which CAS develops in gestation, the severity of the stenosis and the rate of disease progression dramatically impacts fetal cardiac functionality (Tulzer and Arzt 2013). For example, for late onset fetal CAS, that has slow progression, the low rate of CAS identification in-utero is not cause for concern, as the fetus would generally be recommended for postnatal therapy nevertheless (Tulzer and Arzt 2013). However, for early to mid-gestation CAS, with moderate to fast progression, deleterious effects on fetal heart physiology and morphology are to be expected (Tulzer and Arzt 2013). Such physiological and morphological aberrations, resulting from CAS, include, increased LV pressure, LV dilation, reduced SV and reduced myocardial strains (NICE 2018; Ong et al. 2020). As the fetal heart is growing and developing via hyperplasia, the reduced SV and myocardial strains are believed to further inhibit LV development, due to altered cardiomyocyte loading and tension generation in gestational development (Shavik et al. 2017; Yutzey 2017). Therefore, early to mid-gestation CAS may result in the onset of additional CHD.

2.3.3 Pathophysiology of HLHS

HLHS is an umbrella term for a multitude of pathophysiology's pertaining to the underdevelopment of the left heart, which includes the LV, LA, MV and AV (Greenleaf et al.

2016; Pickard et al. 2020). Statistics have shown that HLHS affects approximately 1 in 3,481 newborns and is responsible for approximately 25% of deaths related to cardiovascular disease in infancy (Fruitman 2000).

Figure 2.2 depicts a generalised schematic of a HLHS heart, where there is little to no LV cavity volume, a highly stenotic AV (labelled as AoV in Figure 2.2) and a hyperplastic LV wall. HLHS is generally fatal unless treated as it results in the inability of the LV to support systemic circulation.

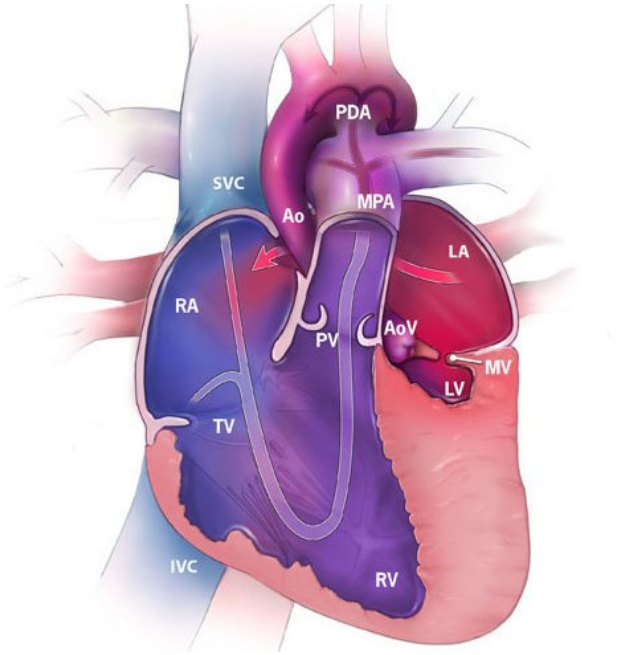

Figure 2.2. *Schematic of an HLHS heart, with an underdeveloped LV, a hypertrophic LV wall and a stenotic AV. Where, RA = right atrium, RV = right ventricle, LA = left atrium, LV = left ventricle, SVC = superior vena cava, IVC = inferior vena cava, MOA = main pulmonary artery, Ao = aorta, PDA = patent ductus arteriosus, TV = tricuspid valve, MV = mitral valve, PV = pulmonary valve and AoV = aortic valve. Image adapted from the Centre of Disease Control and Prevention, shareable under the Creative Common CC0 1.0 Universal Public Domain Dedication* (Centre for Disease Control and Prevention 2013).

2.3.4 Pathogenesis CAS-eHLHS

CAS-eHLHS is a form of CHD occurring in fetal development where there is CAS and there are indicators of HLHS. The aetiology of CAS-eHLHS, like many CHDs, is still unknown. It is believed that the imposed diseased characteristics resulting from CAS can, in certain scenarios, lead to further detrimental LV remodelling, with natural history showing an approximate 73% likelihood of progression to HLHS by birth (Mäkikallio et al. 2006).

CAS-eHLHS, results in major morphological and physiological aberrations, including, globular LV geometries, hypertrophic myocardium, reduced myocardial strains, endocardial fibroelastosis and the presence of mitral valve regurgitation (MVr) (Ishii et al. 2014; Tulzer and Arzt 2013).

2.4 CAS-eHLHS and HLHS Intervention Options

Once CAS-eHLHS has progressed to HLHS, the prognosis is often fatal unless intervened on postnatally (Greenleaf et al. 2016). With scientific and surgical advancements, 70-80% of HLHS patients are now recorded to survive 20 years post-surgeries (Metcalf and Rychik 2020). However, the surgeries are very complex and invasive and have associated complications, which will be discussed in the following section. Pre-natal intervention is now also available, to reduce the likelihood of CAS-eHLHS patients progressing to HLHS. Such intervention will also be introduced and discussed in Section 2.4.2.

2.4.1 Post-natal Intervention for HLHS

The set of Fontan surgeries and/or a heart transplant are the current post-natal options to manage a HLHS birth outcome. The set of Fontan surgeries are considered long-term palliation, and are split into three stages described below (Albers et al. 2010; Metcalf and Rychik 2020):

- Stage I – *Norwood*, performed within days of birth. The surgery aims to enlarge (and if required reconstruct) the aorta and add the Blalock-Taussig shunt between the aorta and pulmonary arteries. The purpose of Stage I is to allow the RV to pump blood to the body, whilst still ensuring enough blood reaches the lungs. These surgical modifications lead to high load on the RV post Stage I.

- Stage II – *Bidirectional Glenn/hemi-Fontan*, performed at approximately 5 months of age. The surgery redirects deoxygenated blood flow from the superior vena cava to the pulmonary artery, thus bypassing the heart and reducing the load experienced by the RV.

- Stage III – *Fontan Operation*, performed in childhood, in which the inferior vena cava is connected to the pulmonary artery, enabling deoxygenated blood to bypass the heart entirely. Stage III further reduces load on the RV and stops oxygenated and deoxygenated blood from mixing in the heart going forwards.

Survival rates following the Fontan surgeries have improved, with one study stating that 70-80% of patients are recorded to survive 20 years post-surgery (Metcalf and Rychik 2020). However, the lifespan of Fontan patients is still compromised due to physical complications associated with the surgeries, such as, protein losing enteropathy, arrhythmia, and clotting (Bernardi et al. 2021; Metcalf and Rychik 2020). Also, more studies are now researching and acknowledging the psychosocial and neurodevelopmental challenges associated with Fontan patients and the subsequent consequences to quality of life (Bernardi et al. 2021; Goldberg et al. 2011; Marshall et al. 2020). Targeted strategies to support the mental health of Fontan patients are now being recommended (Marshall et al. 2020).

Some patients will encounter life-threatening complications associated with the Fontan surgeries, such as refractory heart failure and therefore will require a heart transplant later in life (Kanter et al. 2011). Depending on institutional protocol, donor availability and patient health, a heart transplant may be the primary management option for HLHS patients (Chrisant et al. 2005). However, a heart transplant also has its own set of complexities and complications, such as transplant rejection, risk of infection, failure of donor heart and transplant coronary artery disease. Therefore, although it is a life-saving solution, it is not one without consequence (Dipchand et al. 2013).

2.4.2 Pre-natal Intervention for CAS-eHLHS

Fetal heart interventions aim to normalise haemodynamics in-utero, to promote healthier cardiac growth and development throughout the remainder of gestation (Tulzer and Arzt 2013). Three main lesions for in-utero cardiac intervention are fetal HLHS with intact or restrictive atrial septum, pulmonary atresia with intact ventricular septum and CAS-eHLHS (Friedman and Tworetzky 2020). All interventions for said lesions are catheter based and only performed if there is evidence of worsening cardiac functionality and/or the risk of fetal demise without the intervention (Friedman and Tworetzky 2020).

This thesis specifically focusses on FAV for CAS-eHLHS. FAV aims to widen the stenotic AV of CAS-eHLHS fetal hearts, to promote healthier development in-utero and reduce the likelihood of HLHS. The first form of FAV intervention was undertaken in 1991 (Maxwell et al. 1996). Since 1991, many institutions have adopted and developed the in-utero procedure, with current data showing FAV to have a positive impact on CAS-eHLHS patients, as the likelihood of a HLHS diagnosis at birth is reduced from approximately 73% without FAV (Mäkikallio et al. 2006), to approximately 24-41% with FAV intervention, following a technically successful

intervention, which occurs in approximately 87-94% of interventions (Friedman et al. 2018; Tulzer et al. 2022a). The reduction in progression to HLHS post-FAV is beneficial, as a patient with a BV circulation will not require the set of Fontan surgeries or a heart transplant and will instead undergo relatively minor surgeries in comparison, to correct any re-stenosis of the AV. A recent decision tree analysis, projected an 82% likelihood of transplant-free survival at 6 years of age, following FAV intervention, demonstrating the favourable benefits of the in-utero intervention (Pickard et al. 2020).

Patient selection refinement, improved surgical technique and intervention experience, have helped improve patient outcomes (Patel et al. 2020). One institution reported only 32% of FAVs undertaken between 2000-2008 to be BV at neonatal discharge, which increased to 59% between 2009-2015 (Friedman et al. 2018). However, even with the improved patient outcomes, there are still a substantial number of patients not achieving a BV circulation, post technically successful FAV intervention, for reasons currently unknown (Beattie et al. 2020; Friedman et al. 2018).

2.4.2.1 FAV Intervention Selection Criteria

FAV is performed mid-gestation after CAS-eHLHS has been identified, through echocardiographic examination. Criteria for FAV intervention has developed over the years; however, it is not standardised across institutions. The common theme in determining suitability for FAV intervention however, is whether the fetal heart meets the criteria for an eHLHS diagnosis, which is detailed and agreed upon by two high volume institutions (Friedman et al. 2018; Tulzer et al. 2022a) as:

- Moderate to severe LV systolic dysfunction,
- Monophasic MV inflow,

- Retrograde aortic arch flow,
- Abnormal foramen ovale flow,
- LV long-axis Z Score of >-1.

Other factors that may influence patient suitability for FAV intervention, include gestational age and maternal health. It was also noted in Tulzer et al.'s study that some degree of endocardial fibroelastosis was present across all fetuses imaged (Tulzer et al. 2022a). Although the presence of endocardial fibroelastosis is not included in the selection criteria for FAV intervention, it still may act as an indicator of disease presence, influencing the decision for fetal intervention.

Cases are generally not intervened on if there is evidence the fetal heart will progress to a BV birth outcome without the intervention. For example, aortic stenosis development later in gestation, with mild progression, would not be suitable for in-utero intervention as the patient is likely able to develop sufficiently in gestation (Tulzer and Arzt 2013).

2.4.2.2 FAV Intervention Protocol

FAV intervention is performed on mid-gestation fetal hearts and involves sedating the mother and putting the fetus under analgesics. Following this, under ultrasound guidance, the fetal LV is punctured (Figure 2.3A) with a 17-, 18- or 19-gauge needle and 3-, 4- or 5-mm coronary balloon catheter, dependent on the degree of dilation required (Tulzer et al. 2021b; Tulzer et al. 2021a). When the coronary balloon catheter is aligned in the AV (Figure 2.3B) the balloon is inflated to dilate the valve (Figure 2.3C). Doppler velocity measurements are taken to assess the degree to which the AV has been widened (Figure 2.3D). The expansion of the balloon catheter is performed a few times, to ensure proper resolution of the aortic stenosis before the apparatus is retracted.

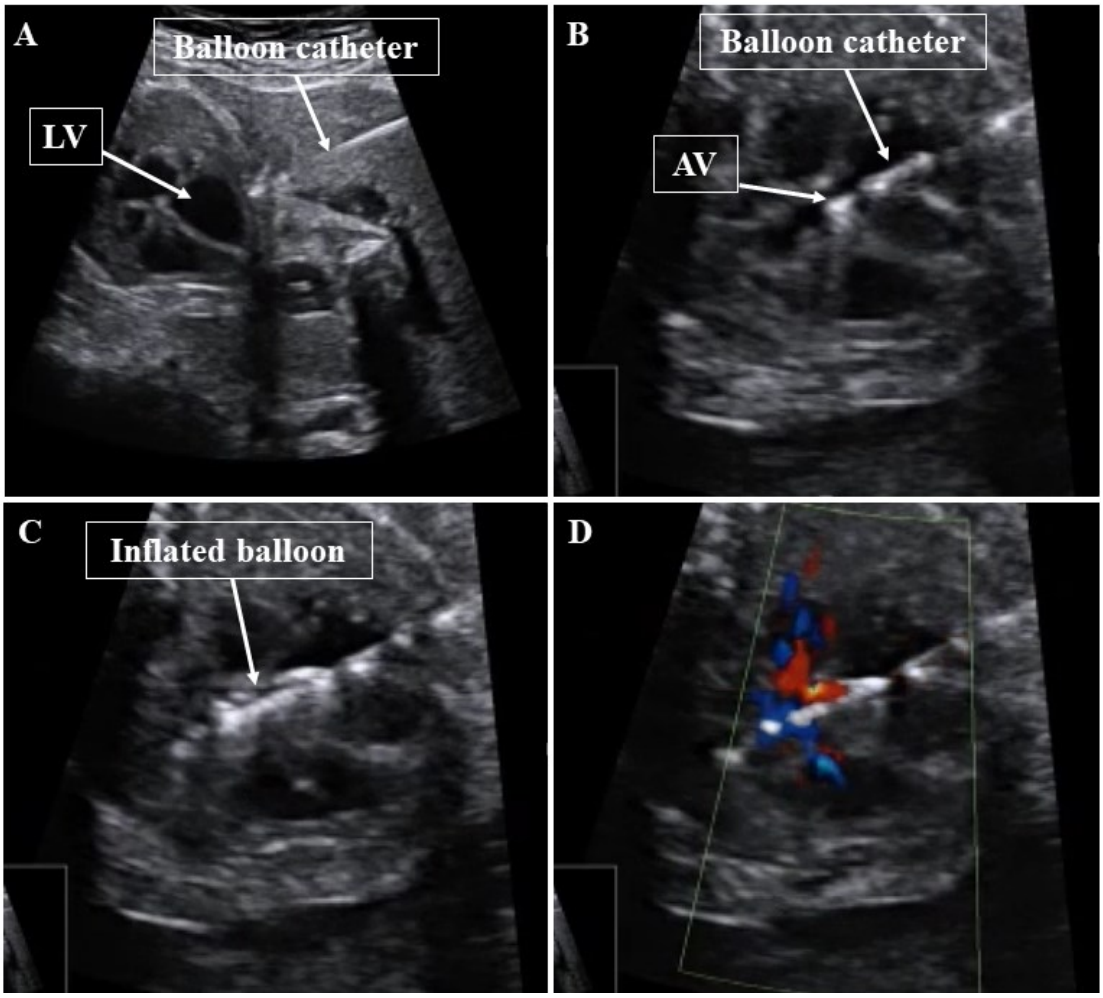

Figure 2.3. *Overview of the stages of FAV intervention. [A] Balloon catheter is puncturing the fetal LV. [B] Under ultrasound guidance the balloon catheter is aligned in the fetal AV. [C] Once aligned in the AV the balloon is inflated to widen the stenotic AV. [D] Doppler velocity measurements are taken to assess the degree in which the stenosis has been relieved. Images taken from a video provided by Dr Gerald Tulzer.*

2.4.2.3 FAV Complications and Risks

Complications associated with FAV intervention include bradycardia and pericardial effusion, with the rate of complications associated with clinician experience, fetal positioning, patient selection, and instrument selection (Patel et al. 2020; Tulzer and Arzt 2013). High

volume institutions have found fetal mortality related to FAV intervention to range from 4-10% (Arzt et al. 2011; McElhinney et al. 2009; Pickard et al. 2020; Tulzer et al. 2022b). Such complications and risk associated with FAV intervention again support the need for further patient selection refinement.

2.4.2.4 Current FAV Patient Selection Refinement

Recent retrospective studies have analysed FAV patient cohorts in an attempt to predict how patients will respond to intervention (i.e., go on to be BV or UV). Tulzer et al. recursively separated 79 FAV patients based on observations to determine variables for predicting FAV outcomes, using classification and regression tree (CART) analysis. The study found that pre-FAV RV/LV length ratio had strong predictive influence and when combined with pre-FAV gestational age and MVr velocity, the CART analysis was able to identify all cases that went on to be BV (Tulzer et al. 2022a). Friedman et al. again performed CART analysis on pre-FAV data and found the best indications of a BV outcome post-FAV, were ascending aorta dimension Z Score and LV pressure estimated (Friedman et al. 2018). Beattie et al. analysed post-FAV predictors of BV outcomes and found a long axis Z Score > -2.3 (i.e., a larger LV long axis) and ejection fraction (EF) > 28% led to an 81.5% chance of a BV circulation at birth (Beattie et al. 2020).

Such predictive work requires multi-centre prospective studies to validate the findings, and if proven to be accurate the predictive parameters identified could be used to refine patient selection criteria, support parental counselling, and aid surgical planning.

2.5 Cardiac FE Studies

FE modelling is the discretisation of a continuous domain into a finite number of elements, where each element represents a portion of the overall structure being analysed. This

approach characterises the domain in question by incorporating essential factors such as material properties, boundary conditions and governing equations. In the field of cardiac biomechanics FE modelling is a valuable numerical tool as it can capture the structure and behaviour of cardiac muscle, allowing for non-invasive exploration, thus providing insights into aspects of cardiology that are challenging to measure *in vivo*. Alternatives to FE modelling, in the context of cardiology, include computational fluid dynamics modelling, which focuses on the numerical analysis of blood flow; biological models, which involve using animal hearts (e.g. porcine, ovine) or human cadaveric hearts to create physiological replicas and characterise cardiac function and fluid structure interaction models, which analyse the interaction of fluid flow and solid structures, therefore, in this context may be used to assess the hemodynamic performance of heart valves. The purpose of this research is to evaluate the biomechanics of the fetal myocardium in CAS-eHLHS fetal hearts pre- and post-FAV intervention; therefore, computational fluid dynamics models and fluid structure interaction models are not relevant for this purpose, whilst biological models are limiting due to the availability of matter that closely represents the fetal cardiac structure and the time-consuming nature of such experiments. Therefore, FE modelling will play a pivotal role in this research to help advance understanding of the biomechanics of CAS-eHLHS fetal hearts.

Currently, the majority of published cardiac FE studies use infant or adult data, due to many reasons, including the availability of images and measurements (such as blood pressure). For example, through FE modelling, Shavik et al. found adult LV myocardial strain to be sensitive to contractility and LV loading conditions (Shavik et al. 2017). Such discoveries are interesting, as certain disease phenotypes will likely have alterations in ventricular loading, contractility and/or strain, therefore the interdependency of these biomechanics characteristics,

how they vary in disease phenotypes and the consequences such variances may have on the morphology and physiology of the LV require further investigation. The application of FE modelling for surgical planning was researched by Cutrì et al., who investigated the biomechanics of one patient specific LV after Stage I Fontan palliation and predicted surgical outcomes with computational techniques, post Stage II (Cutrì et al. 2017). These methods allowed the analysis of stress and strains pre and post Stage II, to comprehend the health of LV, with future work aiming to support decisions on surgical timing and drug support (Cutrì et al. 2017).

A few studies have begun investigating the role biomechanical aberrations have on fetal cardiac functionality. Dewan et al., explored the relationship between fetal myocyte growth rate and restricted ventricular filling, due to mitral stenosis (Dewan et al. 2017). The work alluded to a link between loading on the myocytes from ventricular filling and growth (Dewan et al. 2017). Although the work was done on idealised models, it showed the capabilities of FE in investigating a multitude of fetal morphologies and developing ideology for the causation of morphological aberrations observed in fetal mitral stenosis patients. The most relevant computational publication to this research utilised a simplified electrical circuit also known as a LPM coupled with FE methods (Ong et al. 2020). Where a LPM is a simplified representation of a physical system or components of a physical system, using discrete electrical elements or parameters that are analogous to physiology, in Ong et al.'s case a LPM describing flow in and out of the LV was used, which enabled the study of hypothetical levels of aortic stenosis to investigate different fetal LV disease scenarios (Ong et al. 2020). The study found that aortic stenosis increases LV pressure and myofiber stress and reduces directional strains and SV (Ong et al. 2020). The presence of MVr was shown to moderate the effects of aortic stenosis (Ong et

al. 2020). Ong et al.'s research began to investigate the effect of aortic stenosis and LV hypertrophy on fetal LV functionality and acts as the basis for the following investigations included in this thesis.

2.6 Conclusion

FAV has shown promise in promoting healthier development in-utero and reducing the likelihood of progression to HLHS. However, there is the need to better understand CAS-eHLHS and the impact of FAV intervention, to help refine patient selection criteria, support parental counselling, and aid surgical planning.

Chapter 3: Computational Methods

This chapter describes the steps used to build patient specific models of fetal hearts, the fundamentals of the LPM, and FE methods. These methods will be used throughout this thesis and are therefore meticulously detailed in this chapter as a point of reference.

3.1 Patient Specific Model Generation

Methods and tools to build the patient specific models for both healthy and diseased fetal hearts follow the same process, described below.

3.1.1 Image Acquisition

2D and 4D images with pulse wave Doppler tracings were acquired from two databases. The first database comprised of 44 healthy fetal hearts sourced from the National University Hospital, Singapore. From this database a subset of 6 healthy fetal hearts spanning various gestational ages were selected. The second database comprised of 126 CAS-eHLHS patients sourced from Kepler University Hospital, Austria. Within this dataset 36 patients had 4D images, while the remaining patients only had 2D images available. Notably, at the time of the study, 9 of the 36 patients with 4D images, had usable 4D images accompanied by complete Doppler tracings.

Data acquired from the National University Hospital, Singapore, was done so with the approval of the Domain Specific Review Board under protocol 2014/00056 and by receiving informed consent from all participants. Data acquired from Kepler University Hospital, Austria, was approved by the Institutional Review Board, with the protocol number 1009/2017 and by receiving informed consent from all participants. All data was anonymised.

3.1.2 Image Processing and Segmentation

Firstly, the 4D B-Mode images acquired from the clinical collaborators were analysed in 4DView (FE Healthcare, USA), to evaluate the image quality of each case. Selected 4D B-Mode images were then split into individual unit time steps and exported from 4DView as videos scanning through the transmural depth of the four-chamber plane view at each time point (Figure 3.1A). Each video was then broken down into slices, 0.5 mm apart, from the anterior to posterior

(Figure 3.1B). The Lazy Snap algorithm (Li et al. 2004) was then used to annotate the LV myocardium, left atrium cavity (endocardial wall) and RV cavity (endocardial wall) (Figure 3.1C). The Lazy Snap algorithm is a semi-automatic cutout tool, where the user marks the object they require tracing and the algorithm then determines the pixels that require the least energy to break up, using pixel to pixel recognition (Li et al. 2004). The algorithm provides instant visual feedback of the snapping contour achieved by the object marking (Li et al. 2004). The Lazy Snap algorithm was compared to a leading cutout tool, Magnetic Lasso, for ease of use, efficiency, and quality of results, using a cohort of 14 subjects, where the Lazy Snap algorithm was shown to outperform Magnetic Lasso across all three categories (Li et al. 2004). An example of the manual constraints is shown in Figure 3.1C, where the blue line is tracing the foreground, the red line is helping bound the tracing and the green line is the output bounds based on the algorithm and the constraints manually imposed. The LV myocardium was generally traced for a minimum of 2 time points for healthy cases and 1 for diseased.

Due to the size of the fetal heart and ultrasound resolution, smaller details such as the papillary muscles, chordae tendineae and trabeculae were not included in the tracings or were smoothed out at later points if included. The segmented tracings were exported from the Lazy Snap algorithm as binary images, which were reconstructed as a 3D STL using the Vascular Modelling Toolkit (VMTK). VMTK also initially smoothed any irregularities and instabilities which occurred during the Lazy Snap tracings. Further smoothing of any irregularities was conducted in Geomagic Studio (Geomagic Inc., Morrisville, NC, USA), where the smoothed STL was concurrently overlaid onto the stacked images from the 4D scans in MATLAB, to ensure the match between reconstructed STL and patient data remained and no shrinkage or deviation from imaged data occurred in the smoothing process.

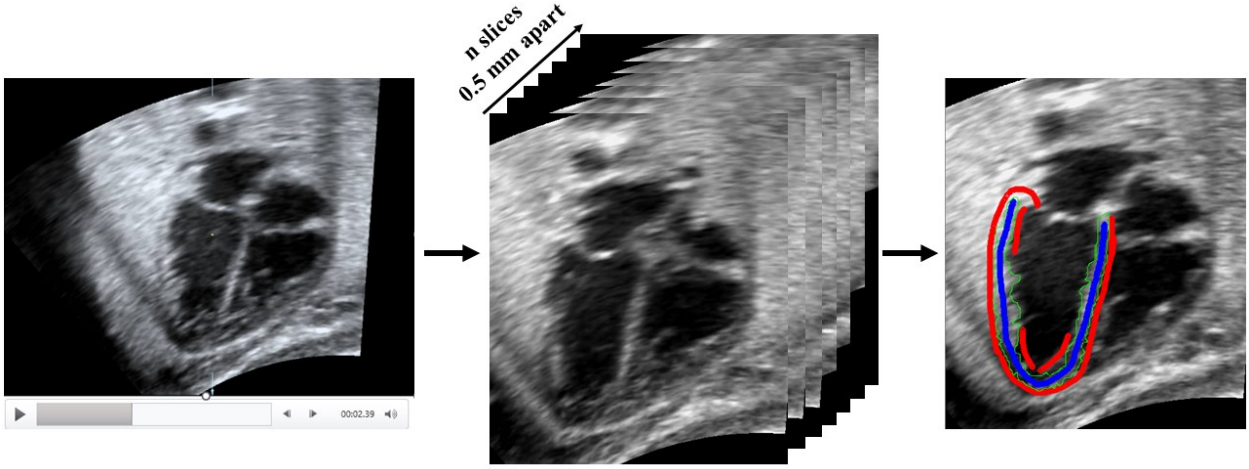

Figure 3.1. *Ultrasound image processing steps. [A] Unit time video capture, which scans the fetal heart from anterior to posterior. [B] Sliced images extracted from each video. [C] Example of Lazy Snap algorithm showing manual tracings in blue and red, with green line showing the bounded output from the algorithm.*

3.1.3 Cardiac Motion Estimation

The image registration steps, with an additional add-on regularisation framework, form the cardiac motion estimation methodology. The add-on regularisation framework was designed and tested by Wiputra et al., with details on how the framework operates following the image registration steps included below for context (Wiputra et al. 2020). Firstly, using the Python module, SimpleElastix, pairwise image registration is conducted to determine what transformation is required to align subsequent 2D images (like those in Figure 3.1B). Forward marching (the process of moving through the path of stacked images) then accumulates the local displacement fields between the stacked images, to produce landmarks acting as the ground truth (Wiputra et al. 2020). With noise present in the images (particularly in fetal heart images), some form of regularisation framework is often incorporated or added to impose some factor of

smoothing and reduce motion estimation error (Wiputra et al. 2020). For example, some form of cyclic constraint may be applied to ensure the original state is achieved at the end of the cardiac cycle, as expected *in vivo*. In this instance, to minimise temporal inconsistencies, an additional add-on regularisation framework, coined b-spline of Fourier (BSF), was designed and deployed post image registration (Wiputra et al. 2020). BSF is a spatial-temporal model, where b-splines are employed to capture the local spatial variations in the stacked images and the Fourier based function is employed to periodically describe the cardiac cycle and employ some degree of temporal smoothing. The BSF model is run in a systematic approach. Firstly, the BSF reference frame is defined. Then consistency correction is iteratively performed to optimise the fit between the BSF frame and the earlier computed image-registration displacement fields. Finally, to calculate the motion of a landmark over time, which are identified in the earlier image registration steps, the landmark coordinate is mapped onto the optimised BSF reference frame (Wiputra et al. 2020). The add-on regularisation framework helps improve spatio-temporal smoothness, temporal consistency and enforce cyclicity, during cardiac motion estimation. The source code for the cardiac motion estimation methods can be found here: https://github.com/WeiXuanChan/motionSegmentation.

In this work, the cardiac motion estimation methods are used over the entire four chambers view of the heart, to capture the motion of the LV myocardial wall and left atrium and RV endocardial wall deformations. Examples of the motion achieved for a healthy fetal LV are included below in Figure 3.2.

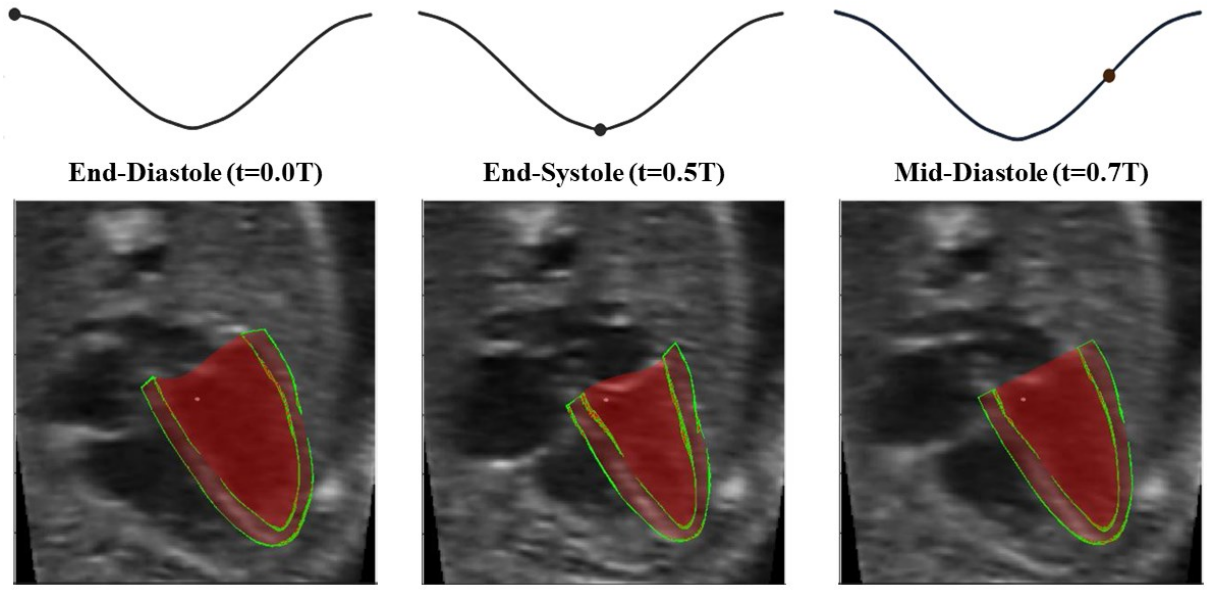

Figure 3.2. *Reconstructed fetal LV superimposed onto a cross-section of the ultrasound image, at 3 time points in the cardiac cycle, where T is the duration of the cardiac cycle. Red – signifies the 3D LV reconstruction, green – identifies the portions of the 3D reconstruction that are in the image plane shown.*

The volume variation over a cardiac cycle for each cavity is calculated through extracting the endocardial wall, and computing the cavity volume at each time step, using the cardiac motion estimation algorithm.

An additional regularisation step was applied to the healthy fetal hearts, as they typically exhibit larger SV and EF compared to the diseased fetal hearts. The additional regularisation step, called additional inputs, required the end systolic volume (ESV) of the healthy fetal hearts to be traced using the earlier discussed Lazy Snap algorithm (Section 3.1.2). The ESV tracing was then used as a secondary anchor, to constrain the ESV time point and better describe the motion of the cavity, ensuring that the cardiac motion estimation algorithm could better capture the larger deformational changes of the healthy fetal hearts.

3.2 LPM Background and Fundamental Equations

In this thesis the LPM model of the fetal circulatory system was coupled to the FE methods, enabling ventricular vascular coupling. Furthermore, the LPM enhances the ability to incorporate disease characteristics, which will be discussed and demonstrated in future chapters. However, before delving into this, it is essential to provide a foundational explanation of the LPM utilised in this study, which is a task undertaken here in Section 3.2.

3.2.1 Background

Mathematical-electrical models which discretise circulatory systems are useful tools to extract data that cannot be measured *in vivo* and predict outcomes based upon different scenarios. Pennati et al., proposed such a model to describe the full fetal heart and vascular bed (Pennati et al. 1997). The LPM uses capacitors, resistors, and diodes to represent the compliance of vessels, the flow of blood and cardiac valves respectively (Pennati et al. 1997). These principles are based upon Otto Frank's original electrical analogy of biological systems, the Windkessel model (Sagawa et al. 1990). Pennati et al.'s LPM was originally built for 38 weeks gestation fetuses and calibrated using lamb data and non-invasive near-term fetal data, such as blood flow rates (Pennati et al. 1997).

3.2.2 Modelling Fundamentals

The LPM comprises of two systems, the heart, and the vascular bed, where the heart refers to the LV, RV, left atrium and right atrium and the vascular bed refers to the 19 compliant vessels, such as the intestinal circulation (IN) and the lower members (LEG), shown in Figure 3.3. The governing equations of the LPM used in this thesis are described in the following publications (Pennati et al. 1997; Pennati. and Fumero. 2000), and are briefly detailed below for

context. Firstly, the instantaneous pressure of the ventricle is computed via the following equation,

$$p_V(t) = U_0 \cdot A(t) + \left(E_{dia} + E_{sys} \cdot A(t)\right) \cdot V(t) + R_v \cdot \frac{dV(t)}{dt}, \qquad \text{Equation 3.1}$$

where: $\frac{dV(t)}{dt}$ is the change in ventricle volume; R_v the ventricle resistance; $E_{dia} + E_{sys}$ are the elastic properties of the ventricle at diastole and systole respectively; and U_0 is the isovolumetric pressure generator constant, with time dependency described via $A(t)$ (Pennati. and Fumero. 2000). Where, change in volume is computed via the flowrates, with an example equation for change in LV volume included below,

$$\frac{dV_{LV}(t)}{dt} = Q_{mv}(t) - Q_{ao}(t), \qquad \text{Equation 3.2}$$

where, $Q_{mv}(t)$ is the flowrate entering the LV via the mitral valve and $Q_{ao}(t)$ is the flowrate leaving the LV, via the aortic valve. The atrium is modelled by a compliance, dependent on time in the cardiac cycle (Pennati et al. 1997), with the additional parameters of amplitude, peak time and width included to define the atrium pressure variation over a cardiac cycle.

The pressure drop through the valves are modelled using Equation 3.3 (Pennati et al. 1997),

$$\Delta p(t) = K \cdot Q(t)^2, \qquad \text{Equation 3.3}$$

in which K is the valvular dissipative coefficient and $Q(t)$ is the volumetric flowrate as a function of time in the cardiac cycle (Pennati et al. 1997). The standard model prevents bi-directional flow.

Each component of the vascular system that is defined in the LPM, for example, the aortic arch (AA), is modelled using mass conservation law (expressed in Equation 3.4 and illustrtated in Figure 3.3 for flow in and out of the AA), where the flow in (Q_{in}) and out (Q_{out}) of the component is equated to the capacitance (C) of the component, also known as the compliance of the vessel, multiplied by change in pressure $\left(\frac{dp(t)}{dt}\right)$,

$$C \cdot \frac{dp(t)}{dt} = \sum Q_{in}(t) - \sum Q_{out}(t). \qquad \text{Equation 3.4}$$

The connection between components in the vascular bed is described using Equation 3.5,

$$\Delta p(t) = R \cdot Q(t) + L \cdot \frac{dQ(t)}{dt}, \qquad \text{Equation 3.5}$$

where R describes the viscous resistance of flow between components, such as the AA and aortic arch (AO1), and L describes the inductance, which represents the inertial phenomena of blood flow and is only present in descriptions of large arteries that are close to the heart, like the connection between AA and AO1, which is illustrated in Figure 3.3.

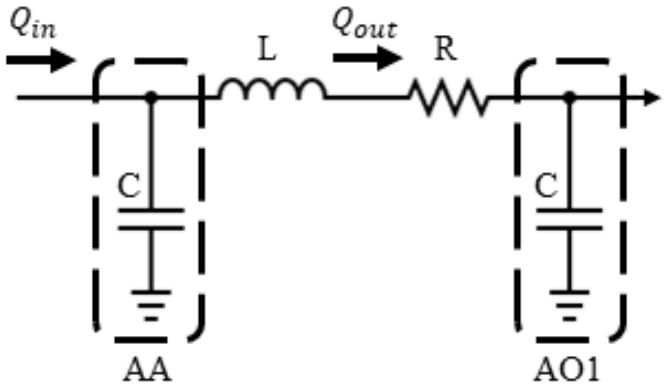

Figure 3.3. *Electric circuit demonstrating flowrate in and out of AA, the connection between AA and AO1 and the associated capacitors of each vessel.*

In fetal shunts, such as the ductus venosus (DV), $D \cdot Q(t)^{\beta}$ is added to Equation 3.5, to describe the unique local haemodynamics occurring at these fetal specific shunts. *D* describes the dissipative behaviour of the fetal shunts and β is the coefficient dependent on local haemodynamics (Pennati et al. 1997; Pennati. and Fumero. 2000).

Figure 3.4 maps the relationship between components of the fetal circulatory system described in this thesis and previous publications (Pennati et al. 1997; Pennati. and Fumero. 2000). Appendix 3.1 contains the original values for each parameter with their full name and associated acronym.

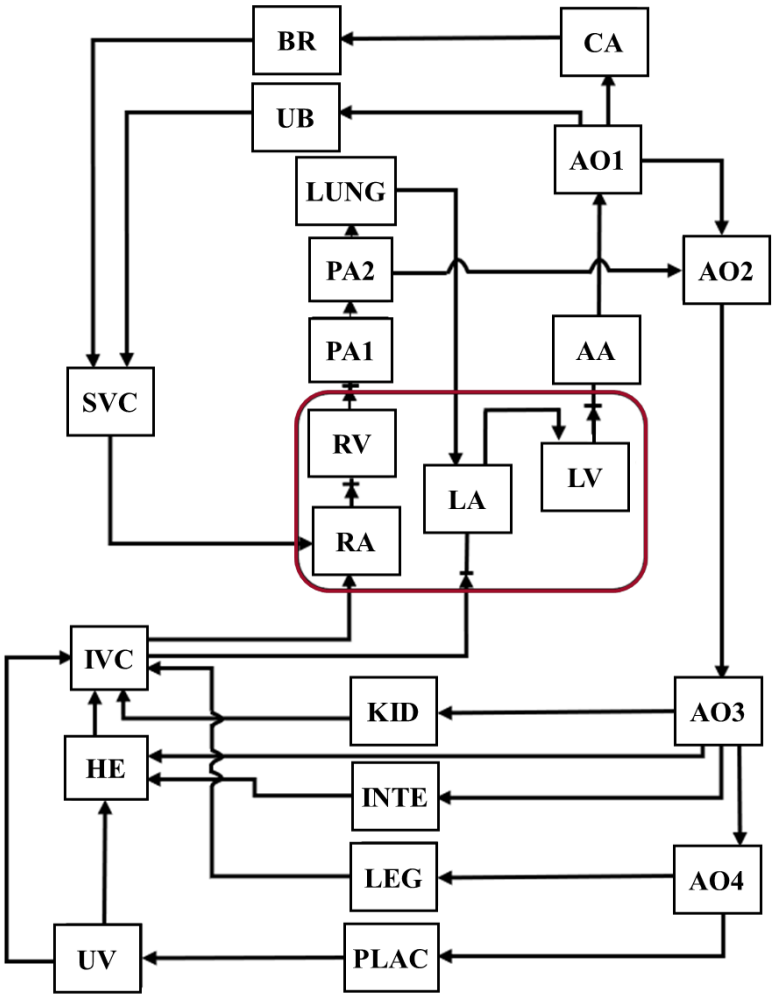

Figure 3.4. *Schematic of LPM representing the fetal circulatory system, where vessels in the red box represent the heart and those outside represent the 19 components of the vascular bed. Arrows show the direction of the flow. Note, AA: ascending aorta, AO1: aortic arch, AO2: thoracic descending aorta, AO3: abdominal descending aorta, AO4: femoral bifurcation, BR: brain, CA: cerebral arteries, HE: liver, INTE: intestinal circulation, IVC: inferior vena cava, KID: kidney, LA: left atrium, LEG: lower limbs, LUNG: lungs, LV: left ventricle, PA1: main pulmonary artery, PA2: pulmonary arteries, PLAC: placenta, RA: right atrium, RV: right ventricle, SVC: superior vena cava, UB: upper body, UV: umbilical vein. Figure adapted from published work* (Pennati. and Fumero. 2000).

3.2.3 Gestational Age Scalability

To overcome the inability to model differing gestational ages in the original LPM (Pennati et al. 1997), Pennati et al. later developed a series of allometric equations to scale all components of the fetal LPM based upon gestational age (Pennati. and Fumero. 2000). The LPM was scaled based on the principle that any biological variable can be related to its body size via the allometric equation shown in Equation 3.6 (Pennati. and Fumero. 2000),

$$Y_{weeks\ gestation} = Y_{38} \cdot \left(\frac{W_{weeks\ gestation}}{W_{38}}\right)^{b}, \qquad \text{Equation 3.6}$$

where, Y_{38} is the reference value, relating to the 38 weeks gestation time point, W_{38} is the fetal weight at 38 weeks gestation, $W_{weeks\ gestation}$ is the fetal weight at weeks gestation being modelled and b is the scaling factor. Fetal weight is computed based on the following relationship with fetal age,

$$log_{10}(W_{weeks\ gestation}) = 0.2508 + 0.1458 \cdot weeks\ gestation - 0.0016 \cdot weeks\ gestation^{2}. \qquad \text{Equation 3.7}$$

The circulatory terms (resistors, capacitors, inductors and dissipative terms) in the LPM, have physical analogies in which their variation with weeks gestation can be derived from. The resistive terms, R, are related to the cylindrical vessel dimensions of each component via Poseuille theory, shown in Equation 3.8,

$$R = \frac{8\mu l}{\pi a^{4}}, \qquad \text{Equation 3.8}$$

where, μ is the blood viscosity, l is vessel length and a is vessel radius. Pennati et al. assumed blood viscosity to remain constant across gestational age and assumed length and vessel radius to

have a scaling factor of 0.33 (Pennati. and Fumero. 2000), in accordance with Holt et al.'s derivation that anatomical quantities can be related to the cube root of body weight, under the assumption of constant density (Holt et al. 1981). Therefore, the resultant scaling factor for the variance of resistance with gestational age was b = -1, and Equation 3.6, was modified to become,

$$R_{weeks\ gestation} = R_{38}\left(\frac{W_{weeks\ gestation}}{W_{38}}\right)^{-1}. \qquad \text{Equation 3.9}$$

Dissipative terms (D) included in the LPM capture energy losses resulting from disordered localised hemodynamics (Pennati. and Fumero. 2000). To compute the dissipative terms, Equation 3.10a and 3.10b were equated and rearranged for D, to provide Equation 3.10c,

$$\Delta P = \frac{\rho k v^2}{2}, \qquad \text{Equation 3.10a}$$

$$\Delta P = DQ^2, \qquad \text{Equation 3.10b}$$

$$D = \frac{\rho k}{2\pi^2 a^4}, \qquad \text{Equation 3.10c}$$

where, ρ is the blood density, k is the experimental coefficient, v is the flow velocity and Q is flow rate. Both ρ and k were assumed to remain constant across gestational age. Then, assuming the radius again has a scaling factor of 0.33, D scales with gestational age via a factor of b = -1.33 and Equation 3.6 can be modified to become,

$$D_{weeks\ gestation} = D_{38}\left(\frac{W_{weeks\ gestation}}{W_{38}}\right)^{-1.33}. \qquad \text{Equation 3.11}$$

L was calculated from previous derivations (Rideout 1972), as shown here,

$$L = \frac{\rho l}{\pi a^2}, \qquad \text{Equation 3.12}$$

and following the same scaling assumptions, b = -0.33 for inductance, therefore Equation 3.6 can be modified to become:

$$L_{weeks\ gestation} = L_{38}\left(\frac{W_{weeks\ gestation}}{W_{38}}\right)^{-0.33}. \qquad \text{Equation 3.13}$$

Finally, C can be described also from previous derivations (Rideout 1972), and represented as,

$$C = \frac{3\pi a^3 l}{2Ew}, \qquad \text{Equation 3.14}$$

where, E is the Young's modulus and w is vessel thickness. The product Ew was assumed to remain constant, with increasing gestational age. Therefore, assuming the same scaling relationship, b = 1.33 for capacitance, and Equation 3.6 can be rewritten as such,

$$C_{weeks\ gestation} = C_{38}\left(\frac{W_{weeks\ gestation}}{W_{38}}\right)^{1.33}. \qquad \text{Equation 3.15}$$

3.2.4 Limitations of the LPM

Pennati et al.'s work was a step towards improving understanding of the fetal circulatory system, through the inclusion of fetal specific circulatory components in the LPM (Pennati et al. 1997; Pennati. and Fumero. 2000). The capability to scale the model for fetal gestational age enabled age specific fetal parameters, such as pressure, that are difficult to measure in-utero, to be estimated (Pennati et al. 1997; Pennati. and Fumero. 2000).

However, the model includes a range of limitations, firstly, the LPM is a simplified representation of the fetal heart, major vessels and placenta, therefore, the model employs lumped parameters to represent various segments of the circulation, to capture the overall behaviour, rather than explicitly describing every detail of the fetal circulatory system, such as,

all veins and arteries. Secondly, the model uses lamb data to define atrial compliance and all compliances outside of the heart and U_0 for the LV, due to the unavailability of fetal data. Also, several assumptions were made in the study (Pennati et al. 1997; Pennati. and Fumero. 2000), which have now been disproven. The assumption that blood viscosity remains constant with gestational age was disproven (Jopling et al. 2009; Kwon et al. 2008), as haematocrit percentage was shown to change with gestation age (Jopling et al. 2009) and the changes in haematocrit levels were shown to vary blood viscosity (Kwon et al. 2008), which means the *b* scaling factor for resistance is based upon incorrect assumptions. Furthermore, the assumption that *Ew* remains constant with gestational age is believed to be incorrect, as Jacot et al. showed the Young's Modulus of neonatal mice LVs to be approximately 3 times greater than at embryonic stages (Jacot et al. 2010) and from clinical based measurements LV wall thickness is shown to increase with gestational age (Daimei et al. 2014). Therefore, *Ew* would be expected to increase with gestational age, indicating that the *b* scaling factor for capacitance is also incorrect.

At the time of publication Pennati et al. was able to show the outputs from the LPM sufficiently matched 2D volume echocardiographic data. However, since Pennati et al.'s work, Johnson et al. has measured fetal intracardiac pressure at multiple gestational ages (Johnson et al. 2000). The ability to validate the LPM with LV pressure data would also improve the accuracy of the LPMs outputs.

Based upon this information, further work was required to evaluate the fit between the age scalable LPM and fetal intracardiac pressure measurements, to determine how the resistance and capacitance scaling should be changed, to account for the earlier assumptions which have now been disproven.

3.3 Fetal LV Myocardium Constitutive Model

The LV myocardium constitutive model is the mathematical description of the myocardial tissue mechanics, throughout the cardiac cycle. The LV myocardium constitutive model described in this section and utilised throughout the following study is built upon previous work (Ong et al. 2020; Shavik et al. 2017).

Equation 3.16 is a governing equation of the myocardium constitutive model and ensures the LV remains in a state of mechanical equilibrium, where $\boldsymbol{\sigma}$ describes the stress tensor, which is the summation of its active ($\boldsymbol{\sigma_a}$) and passive ($\boldsymbol{\sigma_p}$) constituents, as shown in Equation 3.17,

$$\nabla \cdot \boldsymbol{\sigma} = 0, \qquad \text{Equation 3.16}$$

$$\boldsymbol{\sigma} = \boldsymbol{\sigma_a} + \boldsymbol{\sigma_p}. \qquad \text{Equation 3.17}$$

The active properties of the LV myocardium, $\boldsymbol{\sigma_a}$, describe how the myocardium contracts, based on the sigmoidal relationship between chemical activation and the maximum tension of the cardiac muscle in the local fibre direction. The relationship is derived from a published study (Guccione et al. 1993) and is described in Equation 3.18,

$$\boldsymbol{\sigma_a} = T_{0LV} \frac{Ca_0^2}{Ca_0^2 + ECa_{50}^2} C_t e_f \otimes e_{f_0}, \qquad \text{Equation 3.18}$$

where T_{0LV} is the maximum fibre tension, Ca_0 represents the peak intracellular calcium concentration and e_f and e_{f_0} describe the local vectors in the myocardial fibre direction and reference configuration respectively. ECa_{50} which describes the calcium sensitivity dependent on sarcomere length is calculated by,

$$ECa_{50} = \frac{(Ca_0)_{max}}{\sqrt{\exp(B(l-l_0))-1}}, \quad \text{Equation 3.19}$$

where $(Ca_0)_{max}$ is the maximum peak intracellular calcium concentration, B is a constant, l is the sarcomere length and l_0 is the relaxed sarcomere length at which there is no active tension.

C_t in Equation 3.18 describes the temporal variation occurring during calcium activation, calculated by Equation 3.20,

$$C_t = \frac{1}{2}(1 - \cos\omega), \quad \text{Equation 3.20}$$

where ω is dependent on the cycle time, discretised by the following functions,

$$\omega = \begin{cases} \pi\dfrac{t}{t_0} \; when \; 0 \leq t < t_0 \\ \pi\dfrac{t - t_0 + t_r}{t_r} \; when \; t_0 \leq t < t_0 + t_r \\ 0 \; when \; t_0 + t_r \leq t, \end{cases} \quad \text{Equation 3.21}$$

where t_0 is the time to peak tension, which specifies how long it takes the myofibers to contract and t_r is the relaxation time, which is calculated using the following equation,

$$t_r = ml + b, \quad \text{Equation 3.22}$$

where m is the gradient of linear relaxation duration in relation to sarcomere length, b is the time intercept of linear relaxation duration with sarcomere length and l is the sarcomere length, dependent upon the degree of myofibre stretch.

The passive properties, $\boldsymbol{\sigma_p}$, of the myocardium are essential for the definition of ventricular compliance and define the tissue properties when force is not actively being produced. $\boldsymbol{\sigma_p}$ is calculated as,

$$\boldsymbol{\sigma_p} = \frac{1}{J}\boldsymbol{F}\frac{\partial \boldsymbol{W}}{\partial \boldsymbol{E}}\boldsymbol{F^T}, \qquad \text{Equation 3.23}$$

where, J is Jacobian of the deformation gradient tensor, as shown in Equation 3.24,

$$J = det(\boldsymbol{F}), \qquad \text{Equation 3.24}$$

with $\boldsymbol{F}$ calculated by,

$$\boldsymbol{F} = \boldsymbol{I} + \nabla \boldsymbol{U}, \qquad \text{Equation 3.25}$$

and $\boldsymbol{U}$, in Equation 3.25 describes the displacement of coordinates within the myocardium. Following this, $\boldsymbol{W}$, in Equation 3.23 describes the strain energy function, using the Fung type transversely isotropic hyperelastic constitutive model (Guccione et al. 1991; Humphrey and Yin 1987),

$$\boldsymbol{W} = \frac{1}{2}Co(e^{\boldsymbol{Q}} - 1), \qquad \text{Equation 3.26}$$

where Co is the passive stiffness coefficient, initially assigned as 200 Pa based upon Ong et al.'s. conclusions (Ong et al. 2020). The model is then expanded as shown in Equation 3.27, where the Green Lagrange strain tensors (E), in the myocardial fibre (f), sheet (s) and sheet normal (n) directions are defined, with b and the associated subscripts ff, xx and fx describing the stiffness coefficients in the fibre, sheet and shear directions respectively, as seen below,

$$\boldsymbol{W} = \frac{1}{2}Co(e^{b_{ff}E_{ff}^2 + b_{xx}\left(E_{ss}^2 + E_{nn}^2 + E_{sn}^2 + E_{ns}^2\right) + b_{fx}\left(E_{fn}^2 + E_{nf}^2 + E_{fs}^2 + E_{sf}^2\right)} - 1). \qquad \text{Equation 3.27}$$

3.4 Generic Preprocessing and Solver Methods

A description of the preprocessing methods required to initiate an FE simulation and details of the FE formulation solved.

3.4.1 Geometry Meshing

The LV geometries are meshed in Gmsh, an open-source FE mesh generator. The geometries are meshed with at least 2,500 quadratic tetrahedral elements, based on a previous mesh convergence study (Ong et al. 2020).

3.4.2 Myofiber Configuration Assignment

The orientation of the myofibers in the LV myocardium is a crucial factor in defining LV FE problems, as it helps dictate LV contraction, as described by Guccione et al.'s active contraction formulation, defined in Section 3.3 (Guccione et al. 1993). Across all simulations, in this thesis, the helix angle configuration was assigned to the meshed geometries via the Laplace-Dirichlet Rule-Based (LDRB) algorithm (Bayer et al. 2012).

Firstly, the LDRB requires the desired endocardium and epicardium helix angle, transverse angle and sheetlet angle to be inputted. Then the LDRB algorithm solves, first by formulating Laplace's equation, to define the smooth variation of the LV fibres within the LV, then by anchoring the solution under Dirichlet boundary conditions, with is constrained by:

- $\partial\Omega_{apex}$: LV apical surface,
- $\partial\Omega_{base}$: LV basal surface,
- $\partial\Omega_{epi}$: LV epicardial surface,
- $\partial\Omega_{endo}$: LV endocardial surface.

Finally, the Laplace equation is solved, following a series of rules, where the algorithm iteratively adjusts to ensure both the Laplace equation and boundary conditions are satisfied (Bayer et al. 2012). Figure 2.1, in Chapter 2, depicts the coordinate system used to assign the myofiber orientation.

3.4.3 Determining the Unloaded State

A reference geometry, known in literature as the stress-free state, is required to initiate simulations. Generally, the LV is never in a load free state, where pressure, stress and contractile forces are zero, as there is likely to be residual stress present (Krishnamurthy et al. 2015; Wang et al. 2020). However, a state representing something close to the stress-free state is required. In this thesis, methods were adapted from literature (Finsberg et al. 2018), to estimate the unloaded configuration.

The process to calculate the unloaded configuration is disclosed in Figure 3.5. To initiate the algorithm, EDV and end diastolic pressure (EDP) must be assigned. EDV is based on the patient specific volume. EDP was initially assumed as 5 mmHg, based on Johnson et al.'s intracardiac pressure measurements (Johnson et al. 2000), however, the value was varied in later chapters, which will be discussed in due course. Following this, a point in diastolic filling (1 in Figure 3.5) is chosen as the initial estimated state, the model is then unloaded to the estimated load free state (2 in Figure 3.5) and then passive inflation of the geometry occurs to EDP. If the passive inflation is unable to meet the input EDP, the process continues, iteratively adjusting the initial estimated state, until the desired EDP is achieved.

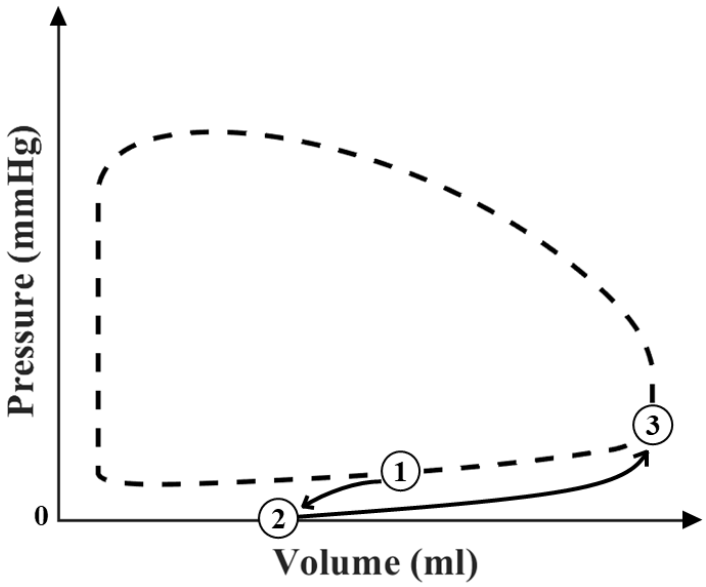

Unloading Geometry

1: Initial estimated state.

1-2: Unloading initial state.

2: Load free state.

2-3: Passive inflation to EDP.

3: EDP and EDV defined by simulation inputs.

Process iteratively run to ensure passive inflation achieves inputted EDP.

Figure 3.5. *Illustration of algorithm employed to determine the LV unloaded configuration.*

Figure adapted from published work (Finsberg et al. 2018).

3.4.4 FE Formulation

The formulation of LV myocardial mechanics problem utilised in this work has been described previously (Mojumder et al. 2020), with details specific to this work described in the following section. All FE models were solved in FEniCS, using the Newton solver to calculate pressure, based on volume changes, using the Lagrangian formulation described in Equation 3.28,

$$\mathcal{L}(\boldsymbol{u}, p, P_{cav}, \boldsymbol{c_1}, \boldsymbol{c_2}) = \int_{\Omega_0} W(\boldsymbol{u})\, d - \int_{\Omega_0} p(J-1)\, dV - P_{cav}\big(V_{cav}(\boldsymbol{u}) - V_p\big) - \frac{1}{2}\int_{\mathrm{d}\Omega_{0,epi}} k_{spring}(\boldsymbol{u}\cdot\boldsymbol{u})\, d\sigma - \boldsymbol{c_1}\int_{\Omega_0} \boldsymbol{u}\, dV - \boldsymbol{c_2}\int_{\Omega_0} \boldsymbol{X}\times\boldsymbol{u}\, dV, \quad \text{Equation 3.28}$$

where W is the earlier defined (Equation 3.27) strain energy function of the myocardium, **u** is the displacement field, p is a Lagrange multiplier, which enforces incompressibility of the myocardial tissue, such that J of the deformation gradient tensor is 1. P_{cav} is the Lagrange multiplier to constrain the cavity volume, ($V_{cav}(\boldsymbol{u})$), to the value fed into the model (V_p), which is based either on the cardiac motion estimation values, in volume constrained modelling methods or the flowrate computed from the LPM. c_1 and c_2 are the Lagrange multipliers for zero mean translation and rotation respectively. k_{spring} is the weak spring applied to the epicardium, to imitate the loading applied by the pericardium and $\boldsymbol{X}$ is the longitudinal location.

To minimise and thus solve the Lagrangian formulation described in Equation 3.29, its weak formulation was obtained by taking the first variation of the Lagrangian formulation as follows (Mojumder et al. 2020),

$$
\begin{aligned}
&d\mathcal{L}(\boldsymbol{u}, p, P_{cav}, \boldsymbol{c_1}, \boldsymbol{c_2}) \\
&\quad = \int_{\Omega_0} \boldsymbol{P} : \nabla\delta\boldsymbol{u}\ dV \\
&\quad - \int_{\Omega_0} \left(pJ\boldsymbol{F^{-T}} : \nabla\delta\boldsymbol{u} + \delta p(J-1)\right) dV - \delta P_{cav}\left(V_{cav}(\boldsymbol{u}) - V_p\right) \\
&\quad - \int_{\Omega_{cav}} PJ\boldsymbol{F^{-T}} : \nabla\delta\boldsymbol{u}\ dV - \int_{\mathrm{d}\Omega_{0,epi}} k_{spring}(\boldsymbol{u}\cdot\delta\boldsymbol{u})\ d\sigma \qquad \text{Equation 3.29} \\
&\quad - \int_{\Omega_0} (\boldsymbol{c_1}\delta\boldsymbol{u} + \boldsymbol{u}\delta\boldsymbol{c_1})\ dV \\
&\quad - \int_{\Omega_0} \{\delta\boldsymbol{c_2}(\boldsymbol{X}\times\boldsymbol{u}) + \boldsymbol{c_2}(\boldsymbol{X}\times\delta\boldsymbol{u})\} dV,
\end{aligned}
$$

Where $\boldsymbol{P}$ is the first Piola Kirchoff stress tensor and $\boldsymbol{F}$ is the deformation gradient tensor.

The problem then becomes finding the condition that satisfies Equation 3.30, which is solved in FEniCS via the Newton solver,

$$d\mathcal{L}(\boldsymbol{u}, p, P, \boldsymbol{c_1}, \boldsymbol{c_2}) = 0. \qquad \text{Equation 3.30}$$

3.4.5 Boundary Conditions

The boundary conditions are, a 90 Pa weak spring (k_{spring} in Equation 3.28) is applied to the epicardium, to imitate the loading applied by the pericardium, and the basal plane of the LV is constrained in the longitudinal direction. An illustration of the boundary conditions is included in Figure 3.6.

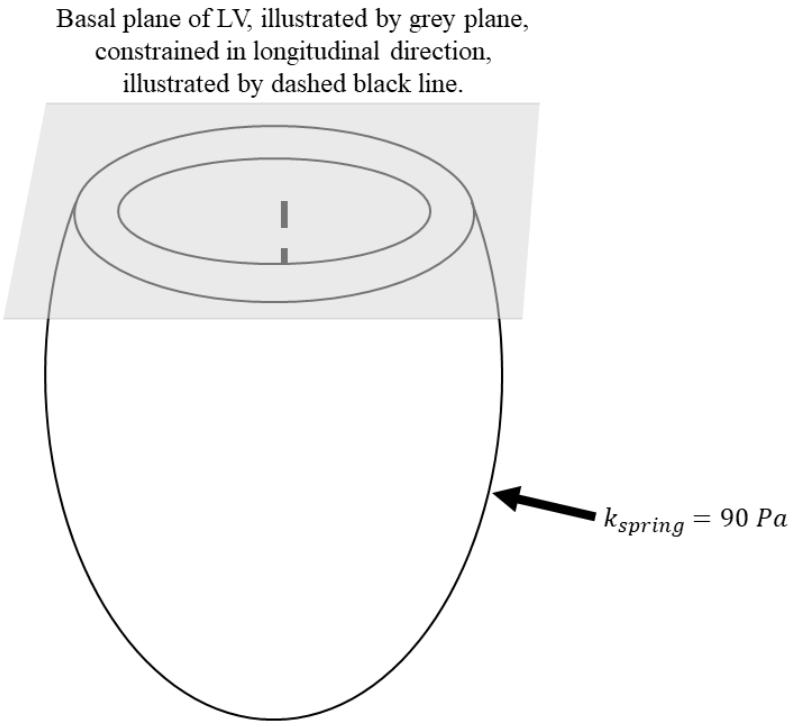

Figure 3.6. *Illustration of boundary conditions applied to the LV, which include a weak spring (k_{spring}) applied to the entire epicardial surface and the basal plane of the LV being constrained longitudinally.*

3.5 Interdependency of Computational Methods

In this thesis two methods are used to investigate the biomechanics of fetal LVs, they are, the volume constrained FE methods and the LPM+FE methods. Both methods enable the biomechanics of the fetal LV to be modelled and analysed, but their approaches differ. Further details of the two methods are described below.

3.5.1 Volume Constrained FE Methods

The first method is the volume constrained FE modelling approach, which utilises the patient specific LV volume variation over time, that is obtained during the model reconstruction and cardiac motion estimation methods. The volume constrained FE approach solves for pressure under the relationship described in Equation 3.29, at every time step for which LV cavity volume is known. The process is relatively computationally inexpensive, however, the process only captures the functionality of the LV. Further comparison of the volume constrained FE approach to LPM+FE approach will be undertaken in Chapter 4.

3.5.2 LPM+FE Methods

Secondly, the LPM+FE modelling approach iteratively solves for volume and pressure, eliminating the need for the image-based volume constraints, and allowing the effect of pressure and flowrates outside of the LV to also be analysed. This is again achieved by solving Equation 3.29, such that at each prescribed time step the ventricular pressure is computed from the FE formulation (Equation 3.29). Then the LV pressure calculated from solving Equation 3.29 is used to compute the flow rates, $q_{mv}(t)$ and $q_{ao}(t)$, at the next time increment, using Equations 3.1 and 3.2, which in turn calculates the volume at the next time step. During isovolumetric phases, where the volumes remain constant, pressure is computed via the FE formulation.

3.5.2.1 Generating LV Behaviour

The LPM+FE method is computationally expensive and takes many cycles to converge. To improve convergence of the LPM+FE methods, and improve the efficiency of the process, an LV behaviour approach was adopted. The LV behaviour is generated as a look up table which computes all possible LV pressures, LV volumes and cardiac time combinations, specific to each model. Once the table is generated, it can be used to iteratively solve for pressure and volume, through the LPM methods, at each point in the cardiac cycle. This also enables additional simulations to be run efficiently, using adapted LPM's. Such method is possible as the FE model has negligible momentum terms, compared to myocardial contractility (active tension) and even stiffness. An example LV behaviour plot is shown in Figure 3.7, where there is an individual point for each possible volume, pressure, and time combination.

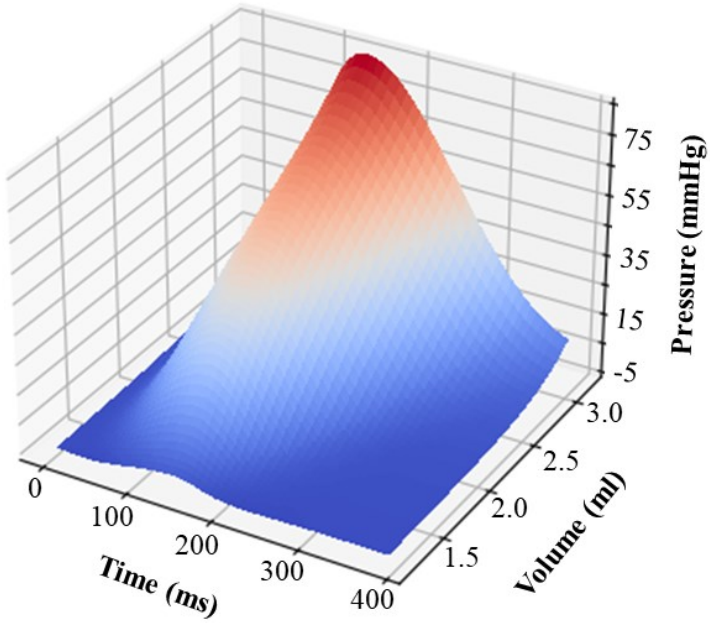

Figure 3.7. *Example LV behaviour, where the relationship between pressure, volume and time is captured for all possible values of a patient specific model.*

3.5.3 Overview of Computational Approaches

Overall, the volume constrained FE approach enables efficient modelling of the biomechanics of the fetal LV. However, the volume constrained approach does not allow for the relationship between pressure, SV and myocardial contractility to be investigated, because the SV is fixed, it also does not model any characteristics outside of the LV. The limitations associated with the volume constrained approach are overcome in the LPM+FE methods, however, the LPM+FE methods are more than 200 times more computationally expensive (case dependent). An overview of both computational approaches is depicted in Figure 3.8.

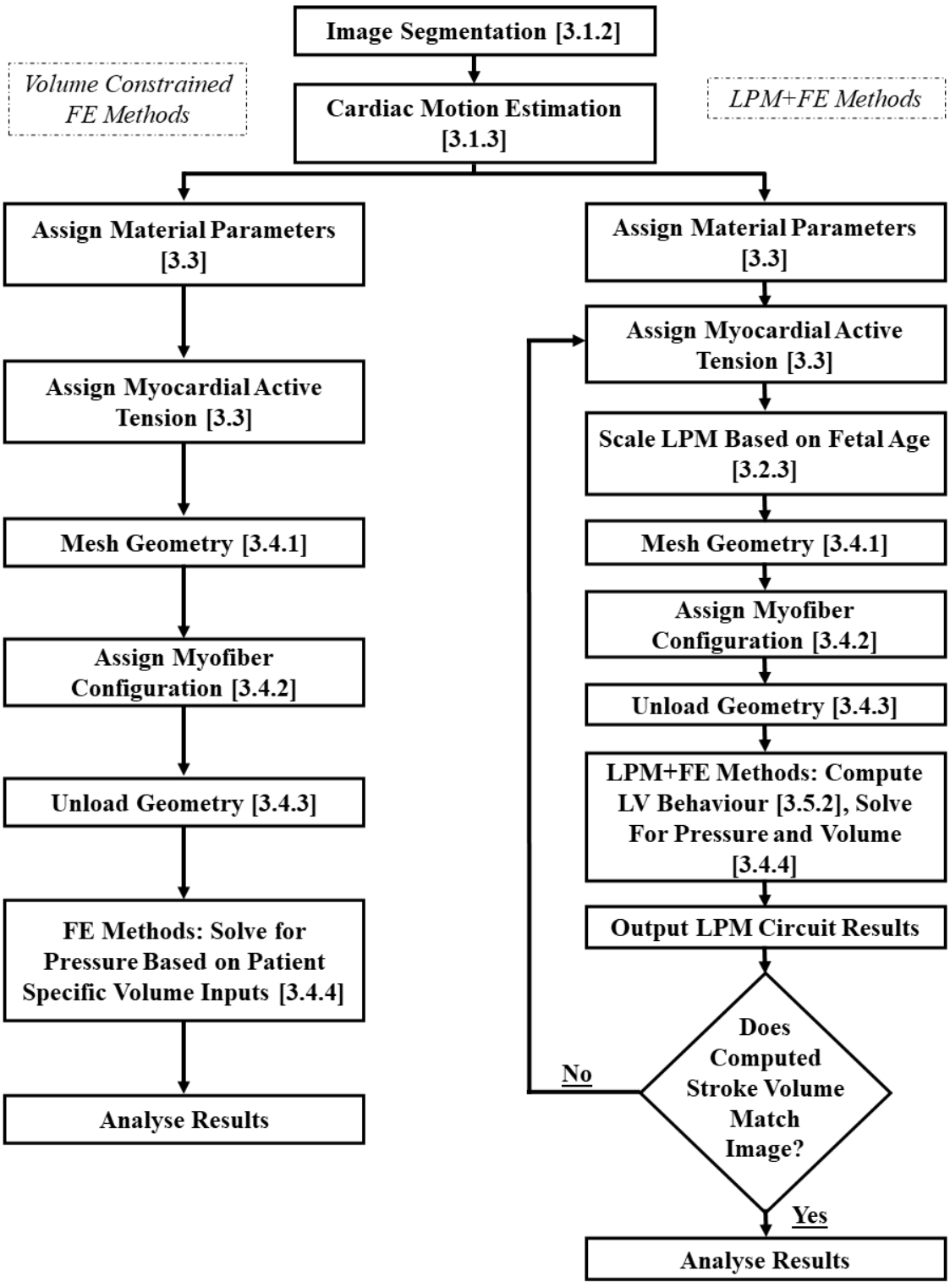

Figure 3.8. *Flow chart of volume constrained FE and LPM+FE modelling protocols. Square brackets refer to the chapter section each step is described in.*

The volume constrained FE and LPM+FE methods source code can be found here: https://github.com/WeiXuanChan/heartFEM.

3.6 Conclusion

Overall, the computational methods described in this section enable the development of patient specific cardiac models, to analyse the functionality of healthy fetal LVs and the impact of disease on fetal heart biomechanics. The computational methodologies described in this chapter will be built upon in Chapters 4, 5 and 6.

Chapter 4: Development of Fetal LPM and FE Methods

In pursuit of fulfilling Aim 2 and Aim 3 and ultimately achieving the Overall Aim, Chapter 4 (Aim 1) was devised to develop fetal FE methods. The initial step required calibrating the LPM model to literature-based pressure measurements (Johnson et al. 2000; Versmold et al. 1981). Subsequently, an exploratory study was conducted to investigate the influence of helix angle configuration on fetal heart functionality, as such work had previously been undertaken on idealised adult LV's and one patient specific adult LV (Palit et al. 2015; Rijcken et al. 1999; Vendelin et al. 2002), but not on the fetal LV. Due to the differing morphology of the fetal and adult LV and the need to assign the helix angle configuration in all FE models of the myocardium, such work was required. Results from the study of the relationship between helix angle configuration and biomechanical functionality were derived from volume constrained FE methods of 5 patient specific fetal LV geometries and 7 idealised LV geometries of various shapes. Briefly, results showed that helix angle configuration substantially impacts peak systolic myofiber stress, cardiac stroke work, myocardial deformational burden, and the spatial variability of myocardial strain. Literature based helix angle configuration measurements resided between the optimal regions for peak systolic myofiber stress, cardiac stroke work and myocardial deformation burden, suggesting development towards a fixed helix angle configuration in gestation is dependent on several factors rather than a single factor. The study also demonstrated how LV shape rather than size impacts the relationship between helix angle configuration and biomechanical functionality, suggesting that LV biomechanical optimality

would be affected in cardiac disorders which alter LV morphology. Finally, an optimisation algorithm was developed primarily by Dr Wei Xuan Chan, where I (Laura Green) supported the development of the optimisation algorithm by adding the ability to adjust for MV inflow and debugging the script. The algorithm aims to enhance patient specificity of the LPM+FE methods, particularly for CAS-eHLHS patients, whilst also allowing for inverse calculation of biomechanical parameters. Testing of the optimisation algorithm demonstrated a sufficient match with patient specific data could be achieved.

Overall Chapter 4 developed LPM and FE methods and advanced knowledge on the relationship between helix angle configuration and biomechanical functionality of differing LV geometries. Work included in Chapter 4 has also been published (Green et al. 2022).

4.1 Introduction

Development of the LPM and FE methods followed a three-pronged approach. Firstly, in Chapter 3.2 it was recommended that an evaluation of the fit between the age scalable LPM, previously published (Pennati et al. 1997; Pennati. and Fumero. 2000), and published fetal intracardiac pressure measurements (Johnson et al. 2000) and descending aorta pulse pressure measurements (Versmold et al. 1981) be conducted. Such work could help determine how the LPM should be calibrated to account for earlier assumptions which have now been disproven (Section 3.2.4).

Secondly, the effect of helix angle configuration on biomechanical functionality and the influence morphology has on such relationship required studying. The helix angle configuration refers to the orientation of the myofibers, which are the primary contractile units of the myocardium. The orientation of these myofibers therefore affects the ability of the heart to contract and is a parameter that must be assigned in FE models of the myocardium. As discussed in Chapter 2, literature has attempted to quantify the fetal heart LV helix angle configuration through histology and imaging, with an average epicardium helix angle of -52° and average endocardium helix angle of +71° (Garcia-Canadilla et al. 2018; Nishitani et al. 2020; Ohayon et al. 1999). Several computational studies have also shown that the fibrous architecture of the adult LV myocardium has great influence on cardiac output (Palit et al. 2015; Pluijmert et al. 2012; Rijcken et al. 1999; Vendelin et al. 2002; Washio et al. 2020). Specifically, Rijcken et al. and Vendelin et al. demonstrated how the helix angle configuration that produced minimal spatial strain variability coincided with functional reports of helix angle configuration in literature (Rijcken et al. 1999) and demonstrated how helix angle configuration impacts the functionality and efficiency of the LV (Vendelin et al. 2002). A later study also used one patient specific LV

geometry to test the effect of 5 helix angle configurations on cardiac functionality, demonstrating the effect helix angle configuration has on passive stiffness and the importance of carefully assigning the helix angle configuration in computational models, due to its impact on simulation outputs (Palit et al. 2015). Washio et al. and Plujimert et al. performed adaptive helix angle remodelling to point in the direction of greatest active tension (Washio et al. 2020) and towards reduced cross-fiber shear strain (Pluijmert et al. 2012), with both models reporting optimised helix angle configurations close to physiological reports in literature. All the above models utilised adult idealised or singular adult patient specific LV models, to investigate the effect of helix angle configuration on biomechanics. The fetal circulation and therefore functionality differs from the adult for several reasons: in the fetal circulatory system oxygenated blood is received from the placenta, rather than the lungs; the fetal circulatory system has three shunts which redirect blood past the lungs and liver; the fetal heart is smaller, and thus has lower contractility; the relationship between the fetal LV and RV differs from the adult; and the fetal LV generally has a more asymmetric morphology (straighter septal wall) compared to the adult LV, due to the fetal ventricles having similar pressures.

As acknowledged, earlier a few studies have quantified the fetal helix angle through imaging techniques (Garcia-Canadilla et al. 2018; Nishitani et al. 2020; Ohayon et al. 1999), however, the effect fetal helix angle has on functionality, whether such helix angle observed leads to biomechanical optimality and how fetal LV shape and size impacts the relationship between helix angle and cardiac functionality, are yet to be investigated. Such points provide thought provoking discussion, as during gestation the fetal heart is developing towards a fixed helix angle configuration, however, functional aberrations and disease remodelling are thought to impact the helix angle configuration (Nielles-Vallespin et al. 2017; Ong et al. 2020). Therefore,

understanding how helix angle configuration impacts healthy fetal heart functionality may lead to more informed computational modelling investigations.

Thirdly, future LPM+FE models of patient specific CAS-eHLHS LVs, require tailored optimisation to account for the unique disease characteristics of each patient. Functionally fetal hearts with CAS-eHLHS experience elevated AV velocities, the presence of monophasic MV inflow and reduced myocardial strains (Friedman et al. 2018; Ishii et al. 2014; Tulzer et al. 2022a) and then following FAV intervention the CAS-eHLHS fetal hearts also experience AVr (Arzt et al. 2011). All mentioned abnormal characteristics resulting from the disease and intervention will require and an adapted modelling protocol, to enhance patient specificity and more accurately capture the disease biomechanics characteristics. To achieve this, an optimisation algorithm will be developed, to tune computational parameters based on echocardiographic data. The approach should not only uphold the model's patient specific nature but will also facilitate the back computation of biomechanical parameters.

To investigate the discussed points the following work was carried out:

1. Assessment and calibration of the LPM.
2. Studying the relationship between helix angle configuration and biomechanical functionality and the influence LV morphology has on such relationship. The following steps were outlined to achieve this:
    I. Firstly, an LPM of the fetal circulatory system was linked to an FE model and compared with volume-constrained FE modelling methods for one fetal patient specific LV and an idealised geometry, to determine the most appropriate computational method to proceed with.

II. The 4 further patient specific LVs were then modelled with the volume-constrained FE methods, based on the conclusions of step I. Multiple helix angle configurations were modelled to understand the effect of helix angle configuration on fetal heart functionality and determine whether the optimal points for biomechanics characteristics' aligned with literature reported helix angle configurations.

III. Image-based and computed volume-constrained FE myocardial strains were then measured and compared to determine which simulated helix angle configurations best matched the patient specific images.

IV. Then an investigation into how LV shape and size affects the relationship between helix angle configuration and LV biomechanics was conducted, utilising idealised geometries to model morphological extremes.

3. An optimisation algorithm was developed for patient specific modelling of CAS-eHLHS fetal hearts.

4.2 Methods

4.2.1 LPM Calibration

As the focus of the thesis is fetal LV functionality in healthy and CAS-eHLHS cases, Johnson et al.'s intracardiac fetal LV pressure (Johnson et al. 2000) and Versmold et al.'s descending abdominal aortic pulse pressure (Versmold et al. 1981) measurements were most appropriate to determine the suitability of the original LPM model (Pennati et al. 1997; Pennati. and Fumero. 2000) to the thesis purpose. Given data limitations and the thesis specific focus on mid-gestation cardiac biomechanics, the LPM was assessed starting from 20 weeks gestation.

The original LPM was written into Ngspice (www.ngspice.sourceforge.net), an open-source electronic circuit simulator, which represents viscous friction along the walls of cylinders via resistors, vessel compliance via capacitors, flow inertia via inductors and local haemodynamics energy losses via dissipative terms. The model requires LV and RV volume and cyclic data inputs, specifically: SV and end diastolic volume (EDV) measurements (Devore et al. 2019), cardiac cycle length (Park et al. 2001; Widnes et al. 2018) and LV and RV cardiac phase data (Alnuaimi et al. 2019). An example of the flowrate curves established from the literature measurements (Alnuaimi et al. 2019; Devore et al. 2019; Park et al. 2001; Widnes et al. 2018), and input into the LPM is included in Figure 4.1.

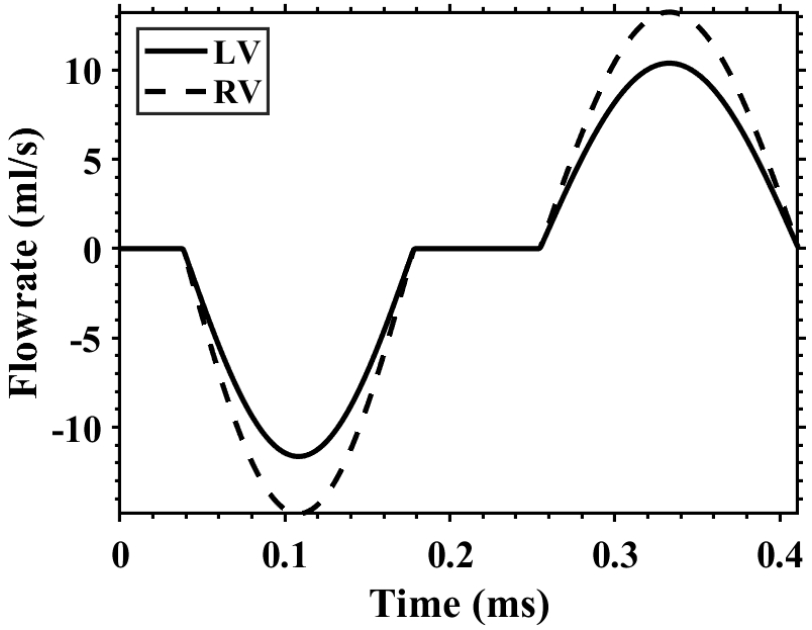

Figure 4.1. *Example of LV and RV flowrates computed from volume* (Devore et al. 2019)*, time* (Park et al. 2001; Widnes et al. 2018) *and phase* (Alnuaimi et al. 2019) *data, for a 30 weeks gestation mean fetal heart.*

The LPM was executed from 20 – 38 weeks gestation at 2 weeks gestation intervals, with each age specific model run for 20 cardiac cycles to ensure steady state was achieved.

LV peak pressure and descending abdominal aorta pulse pressure at the weeks gestation simulated was output and compared to the corresponding literature values (Johnson et al. 2000; Versmold et al. 1981). When compared the original LPM model had a root mean squared error (RMSE) of 13.93 and 13.64 compared to Johnson et al.'s intracardiac pressure measurements and Versmolds et al.'s descending abdominal aorta pulse pressure measurements respectively. The RMSE's of the original models to literature-based data provided further motivation to calibrate the model.

Therefore, to improve the match to Johnson et al.'s intracardiac peak pressure measurements a resistive value (R_{scale}) was added to the resistive allometric relationship (Equation 3.9) and manually calibrated for each weeks gestation modelled, to vary as shown below,

$$R_{scale} = 0.0002567W_{weeks\ gestation}^{3} - 0.01759W_{weeks\ gestation}^{2} + 0.4228W_{weeks\ gestation} - 3.0509 \quad \text{Equation 4.1}$$

and therefore Equation 3.9 from Chapter 3 becomes,

$$R_{weeks\ gestation} = R_{scale} \times R_{38}\left(\frac{W_{weeks\ gestation}}{W_{38}}\right)^{-1}. \quad \text{Equation 4.2}$$

Also, in Chapter 3.2.4, which discusses the limitations of the LPM, the original assumption in Pennati et al.'s model that *Ew* remains constant with increasing gestational age was disproven based on later research ((Daimei et al. 2014; Jacot et al. 2010; Pennati et al. 1997)). It is likely that *Ew* increases with gestational age (Daimei et al. 2014; Jacot et al. 2010).

Therefore, to consider the change in *Ew* with gestational age the power (*b*) became 1. An additional capacitance scaling factor, C_{scale} = 0.22, was then added to improve the fit between simulated and measured descending aorta pulse pressure. This resulted in Equation 3.15 becoming,

$$C_{weeks\ gestation} = C_{scale} \times C_{38} \left(\frac{W_{weeks\ gestation}}{W_{38}} \right)^{1}. \qquad \text{Equation 4.3}$$

4.2.2 Helix Angle Configuration Study Methods

To study the effect of helix angle configuration on LV functionality and the influence LV shape has on this relationship, a series of methods were required and are detailed in the following section.

4.2.2.1 Patient Specific Model Generation

Patient specific geometries of the LV myocardium were segmented using a semi-automatic custom-written Lazy Snapping algorithm (Wiputra et al. 2016). A validated, robust cardiac motion estimation algorithm was then used to track the motion of the LV myocardium (Wiputra et al. 2020), more detailed descriptions of these methods are included in Chapter 3. The reconstructed LV was propagated to all other time points using the cardiac motion tracking. From this, the volume over a cardiac cycle was calculated for each geometry.

Figure 4.2 shows the 5 patient specific LV geometries, in which Cases 1 and 2 are 32 weeks gestation and Cases 3, 4 and 5 are 22 weeks gestation, with the EDV STL superimposed onto the patient specific image and the volume over time variation included.

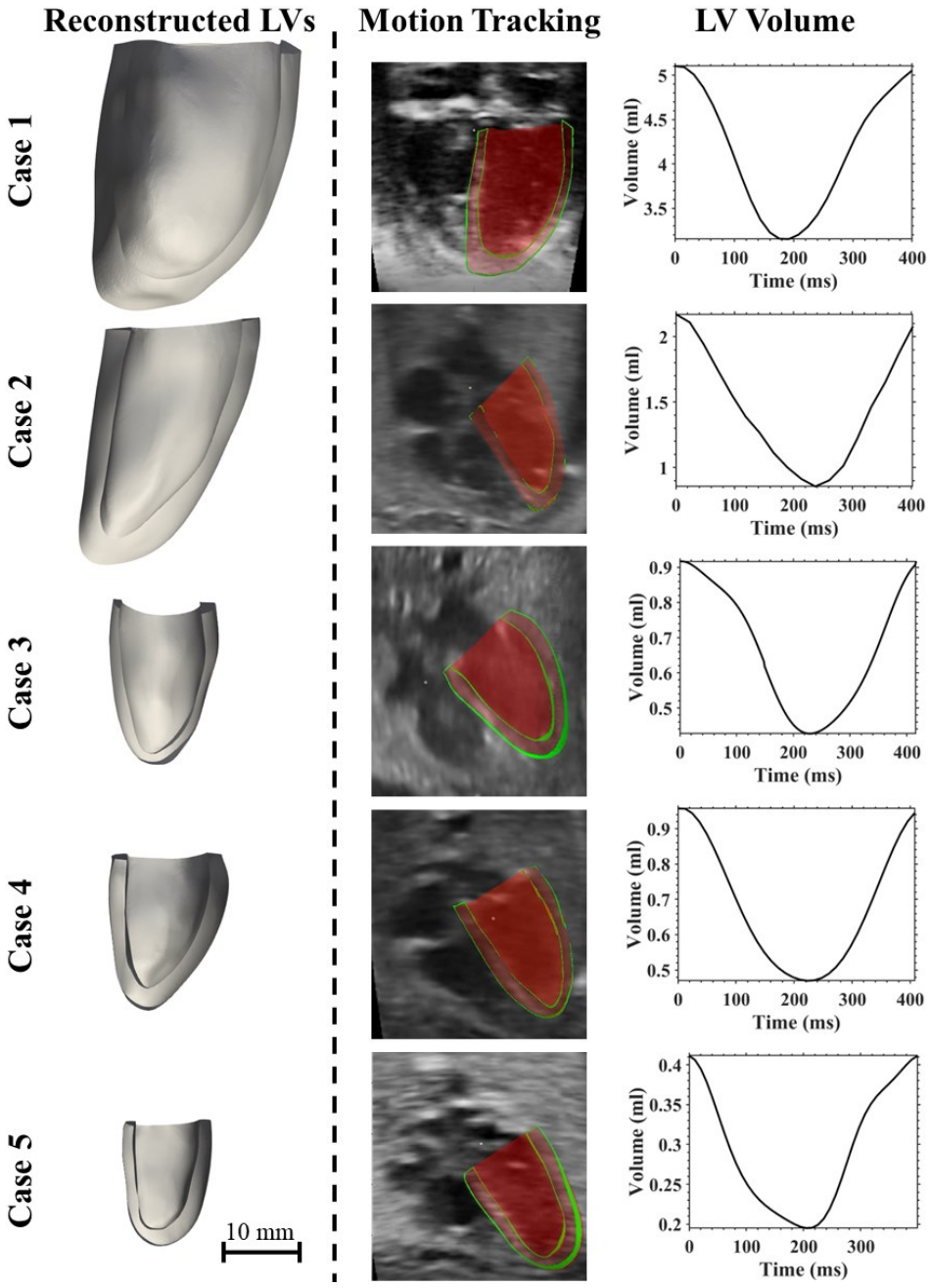

Figure 4.2. *Reconstructed patient specific LV geometries, scaled behind the dashed line. Motion tracking, demonstrating the superimposition of each geometries cardiac motion estimation onto the patient specific echocardiography images, red highlight describes the full geometry, green highlight shows the in-plane elements of geometry. Volume over time data, of each case, extracted from the motion estimation methods, described in the final column.*

4.2.2.2 Idealised Model Generation

To understand how LV geometry influences the relationship between helix angle configuration and biomechanics characteristics', a series of idealised models were generated in SolidWorks CAD software. Initially an asymmetric geometry, with a straight septal wall, 3.00 mm wall thickness, 18.75 mm cavity length and 15.40 mm basal cavity width (Daimei et al. 2014; Devore et al. 2019) was built, to represent the idealisation of a healthy 32 weeks gestation LV, and was coined the "Regular" geometry. 5 subsequent models were built to emulate physiological extremes, including an excessively "Wide" geometry (a half oblate ellipsoid), a "Hemisphere" geometry (representing an idealised dilated LV), "Symmetric" geometry (representing the adult like shape of the LV, as a half prolate ellipsoid), an excessively "Long" geometry and a "Hypertrophic" geometry (with the same dimensions as the symmetric geometry with double wall thickness) (all geometries shown in Figure 4.3). All cavity volumes were conserved to within 2% of the regular geometry. An adult idealised model was also constructed, assuming 9 mm wall thickness, 85 mm cavity length and 45 mm basal cavity width (Gibson et al. 2014; Velagaleti et al. 2014).

All fetal idealised geometries were assigned Case 2's volume over time waveform. The adult idealised geometry volume waveform was adapted from the literature (Khalafvand et al. 2017) and scaled to an EDV of 132 ml and a SV of 81.8 ml (Gibson et al. 2014).

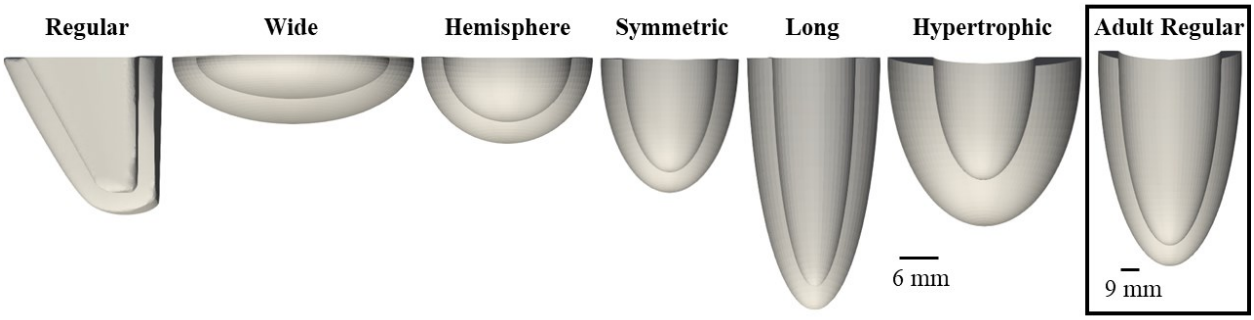

Figure 4.3. *Idealised LV geometries, built to evaluate how geometry impacts the relationship between helix angle configuration and biomechanical functionality. Boxed image is the "Adult" geometry with separate scale bar compared to idealised fetal geometry.*

4.2.2.3 Patient Specific Material Parameter Set-Up

The fundamental theory supporting the description of the myocardial material properties is disclosed in Chapter 3. This section describes the patient specific material parameters used in this study, with supporting literature.

Firstly, t_0, required assigning. *Ex vivo* studies have quantified t_0, with values varying from 100 ms to greater than 250 ms, dependent on what species the material sample was taken from and the heart rate (Guccione et al. 1993; Kirkpatrick et al. 1975; Mulieri et al. 1992; Sewanan et al. 2019; Sonnenblick et al. 1966). This work assumed a t_0 of 140.5 ms, based on Mulieri et al.'s work, as Mulieri et al. derived a relationship between human LV muscle strips and contraction frequency (Mulieri et al. 1992). T_{0LV} for fetal hearts aged 18+4 wks+days gestation has been measured to be 49.9 $\pm$ 9.3 kPa (Racca et al. 2016). Adult hearts T_{0LV} for healthy myocardial tissue has been measured to vary between 88 – 144 kPa (Asner et al. 2016; Gao et al. 2017; Genet et al. 2014; Land et al. 2017; Wang et al. 2013). With limited data of T_{0LV} for fetal hearts aged 20 weeks gestation onwards, but the expectation that contractility

increases with gestational age, T_{0LV} was initially applied as 60 kPa, based on the upper limit of Racca et al.'s measurements of an earlier gestation fetal heart, and then calibrated to align peak LV pressure to Johnson et al.'s, intracardiac LV pressure measurements (Johnson et al. 2000; Racca et al. 2016). l_0 and l_r respectively were based on adult studies (Genet et al. 2014). The parameters b and m described the rate of relaxation and were initially based on Shavik et al.'s values for the adult LV with an 800 ms cardiac cycle and linearly scaled based upon a fetal heart cardiac cycle of 400 ms (Shavik et al. 2018). Following this b and m were minorly adjusted to present more physiological pressure-volume loops. Ca_0, was assigned to be 4.35 μM, based on Guccione et al.'s model describing calcium activation (Guccione et al. 1993), with theory describing this model discussed in Chapter 3. The Co was assigned based upon deductions made in previous studies where, McPherson et al. demonstrated there to be no difference in human fetal and adult myocardium stiffness (McPherson et al. 1976), and Ong et al. went on to follow this deduction and demonstrate how substantial changes in Co had minor effects on peak systolic LV pressure, SV and myofiber stress (Ong et al. 2020). The stiffness coefficients described in Fung's strain energy function are b_{ff}, b_{xx} and b_{fx}, values are based on previous fetal LV models (Ong et al. 2020). All fetal models were assumed to have a cardiac cycle of 400 ms. All parameters defined are also described in Table 4.1.

Table 4.1. Material properties of patient specific models.

Parameter	Symbol	Unit	32 Weeks Gestion		22 Weeks Gestation		
			Case 1	Case 2	Case 3	Case 4	Case 5
Time to peak tension	t_0	ms	140.5	140.5	140.5	140.5	140.5
Maximum tension	T_{0LV}	kPa	52	40	30	30	30
Initial condition sarcomere length	l_0	µm	1.58	1.58	1.58	1.58	1.58
Relaxed sarcomere length	l_r	µm	1.85	1.85	1.85	1.85	1.85
Time intercept of linear relaxation duration with sarcomere length relation	b	ms	-830	-800	-835	-835	-835
Gradient of linear relaxation duration with sarcomere length relation	m	$ms\mu m^{-}$	524	524	524	524	524
Maximum intracellular calcium concentration	Ca_0	µM	4.35	4.35	4.35	4.35	4.35
Passive stiffness coefficient	Co	Pa	200	200	200	200	200
Stiffness coefficient in the fibre direction	b_{ff}	-	29.9	29.9	29.9	29.9	29.9
Stiffness coefficient in the sheet and sheet normal direction	b_{xx}	-	13.3	13.3	13.3	13.3	13.3
Stiffness coefficient in shear directions	b_{fx}	-	26.6	26.6	26.6	26.6	26.6
Cardiac cycle	BCL	ms	400	400	400	400	400

4.2.2.4 Idealised Material Parameter Set-Up

Idealised fetal models had the same material parameters applied to all geometries, to solely evaluate the effect of geometry on the relationship between helix angle configuration and fetal heart functionality. Material parameters were based upon patient specific Case 2. The "Adult" geometry material parameters were based upon previous studies (Shavik et al. 2018) and t_0 was based on Mulieri et al.'s time to peak tension for an 800 ms cardiac cycle (Mulieri et al. 1992). Material parameter values for all idealised models are recorded in Table 4.2.

Table 4.2. *Idealised models material parameters.*

Parameter	Symbol	Unit	Fetal	Adult
Time to peak tension	t_0	ms	140.5	172
Maximum tension	T_{0LV}	kPa	40	91.6
Initial condition sarcomere length	l_0	μm	1.58	1.58
Relaxed sarcomere length	l_r	μm	1.85	1.85
Time intercept of linear relaxation duration with sarcomere length relation	b	ms	-800	-1600
Gradient of linear relaxation duration with sarcomere length relation	m	$ms\mu m^{-1}$	524	1049
Maximum intracellular calcium concentration	Ca_0	μM	4.35	4.35
Passive stiffness coefficient	Co	Pa	200	200
Stiffness coefficient in the fibre direction	b_{ff}	-	29.9	29.9
Stiffness coefficient in the sheet and sheet normal direction	b_{xx}	-	13.3	13.3
Stiffness coefficient in shear directions	b_{fx}	-	26.6	26.6
Cardiac cycle	BCL	ms	400	800

4.2.2.5 Helix Angle Configuration

To assess the effect of helix angle configuration on LV functionality, multiple helix angle configurations required simulating, therefore the helix angle configuration was defined as the transmural-averaged angle ($\bar{\tau}$) and the epicardial-to-endocardial transmural angle difference (τ_{diff}), such that,

$$\text{epicardium fibre orientation} = \bar{\tau} - \frac{1}{2}\tau_{\text{diff}}, \qquad \text{Equation 4.4a}$$

$$\text{endocardium fibre orientation} = \bar{\tau} + \frac{1}{2}\tau_{\text{diff}}. \qquad \text{Equation 4.4b}$$

And a range of configurations were computed, with $\bar{\tau}, \tau_{diff} \in [-90^o, 180^o]$. Examples of imposed helix angle configurations on the symmetric geometry are shown in Figure 4.4.

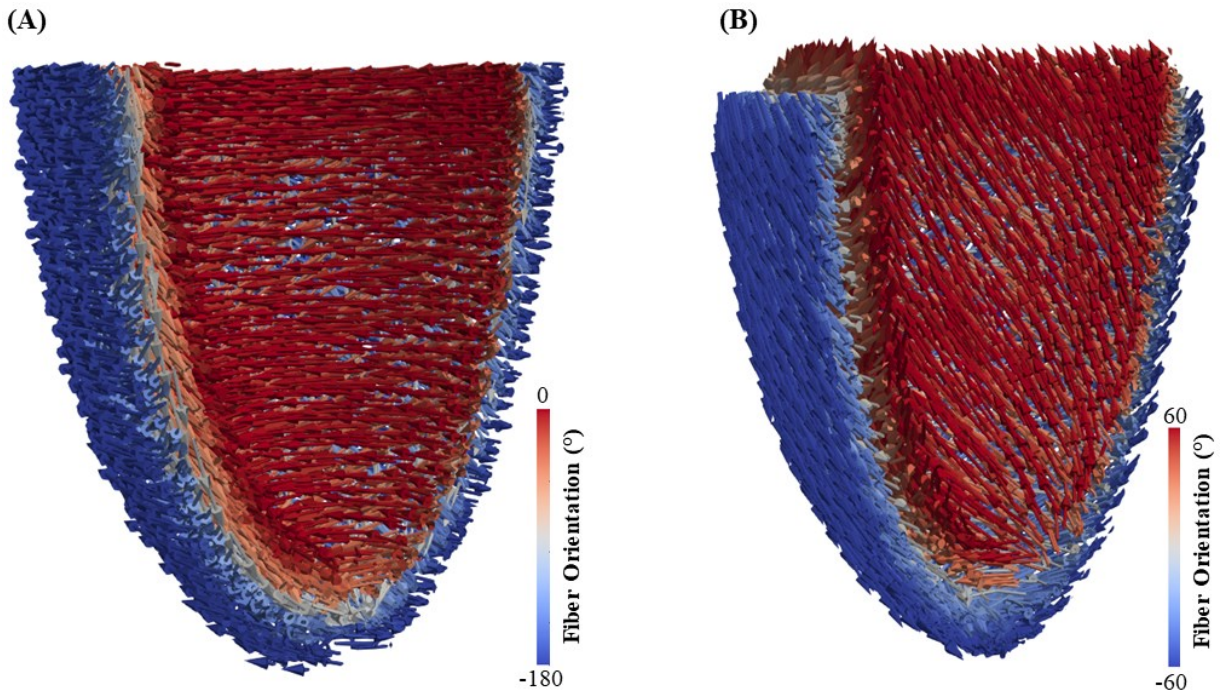

Figure 4.4. *Two examples of imposed fibre vectors (helix angles) on the "Symmetric" geometry. Legend recording the epicardium (blue) to endocardium (red) helix angle configuration, with the helix angle configuration equivalent to [A]* $\bar{\boldsymbol{\tau}} = -90°$, $\boldsymbol{\tau_{diff}} = 180°$ *and [B]* $\bar{\boldsymbol{\tau}} = 0°$, $\boldsymbol{\tau_{diff}} = 120°$.

4.2.2.6 Unloaded Geometry Calculation

To initiate simulations the configuration where the LV is at zero-pressure, also known as the unloaded configuration, must be defined. The unloaded configuration was calculated using the backward displacement method outlined in Chapter 3 (Finsberg et al. 2018), where EDP and EDV are known and the method deflates the LV to a mid-diastolic point, that is the estimated zero-pressure time point, and then passively inflates the LV back to the assigned EDV, using the passive material properties defined in Table 4.2. The method adjusts depending on the inflated LVs distance from EDP and repeats until Equation 4.5 is satisfied. EDV was assigned based on the volume computed in the cardiac motion estimation methods and EDP was assumed to be 5

mmHg based on Johnson et al.'s measurements of fetal intracardiac ventricular pressures (Johnson et al. 2000).

$$\frac{Simulated\ EDP \times 0.0075}{Assigned\ EDP - 1} < 0.0001. \qquad \text{Equation 4.5}$$

4.2.2.7 LPM+FE Modelling Constraints

Case 1 and the symmetric idealised model were simulated using the LPM+FE methods described in Chapter 3 combined with the calibrated model presented in Chapter 4. Both models were simulated at 32 weeks gestation.

Briefly, the LPM+FE methods enable ventricular-vascular coupling of the fetal LV and fetal cardiovascular system. The model is solved by iteratively minimising the weak Lagrangian function described in Chapter 3, for pressure and flowrates. The LPM is age scalable to enable greater patient specificity.

4.2.2.8 Volume-Constrained FE Simulations

A detailed description of the FE formulation is included in Chapter 3. Briefly, the volume-constrained FE methods use the active and passive properties of the myocardium described by Guccione's active contraction model (Guccione et al. 1993) and the Fung type transversely isotropic hyperelastic constitutive model (Guccione et al. 1991; Humphrey and Yin 1987) respectively, to minimise the weak Lagrangian function (described in Chapter 3) based on known LV cavity volume at specific temporal intervals. Therefore, the volume-constrained FE simulations require the volume over a cardiac cycle to be specified, which is extracted from the cardiac motion estimation algorithm (Wiputra et al. 2020). To initiate the volume-constrained simulations a starting geometry of 1/3 diastole was chosen, based on available literature, which

suggested this to be when the LV has the minimum pressure (Di Achille et al. 2018; Gao et al. 2014; Wenk et al. 2012).

Volume-constrained FE models run-time was approximately 1 hour on an Intel Xeon Gold 6240 with 72 CPUs, without multi-CPU use enabled, whereas LPM+FE model run-time using the same processor was approximately 32 hours, making the LPM+FE methods 32 times more computationally expensive compared with the volume-constrained FE methods. Therefore, volume-constrained FE simulations may be more suitable to enable all 12 geometries to be modelled over a large range of helix angle configurations. However, the volume-constrained outputs needed to be compared with the LPM+FE outputs to verify whether it is suitable to continue with the reduced computational cost methods. Therefore, Case 1 and the "Symmetric" idealised model LPM+FE outputs were initially compared with their respective volume-constrained FE outputs, using the structural similarity index (SSIM) (Wang et al. 2004). SSIM involves binarizing all data points of each biomechanics characteristic and computing the pixel variation. The equation to calculate SSIM is,

$$\mathrm{SSIM}(x,y) = \frac{(2\mu_x\mu_y+C_1)(2\sigma_{xy}+C_2)}{(\mu_x^2+\mu_y^2+C_1)(\sigma_x^2+\sigma_y^2+C_2)}, \qquad \text{Equation 4.6}$$

where μ_x and μ_y are the mean intensities from the signals in the x and y direction respectively, C_1 is a constant applied to removed errors caused by instability in the scenarios where $\mu_x^2 + \mu_y^2$ is zero or close to, σ_x and σ_y are the standard deviations of signal contrast in the x and y direction respectively and C_2 acts in the same manner as C_1, for signal contrast.

Once the volume constrained FE methods were deemed suitable to continue with, the remaining 4 patient specific and 6 idealised models were simulated using volume-constrained FE methods.

Overall, the volume-constrained approach has the advantage of reduced computational cost and ensuring the simulations adhere more accurately to the patient specific LV volume over time waveform, while the LPM+FE simulations are not ensured of this adherence.

4.2.2.9 Calculation of FE versus Image Strain Error

Image based 2D myocardial strains were computed (by Meifeng Ren). Methods to calculate the longitudinal and circumferential myocardial strains are illustrated in Figure 4.5, where the mid-wall image at EDV is exported in the long axis and short axis view to calculate the longitudinal and circumferential strains respectively. The myocardium is then manually traced in both views at EDV to act as the reference deformation, the pixel-to-pixel deformation is then tracked throughout the cardiac cycle and the Green Lagrange strains in the longitudinal and circumferential directions are calculated.

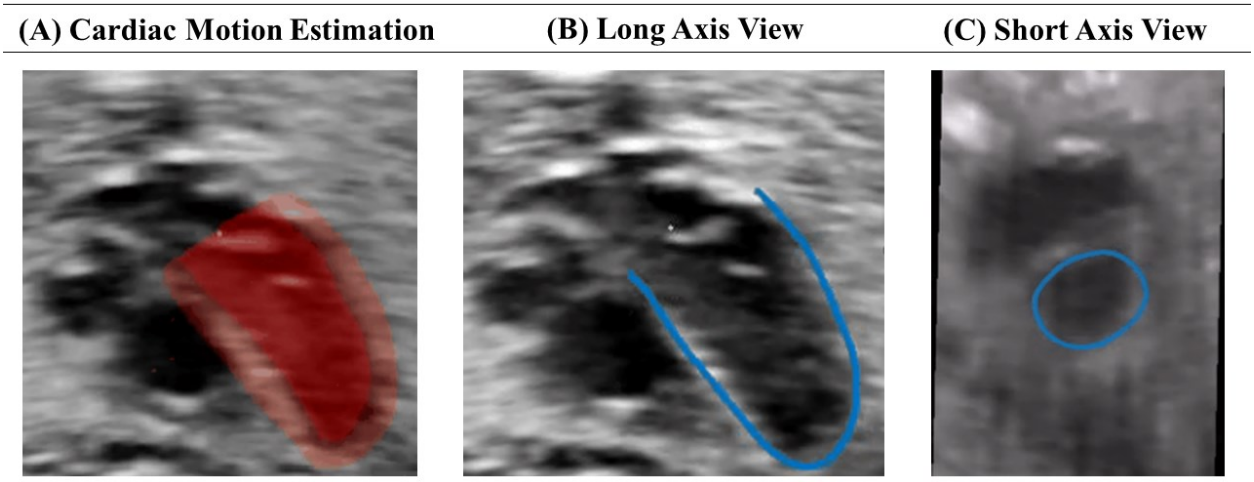

Figure 4.5. *2D Image-based strain calculation. [A] Demonstration of reconstructed LV geometry on image. EDV time point sliced at mid-wall to use as the reference slice in longitudinal axis view [B] and short axis view [C]. Mid-wall pixels are manually identified in both views, shown via the blue tracing.*

FE myocardial strains were compared to that obtained from image-tracking to investigate the range of helix angles that minimised the difference, to identify a likely range of helix angles in the patient specific cases. FE versus image strain error (ER) was defined as,

$$\mathrm{ER} = \left(\varepsilon_{\mathrm{long,FE}} - \varepsilon_{\mathrm{long,echo}}\right)^2 + \left(\varepsilon_{\mathrm{circ,FE}} - \varepsilon_{\mathrm{circ,echo}}\right)^2, \qquad \text{Equation 4.7}$$

where $\boldsymbol{\varepsilon}$ is the end-systolic Green Lagrange strain with end-diastole as the reference, and subscripts "long" and "circ" refer to the longitudinal and circumferential strain directions, and subscripts "FE" and "echo" refer to the source of the strain values.

4.2.2.10 Modelling the Transverse Angle

Initially all models are assumed to have a 0° transverse angle. Limited data exists on the transverse angle of fetal LVs. Therefore, to test if the inclusion of myofiber transverse angle influences the relationship between helix angle configuration and biomechanical function, a sensitivity analysis was conducted. Transverse angle variation was applied to the fetal LVs based on Vendelin et al.'s description, shown in Equation 4.8 (Vendelin et al. 2002),

$$\text{Transverse Angle} = \mu_{\mathrm{length}} * (1 - \varphi^2) * \alpha, \qquad \text{Equation 4.8}$$

where μ_{length} is -1 at the LV apex and linearly varies to 0.5 at the LV base, φ is the linear transmural myocardial distance, given to be -1 at the endocardial surface and 1 at the epicardial surface and α is varied dependent on the magnitudes of transverse angles to be investigated. α was chosen to be 10 and 5, under the assumption that the fetal heart will develop towards a postnatal heart's transverse angle configuration and thus magnitudes representative of that observed in postnatal hearts was the most suitable assumption. Figure 4.6 demonstrates the

transverse angle variation from epicardium to endocardium observed at the apex and base for the assigned α of 10 and 5.

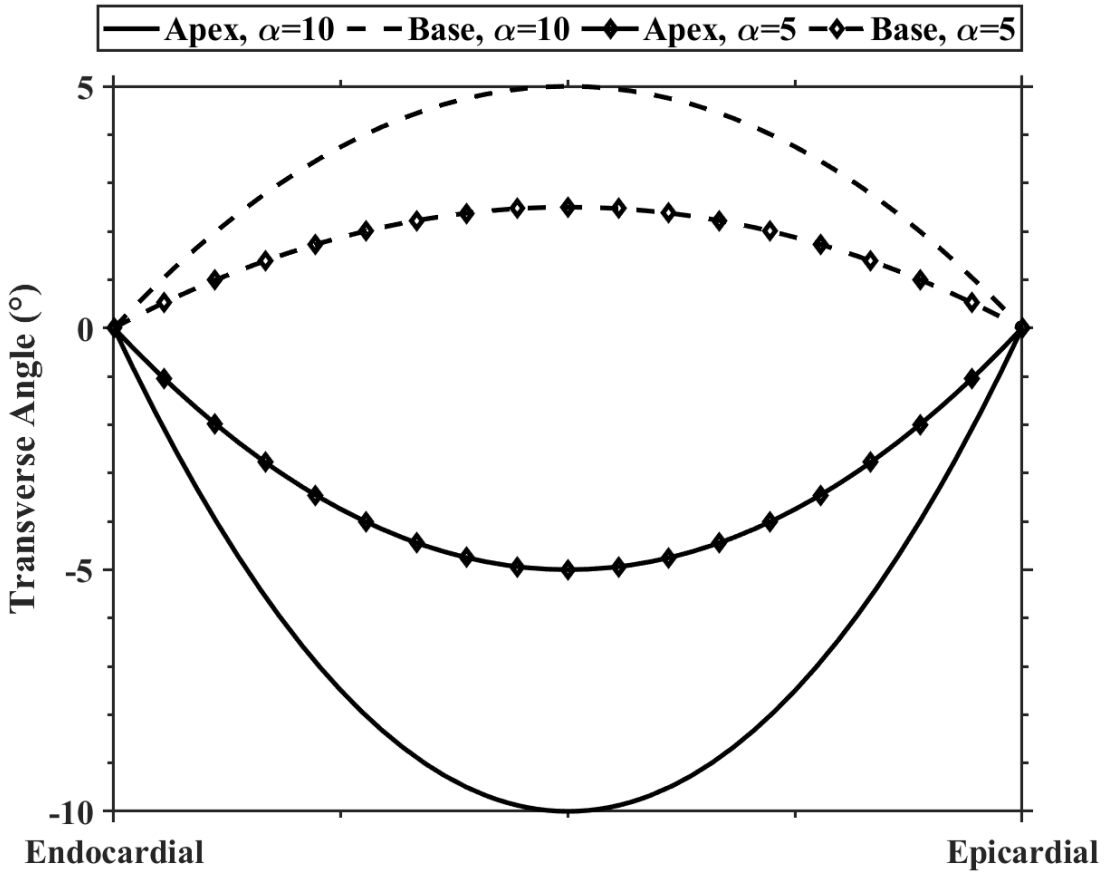

Figure 4.6. *Transverse angle variation in accordance with Vendelin et al.'s study* (Vendelin et al. 2002)*, where alpha has a magnitude of 10 and 5, with linear longitudinal variation. Transverse angle assumed to be 0° at the endocardial and epicardial surfaces, with a linear transverse angle variation assumed between the basal and apical transverse angle data shown in the plots.*

4.2.2.11 Biomechanics Characteristics' Calculations

Stroke work, volume-average myofiber stress (peak systolic myofiber stress), volume average deformational strain energy density amplitude (deformational energy) and transmural

strain variance, were output to investigate the effect of helix angle configuration on these functional biomechanics characteristics. How these parameters are calculated is detailed below.

Stroke Work referred to the work done by the LV on ejected fluid and was calculated as the area within the pressure volume (PV) loop.

Volume-averaged myofiber stress was calculated by analysing the FE results at peak systole time point with the highest pressure, taking the component of the stress tensor in the direction of the helix angle, and performing volume averaging, as shown in Equation 4.9,

$$\text{Myofiber Stress} = \frac{1}{\mathrm{V}} \int_{\mathrm{V}} \overrightarrow{\mathrm{f_d}} \boldsymbol{\sigma} \overrightarrow{\mathrm{f_d}} \, \mathrm{dV}, \qquad \text{Equation 4.9}$$

where V is the volume of the myocardium, $\overrightarrow{f_d}$ is unit vector in the myofiber direction, and $\boldsymbol{\sigma}$ is the stress tensor.

Volume-averaged deformational strain energy density amplitude (deformational energy) was calculated using Equation 4.10, where volume averaged strain energy density at every time point was first calculated, and then the difference between its highest value and its lowest value was found,

$$\text{strain energy density amplitude} = \max\left(\frac{\int_{\mathrm{V}} \mathrm{W(t)\,dV}}{\mathrm{V}}\right) - \min\left(\frac{\int_{\mathrm{V}} \mathrm{W(t)\,dV}}{\mathrm{V}}\right). \qquad \text{Equation 4.10}$$

Transmural strain variance was obtained by first calculating the minimum eigenvalue (λ_{min}) of the strain tensor, which signifies the largest principal contractile strain, and then calculating its standard deviation across a transverse cross-section at the mid-ventricular region, according to Equation 4.11,

$$\text{strain variance} = \sqrt{\frac{\sum\left|\lambda_{\min} - \overline{\lambda_{\min}}\right|^2}{n}}. \qquad \text{Equation 4.11}$$

Each biomechanics characteristic output was then normalised, to aid case to case contour plot comparison, like so:

$$\text{Normalised Value} = \frac{Original\,Value - Minimum\,Value}{Maximum\,Value - Minimum\,Value}, \qquad \text{Equation 4.12}$$

Where, $Original\ value$ was the biomechanics characteristic value output from the simulation, $minimum\ value$ was the lowest value from the range of helix angle configurations investigated of that case and $maximum\ value$ was the highest value from the range of helix angle configurations investigated of that case.

4.2.2.12 Optimality Criteria

Biomechanics characteristics' maps for stroke work, volume-average myofiber stress, deformational energy, and transmural strain variance as a function of helix angle configurations were generated. In this work, the optimal point on each characteristic map was the point with the maximum stroke work, the maximum volume-averaged myofiber stress, the minimum deformational energy, and the minimum transmural strain variance.

4.2.3 Development of the Optimisation Algorithm

An optimisation algorithm was developed to incorporate further patient specificity into the computational methods and was tested on a healthy LV, CAS-eHLHS LV and a CAS-eHLHS LV post-FAV. Firstly, the geometries were built using the same methods described in Section 3.1 and shown below (Figure 4.7).

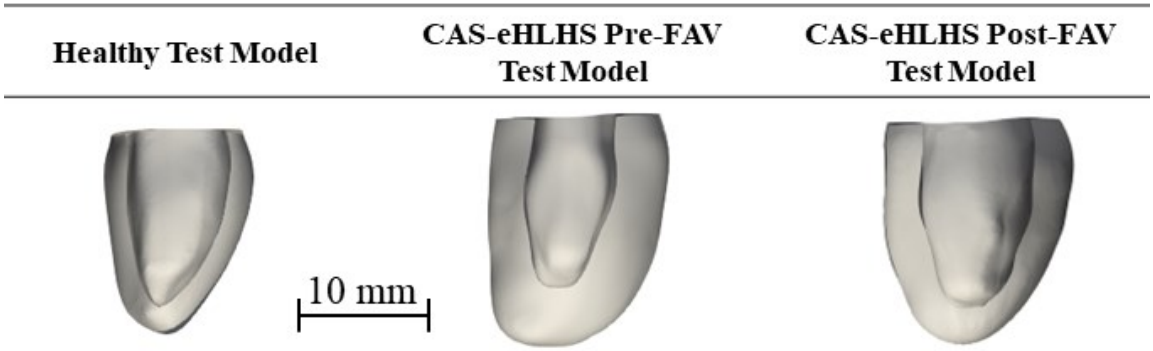

Figure 4.7*. Reconstructed patient specific LV geometries utilised to test to LPM+FE optimisation methods.*

The overall optimisation approach was to perform iterative LPM+FE simulations altering valve flow dissipative coefficients and myocardial contractility, to best match each computational model with clinical measurements (detailed in Figure 4.8). Therefore, through this matching process, the patient specificity of the model could be maintained, and the biomechanics parameters could be back computed.

Specifically for healthy fetal hearts, the LPM was first scaled to the specific gestational age and then unloaded based on Johnson et al.'s estimate of EDP in the healthy fetal LV (Johnson et al. 2000). Iterative LPM+FE simulations were then performed while varying myocardial contractility, a parameter specified in Guccione's active contraction model (Guccione et al. 1993), until, through using a simple gradient descent algorithm, the simulated SV matched that measured from the image, thus back computing the contractility. 60 kPa was used as the initial guess of active tension magnitude, based on the upper limit of experimental measurements of 49.9 $\pm$ 9.3 kPa of fetal myocardium at 18+4 wks+days gestation (Racca et al. 2016).

Then for CAS-eHLHS hearts (pre-FAV), the LPM was again scaled to the specific gestational age. The unloaded configuration was estimated based on left atrium size and capacitance (Wong et al. 2022). Then the patient specific matching process, was more extensively performed. First, iterative simulations were performed while varying flow dissipative coefficients of the AV, MV inflow and MVr, until simulations matched the expected valvular pressure gradient (ΔP), which were calculated from clinical valvular Doppler velocities, using the simplified Bernoulli's equation. Next, iterative simulations were performed while adjusting myocardial contractility, until the simulated SV matched that measured from images. A loop over the two types of iterative simulations was performed, until both valvular ΔP and SV matched measurements from echocardiography images, to within 10% error unless stated otherwise. This thus allowed the back-computation of myocardial contractility. The same process was defined for the CAS-eHLHS patients post-FAV, with the addition of optimising for AVr, like observed in Figure 4.8.

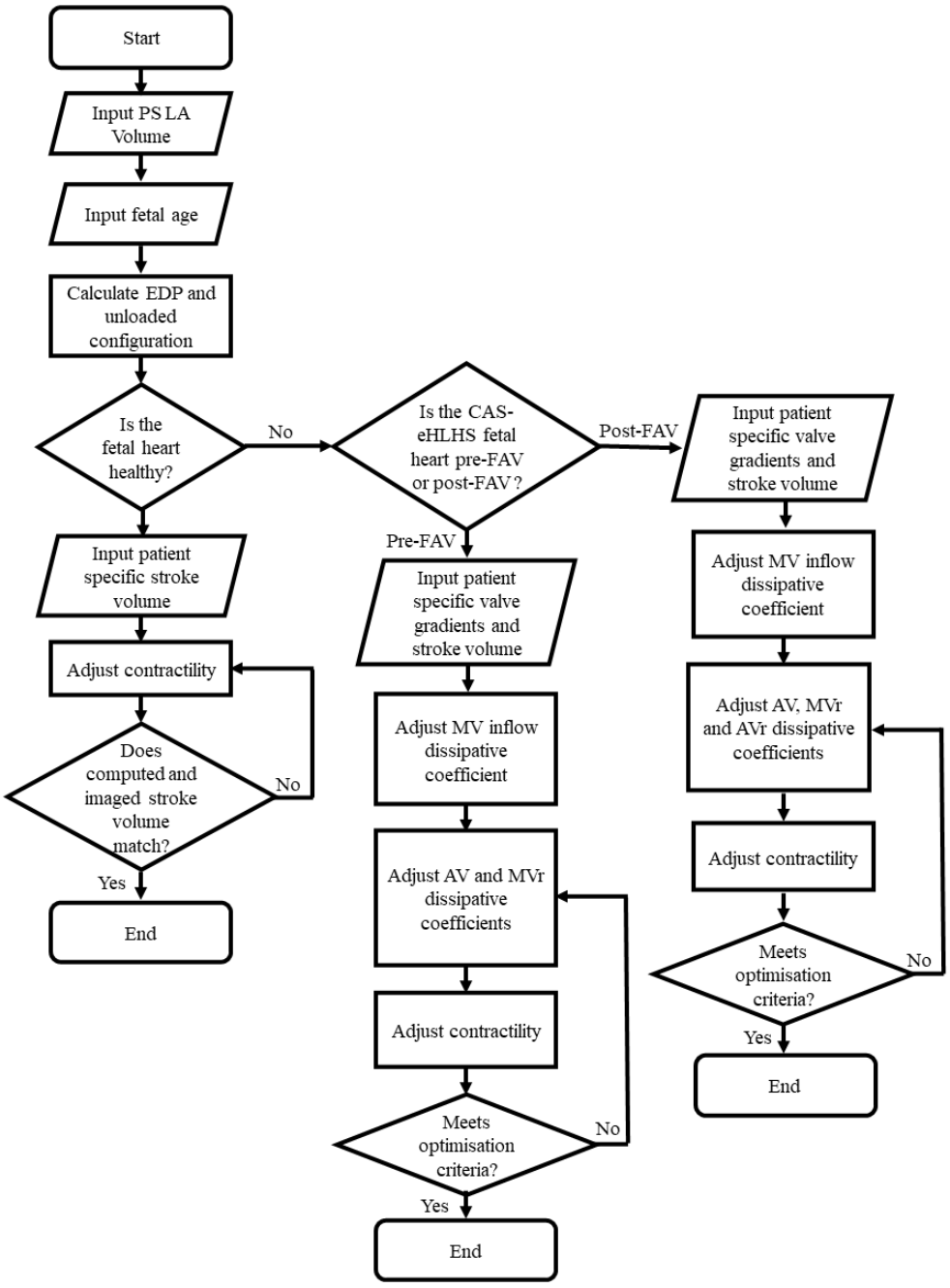

***Figure 4.8**. Flowchart to describe the patient specific optimisation steps for healthy and CAS-eHLHS fetal LVs, using the LPM+FE methods described in Section 3.5.2.*

Dr Wei Xuan Chan led the work developing the optimisation algorithm and I (Laura Green) supported the development of the optimisation algorithm by adding the ability to adjust MV inflow and debugging the script.

4.3 Results

4.3.1 LPM Calibration Results

Through calibrating the LPM, the RMSE was reduced from 13.93 to 2.01 for peak LV pressure and 13.64 to 1.05 for aortic pulse pressure. The improved fit between simulated and measured peak systolic LV pressure and descending aorta pulse pressure is shown in Figure 4.9.

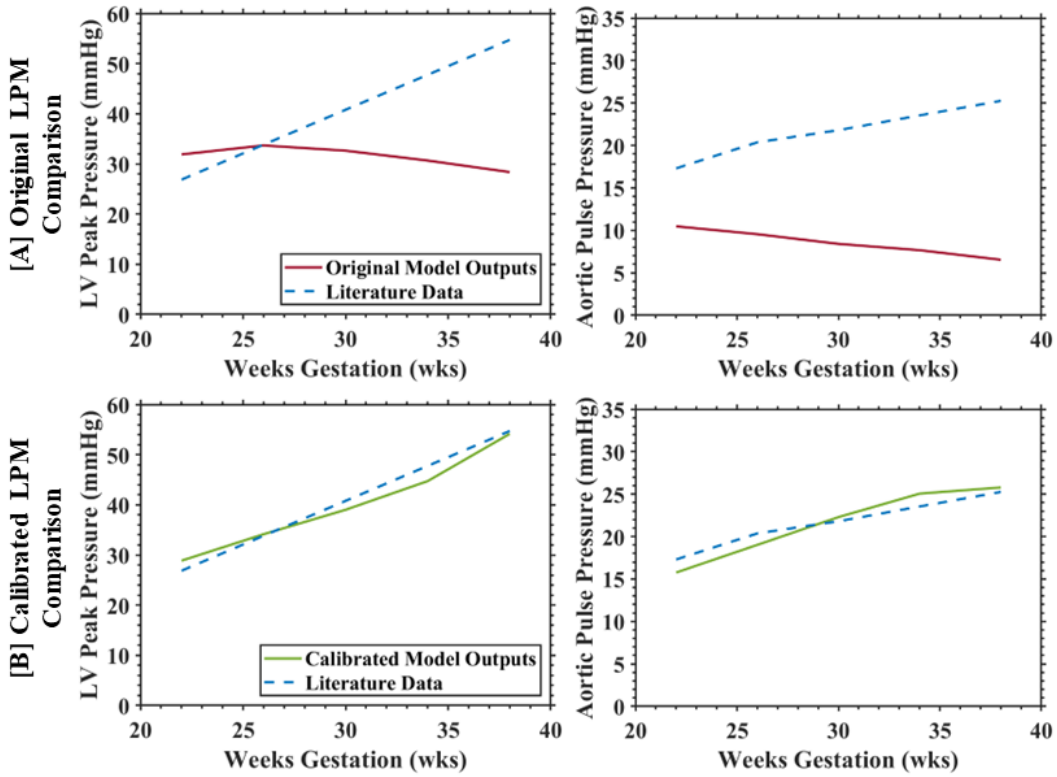

Figure 4.9*. Comparison between simulated and clinically measured peak LV pressure* (Johnson et al. 2000) *and aortic pulse pressure* (Versmold et al. 1981)*, for the original LPM [A]* (Pennati et al. 1997; Pennati. and Fumero. 2000) *and calibrated model [B].*

4.3.2 Helix Angle Study Results

Studying the effect of helix angle configuration on biomechanics characteristics' and the influence LV shape has on such relationship, was a multi-step study. The results from this study are detailed below.

4.3.2.1 LPM+FE and Volume-Constrained FE Equivalence Analysis

Case 1, a 32 weeks gestation patient specific LV was simulated using the full LPM+FE methods for over 100 helix angle configurations. At a helix angle configuration of $\bar{\tau} = 0^o$ and $\tau_{diff} = 120^o$ the model produced a peak pressure of 51.17 mmHg, which matched Johnson et al.'s peak LV pressure measurement at that age to within 1.8% (Johnson et al. 2000). The descending aorta pulse pressure matched literature to within 2.1% (Versmold et al. 1981). Figure 4.10 shows the LV, descending aorta and left atrium pressure tracing and valvular flow rate tracings.

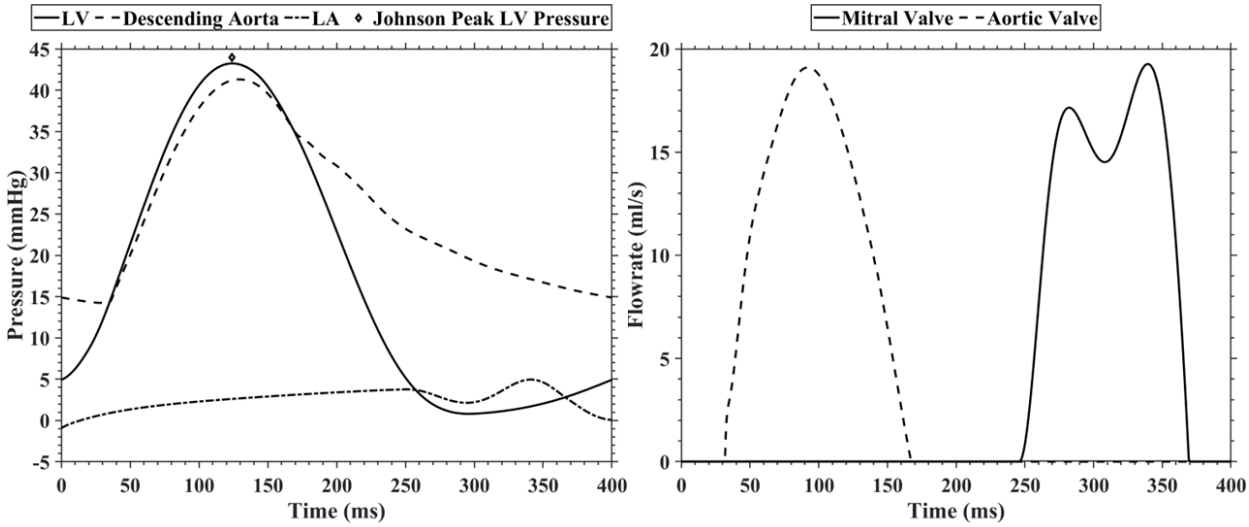

Figure 4.10. *Case 1 key pressure and valvular flowrate tracings from the LPM+FE modelling methods at* $\bar{\tau} = 0^o, \tau_{diff} = 120^o$. *[Left] LV, descending aorta and left atrium pressure variation throughout the cardiac cycle. Diamond marker plotting Johnson et al.* (Johnson et al. 2000) *peak pressure measurements for a 32 weeks gestation LV, matching to within 1.8%. [Right] Mitral and aortic valve flowrates. Note: LA = left atrium.*

The PV loop of $\bar{\tau} = 0^o$ and $\tau_{diff} = 120^o$ is included in Figure 4.11a, displays physiological characteristics, with a peak pressure of 51.17 mmHg, EDP of 5 mmHg and SV of

1.66 ml, which closely matched measurements from the 3D segmentation and motion tracking of the echocardiography images (1.67 ml). Biomechanical function maps shown in Figure 4.11, evaluate cardiac function characteristics against $\bar{\boldsymbol{\tau}}$ and $\boldsymbol{\tau_{diff}}$. The maps include stroke work (work done by the LV), peak volume-averaged myofiber stress per cardiac cycle ("myofiber stress" or stress in the "myofiber" direction), volume-averaged deformational strain energy density amplitude (the deformational burden endured by the myocardium) and transmural strain variance (quantified by the variance in strain across the mid-ventricle transverse plane). Stroke work, peak pressure and work done by the LV produce similar contour variation maps, resulting in the deductions drawn from one being applicable to the others. Such deductions included high outputs when τ_{diff} was below 120°, with helix angle configurations outputs above this threshold rapidly reducing. The spline interpolated peak occurred at $\bar{\tau} = -24.48°$, $\tau_{diff} = 108.80$.

Comparing the results from the LPM+FE simulations with outputs of the same model using the volume constrained FE methods in Figure 4.11, it is apparent the magnitudes vary between modelling methods, however, the trends in surface variation appear to be similar. To quantify the similarity in surface variation between the two methods the SSIM was computed. SSIM was calculated to be 0.991, 0.994, 0.976 and 0.962 for stroke work, peak systolic myofiber stress, deformational burden, and transmural strain variance, respectively. All SSIM values are therefore close to 1, which suggests high similarity. Aside from the isovolumetric contraction and relaxation periods (which is imposed in the LPM+FE methods) the PV loops between the two methods also had similar peak pressure magnitude, ESV and EDV.

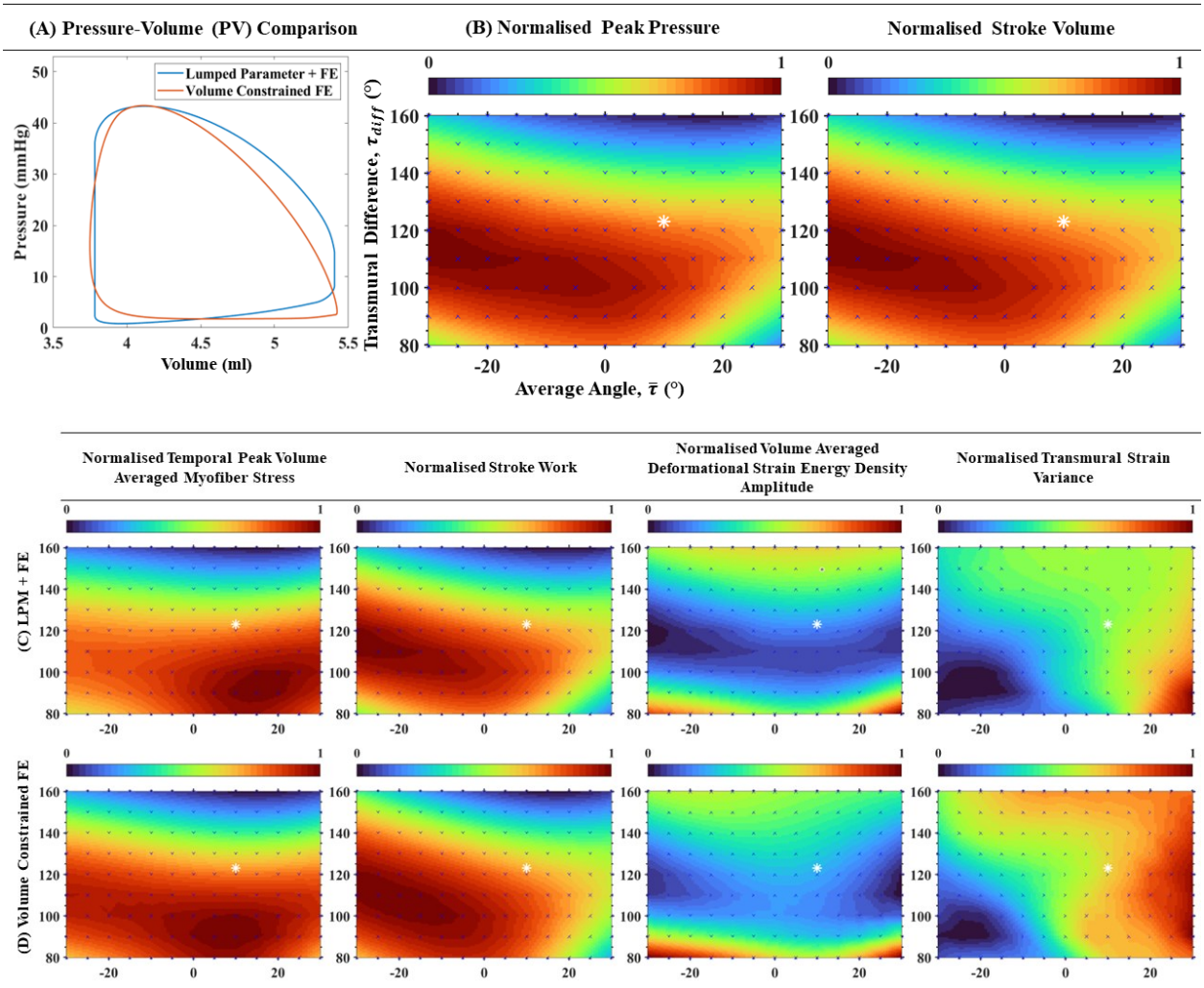

Figure 4.11. *(A) Case 1 LPM+FE and FE PV loop comparison. (B-C) Maps of normalised biomechanical characteristics obtained via the LPM+FE approach, plotted as a function of helix angle configurations. (D) Demonstrating the biomechanics characteristics obtained from the FE approach, demonstrating similarity to that obtained from the LPM+FE approach, based on the SSIM value of each biomechanics characteristic being close to 1. Values on all maps were interpolated from points where data was obtained from simulations (indicated by blue crosses on maps) and all contour maps in this figure contained the same axes as 4.11(B). The white asterisk plots the average literature helix angle configuration of* $\bar{\tau} \cong 9.5^{o}, \tau_{diff} \cong 123^{o}$.

To improve confidence in the methods, the "Symmetric" geometry was also modelled using both LPM+FE and volume constrained FE methods. Initially, the $\bar{\boldsymbol{\tau}}$ and $\boldsymbol{\tau_{diff}}$ range investigated in the patient specific scenario (Figure 4.11) was investigated here also. However, as moving forward all idealised models were to be simulated for -90° ≤ $\bar{\boldsymbol{\tau}}$ ≤ 90° and 40° ≤ $\boldsymbol{\tau_{diff}}$ ≤ 180°, to encompass the range of all possible helix angle configurations, a greater $\bar{\boldsymbol{\tau}}$ was simulated in Figure 4.12, compared to Figure 4.11, to capture the optimal biomechanics characteristic regions.

Figure 4.12 shows the comparison between the outputs of the two simulations methods. The SSIM index was 0.9821, 0.9748, 0.9306 and 0.8013 for temporal peak volume averaged myofiber stress, stroke work, volume-averaged deformation strain energy density amplitude, and transmural strain variance respectively. The SSIM index for transmural strain variance was low. One reason for the slightly lower SSIM index, is the number of non-convergence helix angle configurations at a $\bar{\boldsymbol{\tau}}$ ≤ 10° and $\boldsymbol{\tau_{diff}}$ ≤ 80°, for the LPM+FE modelling methods. This led to inaccuracies in the interpolation between points, causing reduced transmural strain variance in the bottom left corner of the LPM+FE map, as there were no points to guide the interpolation here and thus reducing the SSIM index.

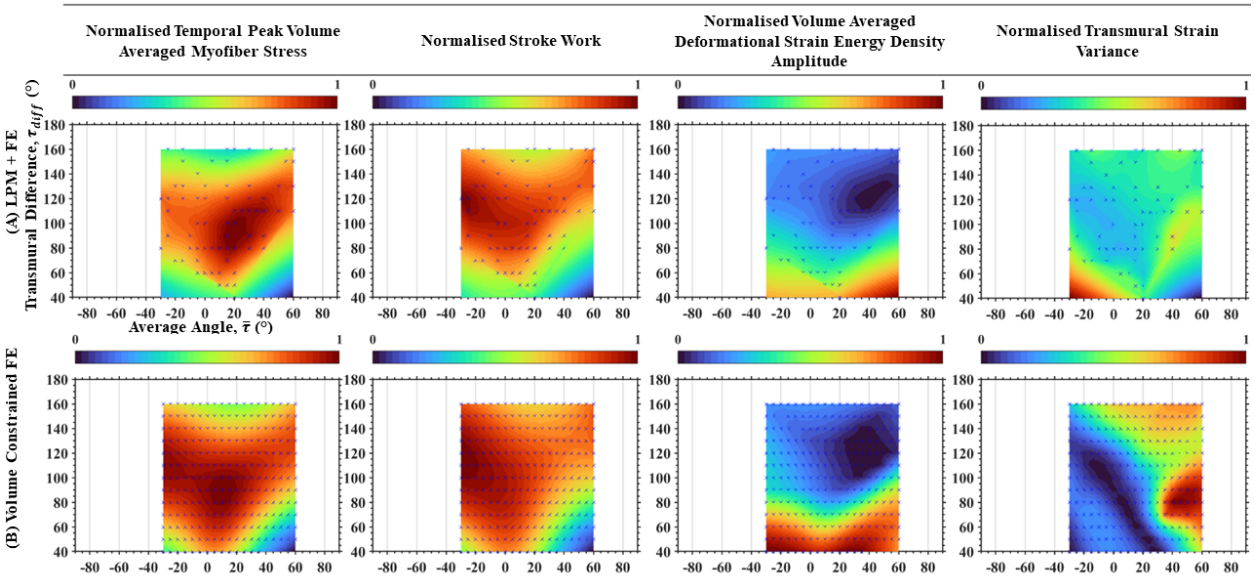

Figure 4.12. *(A) Maps of biomechanical characteristics obtained via the LPM+FE methods, plotted as a function of helix angle configuration, for normalised temporal-peak spatially averaged myofiber stress, normalised stroke work, normalised deformational strain energy density amplitude, and normalised transmural variability of fibre strains. (B) The same biomechanics characteristic maps as (A), but obtained via the volume constrained FE approach, demonstrating similarity to that obtained from the LPM+FE approach for the "Symmetric" model. Simulated values on all maps are depicted by the blue x, values were interpolated to produce contour maps, where the contour describes the biomechanics characteristic in the range of helix angle configurations investigated. Each figure has the same x and y axis as described in the top left plot.*

Based upon the similarities in data between the two methods, quantified by the SSIM index and visual inspection and the reduction in computational cost by 200 times through using the volume constrained FE methods, it was deemed suitable to proceed with the volume

constrained FE methods to be able to investigate a more extensive range of helix angle configurations.

4.3.2.2 Patient Specific Volume Constrained FE Biomechanical Characteristics

The volume-constrained FE approach was utilised to model the remaining 4 patient specific models. Examples of the PV loops for the remaining patient specific models, outputted from the volume constrained FE methods at $\bar{\tau} = 0°$, $\tau_{diff} = 120°$ is included in Figure 4.13.

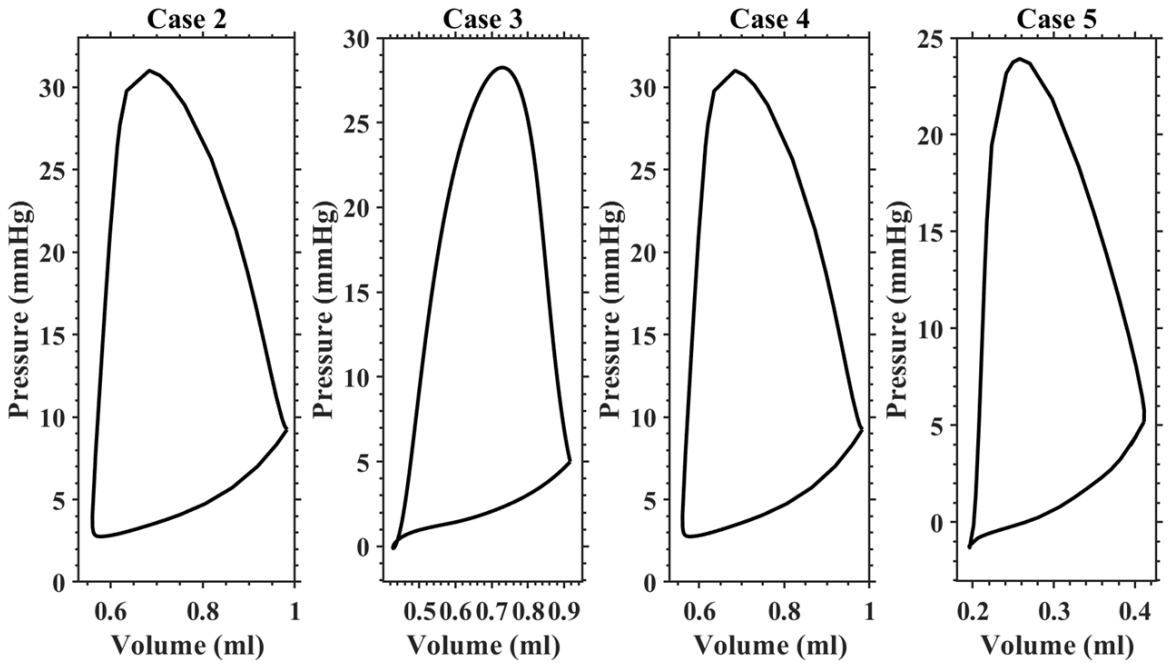

Figure 4.13. *Example PV loops of the remaining patient specific models outputted from the volume constrained FE methods at* $\bar{\tau} = 0°$, $\tau_{diff} = 120°$.

The results from all remaining patient specific simulations investigating the relationship between helix angle configuration and biomechanical functionality are shown in Figure 4.14. Upon visual inspection, the trends in the relationship between helix angle configuration and biomechanics characteristics, across the remaining patient specific cases, is largely like that observed for Case 1 in Figure 4.11. The exception to the above is for Case 4's volume-averaged

deformational strain energy density amplitude (deformational burden) map, which demonstrated a decreasing trend with increasing $\bar{\tau}$ and τ_{diff}. The difference observed is likely due to geometric differences between this LV from the other patient specific models. The Case 4 LV had a more symmetric geometry, whereas the other cases had a more "Regular" fetal geometry, where the apex leaned medially towards the septum, creating a more asymmetric like geometry, with a straighter septal wall, which is the configuration often observed in the fetal heart due to the similar LV and RV pressures at this stage of development.

In these patient specific biomechanics characteristics' map results, the optimal point for myofiber stress was within the range of helix angles investigated for all cases and averaged to be at $\bar{\tau} = 13.57^o \; and \; \tau_{diff} = 91.15^o$ across the 5 patient specific cases. However, for other characteristics, the optimal point was not within the range of angles for some cases.

To determine if the fetal heart helix angle is close to any of the optimality points on these maps, the literature reported fetal helix angle configurations, which ranged from $0^o < \bar{\tau} < 25^o, 110^o < \tau_{diff} < 150^o$, (Garcia-Canadilla et al. 2018; Nishitani et al. 2020; Ohayon et al. 1999) and averaged as $\bar{\tau} \cong 9.5^o, \tau_{diff} \cong 123^o$, were used and marked on the biomechanical maps (Figures 4.14 - 4.16). From Figure 4.14, it could be observed that this average helix angle configuration corresponded to high myofiber stress and moderately high stroke work but was not at the optimality point for either parameter. Further, it was close to or within the region of low deformational strain energy density amplitude. However, in terms of transmural strain variability, it achieved a moderate to moderately high value, across the contour variation. Thus, concluding that the reported helix angle configuration did not achieve optimality in any of the biomechanical parameters investigated but achieved parameter values close to the optimal value

for some parameters. Since the helix angle configuration was closest to the peak systolic myofiber stress optimality point, the hypothesis that myofiber stress was the most important stimulus for fetal heart helix angle remodelling was made.

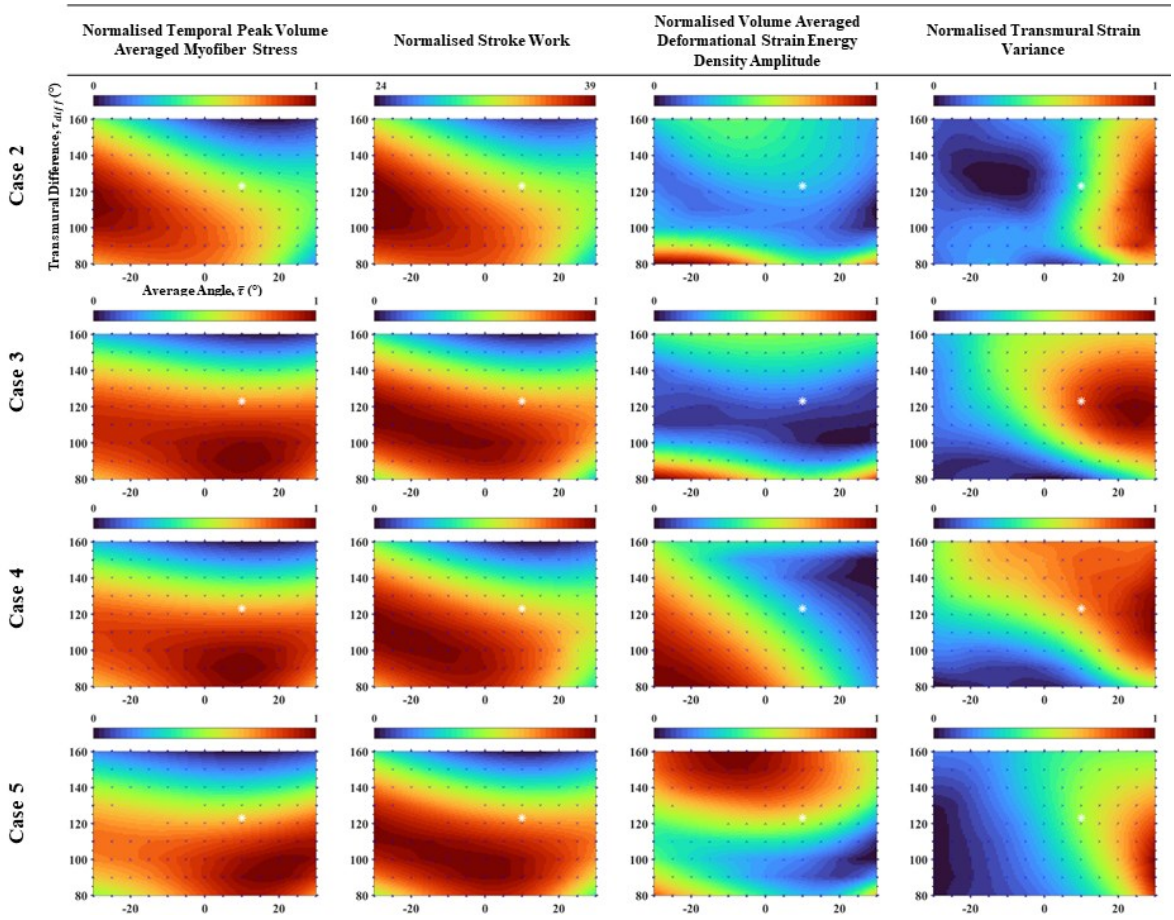

Figure 4.14. *Maps of biomechanics characteristics' plotted as a function of helix angle configurations for the patient specific fetal LV cases, obtained via the volume-constrained FE simulation approach. Simulated values on all maps are depicted by the blue x, values were interpolated to produce contour maps, where the contour describes the biomechanics characteristic in the range of helix angle configurations investigated. Each figure has the same x and y axis as described for Case 2. The white asterisk plots the average literature helix angle configuration* $\bar{\tau} \cong 9.5^o, \tau_{diff} \cong 123^o$.

4.3.2.3 Comparison of Image vs Simulated Circumferential and Longitudinal Strains

Green circumferential and longitudinal strain was calculated from the cardiac motion estimation algorithm (image-based strain measurements), for all cases. During the volume constrained FE modelling, circumferential and longitudinal strain was output for every helix angle configuration. Using Equation 4.6, ER was plotted for each case at every helix angle configuration, to evaluate where error was minimised and thus which simulated helix angle configuration best matched the image. Results of ER at each helix angle configuration, shown in Figure 4.15, demonstrate consistently minimised ER when $\boldsymbol{\tau_{diff}}$ is between 100° and 130°, across all cases. No noticeable trend was observed across $\bar{\boldsymbol{\tau}}$, as generally a minimised ER can be observed at any $\bar{\boldsymbol{\tau}}$ investigated.

The insensitivity of ER minimisation to $\bar{\boldsymbol{\tau}}$ was due to the strain characteristics being more sensitive to $\boldsymbol{\tau_{diff}}$. Visual inspection of a variety of $\bar{\boldsymbol{\tau}}$ values showed $\bar{\boldsymbol{\tau}}$ to alter the extent of LV torsional motion mildly. Separating the ER map for Case 1 in Figure 4.15, into its circumferential and longitudinal error subsets (shown in Figure 4.16), demonstrated how circumferential strain errors were consistently low at all mid to high $\boldsymbol{\tau_{diff}}$ values, whereas longitudinal strain error minimisation was more locally minimised at a mid-range $\boldsymbol{\tau_{diff}}$ values. Both circumferential and longitudinal strain error were again both similarly insensitive to $\bar{\boldsymbol{\tau}}$. This breakdown of ER demonstrates how the circumferential strain error consistently had an improved match to image compared with longitudinal strain error.

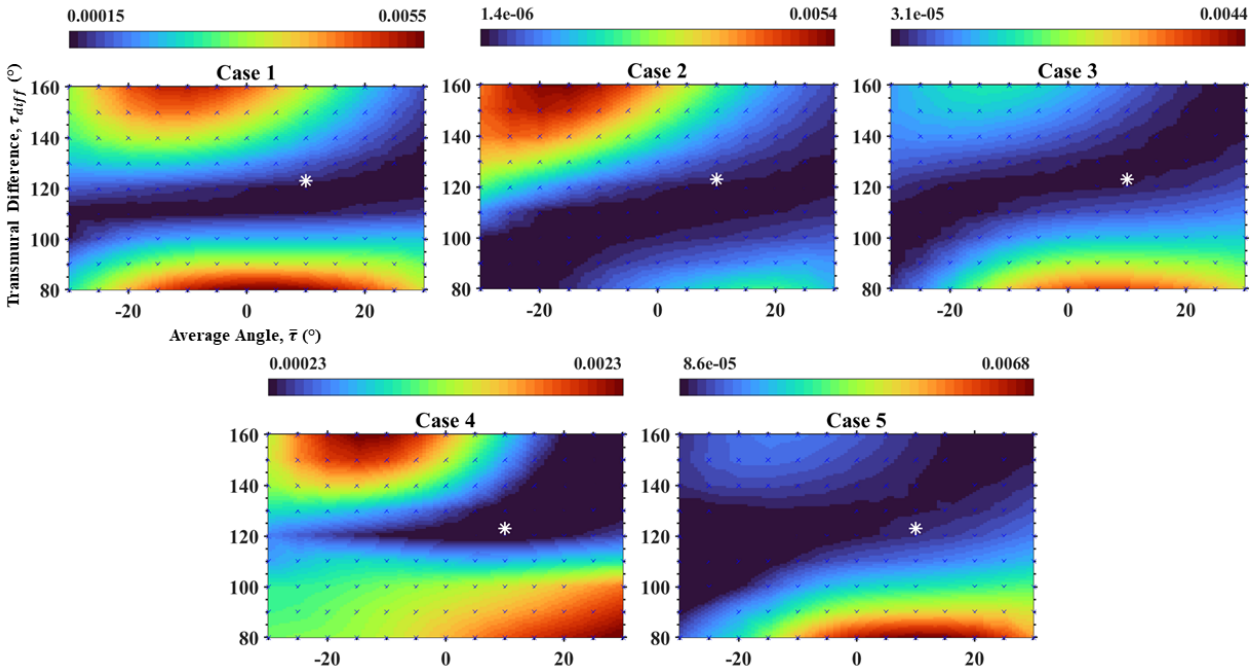

Figure 4.15. *ER according to Equation 4.6, plotted at each helix angle configuration simulated. Simulated values on all maps are depicted by the blue x, values were interpolated to produce contour maps, where the contour describes the combined strain errors in the range of helix angle configurations investigated. Each figure has the same x and y axis as described for Case 1. The white asterisk plots the average literature helix angle configuration* $\bar{\tau} \cong 9.5^{o}, \tau_{diff} \cong 123^{o}$.

The helix angle configuration with the lowest ER (and hence the best match of simulated strain to image) for each patient specific model is recorded in Table 4.3. From Table 4.3 $\bar{\boldsymbol{\tau}}$ ranging from -30° to 25° produces the best image to simulation match across the patient specific models, which is expected from the observation noted about Figure 4.15. $\boldsymbol{\tau_{diff}}$ is more constrained with the best patient specific simulated to image match ranging from 100° to 140°. Based on the data in Table 4.3 and that measurements for $\bar{\boldsymbol{\tau}}$ in literature range between 0° to 25° (Garcia-Canadilla et al. 2018; Nishitani et al. 2020; Ohayon et al. 1999), actual helix angle configurations for the patient specific models investigated are likely to lie in the range $\boldsymbol{0^{o} < \bar{\tau} <}$

$\mathbf{25^o, 110^o < \tau_{diff} < 140^o}$. Errors in strain measurements should be acknowledged due to scan noise associated with fetal ultrasound. Further work could be undertaken to evaluate the impact of scan noise on the accuracy of strain measurements. This could involve artificially increasing scan noise, measuring strain, and analysing the extent to which scan noise influences strain measurement precision.

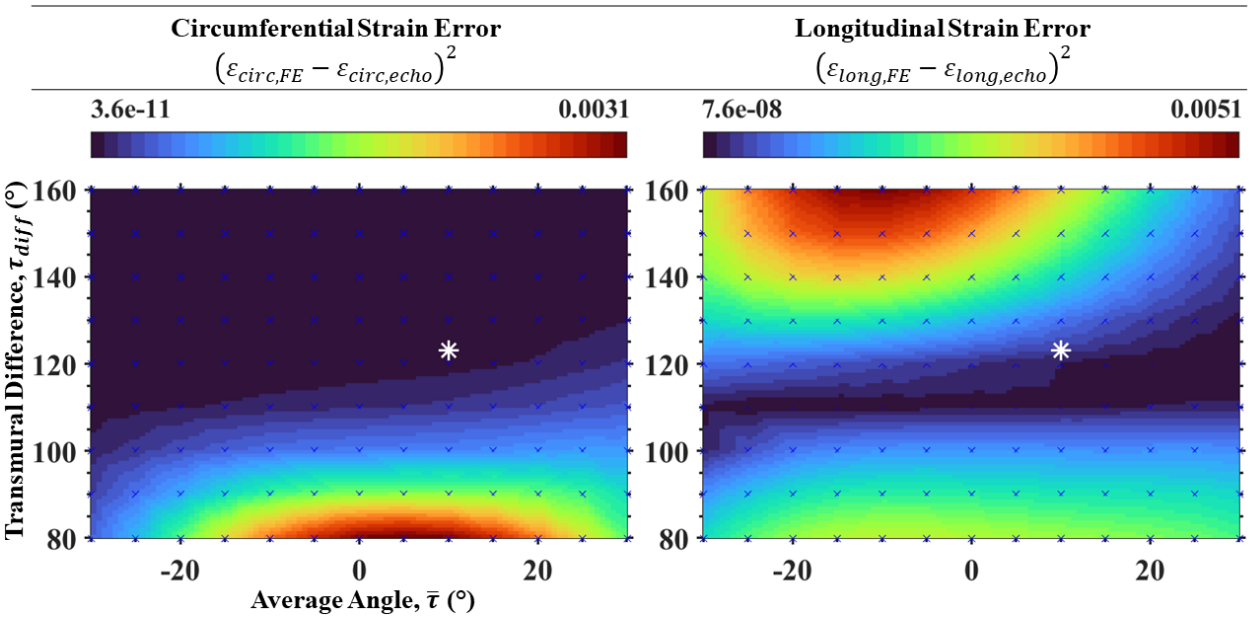

Figure 4.16. *Case 1 error maps between image-based strain calculation and volume-constrained FE strain output at each helix angle configuration for [Left] circumferential strain and [Right] longitudinal strain. Simulated values on all maps are depicted by the blue x, values were interpolated to produce contour maps, where the contour describes the directional strain errors in the range of helix angle configurations investigated. Each figure has the same x and y axis as described for Case 1. The white asterisk plots the average literature helix angle configuration* $\bar{\tau} \cong 9.5^o, \tau_{diff} \cong 123^o$.

Table 4.3. *Details of the helix angle configuration that minimised ER, with details of the exact circumferential and longitudinal strain produced in computational methods compared with image-based methods.*

	Helix Angle at Minimised ER		**Circumferential Strain**		**Longitudinal Strain**	
Case	$\bar{\tau}$	τ_{diff}	*Image*	*Simulation*	*Image*	*Simulation*
1	-20°	110°	8.25%	9.05%	8.95%	8.98%
2	-20°	100°	10.90%	10.83%	7.20%	7.30%
3	-25°	110°	13.60%	13.88%	11.55%	12.03%
4	25°	140°	14.76%	13.31%	12.20%	11.81%
5	-30°	110°	10.10%	12.92%	11.25%	12.22%

4.3.2.4 Effects of LV Morphology on the Relationship Between Helix Angle Configuration and Functionality

To investigate how the effect of LV shape impacts the relationship between helix angle configuration and fetal heart functionality, the methods applied in the patient specific modelling were again applied to the 7 idealised models described in Figure 4.3. The idealised models were simulated for a wider array of helix angle configurations to investigate the full range of possible outcomes. For the "Long" geometry, results for $\boldsymbol{\tau_{diff}}$ below 70° are not shown, as the FE model was unable to converge in many instances in this region, due to the extremely elongated geometry.

Figure 4.17 includes the biomechanics characteristic maps for all idealised model outputs. From initial visual inspection biomechanical optimality is highly dependent on LV geometry, due to the changes in contour variation that appear when LV geometry is varied.

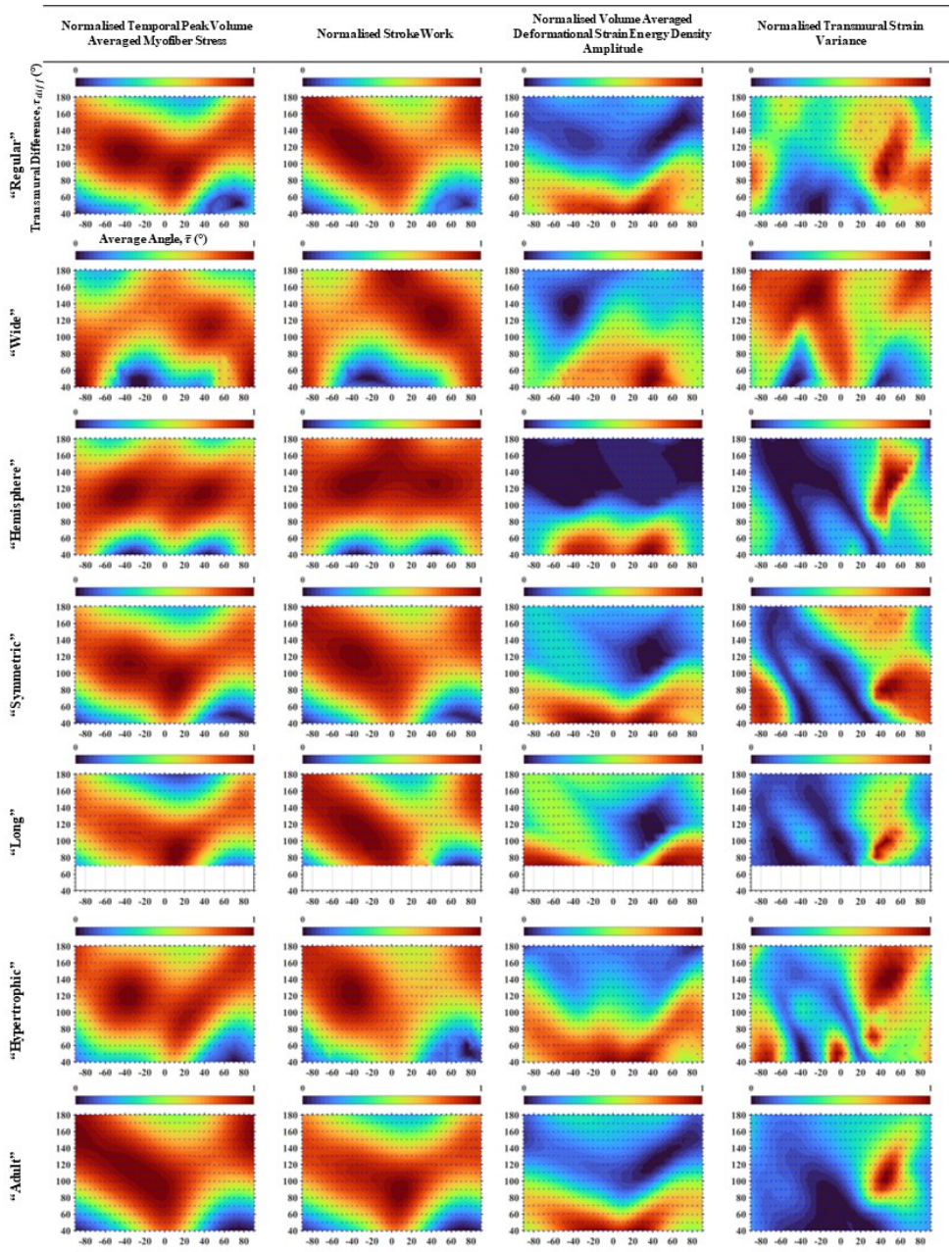

Figure 4.17. *Maps of normalised biomechanics characteristics' plotted as a function of helix angle configurations for all idealised geometries. Simulated values on all maps are depicted by the blue x, values were interpolated to produce contour maps, where the contour describes the biomechanics characteristic value in the range of helix angle configurations investigated. Each figure has the same x and y axis as described in the "Regular" model. The white asterisk plots the average literature helix angle configuration* $\bar{\tau} \cong 9.5^o, \tau_{diff} \cong 123^o$.

Firstly, comparing the “Regular” and “Symmetric” geometries, allowed the impact of shape symmetry to be investigated. These geometries produced similar stroke work and temporal peak volume averaged myofiber stress variation maps, as seen in Figure 4.17. The most notable difference between the “Regular” and “Symmetric” geometries biomechanics characteristic maps was in volume averaged deformational strain energy density amplitude. Volume averaged deformational strain energy density amplitude was greatly affected by the geometry change, and the results from the “Regular” geometry produced similar results as the majority of the patient specific models (except Case 4), with a horizontal band of low values. Case 4 and the “Symmetric” geometry produced similar deformational burden maps, which had a low region at $20° < \bar{\tau} < 60°$, $100° < \tau_{diff} < 160°$. Figure 4.18 visualises these comparisons with the similarities between Case 1 and the “Regular” geometry and Case 4 and the “Symmetric” geometry, where the idealised models have the same range as the patient specific models when analysing data within the white box. Upon observation Case 4 had a more symmetric geometry, which explains why the results produced differed so greatly from the other patient specific cases and instead was more in line with the “Symmetric” results for deformational burden.

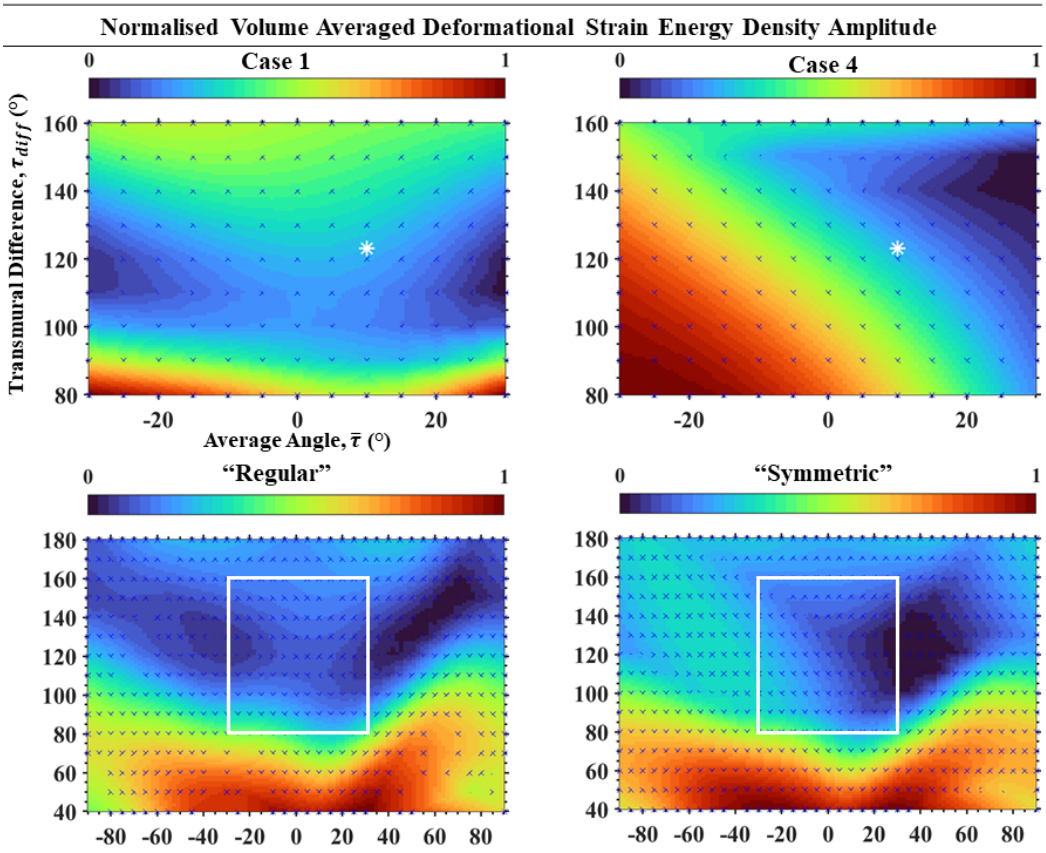

Figure 4.18. *Comparing Case 1 and the "Regular" model and Case 4 and the "Symmetric" models normalised volume averaged deformational strain energy density amplitude, to demonstrate the impact on results when going from a regular fetal geometry to a more symmetric geometry. White box on idealised model's biomechanics characteristic maps identifying the same region as the patient specific models. Simulated values on all maps, depicted by the blue x, values interpolated to produce contour maps, where the contour describes the biomechanics characteristic value in the range of helix angle configurations investigated. Each figure has the same axis as described for Case 1. The white asterisk plots the average literature helix angle configuration* $\bar{\tau} \cong 9.5^{o}, \tau_{diff} \cong 123^{o}$*, for the patient specific models.*

The "Wide," "Hemisphere," "Symmetric," and "Long" geometries represented a gradual increase in aspect ratio (ratio of longitudinal to lateral dimensions). Specifically, the "Wide" and

“Symmetric” geometries aspect ratios were reciprocals of one another, with an example of “Symmetric” to “Wide” geometrical rotation drawn in Figure 4.19, where the “Symmetric” geometry is a half prolate ellipsoid, and the “Wide” geometry is a half oblate ellipsoid, of the prolate ellipsoid rotated 90°. Therefore, the biomechanical functionality of these two geometries would be similar if the helix angle configuration was offset by 90°. This theory is illustrated in Figure 4.17, where temporal peak volume averaged myofiber stress, stroke work and volume averaged deformational strain energy density amplitude optimal points are offset 90°, when comparing the like for like maps between the “Symmetric” and “Wide” geometries, which displays a gradual shift in biomechanical optimality with the increase in aspect ratio. This result is notable, as it illustrates the impact LV geometry has on the relationship between helix angle configuration and biomechanical functionality.

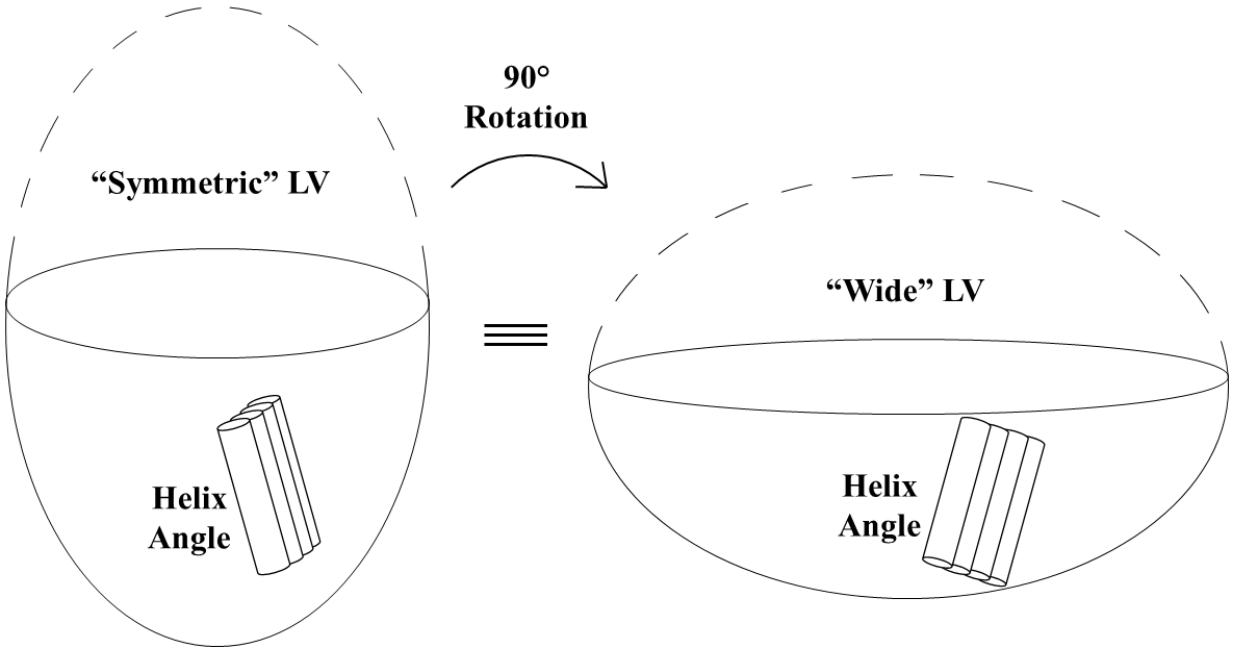

Figure 4.19. *Representation of the geometrical rotation required to go from the "Symmetric" to "Wide" LV.*

The “Hypertrophic” model was the “Symmetric” model with a 2 times uniform wall increase. When comparing the “Symmetric” vs “Hypertrophic” biomechanical optimality maps, only minor differences were observed. Specifically, magnitudes of biomechanical parameters varied between the “Symmetric” and “Hypertrophic” results and contour variation and therefore biomechanical optimality for volume averaged deformational strain energy density amplitude varied between models. Such results suggest that alterations in LV wall thickness do affect biomechanical optimality.

Transmural strain variance was computed to analyse which helix angle configurations minimised the biomechanical parameter. Across the idealised models a range of helix angle configurations resulted in low regions of transmural strain variance. The “Regular” model produced a more localised region of transmural strain variance, with the parameter at its optimal point when $\bar{\tau} \approx$ -29°, $\tau_{diff} \approx 51°$. Through visual inspection of the remaining results, transmural strain variance optimal helix angle configuration drastically varies, with two localised optimal regions for the “Wide” geometry and then the “Hemisphere”, “Symmetric”, “Long” and “Hypertrophic” models being variations on one another. The shift in biomechanical optimality for transmural strain variance demonstrates how the biomechanical parameter is strongly influenced by LV geometry.

To determine the impact of LV size on the relationship between biomechanical functionality and helix angle configuration, results from the fetal “Symmetric” model and the “Adult” model were compared. The “Adult” model exhibits the same morphometrics as the fetal “Symmetric” model, at a larger scale. Only minor differences in surface variation for stroke work and temporal peak volume averaged myofiber stress were found. Moderately higher changes to surface variation between the “Symmetric” and “Adult” models occurred for volume averaged

deformational strain energy density amplitude and transmural strain variance. This suggested that size scaling the LV from fetal to adult sizes did not play a major role in determining the effects of helix angle configurations on functionality, or in the biomechanical optimality of the heart.

4.3.2.5 Effects of Transverse Angle on the Relationship Between Helix Angle Configuration and Biomechanical Functionality

To test the effects of transverse angle on the relationship between helix angle configuration and biomechanical functionality the two descriptions of transverse angle variation described in Figure 4.6, were imposed onto Case 1. To reiterate, the description of transverse angle was based upon Vendelin et al.'s description, with a 0° transverse angle imposed at the epicardial and endocardial boundaries, and the transverse angle assumed to peak at the mid-wall (Vendelin et al. 2002).

The inclusion of transverse angle had minimal impact on the surface variation when investigating the relationship between helix angle configuration and biomechanical functionality (Figure 4.20). Therefore, transverse angle was not included in any further simulations.

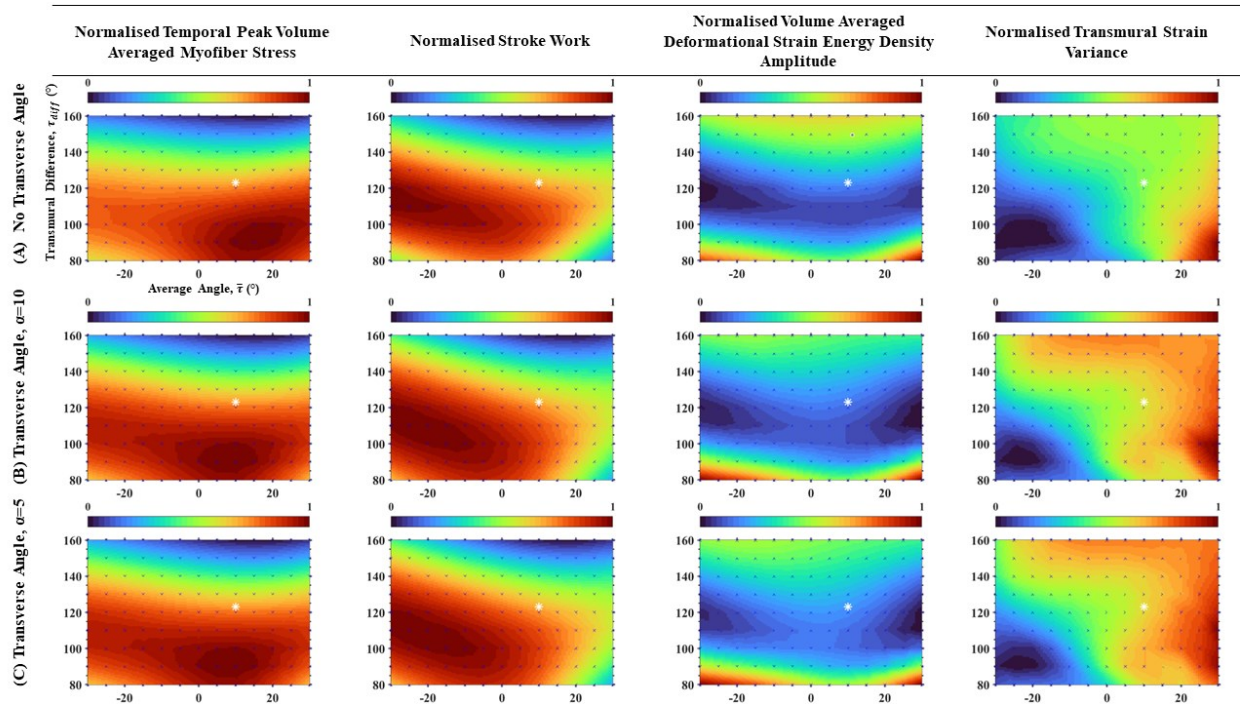

Figure 4.20. *Biomechanical characteristics output to analyse the impact transverse angle has on the relationship between helix angle configuration and biomechanical functionality. (A) Case 1 results with 0° transverse angle. (B) Case 1 with imposed transverse angles where α = 10, in Equation 4.8. (C) Case 1 with imposed transverse angles where α = 5, in Equation 4.8. Simulated values on all maps, depicted by the blue x, values interpolated to produce contour maps, where the contour describes the biomechanics characteristic value in the range of helix angle configurations investigated. Each figure has the same axis as described for Case 1. The white asterisk plots the average literature helix angle configuration* $\bar{\tau} \cong 9.5, \tau_{diff} \cong 123^{o}$*, for the patient specific models.*

4.3.3 Evaluation of Optimisation Algorithm Performance

After the LPM+FE optimisation process was established, it was tested on the 3 patient specific geometries, shown in Figure 4.7. Table 4.4 documents how a sufficient match was

achieved between simulation and imaged data for each model, when using the optimisation algorithm.

Table 4.4. *Image vs simulation match for all test models, when using the optimisation algorithm.*

	ID	SV (ml)	AV ΔP (mmHg)	MV ΔP (mmHg)	AVr ΔP (mmHg)	MVr ΔP (mmHg)
Image	Healthy	0.49	-	-	-	-
Simulation		0.49	-	-	-	-
Image	CAS-eHLHS	0.085	37.30	42.91	-	42.91
Simulation	(Pre-FAV)	0.084	39.59	42.56	-	42.56
Image	CAS-eHLHS	0.31	13.96	2.15	20.43	32.21
Simulation	(Post-FAV)	0.32	15.39	2.77	19.40	30.96

4.4 Discussion

Chapter 4 firstly calibrated the LPM, based on information reviewed in Section 3.2.4. The LPM was calibrated in such a way that minimally changed the relationships derived in the original model (Pennati et al. 1997; Pennati. and Fumero. 2000), whilst still improving the match to literature-based measurements (Johnson et al. 2000; Versmold et al. 1981). Overall, a reduction in RMSE error, between model and literature-based data, was observed compared to the original LPM (Pennati et al. 1997; Pennati. and Fumero. 2000). Secondly, the effects of helix angle configuration on fetal heart functionality, using patient specific fetal geometries and idealised geometrical extremes was studied. Thirdly, an optimisation algorithm was developed (primarily by Dr Wei Xuan Chan), for future patient specific modelling of healthy and CAS-eHLHS cases. The optimisation algorithm iteratively alters valve flow dissipative coefficient and myocardial contractility, to best match each computational parameter with the associated clinical measurement. Through this formulised matching approach patient specificity could be incorporated into the LPM+FE methods, whilst providing consistency in the model generation techniques for fairer comparison and enabling the back computation of myocardial contractility.

The main discussion points of this chapter however derive from work studying the relationship between helix angle configuration and biomechanics characteristics' and the influence LV shape has on such relationship and will be the focus of discussion from this point on.

Firstly, the biomechanics characteristics' (stroke work, myofiber stress, deformational burden and transmural strain variance) were investigated based on their individual benefits to cardiac function and to compare results from the helix angle configuration study with previous conclusions in literature. Firstly, as stroke work quantifies the cardiac pumping output, which is the primary function of the heart, it would be expected for stroke work to be optimised towards higher values during fetal development. Secondly, high myofiber stress indicates full engagement of the myocytes to produce contractile forces in the direction of the highest stresses and Washio et al. found that anticipating adult LV myocyte helix angle to remodel towards the direction of highest stress (Washio et al. 2020), it would also be expected for the fetal heart to be developing towards high myofiber stress. Thirdly, deformational burden characterises the occurrence of excessive microstructural damage that imposes high metabolic burden, resulting in cellular tissue repair, it would thus be reasonable to expect low deformational burden to be an optimality criterion for cardiac development. Finally, transmural strain variance was quantified to understand the effect of strain distribution through the myocardial wall when different helix angle configurations were imposed. Pluijmert et al. simulated adaptive remodelling of adult LV helix angle configurations as a response to biomechanical stimuli and found the helix angle configuration to reorientate to the principal strain direction and such remodelling of the helix angle configuration produced physiological helix angle configurations (Pluijmert et al. 2012). Studies by Vendelin et al. and Rijcken et al. demonstrated how helix angle configuration

substantially impacts the cardiac biomechanics of adult LVs and such studies proposed that the homogeneity of strains and stresses were two such optimality conditions that would yield helix angle configurations that were close to those recorded in literature for adult LVs (Rijcken et al. 1999; Vendelin et al. 2002). However, investigations in adult sheep conflicted with results by Vendelin et al. (Vendelin et al. 2002) and found that histologically measured helix angles did not coincide with predictions made from computationally optimising LV functionality (Ennis et al. 2008).

Like reports from adult studies (Pluijmert et al. 2012; Rijcken et al. 1999; Vendelin et al. 2002), this study also found that helix angle configuration influenced the biomechanics of the LV. Although, previous studies were exclusively based on adult LV geometries, generally using an idealised LV geometry (Rijcken et al. 1999; Vendelin et al. 2002) or a single patient specific adult LV (Palit et al. 2015). However, this study departed from such work, by testing several image-based patient specific fetal LV geometries, against a greater number of biomechanical parameters, whilst also studying the effect of LV shape on the relationship between helix angle configuration and biomechanical functionality. It was important to study the fetal LV geometries relationship between helix angle configuration and biomechanical functionality, rather than infer results from adult studies, for several reasons. Firstly, the fetal LV is developing towards a fixed helix angle configuration in gestation, therefore, developing understanding of the mechanisms that may lead to this helix angle configuration will help improve understanding of fetal cardiac development. Secondly, the fetal LV geometry differs from the ellipsoidal adult LV geometry. The fetal LV and RV are of similar pressures which results in a straighter septal wall and a more asymmetric LV geometry in gestation. Thirdly, disease development in gestation can result in morphological aberrations, as the helix angle configuration is developing towards a fixed

alignment in gestation. It would therefore be interesting to understand how the relationship between helix angle configuration and biomechanical optimality is affected at different LV geometries.

Results from this study demonstrated how helix angle configuration impacts the homogeneity of stresses and strains. However, the results contradicted findings from Vendelin et al. (Vendelin et al. 2002) and Rijcken et al. (Rijcken et al. 1999), who both stated physiological helix angle configurations to occur close to the biomechanically optimal regions of stress and strain. The differences in this study's results and literature findings are likely due to the difference between the adult idealised models used in previous studies compared with the patient specific fetal geometries used in this study.

Instead, it was found that no commonly reported fetal helix angle configuration aligned with the optimal value for any biomechanics characteristic investigated. However, parameters that were somewhat optimised included low deformational burden, high myofiber stress and stroke work. The average literature based fetal helix angle configuration of $\bar{\tau} \cong 9.5^o, \tau_{diff} \cong 123^o$, was between the optimal points of these biomechanics characteristics', suggesting that the fetal LV helix angle configuration is remodelling towards multiple biomechanical stimuli concurrently, thus achieving semi-optimality in all parameters, and true optimality in none. Future work is warranted to test this hypothesis.

Comparing the patient specific FE myocardial longitudinal and circumferential strains to those measured from their corresponding echocardiography images, it was found that a helix angle configuration of $0^o < \bar{\tau} < 25^o, 110^o < \tau_{diff} < 130^o$ could enable a good match between FE strains and image strains. Therefore, based on this conclusion, and its alignment with

literature-based reports of helix angle configuration, it would currently be suggested to assign $\bar{\tau} \cong 9.5^o, \tau_{diff} \cong 123^o$, the average fetal helix angle configuration measured in literature (Garcia-Canadilla et al. 2018; Nishitani et al. 2020; Ohayon et al. 1999), to future computational models. Also, the approach in estimating actual helix angle configuration through comparing image-based myocardial strains to the simulated values, may help back computed actual helix angle configurations in future studies.

The investigation of LV shape, through changes in aspect ratio, wall thickness and LV shape symmetry, on the relationship between helix angle configuration and biomechanical functionality led to some interesting conclusions. Firstly, the optimality maps for all biomechanics characteristics' were sensitive to changes in LV geometry, including geometry symmetry, wall thickness and aspect ratio. This supports previous hypothesises of helix angle remodelling, during fetal cardiac dysfunction (Torre et al. 2014) and congenital heart malformations (Tulzer et al. 2021b). Secondly, the optimal points between the "Symmetric" fetal model and "Adult" did not differ and therefore, it may be reasonable to assume morphological changes due to disease also shift the biomechanics optimality in adult hearts, for example in heart failure patients (Nauta et al. 2020). This theory would require further investigation using a range of healthy and diseased patient specific adult LV models. Thirdly, the comparison between the "Regular" and "Symmetric" geometry helped explain the difference observed in deformational burden optimality maps for Case 4 compared to the other patient specific cases, as Case 4 had a more symmetric structure, like that of the idealised "Symmetric" and "Adult" geometries.

Limitations of the helix angle configuration study include the idealisation that the helix angle varied linearly from the epicardium to the endocardium, and that the same transmural helix

angle configuration applies to any location on the LV wall. Although most experimental studies found that the linear transmural variation to be true through the entire LV wall (Nishitani et al. 2020) or bulk of the myocardium (Rohmer et al. 2007), some studies reported non-linear transmural variation (Garcia-Canadilla et al. 2018), and several studies have reported that different regions of the heart have varied helix angle configurations (Ennis et al. 2008; Garcia-Canadilla et al. 2018). Further to this the effect of sheetlet sliding was not investigated (Nielles-Vallespin et al. 2017). These idealisations could have led to errors in the results. Secondly, the RV, which could have affected the LV biomechanics, was not included in the FE simulations. Finally, the use of the volume constrained FE approach relied on smoothed volume over time waveforms, that did not show isovolumetric behaviour. This may have minorly impacted results, however the biomechanics characteristics' investigated were not taken from regions of isovolumetric contraction or relaxation.

4.5 Conclusion

Firstly, calibration of the LPM helped improve the match between the model and literature-based data. A study of the relationship between helix angle configuration and biomechanics characteristics' found that helix angle configurations had substantial influence on fetal heart biomechanics and function. Showing that literature reported fetal heart helix angle configurations achieved close to optimal values in maximising LV work done, maximising stress in the helix angle orientation, and minimising the deformational burden of the myocardial tissue, but were not at the optimal configuration of any of these criteria. The literature reported helix angle configuration enabled a close match between the myocardial strains measured from the echocardiography images and the myocardial strains outputted at literature reported helix angles from the FE modelling, providing some validation for the configuration. It would therefore be

suggested that future fetal LV simulations adopt the helix angle configuration of approximately $\bar{\tau} \cong 9.5^o, \tau_{diff} \cong 123^o$, until the capability to accurately estimate patient specific helix angle configurations becomes feasible. Furthermore, it was found that the relationship between helix angle configurations and biomechanical outcomes was brought about by the "Asymmetric" geometry of the fetal LV, which was sensitive to geometric changes, including changes in wall thickness and LV chamber aspect ratio, but was not sensitive to size scale of the LV, when comparing the fetal "Symmetric" and "Adult" geometries. This suggested that the conclusion of changes in biomechanical optimality due to disease is also applicable to the adult LV. Finally, an optimisation algorithm was developed to incorporate further patient specificity into the LPM+FE methods, enabling the back computation of myocardial contractility. The optimisation algorithm was shown to match well with patient specific data. Overall, Chapter 4 enabled LPM+FE methods to be developed to support the fulfilment of the Overall Aim.

Chapter 5: Characterising the Biomechanical Environment of CAS-eHLHS LVs

From retrospective studies FAV intervention has shown promise in reducing the likelihood of a UV birth outcome, from approximately 73% to approximately 24-41% (Friedman et al. 2018; Gardiner et al. 2016; Mäkikallio et al. 2006; Tulzer et al. 2022a). However, there is still a substantial proportion of cases not developing towards a BV outcome (Friedman et al. 2018; Gardiner et al. 2016; Tulzer et al. 2022a), post technically successful FAV intervention, suggesting clinical scans alone lack satisfactory predictive capabilities, and patient selections from scans is not sufficiently accurate. Therefore, image-based patient specific cardiac FE modelling was performed to firstly improve understanding of the biomechanical implications of CAS-eHLHS and then investigate if biomechanical parameters have stronger predictive capabilities than echocardiographic clinical data, to support improved patient selection. Biomechanical analysis of the patient specific CAS-eHLHS models suggested that CAS-eHLHS cases that respond well to intervention (go on to be BV, as opposed to UV) tend to be biomechanically "stronger" and larger, with generally larger myocardial contractility and LV size. Interestingly, peak systolic myofiber stress had a uniquely great ability in differentiating between models that would go on to be BV or UV post-FAV. Image-based analysis of the CAS-eHLHS cases, using clinical echocardiographic measurements was generally unable to distinguish between cases that would go on to be UV or BV as clearly. A simplified equation for

estimating peak systolic myofiber stress was derived for quick and easy estimation of myofiber stress, from echocardiographic measurements and was shown to outperform other predictive indicators in the retrospective cohort of 37 cases. Therefore, peak systolic myofiber stress may have high potential in improving the ability to predict outcomes and accurately select patients for FAV. Work included in Chapter 5 has also been published (Green et al. 2024).

5.1 Introduction

A natural history study has shown CAS-eHLHS fetal hearts to have a 73% likelihood of progression to HLHS by the time of birth (Mäkikallio et al. 2006). Progression to the malformation was especially likely for cases with retrograde transverse aortic arch flow, left-to-right flow across the foramen ovale, and monophasic mitral inflow. The aortic obstruction in these cases leads to high LV pressure, globular LV shapes, hypertrophy of LV walls, diminished LV contractile deformation, high AV velocity, and MVr, which also causes high left atrium pressure and left atrium distension (Tulzer and Arzt 2013). These abnormalities are likely detrimental to the growth of the LV and are likely the cause of subsequent hypoplastic development, which leads to a UV birth outcome, a theory supported by animal model studies, which reported that biomechanical aberrations led to cardiac maldevelopment and congenital heart malformations (Eghtesady et al. 2007; Rugonyi 2016).

FAV was found to be promising for CAS-eHLHS patients, by reducing the risk of progression to HLHS from approximately 73% to approximately 24-41% (Friedman et al. 2018; Gardiner et al. 2016; Mäkikallio et al. 2006; Tulzer et al. 2022a). FAV is a catheter-based intervention which widens the aortic obstruction (further details on the intervention given in Chapter 3), to normalise several of the above abnormal features, which will likely restore LV growth, thus reducing the likelihood of a UV outcome. However, FAV carries with it a 4-10% procedural related loss (Arzt et al. 2011; McElhinney et al. 2009; Pickard et al. 2020; Tulzer et al. 2022b), and FAV damages the AV and causes AVr, such that at birth, valve replacement procedures such as the Ross-Konno procedure is often required (Freud et al. 2014). Although, being functionally BV at birth simplifies postnatal surgical treatment, improving survival and

reducing morbidity. A recent cost-benefit analysis showed that FAV confers a modest medium-term (age 6) survival benefit from 72% to 82% (Pickard et al. 2020).

Current patient selection criteria for FAV includes: the presence of LV systolic dysfunction; monophasic MV inflow, bidirectional transverse aortic arch flow; an LV long axisZ score >-1; and left to right shunting through the foramen ovale (Friedman et al. 2018; Tulzer and Arzt 2013). However, a substantial proportion of fetuses selected for FAV did not avoid progression to a UV birth outcome, suggesting a current inability to accurately predict outcomes, and that current selection criteria for the intervention can be refined to more accurately identify patients that will benefit from the intervention (Friedman et al. 2018; Gardiner et al. 2016; Mäkikallio et al. 2006; Tulzer et al. 2022a). More accurate patient selection can prevent the selection of cases that are unlikely to positively respond to the intervention, and thus avoid unnecessary procedural risks. It may also lead to the identification of cases that are likely to respond to the intervention, but that are outside of the current selection criteria. For this reason, there has been continued investigation into biomarkers that are indicative of outcomes (Beattie et al. 2020; Friedman et al. 2018; Prosnitz et al. 2018).

Biomechanics evaluation of the CAS-eHLHS fetal heart, or the investigation of its force dynamics in relation to its motion and deformation, is important. This is because the CAS-eHLHS heart has drastically different biomechanical characteristics from the healthy heart, the FAV intervention is essentially a mechanical intervention in nature, and the heart is likely to be mechanosensitive in its growth, where abnormal biomechanics may play a significant role in the progression to malformation. Cardiac FE modelling is a good approach for investigating myocardial biomechanics and has been very useful in improving understanding of a multitude of heart diseases in the past (Dewan et al. 2017; Ong et al. 2020; Shavik et al. 2021; Wisneski et al.

2020). For example, Ong et al. previously used such a model to elucidate the effects of how various CAS-eHLHS characteristics impact cardiac function and biomechanics (Ong et al. 2020). A previous FE model coupled with a myocardial growth mathematical model showed that reduced strain stimuli can potentially explain the gestational development of some HLHS cases (Dewan et al. 2017). FE modelling performs an assessment of the physics of the heart's function and can provide biomechanics parameters that are difficult to directly obtain from clinical measurements, such as myocardial stresses and the extent of active tension generation, which may be useful for predicting outcomes.

Chapter 5 performs image-based, patient specific FE modelling of CAS-eHLHS and healthy hearts to better understand the biomechanical characteristics of CAS-eHLHS. Biomechanical characteristics performance in predicting FAV intervention outcomes is then compared with clinical measurements, and a method for real-time estimation of intervention outcome is derived and tested based on the data available.

5.2 Methods

5.2.1 Image Acquisition

4D echocardiography images of 9 fetal hearts with CAS-eHLHS and 6 healthy hearts were acquired using the GE Voluson E10 (GE Healthcare, Chicago, IL, USA) ultrasound machine. Images were taken in the spatio-temporal image correlation mode, at sweeps of 10-15s and capture rate of 70-90 frames per second. All images were obtained with informed consent from the Kepler University Hospital, Austria, under Institutional Review Board protocol 1009/2017, and from the National University Hospital Singapore under Domain Specific Review Board protocol 2014/00056. 2D echocardiography and Doppler measurements for a further 28 CAS-eHLHS fetuses undergoing intervention, acquired with the Vivid E95, was further used

together with the first 9 CAS-eHLHS cases for analysis on predictive capabilities of various parameters.

5.2.2 Intraventricular Pressure Measurements

During some interventions, the use of a pressure guidewire (Pressurewire X, Abbott Laboratories) to measure fetal intracardiac pressure was included. The pressure values were extracted simultaneously to the intervention, where the high-fidelity pressure sensor was positioned proximal to the tip of the balloon catheter, and records LV pressure measurements and aortic pressure measurements. The methods for retrieving intracardiac pressure measurements are based on published work (Goldstein et al. 2011). The use of the pressure guidewire during FAV intervention was approved under protocol 1136/2018. Where possible, such pressure measurements act as validation for the patient specific pre-intervention models.

5.2.3 Patient Characteristics

Healthy control cases were from ages of 21+2 wks+days to 32+0 wks+days gestation. CAS-eHLHS were from ages of 22+4 wks+days to 32+0 wks+days gestation and were selected for FAV intervention, by Dr Andreas Tulzer and Dr Gerald Tulzer, via the following characteristics: dilated and poorly contracting LV, left to right shunting at atrial level, retrograde aortic arch flow, and no signs of AV atresia.

Characteristics of the patients included in the study are given in Table 5.1, including age, disease features, postnatal outcomes, and postnatal procedures. Throughout the study, the disease cases are denoted by a ‘D’ in front of the ID number and healthy cases by a ‘H’. A BV circulation outcome was defined, by Dr Andreas Tulzer and Dr Gerald Tulzer, when the LV was the only source of systemic circulation and where there was an absence of pulmonary hypertension at 1 year of age. Diseased cases outside of this definition were designated as UV. A

UV outcome is fatal unless the neonate receives a heart transplant or undergoes extensive and invasive procedures, detailed in Chapter 2. Postnatal procedures for cases with BV outcomes included AV dilation or the Ross-Kono procedure, while that for cases with UV outcomes included the Norwood procedure, Ross-Kono and BV-UV conversion.

Table 5.1. *Patient characteristics of CAS-eHLHS cases before intervention. In diseased cases, age is the fetal age at the pre-FAV scans, which generally occurs 1-3 days before FAV intervention. Y - yes, N - no, Dil – balloon dilation of the AV, RK - Ross-Kono procedure, NW - Norwood Procedure, Conv - BV to UV conversion. N/A – no procedure as parents chose comfort care at an alternative centre; procedure planned for this patient was Ross-Konno surgery, with patient believed to progress to a BV outcome classification, therefore, for the purpose of this study the patient was classified as BV.*

Case	Postnatal Circulation	Age (wks+days)	Multiple FAVs	Bradycardia	Pericardial Effusion	LV Thrombus	Hydrops	Postnatal Procedures
D1	BV	24+6	N	Y	N	N	N	Dil.
D2	BV	29+0	Y	N	N	N	Y	RK
D3	BV	29+3	N	N	N	N	N	RK
D4	BV	29+6	N	Y	N	N	N	N/A
D5	BV	30+1	N	N	N	N	N	-
D6	UV	22+4	N	N	N	Y	N	NW
D7	UV	24+6	N	Y	N	N	N	NW
D8	UV	27+2	N	N	N	N	N	NW
D9	UV	29+1	Y	N	N	N	N	NW,RK, Conv.
H1	-	21+2	-	-	-	-	-	-
H2	-	21+3	-	-	-	-	-	-
H3	-	21+4	-	-	-	-	-	-
H4	-	24+0	-	-	-	-	-	-
H5	-	28+0	-	-	-	-	-	-
H6	-	32+0	-	-	-	-	-	-

5.2.4 Image Processing of Fetal Echocardiography

From the fetal echocardiography images, morphometric measurements of the heart chambers, including LV and RV longitudinal length (Tulzer et al. 2022a), LV posterior wall thickness (PWT), LV inner diameter at diastole (LVID), ascending aorta diameter and relative wall thickness (RWT), were taken by a collection of independent observers, and then averaged.

RWT was calculated as,

$$RWT = \frac{2 \times PWT}{LVID}, \quad \text{Equation 5.1}$$

and aspect ratio was calculated as,

$$Aspect\ ratio = \frac{LVID}{LV\ Length}. \quad \text{Equation 5.2}$$

Patient specific reconstruction of 3D computational models of fetal hearts was obtained using methods previously described in Chapter 3. In brief, stacked 2D images were extracted from the 4D scans, at 0.5 mm intervals, at one time point. A Lazy Snap algorithm (Li et al. 2004) was then used to trace the endocardial and epicardial boundaries and the traced slices were reconstructed using VMTK. Any irregularities in the reconstructed geometry were smoothed in Geomagic (Geomagic Inc., Morrisville, USA). Figure 5.1 depicts all patient specific geometries modelled in this study.

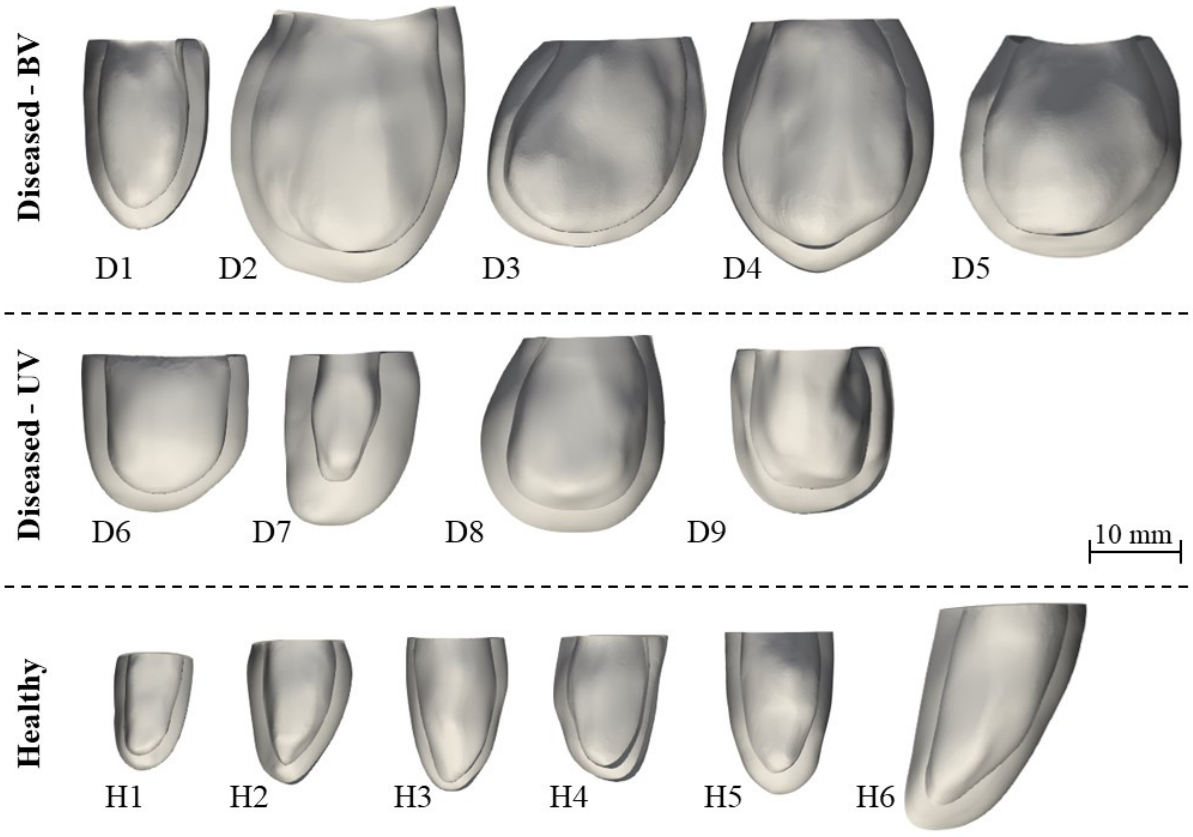

Figure 5.1. *All reconstructed cardiac geometries used in this study. [Top row] Models that went on to be BV at birth. [Middle row] Models that went on to be UV at birth. [Bottom row] Healthy models. Scale bar shown in the top left.*

The cardiac motion estimation algorithm was described in detail in Chapter 3 and can be briefly explained as such: the cardiac motion was modelled as a cyclic and spatially consistent b-spline of Fourier whole-field motion model and was curve-fitted to the displacement fields from pair-wise image registration of images from all consecutive time frames (Wiputra et al. 2020). Using the estimated cardiac motion, the reconstructed LV geometry at EDV was animated over the cardiac cycle. For CAS-eHLHS diseased LVs, motion was diminished, and this was sufficient to extract accurate motions from images. For healthy LVs, greater cardiac motions and

deformations occurred, and reconstruction at end-systole was needed to enhance motion estimation, by including the registration results of the end-diastole to end-systole time points to the curve fitting, as previously described (Wiputra et al. 2020). An example of the geometries imposed onto the motion tracking is included in Figure 5.2.

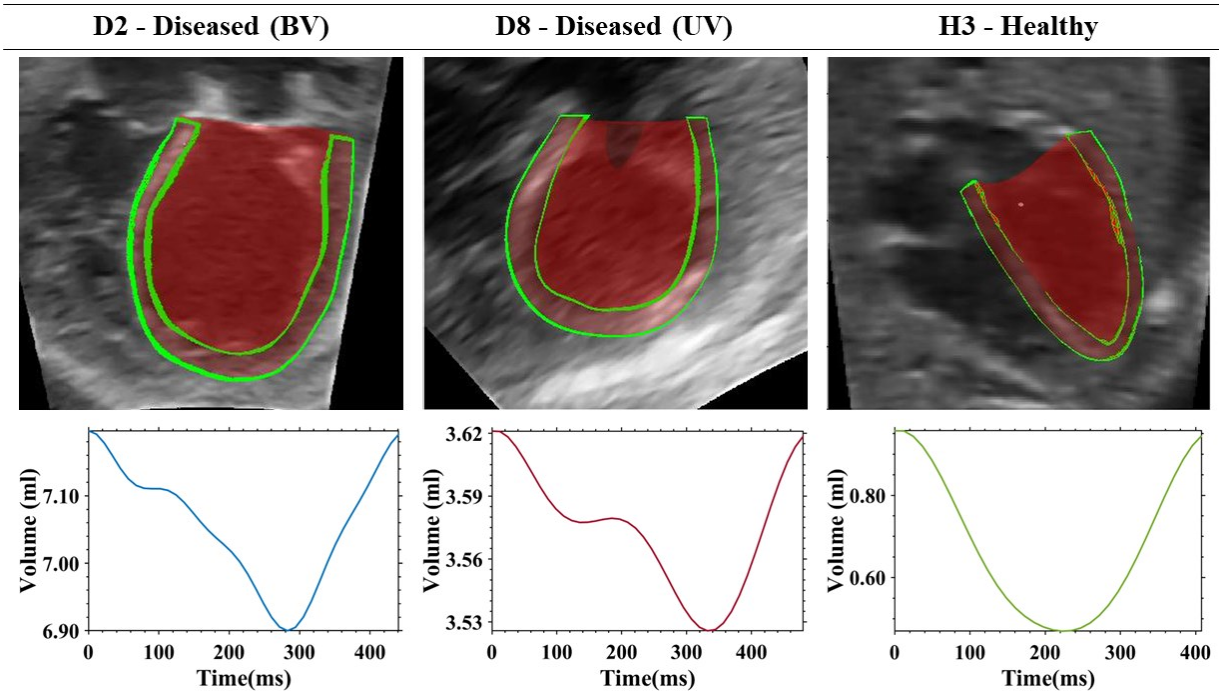

Figure 5.2. *[Top row] Reconstructed geometries superimposed onto associated echocardiography image, green outline highlighting geometry proportion close to current image plane. [Bottom row] Volume over time variation of each geometry output from cardiac motion estimation methods.*

The volume data extracted from the model reconstruction and cardiac motion estimation methods, for the LV, RV and LA, are disclosed in Table 5.2, along with the cardiac cycle time.

Table 5.2. *Cardiac cycle length and volume data extracted from the image segmentation and cardiac motion estimation methods.*

	Cardiac Cycle (ms)	**LV EDV (ml)**	**LV SV (ml)**	**RV EDV (ml)**	**RV SV (ml)**	**LA EDV (ml)**	**LA SV (ml)**
D1	400	1.49	0.28	0.96	0.46	1.39	0.39
D2	441	7.20	0.30	4.03	1.44	2.58	0.44
D3	450	5.21	0.50	5.53	1.33	2.85	0.54
D4	490	6.67	0.17	4.65	1.53	2.78	0.38
D5	419	6.39	0.82	6.14	1.90	2.67	0.51
D6	408	1.98	0.10	2.91	1.09	1.04	0.13
D7	392	1.02	0.085	2.96	1.22	1.12	0.36
D8	480	3.62	0.095	4.44	0.96	1.99	0.20
D9	479	2.94	0.28	2.59	0.74	5.42	0.24
H1	400	0.41	0.22	0.65	0.29	-	-
H2	416	0.92	0.49	0.63	0.38	-	-
H3	408	0.96	0.49	0.72	0.32	-	-
H4	400	1.19	0.62	1.15	0.61	-	-
H5	400	1.36	0.82	1.48	0.63		
H6	402	2.17	1.32	2.90	1.50	-	-

3D LV myocardial Green Lagrangian strains (Equation 5.3) were computed from the images in both the longitudinal and circumferential directions along mid-wall coordinates. The mid-wall coordinates were identified by averaging the epicardial and endocardial boundaries (Figure 5.3A), from the 4-chamber or transverse echocardiography view, using previously documented techniques (Ren et al. 2023). The motion of the mid-wall coordinates was tracked using the cardiac motion estimation algorithm, with the anterior and inferior slices were removed, due to increased noise in these regions.

$$Green\ Lagrangian\ Strain = \frac{1}{2}(F^T \cdot F - I), \qquad \text{Equation 5.3}$$

where F was the deformation gradient tensor and I is the identity matrix.

The strains in the longitudinal and circumferential direction were then visualised in Paraview (Figure 5.3B) and spatially averaged.

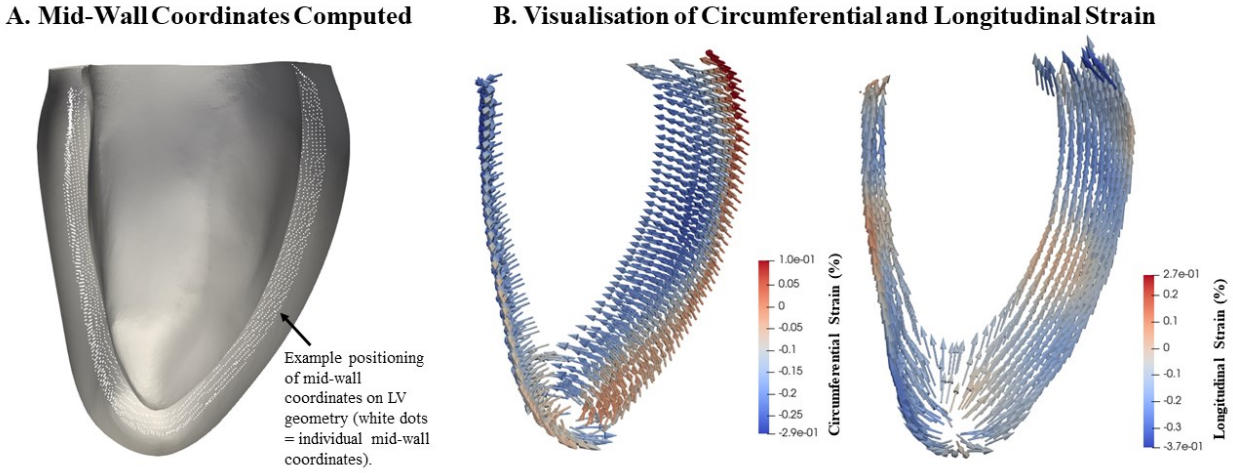

Figure 5.3. *[A] Mid-wall coordinates calculated from averaging the image-based epicardium and endocardium boundaries, depicted by the white dots and overlaid on to the reconstructed LV geometry. [B] Example circumferential and longitudinal strain visualisation.*

5.2.5 Computational Modelling Methods

Image-based, patient specific LPM+FE modelling of fetal LV myocardial biomechanics was performed in accordance with the fundamental methods described in Chapter 3. Briefly, the FE model was connected to an age scalable LPM to enable ventricular-vascular coupling (Pennati et al. 1997; Pennati. and Fumero. 2000). The FE methods constituted of the passive and active properties of the fetal LV myocardium, where the Fung type transversely isotropic hyperelastic constitutive model (Guccione et al. 1991; Humphrey and Yin 1987) described the passive myocardial behaviour and the active behaviour was described by Gucciones active tension model (Guccione et al. 1993). The material parameters assigned remained constant from patient to patient and are detailed in Table 5.3.

Table 5.3. *Passive and Active Myocardial Material Parameters.*

Parameter	Symbol	Unit	Value
Passive stiffness coefficient	Co	Pa	200
Stiffness coefficient in fibre direction	b_{ff}	-	29.9
Stiffness coefficient in sheet and sheet normal direction	b_{xx}	-	13.3
Stiffness coefficient in shear directions	b_{fx}	-	26.6
Shape of peak isometric tension-sarcomere length relation	B	μm−1	4.75
Sarcomere length under no active tension	l_0	μm	1.58
Relaxed sarcomere length	l_r	μm	1.85
Time intercept of linear relaxation duration with sarcomere length	b	ms	-800
Gradient of linear relaxation duration with sarcomere length relaxation	m	msμm−1	524
Maximum intracellular calcium concentration	Ca_0	μM	4.35

For all models, the helix angle configuration was assumed to vary linearly from the epicardium to endocardium, from -52° to +71° respectively (example in Figure 5.4A), which was the average helix angle configuration reported in 3 previous fetal LV tissue studies (Garcia-Canadilla et al. 2018; Nishitani et al. 2020; Ohayon et al. 1999).

Before computations, the unloaded state of the LV, or the theoretical geometry of the heart at zero LV cavity pressure, was calculated and assumed to be the stress-free condition. This was achieved via Finsberg et al.'s backward displacement method (Finsberg et al. 2018), described in Chapter 3. Briefly, the method is as follows: LV pressure loading was iteratively applied from the load-free state to the end diastolic state until the targeted end-diastolic pressure and volume was achieved, at every iteration the load-free state was adjusted by changing the pressure, based on the inverse of the loading deformation. The targeted EDP was set as 5 mmHg for healthy hearts (Johnson et al. 2000), but this was adjusted incrementally upwards in 1 mmHg intervals if negative pressures were encountered during early diastole. For diseased cases, end-diastolic pressure was assigned by the end-diastolic left atrium pressure, obtained by assuming a

linear relationship between left atrium size and pressure (LA compliance) (Matsuda et al. 1990). This models the abnormal left atrium pressurisation in diseased cases.

LV myocardium models reconstructed from echocardiography images were used for FE modelling and were meshed into a minimum of 2,500 quadratic tetrahedral elements (Figure 5.4B), which was sufficient for mesh convergence as shown in a previous study (Ong et al. 2020).

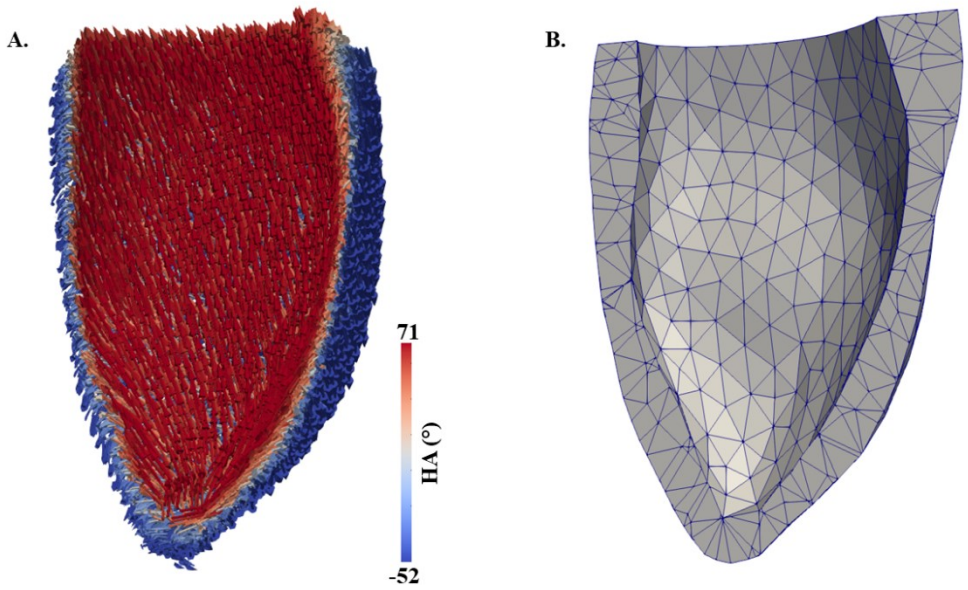

Figure 5.4. *[A] Example of fibres applied to H3, with negative fibres at the epicardial surface and linear transmural variation to the positive angle at the endocardial surface. [B] Example of mesh applied to H3.*

The formal FE simulation was performed by minimising the weak formulation of a Lagrangian function described by Shavik et al. (Shavik et al. 2018), which enforces tissue stress equilibrium, incompressibility, and a specific cavity volume to yield cavity pressure, using the Newton Solver in the FEniCS software. The boundary conditions were like that previously

reported (Shavik et al. 2018), with the basal plane of the LV constrained in the longitudinal direction and a weak 90 Pa spring applied to the entire epicardium at the load-free state, to simulate interactions with surrounding tissues and to constrain translational motion of the model. The model was executed for 30 cycles, to ensure steady state was achieved. The full FE formulation is described in Chapter 3.

5.2.5.1 Patient Specific Modelling Optimisation

The LPM+FE optimisation methods were performed using the optimisation algorithm established in Chapter 4 (Figure 4.8 provides a process overview), for healthy and CAS-eHLHS patients. Briefly the methods were iteratively performed by altering valve flow dissipative coefficients and myocardial contractility, to best match each computational model with clinical measurements. Through this matching process, the patient specificity of the model could be maintained, and myocardial contractility could be back computed.

5.2.6 Statistical Analysis

Z Scores for echocardiography measurements parameters were computed using healthy population data from Luewan et al. for LVID and PWT (Luewan et al. 2011), from Devore et al. for LV and RV longitudinal length, EDV, SV and EF (Devore et al. 2019; DeVore et al. 2017) and Chen et al. for ascending aorta dimensions (Chen et al. 2022). For biomechanics parameters from computational outputs, no population data was available to eliminate the age dependent variation, therefore, when a computational parameter showed a trend of variability with age, it was normalised with the regression line of the healthy cohort, before being analysed.

The Mann-Whitney U test was performed on all data comparisons, due to small sample sizes. Statistical significance assumed when $P < 0.05$.

To estimate the effect size of differences in specific parameters between the BV and UV groups the Cohen's D value was calculated as,

$$d = \frac{\bar{x}_{BV} - \bar{x}_{UV}}{s_p} \times corr, \qquad \text{Equation 5.4}$$

where $\bar{x}$, is the mean value of the parameter for the UV or BV group as indicated by the subscript, s_p is the pooled standard deviation and $corr = 0.7839$ and is the correction factor for when N < 50.

5.2.7 Principal Component (PC) Analysis and Regression Analysis

A simple linear mathematical model was developed for rapid computation of peak-systolic volume-averaged myocardial stress from clinically measured parameters. PC analysis was first used to seek modes or combinations of parameter values that could best describe variability between diseased fetal cases. The number of principal components needed for a cumulative representation of >90% of the variability was noted, and then regression was performed to determine the coefficients for these modes, so that a weighted sum of these modes could be used to estimate peak systolic myofiber stress.

5.2.8 Receiver Operating Characteristic (ROC) Analysis

To determine which pre-FAV characteristic has the greatest capability in distinguishing BV versus UV outcomes, ROC analysis was performed on retrospective images (n=37). Where the curve is the sensitivity versus 1-specificty, defined as,

$$x\ axis = 1 - \ Specificity = 1 - \frac{False\ Positive}{False\ Positive + True\ Negative}, \qquad \text{Equation 5.5}$$

and,

$$y\ axis = Sensitivity = \frac{True\ Positive}{True\ Positive + False\ Negative}. \quad \text{Equation 5.6}$$

The area under the curve (AUC) quantifies the predictive capabilities of each parameter. The sample size includes the 9 diseased cases where the 4D images were used for FE simulations and a further 28 cases that had 2D images available (some of the retrospective data was also analysed in a previous study (Tulzer et al. 2022a)). The analysis was performed on parameters within this study, and for RV/LV longitudinal length ratio and estimated peak LV pressure, which were identified in literature as promising pre-FAV parameters for indicating post-FAV outcomes (Friedman et al. 2018; Tulzer et al. 2022a).

5.3 Results

5.3.1 Echocardiography Measurements versus Simulation Match

After the iterative FE modelling optimisation process, the percentage error between simulation parameters and echocardiography-measured parameters were 2.55 ±3.56%, 6.43 ±4.20%, and 4.80 ±3.94% for SV, AV ΔP and MVr ΔP respectively. MV ΔP were minimised to within 0.7 mmHg of the image-based value. Table 5.4 records each image-based value and that achieved in the simulations, for diseased and healthy cases.

Table 5.4. *Image vs simulation match for all models. Where disease models were optimised for SV and valvular ΔP and healthy models SV.*

Cases	Data Type	SV (ml)	MV Δ***P*** (mmHg)	MVr Δ***P*** (mmHg)	AV Δ***P*** (mmHg)
D1	Image	0.28	3.69	66.75	48.12
	Simulation	0.31	3.32	65.39	47.60
D2	Image	0.30	3.24	36.00	5.06
	Simulation	0.33	3.58	32.78	4.88
D3	Image	0.50	1.49	39.94	4.87
	Simulation	0.50	2.02	36.32	5.65
D4	Image	0.17	1.11	39.74	20.43
	Simulation	0.17	1.37	36.76	21.23
D5	Image	0.82	1.90	49.31	6.25
	Simulation	0.81	2.37	48.14	5.65
D6	Image	0.10	0.55	27.04	13.54
	Simulation	0.10	1.02	27.30	13.91
D7	Image	0.085	2.56	42.91	37.30
	Simulation	0.084	2.80	42.56	39.59
D8	Image	0.095	1.69	13.10	3.61
	Simulation	0.088	1.28	13.31	3.38
D9	Image	0.28	5.28	33.57	19.35
	Simulation	0.29	5.97	31.23	21.41
H1	Image	0.22	-	-	-
	Simulation	0.22	-	-	-
H2	Image	0.49	-	-	-
	Simulation	0.49	-	-	-
H3	Image	0.49	-	-	-
	Simulation	0.49	-	-	-
H4	Image	0.62	-	-	-
	Simulation	0.62	-	-	-
H5	Image	0.82	-	-	-
	Simulation	0.83	-	-	-
H6	Image	1.32	-	-	-
	Simulation	1.31	-	-	-

5.3.2 Model Validation

Model validation of fetal biomechanics simulations remains a challenge, due to limited data availability. In this study 1 proper set of pressure measurements was achieved during FAV intervention. The measurements are recorded in Table 5.5 and are the values before the AV had been widened via the balloon catheter (pre-FAV measurements). Overall, a sufficient match was achieved between *in vivo* and simulation pressure values in the LV and aorta, however, this comparison was only possible for one patient case, which limits the robustness of the validation currently.

Table 5.5. *Pressure guidewire measurements versus simulated pressure values for D3.*

	Peak LV Pressure (mmHg)	**Peak Aortic Pressure (mmHg)**
D3 *In Vivo*	45.56	43.98
D3 Simulated	49.72	45.21

5.3.3 Echocardiography Anatomic and Functional Measurements

Echocardiography cardiac anatomic and functional measurements for pre-FAV and healthy control hearts are shown in Figure 5.5. Pre-FAV peak valvular velocity measurements (Figure 5.5A-C) showed no statistical significance between the BV and UV disease sub-groups, although both AV and MV antegrade velocities were substantially higher than healthy hearts. Both BV and UV disease sub-groups had elevated EDV Z Scores from healthy controls, but the difference was only significant between BV and healthy groups, and not between BV and UV groups (Figure 5.5D). Both BV and UV groups had significantly lower SV and EF Z Scores than healthy groups but again, there was no significant difference between BV and UV groups (Figure 5.5E-F). The BV group had significantly higher LV and RV longitudinal length than controls (Figure 5.5G-H), and although BV LV longitudinal length was generally higher than the UV

group, the difference was not significant. Similarly, the BV group generally had higher LVID (Figure 5.5J), lower RWT (Figure 5.5M), and higher aspect ratio (Figure 5.5K), than the UV group and healthy controls, but again significance was found only between the BV and control group. No significance was observed across all groups in RV/LV length ratio (Figure 5.5I) and PWT (Figure 5.5L). For ascending aorta diameter Z Score, healthy patient specific data was not available for ascending aorta calculations and therefore the standard deviation of normative data has been included in Figure 5.5N (Chen et al. 2022). No statistical significance was found between BV and UV groups, but both BV and UV groups were significantly greater than healthy controls. In terms of strains, both BV and UV groups were significantly smaller than healthy controls, for circumferential and longitudinal strains and between the BV and UV subgroups for circumferential strain but again, no significance was observed between the BV and UV groups longitudinal strain (Figure 5.5O-P).

Overall, the data demonstrated that diseased hearts were larger than healthy hearts and had lower strains and SV. Between the BV and UV groups, BV hearts tended to have larger average dimensions and higher average strains than UV hearts. However, statistical significance was not found for any echocardiography measurements investigated in the BV UV subgroup, aside from circumferential strain, and there was consistently significant overlap in measurements between the two groups, suggesting that it would not be easy to distinguish between the two groups with echocardiography measurements alone.

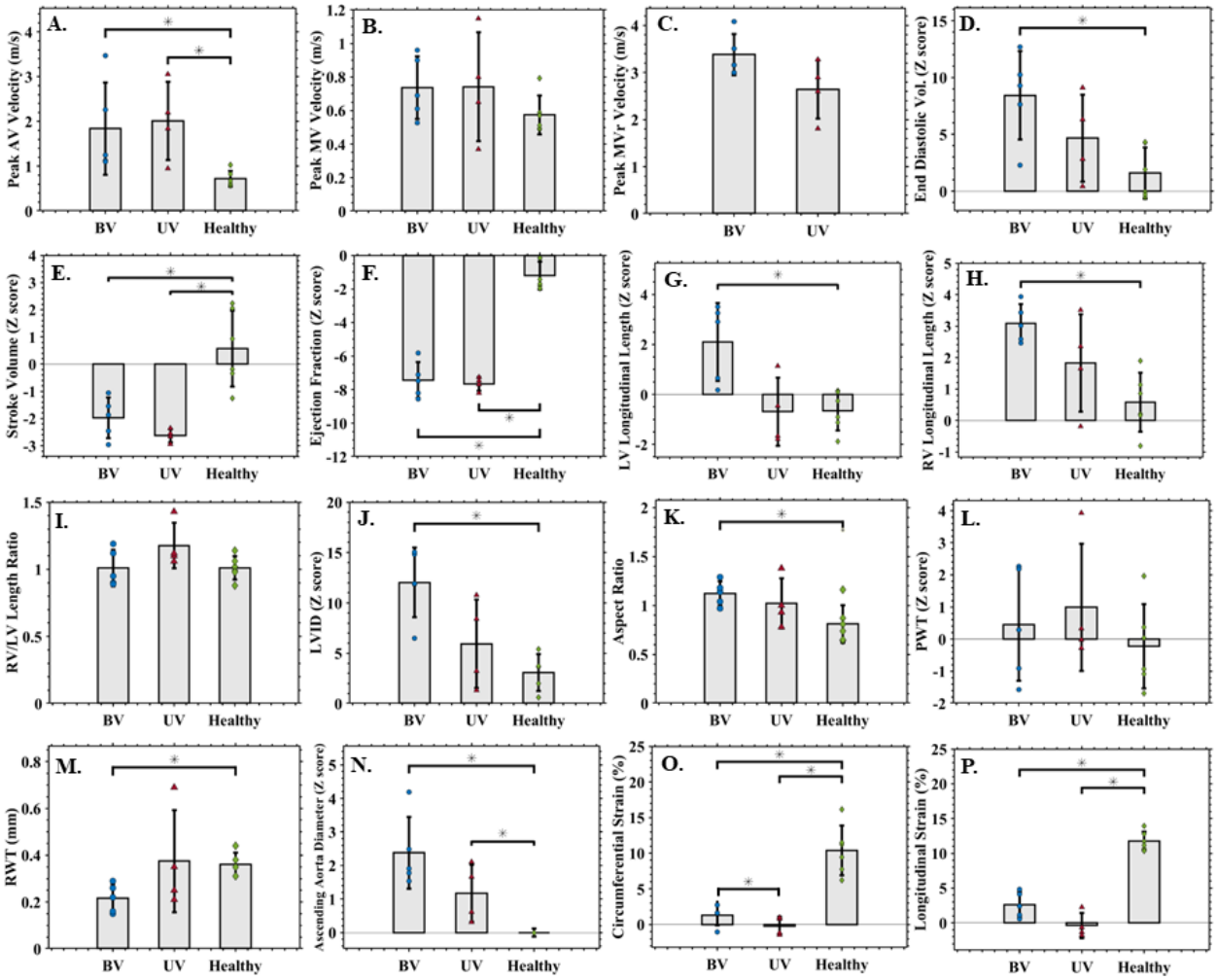

Figure 5.5. *Imaged-based measurements overlayed onto mean and standard deviation bar plots, for the BV and UV diseased groups, with data for healthy controls included where appropriate. * $p<0.05$. sample sizes were n=5 for BV, n=4 for UV and n=6 for healthy controls. For ascending aorta diameter, literature data was used* (Chen et al. 2022) *as measurements could not be clearly obtained from some of the images.*

5.3.4 Image-Based Computational Cardiac Biomechanics

Figure 5.6 shows representative results from the image-based FE simulations, showing that the resulting PV loops and spatially averaged myofiber stress over the cardiac cycle were reasonably physiologic. Appendix 5.2 includes the remaining PV loops and characteristics

extracted from the PV loops, such as peak pressure and work done will be presented and evaluated in the following sections.

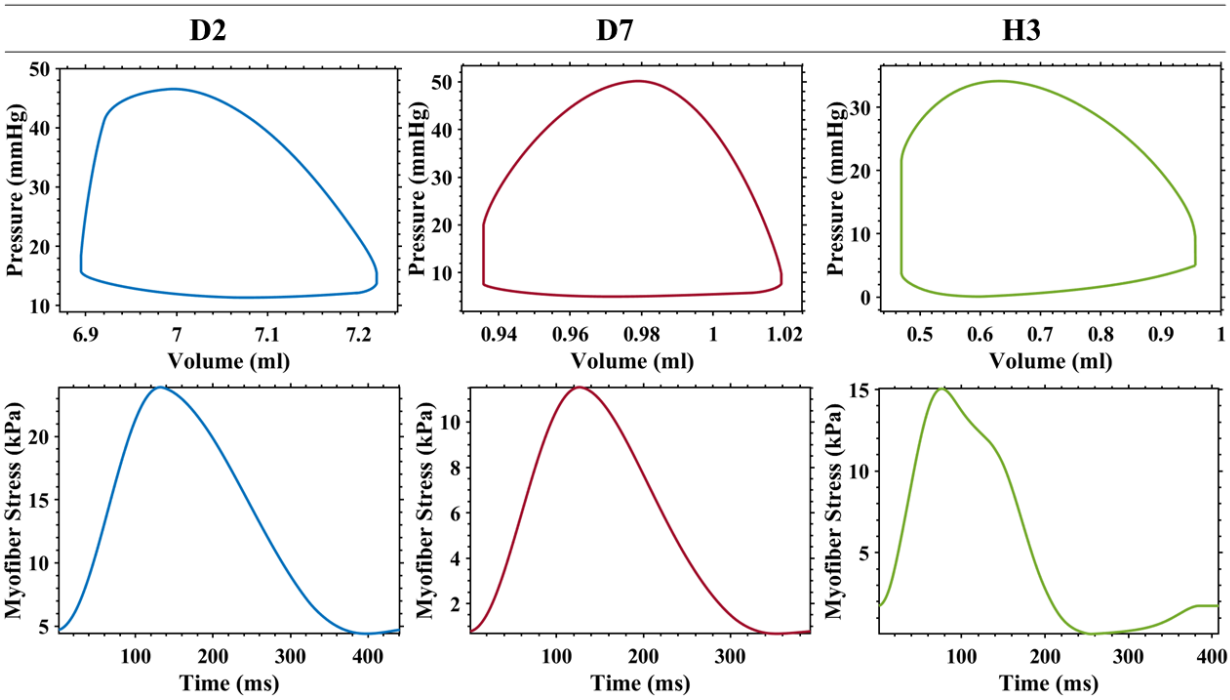

Figure 5.6. *PV loop and myofiber stress variation over a cardiac cycle example outputs from biomechanics simulations for a BV model (D2), UV model (D7) and healthy model (H3).*

Biomechanical parameters output from the computational models are included in Table 5.6, with statistical analysis performed between the disease subsets (BV and UV) and healthy cases.

Table 5.6. *Model specific biomechanics characteristics', with statistical analysis.*

	Peak LV Pressure (mmHg)	EDP (mmHg)	Work Done (mmHg)	Peak Systolic Myofiber Stress (kPa)	Contractility (kPa)
D1	73.55	7.33	21.05	22.19	39.59
D2	46.54	12.07	8.48	23.87	26.41
D3	49.72	12.78	15.93	21.91	27.64
D4	49.99	13.01	4.84	21.66	24.17
D5	61.05	11.46	34.75	29.61	37.93
D6	35.83	8.48	2.22	12.93	16.78
D7	50.14	5.54	2.98	11.53	21.65
D8	24.80	11.11	1.05	8.96	8.21
D9	48.44	5.00	3.57	13.53	41.67
H1	21.05	5.00	3.57	7.91	41.67
H2	34.43	6.00	13.24	13.88	61.02
H3	34.13	5.00	13.05	15.05	60.41
H4	38.29	7.00	18.87	12.99	66.28
H5	28.83	7.00	17.15	10.27	73.65
H6	46.96	12.00	47.82	13.04	92.96
BV-UV P value	0.19	-	0.032	0.016	0.016
BV-Healthy P value	0.0087	-	1.00	0.0043	0.0043
UV-Healthy P value	0.35	-	0.020	0.61	0.0095

As previously stated, parameters output from biomechanics simulations generally do not have the population data available to compute Z Scores to account for variations due to gestational age. Therefore, if peak LV pressure, work done, peak systolic myofiber stress and myocardial contractility of the healthy patients varied with gestational age, the regression line of this variation was used to normalise the individual case values going forward, minimising the influence of gestational age, when analysing the results.

Peak LV pressure was known to increase with gestational age according to previous invasive measurements, therefore peak LV pressure of each patient was normalised by the

expected value calculated from the literature regression line (Johnson et al. 2000), where the regression line and simulated pressure values are shown in Figure 5.7A. From the trends of computed results, LV work done (the area within the PV loop), and myocardial contractility of healthy models increased with gestational age from regression analysis (Figure 5.7B and D) and therefore, these biomechanics parameters were normalised by the expected value of a healthy heart of the same age from the regression analysis, before the comparisons between groups were performed. Peak systolic myofiber stress appeared to have little change over gestational age for the healthy cases (Figure 5.7C) and therefore, no normalisation was undertaken for myofiber stress values.

From the normalised quantifications, diseased hearts were found to have generally higher LV pressures compared to the healthy controls and the UV group, but no statistical significance was found (Figure 5.7E). Diseased hearts had significantly lower work done than healthy hearts, and the BV hearts produced higher work than the UV hearts, but no significance was found between the two groups (Figure 5.7F). In terms of peak systolic myofiber stress, UV hearts had very similar values to healthy hearts, whereas the BV hearts had a drastic elevation in peak systolic myofiber stress (more than two-fold), which was significantly higher than both the UV and healthy groups, with no data overlap between the groups (Figure 5.7G). In terms of myocardial contractility, both diseased groups were significantly lower than healthy controls, and a significant difference was observed between BV and UV groups. However, there was some overlap between the UV and BV data.

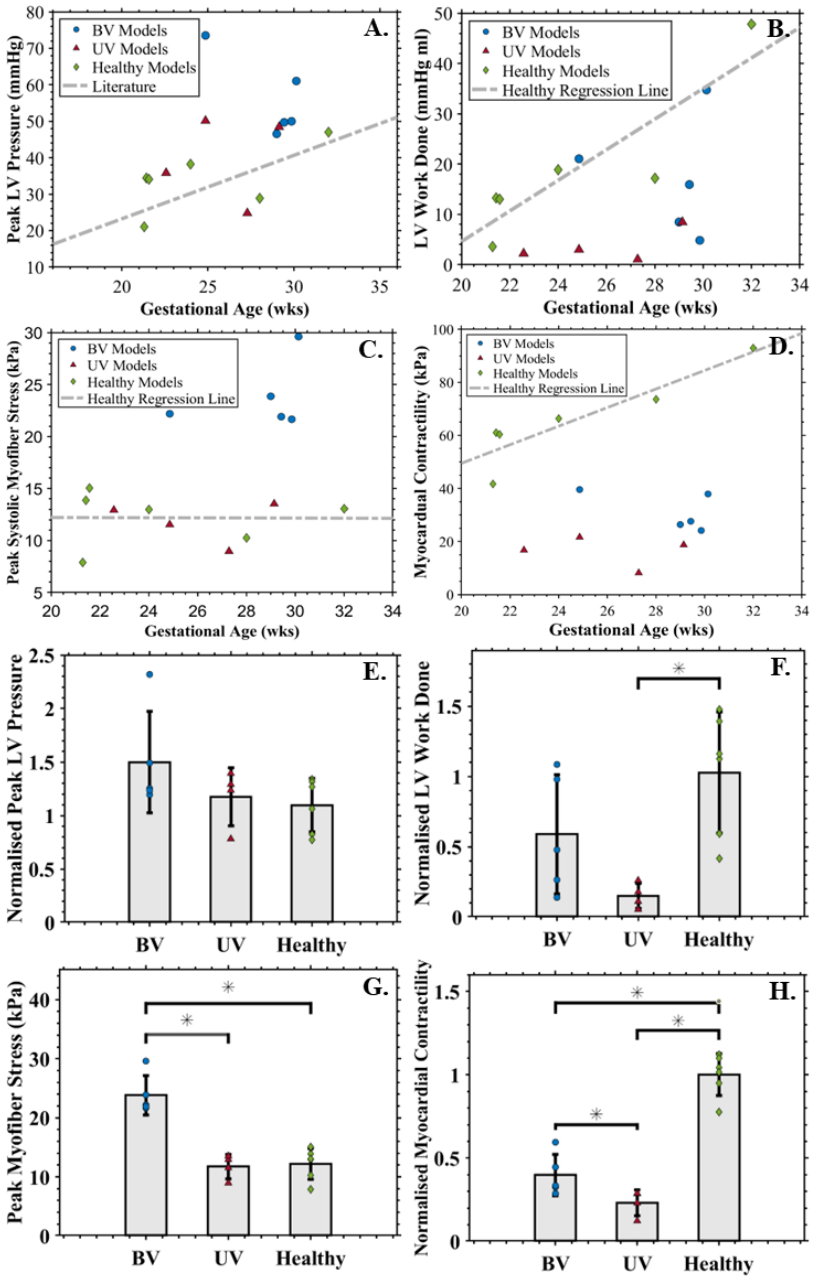

Figure 5.7. *FE outputs for the BV (n=5) and UV (n=4) diseased groups and healthy controls (n=6). [A-D] Parameters plotted with respect to gestational age. The expected normative values (dotted line) were obtained literature* (Johnson et al. 2000) *for [A], and from regression of the healthy control data for [B-D]. [E-H] Shows the same biomechanics parameters after normalisation, by the expected normative values from the corresponding gestational age, expressed as data points superimposed on mean and standard deviation bar plots. * $p<0.05$.*

Overall, the data demonstrated that diseased hearts had significantly altered biomechanics, including elevated LV pressure, and decreased circulatory work done and lower myocardial contractility, compared to healthy hearts, and BV hearts experienced high myocardial stresses. Between the BV and UV groups, both contractility and peak systolic myofiber stress were significantly different. However, peak systolic myofiber stress was very different between BV and UV hearts, with little overlap between the two groups. This was thus potentially a good parameter for distinguishing the two groups, to predict FAV outcomes.

5.3.5 Image and Computational Parameter Effect Size

To quantify all the investigated parameters' ability to distinguish between UV and BV groups, the Cohen's D standardised mean difference was computed (Table 5.7), where, the larger Cohen's D value, the greater parameter ability in distinguishing between BV and UV patients' pre-FAV intervention.

The results of Table 5.7 are plotted in Figure 5.8 and show that peak systolic myofiber stress had the highest Cohen's D value. This was followed by echo-measured ventricular size parameters, such as LV longitudinal length and longitudinal strain, which were close to the biomechanics parameters, normalised work done and myocardial contractility in Cohen's D value.

Table 5.7. *BV UV Cohen's D values for image and computational parameters investigated.*

	Cohen's D
Peak AV Velocity	0.14
Peak MV Velocity	0.013
Peak MVr Velocity	1.08
EDV (Z Score)	0.77
SV (Z Score)	0.92
EF (Z Score)	0.22
LV Longitudinal Length (Z Score)	1.50
RV Longitudinal Length (Z Score)	0.84
PWT (Z Score)	0.23
LVID (Z Score)	1.21
RWT	0.78
Aspect Ratio	0.40
RV/LV Length Ratio	0.85
Ascending Aorta (Z Score)	0.98
Circumferential Strain	0.88
Longitudinal Strain	1.28
Normalised Peak LV Pressure	0.66
Normalised Work Done	1.12
Peak Systolic Myofiber Stress	3.44
Normalised Myocardial Contractility	1.25

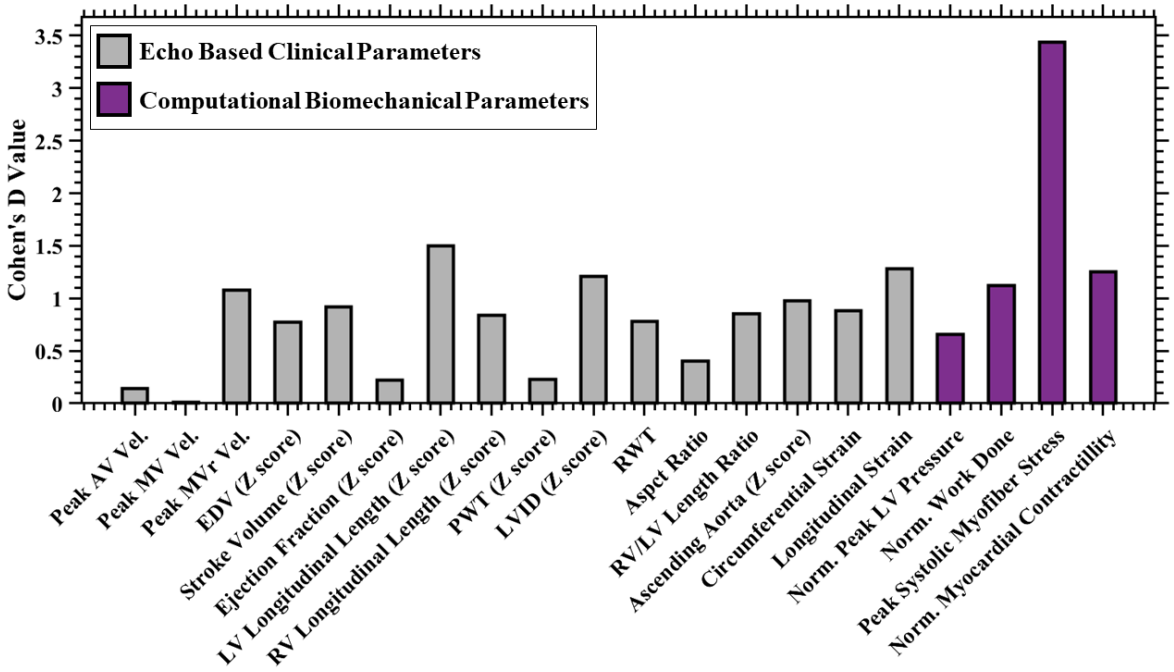

Figure 5.8. *Cohen's D values for all parameters investigated in the study, representing the parameters' ability to differentiate between BV and UV outcomes with pre-FAV data.*

5.3.6 Relationship Between Image Based Measurements and Peak Systolic Myofiber Stress

To understand the dependencies of the peak systolic myofiber stress, correlation analysis was performed between peak systolic myofiber stress and echocardiography parameters. The correlation analysis was initially performed on all cases modelled (healthy and diseased) and then on just the diseased cases. Results analysing all cases modelled (in Figure 5.9) showed that peak systolic myocardial stress had a good positive correlation with LV size parameters (EDV, longitudinal length and LVID) RV longitudinal length, and MVr, and a good negative correlation with RWT. Furthermore, the regression with LV length, RWT, SV, EDV and MVr had P values < 0.05, demonstrating significant relationships. Observations stated when analysing all cases modelled, generally agreed with observations from the regression analysis of diseased cases only. However, the addition of a strong positive correlation between peak systolic myofiber stress and SV was also observed only when analysing the diseased cases.

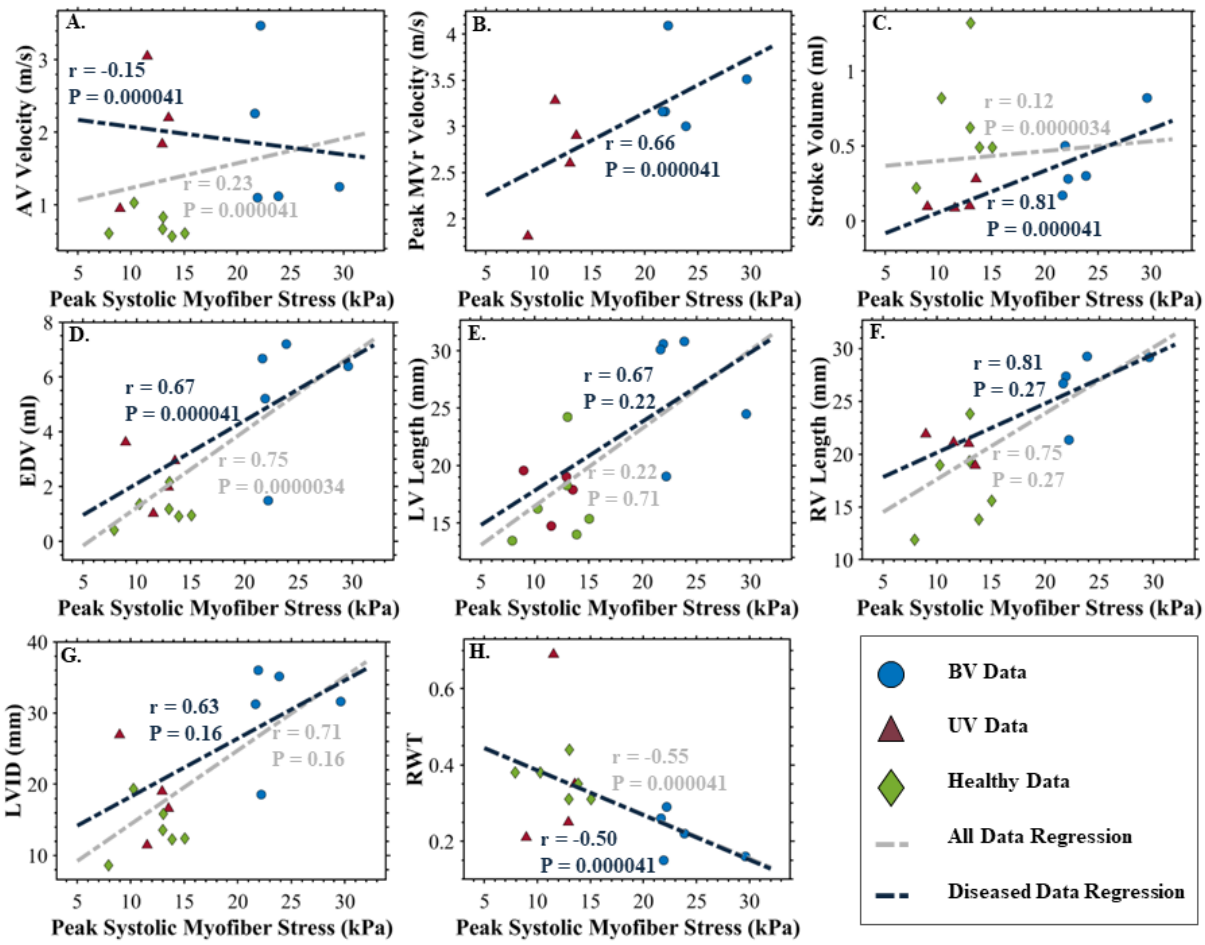

Figure 5.9. *Investigating the relationship between peak systolic myofiber stress and various metrics of LV size and function. Regression line of all data (healthy and diseased) in grey and regression line of just diseased data in dark blue.*

When analysing all cases, the correlations are logical from the theoretical standpoint. Firstly, myocardial stress was determined via a force balance between the cavity blood pressure and tensile forces in the myocardial walls, and was thus higher with greater systolic pressure, which was the driver of regurgitation. Myofiber stress thus correlated positively with MVr. Further, myocardial wall stresses could be approximated by myocardial wall forces divided by cross-sectional area, which was determined by wall thickness. Myofiber stress thus correlated

negatively with RWT. The relationship between cavity pressure and wall tension was further governed by the shape of the LV chamber, as could be illustrated by the hoop stress theory, which stated that larger chambers had higher wall tension. Myofiber stress thus correlated positively with LV size.

These results suggested that it is possible to derive a parameter to theoretically represent peak systolic myocardial stress, for easier calculation via a simple function of echocardiography parameters. This would enable fast and easy estimation of myocardial stress from echocardiography scans, which could be used to distinguish between UV and BV groups, and to predict FAV outcomes.

To derive an estimation for peak systolic myofiber stress PC analysis was performed, with parameters that had a good correlation with peak systolic myofiber stress, AV velocity, MVr velocity, LV longitudinal length, RV longitudinal length, LVID, RWT, EDV and SV (Note: EDV and SV were calculated by applying the half prolate ellipsoid equation to describe LV volume at EDV and ESV). The resulting top three modes described 93.05% of the cumulative proportion and are shown in Equation 5.7. The regression coefficients obtained from the subsequent regression between the modes and peak systolic myofiber stress are shown in Equation 5.9.

$$\left[\overrightarrow{PC_1} \quad \overrightarrow{PC_2} \quad \overrightarrow{PC_3}\right] = \begin{bmatrix} 0.3393 & -0.4374 & 0.2430 \\ 0.01739 & -0.7685 & -0.002620 \\ -0.4014 & -0.07994 & 0.4159 \\ -0.4041 & -0.2020 & 0.2223 \\ -0.4352 & 0.04481 & 0.1248 \\ 0.3460 & -0.1418 & 0.4632 \\ -0.4150 & -0.02060 & 0.2708 \\ -0.2807 & -0.3851 & -0.6443 \end{bmatrix}, \qquad \text{Equation 5.7}$$

$$[a_0 \quad a_1 \quad a_2 \quad a_3] = [-24.9240 \quad -1.9403 \quad -5.5865 \quad -3.4160]. \qquad \text{Equation 5.8}$$

Through combining the PC modes and regression coefficients, as shown in Equation 5.9,

$$Estimated\ Peak\ Systolic\ Myofiber\ Stress = a_0 + a_1\overrightarrow{PC_1}\cdot\vec{V} + a_2\overrightarrow{PC_2}\cdot\vec{V} + a_3\overrightarrow{PC_3}\cdot\vec{V}. \quad \text{Equation 5.9}$$

Where $\vec{V}$ is the column vector of the echocardiography parameters, as shown in Equation 5.10,

$$\vec{V} = \begin{bmatrix} AV\ Velocity \\ MVr\ Velocity \\ LV\ Longitudinal\ Length \\ RV\ Longitudinal\ Length \\ LVID \\ RWT \\ EDV \\ SV \end{bmatrix}. \quad \text{Equation 5.10}$$

The final function for the estimation of peak systolic myocardial stress is derived to be,

$$Estimated\ Peak\ Systolic\ Myofiber\ Stress = -24.9240 + 0.9550V_1 + 4.2687V_2 - 0.1952V_3 + 1.1530V_4 + 0.1677V_5 - 1.4611V_6 - 0.004771V_7 + 4.8968V_8, \quad \text{Equation 5.11}$$

where the echocardiography parameters included are, V_1 = AV velocity, V_2 = MVr velocity, V_3 = LV longitudinal length, V_4 = RV longitudinal length, V_5 = LVID, V_6 = RWT, V_7 = EDV and V_8 = SV.

The estimated peak systolic myofiber stress, calculated from Equation 5.11 correlated well with the actual peak systolic myofiber stress from FE simulations, as demonstrated by Figure 5.10.

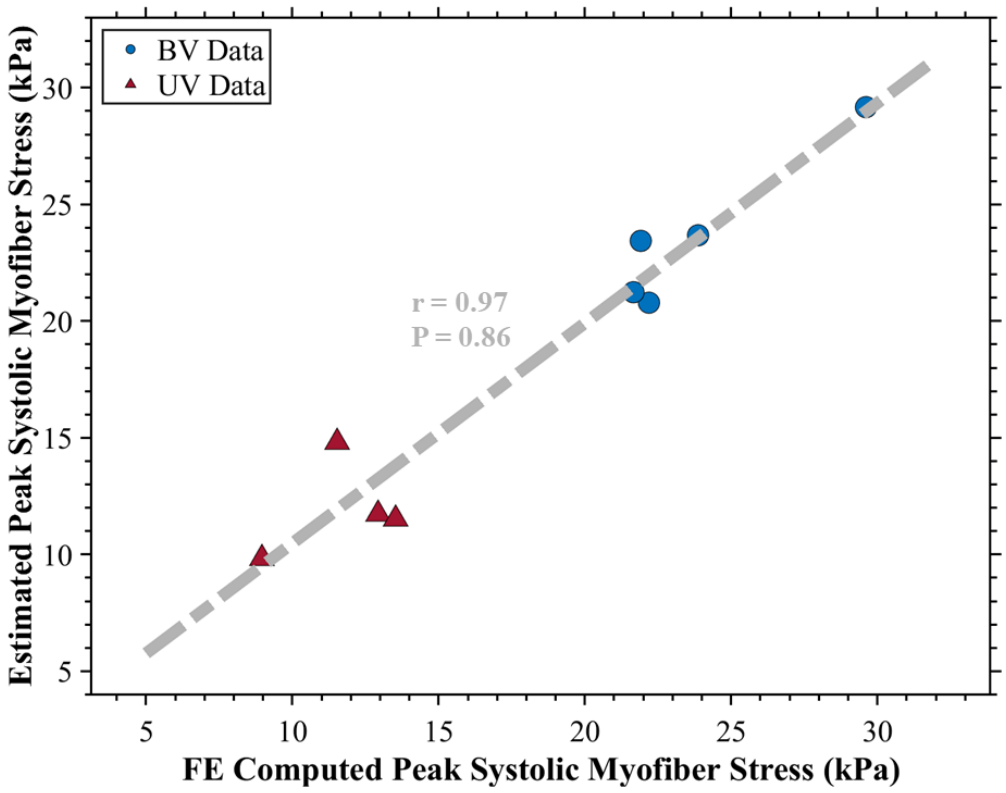

Figure 5.10. *Using Equation 5.11, the estimated peak systolic myofiber stress value was close to the actual peak systolic myofiber stress value from FE computational modelling.*

5.3.7 Evaluation of FAV Outcome Prediction Techniques

ROC analysis was performed to determine the ability of estimated peak systolic myofiber stress in classifying BV versus UV outcomes, to compare it with that of other known pre-FAV indicators of post-FAV outcomes (Friedman et al. 2018; Tulzer et al. 2022a) and against the individual echocardiography parameters within Equation 5.11. Measurements used to compute Figure 5.11 are provided in Appendix 5.1. The results show estimated peak systolic myofiber stress to have the largest area under the curve (AUC), equalling 0.91, and therefore the greatest capability in distinguishing BV versus UV outcomes. The next best performing parameters were LV longitudinal length Z Score (AUC=0.84) and EDV Z Score (AUC=0.83).

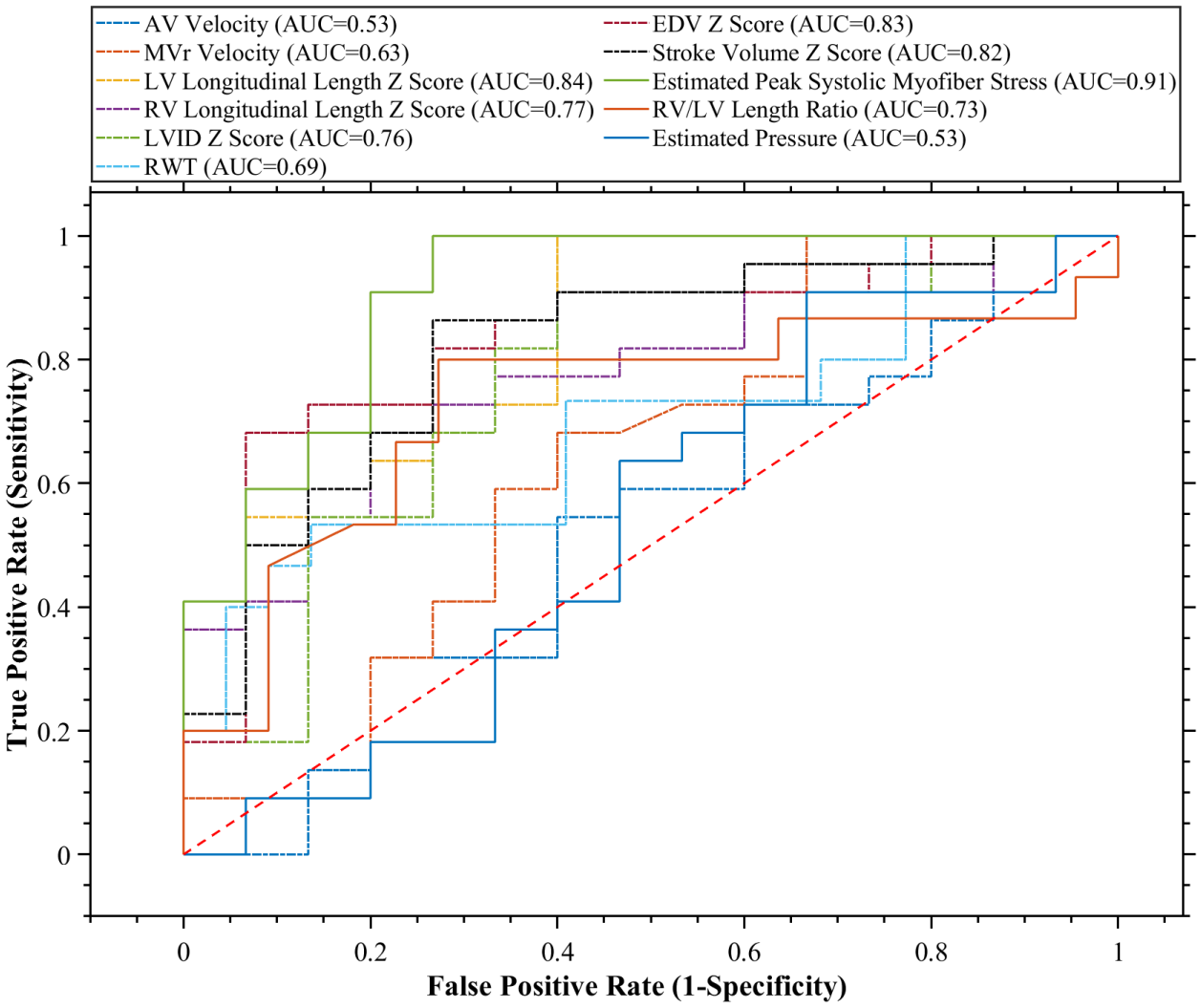

Figure 5.11. *ROC curves computed from retrospective data (n=37) for the individual classes of Equation 5.11, estimated peak systolic myofiber stress and literature-based pre-FAV predictors of post-FAV outcomes* (Friedman et al. 2018; Tulzer et al. 2022a)*. AUC values for each ROC included in legend.*

From the ROC analysis of estimated peak systolic myofiber stress, the threshold of stress = 17.4 kPa provides 100% sensitivity, and approximately 73% specificity (thus correctly predicting all BV cases), the threshold of stress = 26.1 kPa provides approximately 41% sensitivity and 100% specificity (thus correctly predicting all UV cases), while the threshold of

stress = 17.4 kPa corresponds to the highest accuracy (average of sensitivity and selectivity weighted by prevalence), which correctly predicts 100% of BV cases and approximately 73% of UV cases.

5.4 Discussion

Performing retrospective analysis of CAS-eHLHS fetal hearts has improved understanding of the biomechanics of CAS-eHLHS and enabled the identification of clinical and biomechanical parameters that have a high likelihood of predicting UV versus BV birth outcomes, after FAV intervention. The research is different from previous such works in that it was the first study to perform advanced patient specific biomechanics simulations to obtain biomechanics parameters, to support current clinical parameters in predicting FAV intervention outcomes. The simulations enabled the careful back-computation of the myocardial contractility and LV pressure, through adjusting such parameters to best fit echocardiographic image features, such as aortic valve antegrade flow, while adhering to detailed biomechanics formulations, and it provided information on myocardial stresses, which are not measurable clinically. Importantly, the results showed that myocardial stress is uniquely large in the BV group and, is potentially, a better parameter for predicting UV versus BV outcomes, than all currently proposed clinical parameters.

Healthy and diseased models were sufficiently optimised with the percentage error between simulation parameters and echocardiography-measured parameters being 2.55 ±3.56%, 6.43 ±4.20%, and 4.80 ±3.94% for SV, AV ΔP and MVr ΔP respectively. MV ΔP was minimised to within 0.7 mmHg of the image-based value. The ability to validate such computational methods remains challenging because of the scarcity of fetal measurements, particularly for fetal hearts with CAS-eHLHS. The methods for FE modelling in this study rely

on well-established and previously validated models. For instance, a published and validated cardiac motion estimation algorithm (Wiputra et al. 2020) is used to estimate patient specific SV and the description of myocardial active contraction is based on Guccione's active tension model (Guccione et al. 1993). In addition to the established model validation previously performed, further validation of the combined computational approach was undertaken, as one diseased case modelled also had intracardiac pressure measurements taken, during the intervention. Such comparison showed peak LV pressure simulated to match the measured *in vivo* value to within 9.13% and peak ascending aorta pressure simulated to match the measured *in vivo* value to within 2.80%. This was considered a reasonable match, between simulation and *in vivo* measurements, considering all the variabilities within the model generation methods, including assuming ΔP based on the simplified Bernoulli equation and applying a fixed helix angle configuration to all cases. However, the conclusion on model validation is still limited, as proper intracardiac pressure measurements were only available for one patient.

Overall measurements output in this work agreed well with previous investigations on the differences between UV and BV groups. Firstly, the data showed that BV groups had generally higher mean circumferential and longitudinal strains than UV groups, which were significantly lower than control groups. Ishii et al. reported in a larger cohort study (n=57) that there were similarly diminished strain magnitudes in diseased hearts and found significant differences between UV and BV groups for circumferential strains in 1 out of 6 segments of the LV and for longitudinal strains in 3 out of 6 segments of the LV (Ishii et al. 2014). However, as the study sample size was smaller (n=15), statistical significances was only found between the BV and UV circumferential strain measurements.

Secondly, the data showed that the BV group had higher EDVs (Figure 5.5D), LV longitudinal lengths (Figure 5.5G), RV longitudinal lengths (Figure 5.5H) and LVIDs (Figure 5.5J) than the UV group, but differences between the disease subsets were not statistically significant. This aligns with previous studies, which analysed retrospective data and found cases that went on to be born as BV after intervention generally had larger LV long axis Z Scores (Friedman et al. 2018) and larger left heart structures (including, aortic valve Z Score, LV short axis Z Score and LV long axis Z Score) (McElhinney et al. 2009) at the pre-FAV time point. Again, the smaller sample size of this study likely prevented any observation of statistical significance between the diseased subsets, but the data from the study generally corroborated with literature on the direction of the UV versus BV differences.

Thirdly, the simulation results showed LV pressures were generally higher in BV hearts compared to UV hearts, but differences were not significant. McElhinney et al. estimated LV pressure from valve Doppler measurements and found that BV cases had significantly high LV pressures compared with UV cases at the time of intervention (McElhinney et al. 2009), which corroborated the observations of this study, so the lack of significance could again be attributable to the small sample size. Further, it should be noted that McElhinnery et al. did not factor in pressure variation with gestational age (Johnson et al. 2000), when analysing LV pressure calculations as was done in this study. When analysis reverted to LV pressures without the age-normalisation (Table 5.6), the difference between UV and BV groups were larger than if normalisation was done.

The main finding was that peak systolic myofiber stress was the best pre-FAV parameter to distinguish between UV and BV cases, and this outperformed all other parameters, including several that are proposed in previous studies (Friedman et al. 2018; Ishii et al. 2014; Tulzer et al.

2022a). For example, Tulzer et al. proposed that RV to LV length ratio and LV pressure calculations (based on peak MVr velocity) were good predictors of BV birth outcome (Tulzer et al. 2022a), Friedman et al. reported a high probability of a BV birth outcome in cases where peak LV pressure was >47 mmHg and ascending aorta Z Score was ≥0.57 (Friedman et al. 2018), while Ishii et al. reported higher LV longitudinal and circumferential strains in BV compared to UV cases (Ishii et al. 2014). Through the comparison of these parameters against peak systolic myofiber stress, the latter was still found to perform better, as it had a larger difference between UV and BV as indicated by Cohen's D value (Figure 5.8). This suggested peak systolic myofiber stress was likely the best predictor of UV versus BV outcomes.

When thinking about the fundamentals of peak systolic myofiber stress, there are likely physiological explanations for why hearts with stronger contractility and higher stresses progress to reach a BV outcome instead of a UV outcome, post FAV intervention. For example, stronger hearts are likely to support better contractile deformations after FAV intervention, providing better biomechanical stimuli for growth of the LV and thus supporting better growth and development before birth. Further, higher myocardial stresses in the BV patients suggest that the myocardium in these cases resisted pathological hypertrophy and dilation remodelling, despite high tissue stresses, while retaining a strong functional ability to generate pumping pressures. This might suggest that the myocardium is healthier and could elicit better growth and remodelling responses after intervention. Generally, the results suggested that the biomechanically "stronger" LV is more likely to respond positively to FAV, by progressing to a BV birth outcome.

The initial results from the patient specific computational models suggested that there is utility in performing detailed biomechanical simulations of fetal hearts. Such models could aid

more accurate selection of patients for FAV intervention, helping maximise the chances that the selected patients will respond to the intervention and minimise the chances of selecting a patient who would not respond, as this could unnecessarily expose the patient to intervention related risks. However, presently, biomechanical simulations are computationally expensive, and involve multiple processing steps including the computational reconstruction of the heart's structure and motion. To mitigate the computational expense incurred through the derivation of peak systolic myofiber stress, an alternative method for deriving peak systolic myofiber stress was formulated. This was achieved by relating peak systolic myofiber stress to echocardiographic parameters, through PC analysis and regression coefficients. The final simplified equation enables peak systolic myofiber stress to be quickly estimated with image-based parameters alone, as shown in Equation 5.11. Although the equation for estimated peak systolic myofiber stress will not be as accurate as the FE simulations, evidence in Figure 5.10 demonstrated that the estimation of peak systolic myofiber stress was able to retain its ability to clearly distinguish BV and UV groups, despite the small sample sizes. This equation could be used clinically to predict UV or BV birth outcomes after FAV intervention on CAS-eHLHS patients, to help improve accuracy of patient selection and parental counselling.

To extend the testing of peak systolic myofiber stress' predictive capabilities, ROC analysis was performed using the method for estimating peak systolic myofiber stress (Equation 5.11) and comparing its predictive capabilities against individual clinical measurements and literature-based pre-FAV predictors of post-FAV outcomes (Friedman et al. 2018; Tulzer et al. 2022a). The analysis was performed on a retrospective cohort of 37 CAS-eHLHS cases and the method for estimating peak systolic myofiber stress remained the best predictor of UV versus BV post-FAV, as the parameter had the highest AUC in the ROC analysis. However, it is likely

that there are errors involved in estimating myocardial stresses under the current methodology, which could result in some reduction of predictive performance. In the future, it may be possible to perform real-time biomechanics simulations via machine learning, particularly with physics informed neural networks, to resolve the issue of computational cost, when computing peak systolic myofiber stress from patient specific simulation.

From the ROC analysis, a potentially useful peak systolic myofiber threshold can be obtained for use in predictions. The threshold of stress = 17.4 kPa provides 100% sensitivity, and approximately 73% specificity (thus correctly predicting all BV cases), the threshold of stress = 26.1 kPa provides approximately 41% sensitivity and 100% specificity (thus correctly predicting all UV cases), while the threshold of stress = 17.4 kPa corresponds to the highest accuracy (average of sensitivity and selectivity weighted by prevalence), which correctly predicts 100% of BV cases and approximately 73% of UV cases. Presently, it is unclear which is the most clinically beneficial threshold to use, and further risk versus benefit analysis should be conducted. For example, recent thought about FAV is that even for UV outcomes, the FAV intervention could have reduced disease severity and improved survival benefits, and such a notion warrants further studies.

There are several limitations of this study. Firstly, the sample size is small, and future studies with larger sample sizes are likely to enhance the current analysis and produce positive refinement to the prediction model in Equation 5.11. Secondly, all CAS-eHLHS patients analysed in the study had already been selected for FAV intervention, therefore imposing bias, and it would be recommended to widen the study, to help mitigate this limitation. Thirdly, the biomechanics computations required idealisations, such as the assumption of the same helix angle spatial variability configuration, LPM values, and myocardial stiffness for all cases. Also,

during the optimisation loops, the best possible match with imaged parameters was obtained, but some match errors remained. Finally, it must be acknowledged that CAS-eHLHS data was only obtained from 1 institute and BV or UV outcome largely depends on the institutional experience and management algorithm, which is not standardised between centres.

5.5 Conclusion

A retrospective analysis of CAS-eHLHS patients was performed to understand the biomechanical implications of CAS-eHLHS and determine the best parameters for distinguishing between cases with UV and BV outcomes post-FAV, at the pre-FAV intervention stage. Methods involved using a combination of physiological measurements from echocardiography images and biomechanics parameters from image-based, patient specific FE simulations. The CAS-eHLHS cases were shown to have reduced myocardial strains, elevated LV pressure, reduced SV, reduced work done and reduced myocardial contractility, demonstrating how CAS-eHLHS can compromise biomechanically functionality compared to age-matched healthy LVs. The biomechanics parameters, peak systolic myofiber stress and back-computed myocardial contractility seemed to be promising metrics to differentiate between UV and BV cases. Importantly, spatially averaged peak-systolic myofiber stress had a uniquely large difference between UV and BV cases, pre-FAV, suggesting that it has the potential of being a better indicator of UV versus BV outcome than all other current clinical measurements. A simplified equation for estimating myocardial stress showed that this parameter has better predictive capabilities compared to echocardiography measurements. The work suggests that peak systolic myofiber stress could be helpful in clinical evaluation, to improve patient selection for FAV intervention, support parental counselling and aid earlier preparation for future surgical planning.

To apply this methodology in a clinical setting, a longitudinal and multi-centre study would be imperative.

Chapter 6: Biomechanical Effects of FAV Intervention

Fetal CAS-eHLHS can progress to a UV birth malformation. Catheter-based FAV intervention can resolve the stenosis and reduce the likelihood of progression of the malformation. However, there is limited understanding of the biomechanical impact of FAV intervention and how the LV subsequently responds. To address this 4 pre-FAV FE models, optimised for image-based characteristics in Chapter 5 were used. The pre-FAV models were used to conduct virtual FAV intervention. Following this, the post-FAV scans of the corresponding patients were modelled and optimised for image-based characteristics. The patient specific pre- and post-FAV simulations were then compared. Virtual FAV intervention simulations showed that FAV generally enabled partial restoration of several physiological features towards healthy levels, including increased SV and myocardial strains, reduced AV and MVr velocities, reduced LV and left atrium pressures, and reduced peak myofiber stress. FAV intervention often leads to AVr, and the virtual FAV simulations showed that the inclusion of AVr could compromise the ability for depressurisation of LV and left atrium but could substantially increase SV and deformational stimuli on the myocardium. Investigation of post-FAV scans and simulations showed FAV intervention could only enable partial reduction of AV flow dissipative coefficient. Further to this, the contractility of the LV and peripheral vascular resistance could change in response to intervention, preventing decreases in AV velocity and LV pressure, compared with what would be anticipated from stenosis relief. This suggested that case-specific post-FAV modelling is required to fully capture the functionality of the heart. Overall, image-based FE modelling could provide mechanistic details of the effects of FAV

intervention, but computational prediction of acute outcomes was difficult due to a patient dependent physiological response to FAV.

6.1 Introduction

To recap, fetal hearts diagnosed with CAS-eHLHS present physiological, functional, and morphological aberrations, such as elevated LV pressure, reduced LV SV, retrograde transverse aortic arch flow, reduced myocardial strains, globular LV structures, endocardial fibroelastosis and monophasic MV inflow (Freud et al. 2014; Friedman et al. 2014; Ishii et al. 2014; Mäkikallio et al. 2006; Tulzer et al. 2022a). Such aberrations can lead to adverse remodelling in gestation, with a natural history study showing there to be a 73% likelihood of progression from CAS-eHLHS to HLHS by the time of birth (Gardiner et al. 2016; Mäkikallio et al. 2006).

FAV intervention, is a mid-gestation in-utero catheter-based intervention, undertaken on CAS-eHLHS patients to widen the stenotic AV. Under ultrasound guidance the balloon catheter is inflated across the stenotic AV multiple times, to widen the valve, allowing increased blood flow, with the intention to promote healthier development in gestation. Patient selection criteria for FAV intervention varies among institutes, however, commonly if the fetus meets the criteria for evolving hypoplastic left heart syndrome, which is moderate to severe LV dysfunction, retrograde aortic arch flow and the presence of left-to-right foramen ovale shunting (Friedman et al. 2018), with the inclusion of functional metrics such as an LV long axis Z score >-1.0 (Tulzer et al. 2022a), the fetus will be selected for FAV intervention. Through retrospective studies FAV intervention has been shown to promote healthier development in gestation, by reducing the likelihood of a HLHS outcome (Friedman et al. 2018; Gardiner et al. 2016; Mäkikallio et al. 2006; Tulzer et al. 2022a).

Following a technically successful FAV intervention, LV myocardial strains were shown to increase (Ishii et al. 2014) and LV function was shown to significantly improve (Wohlmuth et al. 2016). The functional improvements, post-FAV, highlight the LVs ability to biomechanically

respond to the essentially mechanical intervention of FAV. However, there is still limited in-depth understanding of the biomechanical effects of FAV intervention on the LV myocardium. For example, it is not completely clear how much stenosis relief is generally achieved, how various extents of stenosis relief affect LV pressure, SV and myocardial strains, and how much reduction of abnormally high LV and left atrium pressures can be achieved. Further, a side-effect of FAV intervention is AVr (Arzt et al. 2011), as the valvuloplasty tends to damage the AV, but currently the effects of AVr on myocardial biomechanics and function is unclear.

Image-based FE computational modelling is a robust approach for simulating the contractile ability, pumping function, and biomechanics details of the heart (Shavik et al. 2018; Zheng et al. 2023; Zheng et al. 2022), helping comprehend how the stresses, strains, SV, and pressure of the heart adapt due to disease remodelling or intervention. FE modelling of the fetal heart has previously aided better understanding of the biomechanics of the fetal heart as well (Green et al. 2022; Ong et al. 2020).

In this study image-based, patient specific FE modelling of CAS-eHLHS fetal hearts was performed to improve understanding of the mechanistic effects of FAV intervention on the fetal LV's function and biomechanics. First virtual FAV interventions were modelled on pre-FAV scans to determine the effects of stenosis relief alone. Then, after establishing pre-FAV and post-FAV patient specific FE models, the results from the modelling were compared, to investigate specific physiological changes across FAV intervention.

6.2 Methods

6.2.1 Image Acquisition

4D echocardiography images of 4 CAS-eHLHS fetal hearts pre- and post-FAV intervention were acquired using the GE Voluson E10 (GE Healthcare, Chicago, IL, USA) ultrasound machine. Images were taken in the spatio-temporal image correlation mode, at sweeps of 10-15s and a capture rate of 70-90 frames per second. All images were obtained with informed consent from the Kepler University Hospital, Austria, under Institutional Review Board protocol 1009/2017.

6.2.2 Patient Characteristics

The characteristics of the patients included in the study are described in Table 1. Virtual FAV intervention simulation methods used the age at FAV intervention, patient specific post-FAV simulation methods used the age at the post-FAV scans.

Table 6.1. *Patient characteristics of CAS-eHLHS cases before intervention. Y - yes, N - no, Dil – balloon dilation of the AV, RK - Ross-Kono procedure, NW - Norwood Procedure. "D" followed by a number relates to the case ID, in the same form as reported on in Chapter 5.*

	D1	**D3**	**D6**	**D7**
Age at FAV (wks+days)	24+6	29+3	22+4	24+6
Age at Post-FAV Scan (wks+days)	25+0	30+2	22+6	25+0
Postnatal Circulation	BV	BV	UV	UV
Multiple FAVs	N	N	N	N
Bradycardia	Y	N	N	Y
Pericardial Effusion	N	N	N	N
LV Thrombus	N	N	Y	N
Hydrops	N	N	N	N
Postnatal Procedures	Dil.	RK	NW	NW

6.2.3 Image Processing

For patient specific FE simulation of both pre-FAV and post-FAV LVs, 3D reconstructions of the LV myocardium, left atrium cavity and RV cavity were first performed as previously reported and described in Chapter 3 (Green et al. 2022). Briefly, 2D slices were extracted from the 4D volume files, then binary segmentation of the myocardium was performed using a lazy snap algorithm (Li et al. 2004). 3D reconstruction was then performed with VMTK (www.vmtk.org), with the reconstructed geometries smoothed in Geomagic (Geomagic Inc., Morrisville, NC, USA). 3D motions of the LV, left atrium and RV were extracted using a validated cardiac motion estimation algorithm (Wiputra et al. 2020). Briefly, the algorithm models motion in the image with spatial b-spline of temporal Fouriers, curve-fitted to the displacement fields from pair-wise image registration 3D images of consecutive time points. The final reconstructed LV geometries are depicted in Figure 6.1.

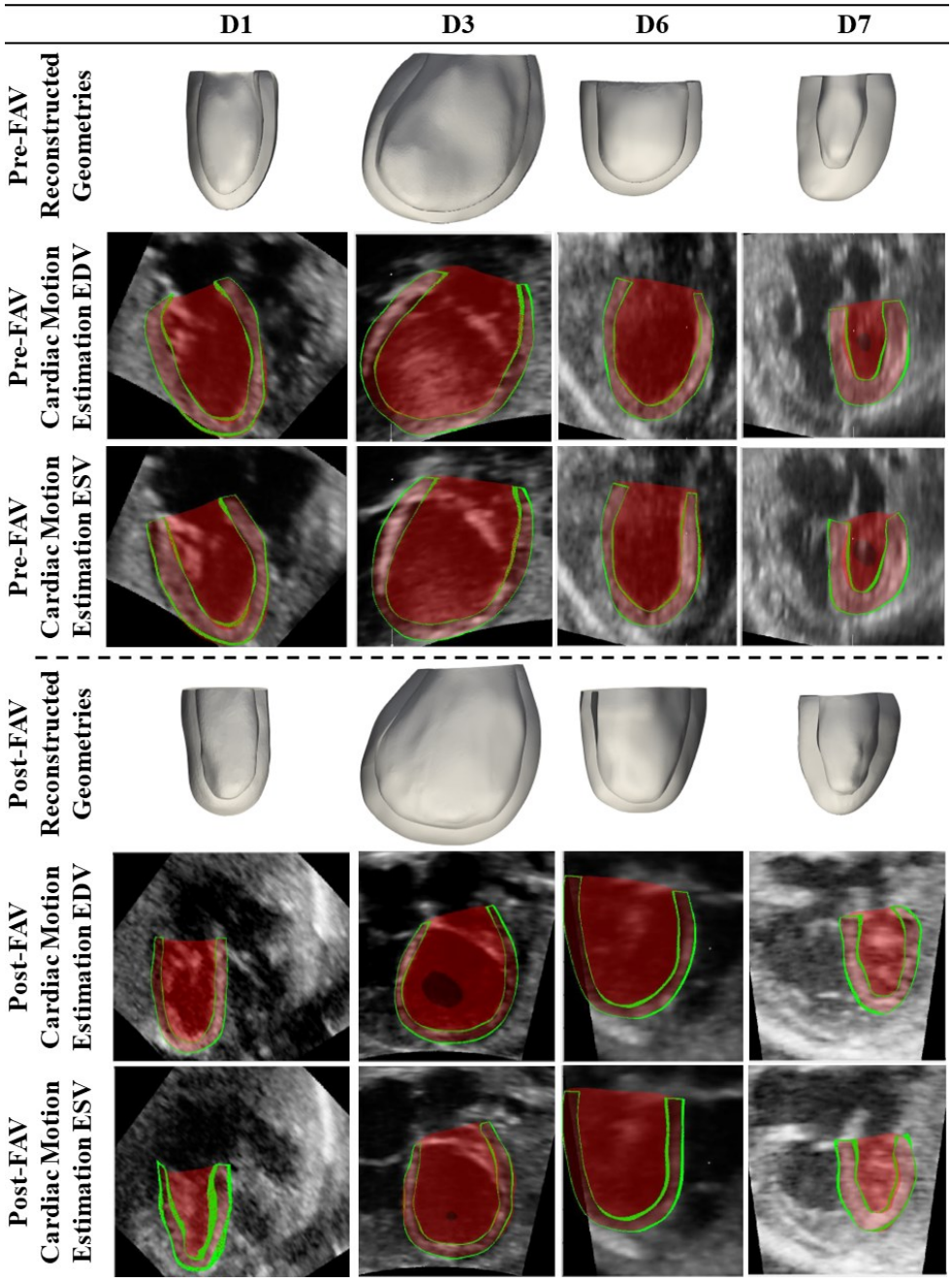

Figure 6.2. *Patient specific geometries, reconstructed from pre- and post-FAV echocardiographic data, with the reconstructed geometries superimposed onto associated echo image, to depicting cardiac motion estimation results, for all patients pre- and post-FAV at EDV and ESV time points. The green outline highlights the geometry proportion close to current image plane.*

From the image-based cardiac motion estimation methods, myocardial strains could be computed using previous methods, like that described in Section 5.2.4 and published (Ren et al. 2023). Briefly, LV myocardial Green Lagrangian strains (Equation 6.1) were computed in both the longitudinal and circumferential directions, along a mid-wall line, identified by averaging the epicardial and endocardial boundaries, from the 4-chamber or transverse echo view and then spatially average.

$$Green\ Lagrangian\ Strain = \frac{1}{2}(F^T \cdot F - I), \qquad \text{Equation 6.1}$$

where F was the deformation gradient tensor and I is the identity matrix.

6.2.4 Computational Modelling Methods

Image-based, patient specific FE Modelling of fetal LV myocardial biomechanics was performed in accordance with the methods described in Chapter 3. The FE model was connected to an age scalable LPM to enable ventricular-vascular coupling (Pennati et al. 1997; Pennati. and Fumero. 2000). Briefly, the FE methods constituted of the passive and active properties of the fetal LV myocardium, where the Fung type transversely isotropic hyperelastic constitutive model (Guccione et al. 1991; Humphrey and Yin 1987) described the passive myocardial behaviour and the active behaviour was described by Gucciones active tension model (Guccione et al. 1993). The material parameters assigned remained constant from patient to patient and are detailed in Table 6.2.

Table 6.2. *Finite element modelling parameters required for both the passive and active description of the myocardium.*

Parameter	Symbol	Unit	Value
Passive stiffness coefficient	Co	Pa	200
Stiffness coefficient in fibre direction	b_{ff}	-	29.9
Stiffness coefficient in sheet and sheet normal direction	b_{xx}	-	13.3
Stiffness coefficient in shear directions	b_{fx}	-	26.6
Shape of peak isometric tension-sarcomere length relation	B	μm−1	4.75
Sarcomere length under no active tension	l_0	μm	1.58
Relaxed sarcomere length	l_r	μm	1.85
Time intercept of linear relaxation duration with sarcomere length	b	ms	-800
Gradient of linear relaxation duration with sarcomere length relaxation	m	msμm−1	524
Maximum intracellular calcium concentration	Ca_0	μM	4.35

The myocardium helix angle configuration was assumed to be the same for all patients and was assigned based on the average of 3 previous publications, which quantified the fetal helix angle configuration (Garcia-Canadilla et al. 2018; Nishitani et al. 2020; Ohayon et al. 1999). Therefore, the myocardium helix angle configuration was assumed to vary linearly from -52° at the epicardium to +71° at the endocardium.

To calculate the unloaded (zero chamber pressure) state of the LV, Finsberg et al.'s backward displacement method (Finsberg et al. 2018) was adopted. This method involves iteratively simulating the unloading of an initial diastolic LV geometry to the load-free state and then performing diastolic pressure loading of the load-free state to end-diastole, while adjusting the pressure of the initial LV geometry, until the targeted end-diastolic pressure and volume was achieved, further details on this method can be found in Chapter 3. In CAS-eHLHS cases, the left atrium is often pressurised and enlarged (Tulzer et al. 2022a), which in turn elevated EDP. Therefore, EDP was assigned in the backward displacement method by patient specific

estimation of EDP through assuming a linear relationship between left atrium size and pressure (LA compliance) (Matsuda et al. 1990; Wong et al. 2022).

LV myocardium models reconstructed from echocardiography images, shown in Figure 6.1, were used for FE modelling, and were meshed into a minimum of 2,500 quadratic tetrahedral elements, which was sufficient for mesh convergence as shown in a previous study (Ong et al. 2020).

The formal FE simulation was performed by minimising the weak formulation of a Lagrangian function described by Shavik et al. (Shavik et al. 2018), which enforces tissue stress equilibrium, incompressibility, and a specific cavity volume to yield cavity pressure, using the Newton Solver in the FEniCS software. The boundary conditions were like that previously reported (Shavik et al. 2018), with the basal plane of the LV constrained in the longitudinal direction and a weak 90 Pa spring applied to the entire epicardium at the load-free state, to simulate interactions with surrounding tissues and to constrain translational motion of the model. The model was executed for 30 cycles, to ensure steady state was achieved. The full FE formulation is described in Chapter 3.

6.2.4.1 Virtual FAV Intervention Methods

Virtual FAV was performed by modulating the LPM of the patient specific image-based FE models of pre-FAV fetal LVs (with case IDs: D1, D3, D6 and D7), reported on in Chapter 5.

The optimisation methods developed in Chapter 4 incorporate patient specificity into the LPM+FE models. Briefly the methods involved scaling the LPM to the patient specific pre-FAV age and performing iterative FE simulations, while varying AV, MV inflow and MVr flow dissipative coefficient and peak myocardial active tension (also known as myocardial

contractility). This process was performed until the simulated valvular ΔP's matched echo-measured gradients, calculated using the simplified Bernoulli equation and doppler velocities, and the simulated SV matched that from echocardiographic images. Through this matching process, the patient specificity of the model was maintained, and the valve dissipative coefficients and peak myocardial active tension could be back computed. In this process, valve dissipative coefficients were modelled as,

$$\Delta P = K \cdot Q^2, \qquad \text{Equation 6.2}$$

where K is the valvular dissipative coefficient, and Q is the volume flow rate. During the optimisation and adjustment, only K was adjusted. Peak myocardial active tension was initially set as 60 kPa, based on the upper limit of experimental measurements (Racca et al. 2016), and then adjusted to match SV.

If less than 10% error between patient data and simulation results could not be achieved, the age scaling of the LPM was adjusted, and the iterative matching process repeated. This age scaling adjustment represented a way to adjust for fetal body size variability or body developmental maturity.

From the optimised pre-FAV models, AV dissipative coefficient was reduced to simulate the widening the AV and relief of stenosis via FAV intervention, by reducing valvular coefficient, K. A few magnitudes of reduction were simulated, between the valvular dissipative coefficient value of the pre-FAV LV to that of an age-matched healthy LV, as defined by the LPM. The process of simulating relief of the AV was then repeated for two levels of AVr severity. This was because a range of AVr velocities was possible, as indicated by the relatively wide standard deviation of regurgitation velocity (1.92±0.87 m/s) from a clinical database of 44

cases, Figure 6.2. The two levels of AVr severity were computationally assigned as such, moderate AVr, regurgitant valve dissipative coefficient was equal to the AV antegrade flow, and high AVr, regurgitant valve dissipative coefficient was 10x that of the AV antegrade flow. By this definition, a more severe AVr had a higher regurgitation flow dissipative coefficient that would translate to higher AVr velocity, via Bernoulli's equation. This fits with the clinical approach, where severity of AVr is defined by regurgitation velocity magnitude.

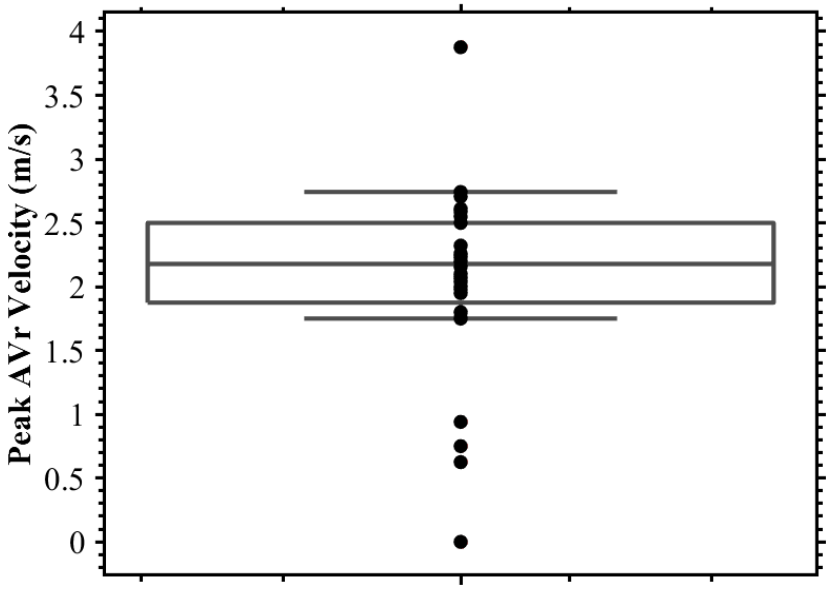

Figure 6.2. *Retrospective data collection of post-FAV AVr velocities (n=44).*

A sensitivity analysis was performed to assess how other physiological features (such as a change in heart rate, increased vascular resistance, and increased myocardial contractility) affected valve velocities and SV, and how they contributed to the match between virtual FAV intervention and image-based measurements.

6.2.4.2 Patient Specific Post-FAV Intervention Methods

The patient specific post-FAV FE modelling was conducted under the same protocol as that for pre-FAV FE modelling (described briefly in the earlier Section 6.2.4.1 and in more detail

in Chapter 4), with the addition of matching the patient specific AVr ΔP, as post-FAV hearts have AVr but pre-FAV hearts do not.

6.2.4.3 Quantifying Disease Severity

To aid analysis a simple metric was formulated to quantify disease severity, by relating the optimised pre-FAV AV dissipative coefficient to the age-matched healthy AV dissipative coefficient, like so,

$$Disease\ Severity\ Metric = log\left(\frac{Pre\ FAV\ AV\ Dissipative\ Coefficient}{Age\ Matched\ Healthy\ AV\ Dissipative\ Coefficient}\right). \quad \text{Equation 6.3a}$$

With a subsequent metric to quantify relative disease improvement following FAV intervention formulated like so,

$$FAV\ Improvement\ Metric = log\left(\frac{Pre\ FAV\ AV\ Dissipative\ Coefficient}{Post\ FAV\ AV\ Dissipative\ Coefficient}\right). \quad \text{Equation 6.3b}$$

6.2.5 Computational Biomechanics Characteristics

From the LPM+FE methods a series of biomechanics parameters could be output to aid analysis of the models generated. SV was extracted based on the cardiac motion estimation algorithm, peak LV and left atrium pressure were extracted directly from the computational methods. Peak myofiber stress was calculated by computing the stress in the myofiber direction (direction of the helix angle), and then performing spatial averaging over the entire myocardial volume, as follows,

$$Myofiber\ Stress = \frac{1}{V}\int_V \overrightarrow{f_d}\boldsymbol{\sigma}\overrightarrow{f_d}\, dV, \quad \text{Equation 6.4}$$

where V is the volume of the myocardium, $\overrightarrow{f_d}$ is the unit vector in the myocardial direction, and $\boldsymbol{\sigma}$ is the stress tensor at peak systole. Work done, was quantified by calculating the area inside the PV loop and describes the ability of the LV to eject fluid.

6.3 Results

6.3.1 Effects of FAV Intervention on Fetal Heart Biomechanics and Function

The pre-FAV simulations were iteratively conducted to optimise for patient specific characteristics, such that myocardial contractility and LV heart valve dissipative coefficient were adjusted to ensure a good fit with imaged SV and Doppler valve gradients for AV and MV antegrade and regurgitation flows respectively. In essence, this was a back computation of the myocardial contractile force generation and AV stenosis severity. Table 6.3 shows that a good match was obtained.

Table 6.3. *Image vs simulation match for all pre-FAV models*

	ID	SV (ml)	AV ΔP (mmHg)	MV ΔP (mmHg)	MVr ΔP (mmHg)
Image	D1	0.28	48.12	3.69	66.75
Simulation		0.31	47.60	3.32	65.39
Image	D3	0.50	4.87	1.49	39.94
Simulation		0.50	5.65	2.02	36.32
Image	D6	0.10	13.54	27.04	27.04
Simulation		0.10	13.91	27.30	27.30
Image	D7	0.085	37.30	42.91	42.91
Simulation		0.084	39.59	42.56	42.56

From the optimised image-based FE simulations for the pre-FAV scenario, virtual FAV intervention was simulated by reducing flow dissipative coefficient of the stenotic AV, and by introducing AVr, which commonly occurred after the intervention (Bradford et al. 2022). The

virtual FAV intervention altered only AV flow dissipative coefficient and introduced two levels of AVr, every other parameter was kept at the pre-FAV level, so that the mechanical nature of FAV intervention could be isolated, to better understand the biomechanical effects specific to this modulation of the AV. A previous study found that the reduction in stenosis via FAV intervention can be variable and span a range of magnitudes (Wong et al. 2023). As such, multiple simulations were conducted over a range of reduced AV flow dissipative coefficient.

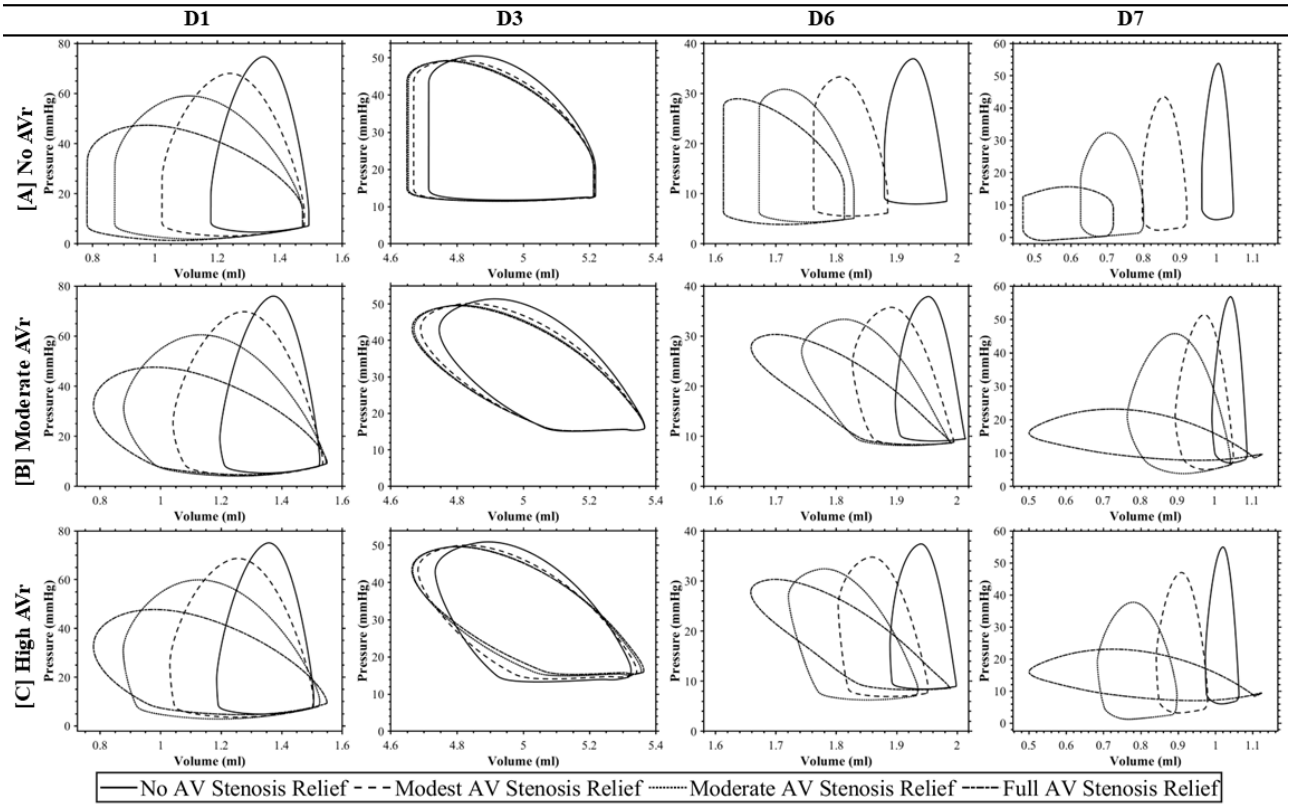

Figure 6.3. *PV loops from patient specific pre-FAV scans of 4 patients, along with those from simulations of virtual FAV intervention. [A], [B], and [C] rows corresponded to simulations assuming no AVr after FAV intervention, moderate AVr after FAV intervention, and high AVr after FAV intervention, respectively. Simulations assumed 3 levels of stenosis relief resulting from FAV which were modest, moderate, and full relief of stenosis.*

PV loop results from virtual FAV simulations are shown in Figure 6.3. Generally, it is observed that relieving the AV stenosis leads to reduced LV pressure and greater SV, the extent of which directly depended on the level of stenosis relief. Different patients also experienced different extents of LV depressurisation and SV augmentation, which were likely dependent on the stenosis severity. Patient D3, for example, had a milder stenosis, based on the disease severity metric defined in Equation 6.3a and documented in Table 6.5, and thus did not undergo a drastic change after FAV. When AVr was introduced (Figure 6.3B and C), the LV effectively had regurgitation in both the mitral and aortic valves, and the PV loops no longer exhibited isovolumic periods and appeared slanted. AVr caused the LV to fill more during diastole, leading to an increase in EDV, thus increasing SV. This increase could be drastic, like that observed in patients D6 and D7. AVr also increased EDP, due to the greater filling volume, and slightly increased peak systolic pressure, likely due to additional engagement of contractile myofibers, resulting from the greater filling volume. This meant that the atria pressure could fail to decrease from the diseased baseline, and in some instances increase further.

Figure 6.4 shows further virtual FAV results for the same patients. Here, the parameter values for the healthy fetal heart are indicated by the horizontal grey dotted line. These age dependent healthy parameters were obtained from Parasuraman et al. for AV velocity (Parasuraman et al. 2013), from Johnson et al. for intracardiac pressure measurements during peak systole and end diastole (Johnson et al. 2000), where the diastolic LV pressures were assumed to indicate peak left atrium pressures, and from Devore et al. for SV measurements (Devore et al. 2019). Healthy fetal heart myofiber stresses have not been reported in literature. Therefore, healthy LV peak systolic myofiber stress was estimated based off the 6 image-based healthy fetal LVs modelled in Chapter 5. The healthy peak systolic myofiber stress of the 6

healthy cases averaged as 12.19±2.62 kPa and appeared to be invariant with age. Therefore, the value of 12.19 kPa was assigned as the healthy benchmark in Figure 6.4U-X.

Generally, the reduction in AV dissipative coefficient (from the right of each plot to the left) produced substantial reductions in AV velocity (Figure 6.4A-D) and LV pressure (Figure 6.4M-P), due to the relief of the stenotic flow and LV fluid congestion, but the extent of the reduction was dependent on how high the pre-FAV AV velocity was. For example, for patient D3, the initial AV velocity and LV pressure were only modestly high, and thus the reduction was not as drastic. FAV also generally decreased MVr velocity (Figure 6.4E-H), due to more AV outflow after FAV intervention, but the effects on MVr were modest compared to those on AV velocity and LV pressure. Along with the improved AV outflow, SVs substantially improved (Figure 6.4I-L), and along with the reduction in LV pressure, myofiber stresses were substantially reduced (Figure 6.4U-X). Again, the changes with FAV depended on the initial disease severity. Thus, overall, substantial restoration of LV biomechanics and function towards the healthy state could be achieved with FAV intervention, if stenosis relief was robust, pointing to the robust benefits that could be brought by FAV intervention.

The effects of FAV intervention on left atrium pressure were more complex (Figure 6.4Q-T) and depended on the severity of AVr after FAV. If there was no AVr, decreased AV dissipative coefficient generally led to depressurisation of the LA. However, with AVr, the left atrium pressure did not depressurize effectively. This was because when AVr was present in the virtual FAV simulations, EDP of the LV was higher, which was then passed back to the LA. Here, it was assumed that AVr severity was dependent on the extent of stenosis relief (AVr valve dissipative coefficient was a fixed fraction of that of AV forward flow), which is a likely scenario as a more robust valvuloplasty tends to induce more valve damage. For this reason, the

effect of AVr preventing left atrium depressurisation was more obvious at lower AV dissipative coefficient in Figure 6.4Q-T (towards the left side of the plots, where there was more stenosis relief). For scenarios with strong MVr and high MVr velocities, this above effect of AVr on left atrium pressure was weak (D1 and D2), and the difference between AVr scenarios were not too far from the no AVr scenario. This was because strong MVr flow caused left atrium pressure buildup even without AVr. Conversely, for patients with lower MVr velocities (D6 and D7), the presence of AV regurgitation made substantial difference for left atrium pressure. Thus, it was likely that in many cases, the acute effect of FAV would not include a depressurisation of the LA. However, if the AVr improved/resolved over subsequent gestational development, which has been observed in literature (Marshall et al. 2005), left atrium pressure would likely depressurise.

The presence of AVr also had significant effects on LV pressure and SV. Regurgitation could further elevate SV beyond the elevation brought by stenosis relief (Figure 6.4I-L). Complete relief of stenosis without AVr could bring SV up by 12-190%, while complete relief of stenosis with high AVr increases SV by 20-633%. While the improvements to SV did not correspond directly to the same improvement in aortic output, as much of the SV is MVr into the LA, it nonetheless improved the motion of the LV and increased deformational stimuli. Given that SVs of CAS-eHLHS can be very low pre-FAV, as shown in Figure 6.4I-L, this additional motion and deformational stimuli provided could be useful to encourage growth response of the LV to avoid a UV birth outcome. As for LV pressure, the effect of AVr on elevating LV pressure was greater if the baseline LV pressure was low, like that observed in D6 and D7, and was milder if the baseline LV pressure was high, like that observed in D1 and D3.

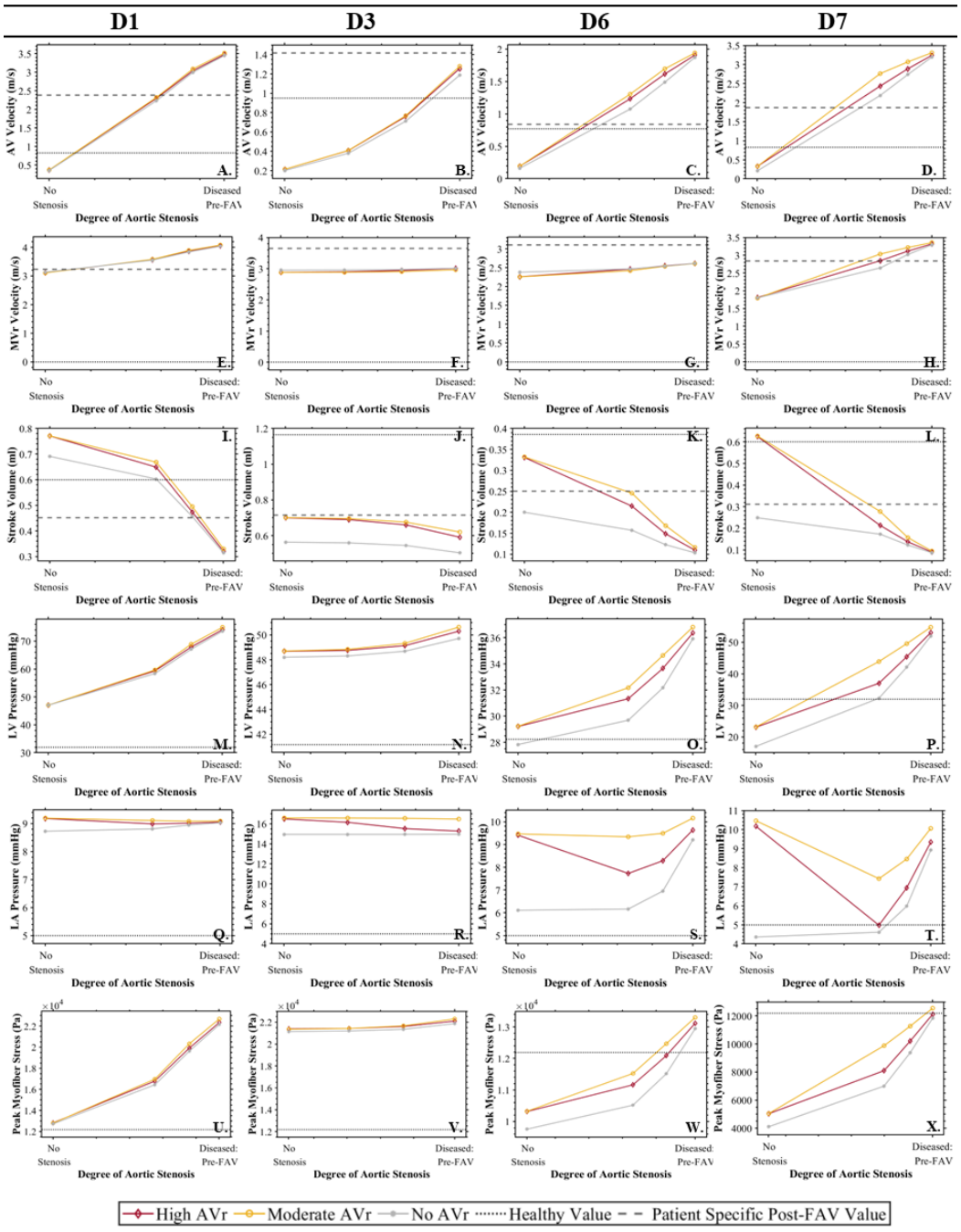

Figure 6.4. *Cardiac physiological characteristics post virtual FAV interventions. Characteristics were plotted across a range of AV stenosis severities, with the no stenosis state equating to the age-matched healthy dissipative coefficient and 3 levels of AVr were simulated. Values for an age-matched healthy subject are included in all plots, with the AV and MVr velocity and SV extracted from the patient specific post-FAV values included in plots [A-L].*

6.3.2 Sensitivity Analysis of Virtual FAV Intervention

In Figure 6.4, the grey dashed lines presented in Figures 6.4A-L marked the echocardiographic measurements from follow up scans of the same patients very shortly after FAV intervention. Results from the virtual FAV intervention simulations (in red, yellow or grey), however, did not always intersect with this post-FAV measurement (dashed lines). For 4 plots, such as for AV forward flow velocity for patient D3 (Figure 6.4B), and MVr velocity for patients D3 and D6 (Figure 6.4F and G), an intersection was not found, suggesting that the range of post-FAV scenarios simulated did not match the actual post-FAV situation. Since the virtual FAV intervention emulated only changes to the AV flow dissipative coefficient, without a change to other physiology, such as contractility and peripheral vascular resistances, the mismatch in some cases suggested that there were other physiological changes, in addition to the changes to AV dissipative coefficient and the presence of AVr. For example, it was likely that D3s myocardial contractility increased post-FAV, such that the post-interventional AV velocity was higher than those predicted by virtual FAV simulations.

Therefore, a sensitivity analysis was performed, to understand how certain physiological changes after FAV intervention could impact the fetal heart, to better understand what were the physiological factors that could account for the mismatch between image-data and virtual FAV intervention in Figure 6.4. D3 was chosen for the sensitivity analysis, as this was the patient with the worst match between virtual FAV simulations and actual post-FAV measurements. The virtual FAV simulation that had a moderate reduction in AV stenosis and high AVr was used as the baseline simulated case, to then explore how an altered heart rate, increased peripheral vascular resistance, and contractility affected the cardiac behaviour.

Percentage change in beats per minute (BPM) was retrospectively collected for a cohort of n=40 (Figure 6.5). The average BPM increased by 1.77% post-FAV compared to pre-FAV intervention, with a standard deviation of ±8.23%. This data was collected to inform the sensitivity analysis with change in BPM, where a two standard deviation or 16.46% increase in BPM was applied. Changes in increased peripheral resistance and contractility were applied arbitrarily, to evaluate how excess increases would impact functionality, due to the limited data available.

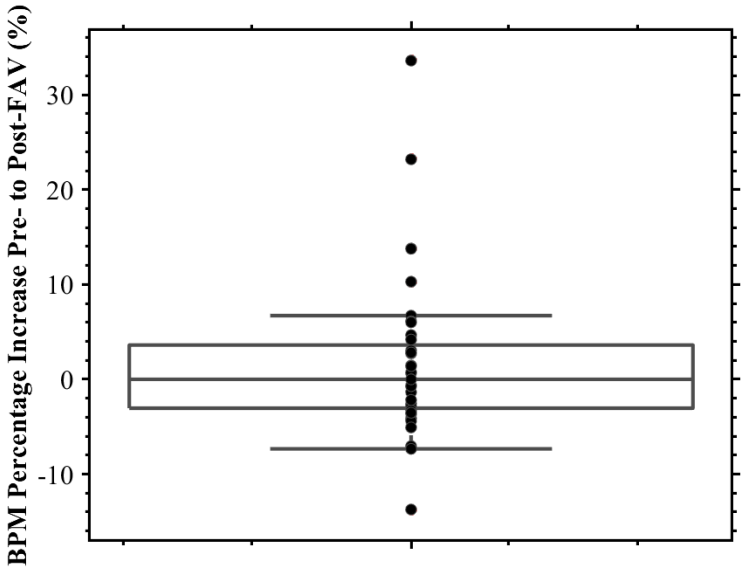

Figure 6.5. *Retrospective data collection of percentage change in BPM from pre- to post-FAV (n=40).*

Figure 6.6 shows the results of the sensitivity analysis. In the database available (n=44) retrospective analysis of pre- to post-FAV BPM showed little overall change (1.77±8.23% change from 0.65±5.82 bpm at pre-FAV), as shown in Figure 6.5. A simulated two standard deviations or 16.46% increase in heart rate (BPM) during the virtual FAV simulation yielded little change to AV and MVr velocities but caused mild decreases in AVr velocity and SV.

Further a 100% increase in systemic vascular resistance, which meant doubling the peripheral resistive components of the LPM, caused a decrease in AV and AVr velocity and SV, but did not affect MVr velocity. Finally, myocardial contractility was increased from 21.91 kPa to 32.87 kPa (a 50% increase) which remained lower than Racca et al.'s measurements of 49.9±9.3 kPa for an 18.57 weeks gestation healthy fetal LV (Racca et al. 2016), and led to a substantial increase in AV, AVr and MVr velocities and SV.

Due to the small magnitudes of effects, heart rate is unlikely to explain the mismatch between virtual FAV simulation and post-FAV measurements. Further to this, Patient D3's BPM did not change from pre- to post-FAV, measuring at 133 BPM during both scans, further supporting the unlikeliness of BPM being able to explain the mismatch between virtual FAV simulation and post-FAV measurements. Contractility, however, had large effects, and increased all 4 measurements, in Figure 6.6, closer to the actual post-FAV measurements. An increase in contractility was thus likely to have occurred after FAV intervention, which could explain the mismatch. However, increasing contractility to improve the virtual FAV intervention comparison with imaged AV, AVr and MVr velocities, would elevate SV beyond the actual post-FAV measurements, it was thus likely that an increase in peripheral resistance accompanied the increase in contractility, to bring SV down.

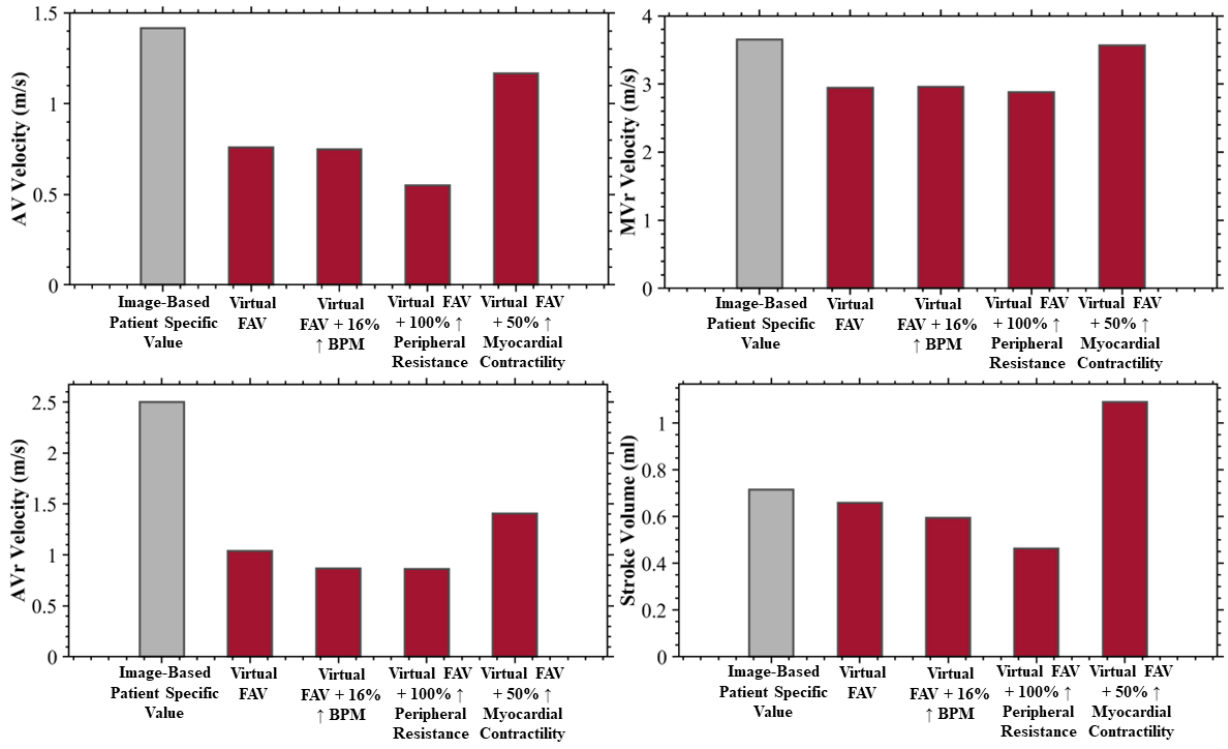

Figure 6.6. *Sensitivity analysis on how change physiological changes to heart rate, peripheral vascular resistance and heart rate affected valve velocities and SV of the post-FAV fetal heart for patient D3. Red bars correspond to virtual FAV simulations assuming high AVr and moderate stenosis reduction by FAV intervention, with and without such physiological changes. The grey bar plots the actual post-FAV echo measurement value for D3.*

6.3.3 Patient Specific Post-FAV Intervention Biomechanics

To better understand the patient specific actual post-FAV biomechanics, image-based simulations were conducted on the same patients, using their post-FAV scans. Table 6.4 describes the match achieved between simulated data and image-based patient value. Combined with Table 6.3 errors for SV were -0.74±4.57%, while that for valve gradients were -2.14±14.24%. D6s post-FAV MVr ΔP was especially difficult to match, and had an error of 38%, which could be due cumulatively to errors in echo measurements and idealisation assumptions of the FE and lumped parameter model.

Table 6.4. *Image vs simulation match for all post-FAV models*

	ID	SV (ml)	AV ΔP (mmHg)	MV ΔP (mmHg)	AVr ΔP (mmHg)	MVr ΔP (mmHg)
Image	D1	0.45	22.66	3.62	19.36	48.96
Simulation		0.45	22.77	3.91	17.38	44.52
Image	D3	0.71	8.02	2.54	25.00	53.40
Simulation		0.69	8.35	3.17	21.49	55.43
Image	D6	0.25	2.86	1.69	13.99	38.44
Simulation		0.24	3.01	1.67	16.40	23.81
Image	D7	0.31	13.96	2.15	20.43	32.21
Simulation		0.32	15.39	2.77	19.40	30.96

Figure 6.7 shows the post-FAV PV loops compared to pre-FAV loops, demonstrating that generally, FAV substantially increased SV. However, interestingly, peak systolic pressure did not always reduce from its high diseased magnitude, despite the reduction in AV stenosis. While pressure was reduced in patients D1 and D7, from pre- to post-FAV intervention, it was elevated in patients D3 and D6. This was likely due to changes in myocardial contractility. While stenosis relief reduced pressure, increased contractile forces elevated it, and the net effect could be an increase for some cases. For all cases, the post-FAV peak systolic LV pressure remained elevated and did not come down to the healthy LV level, depicted by the horizontal dotted line in Figure 6.7.

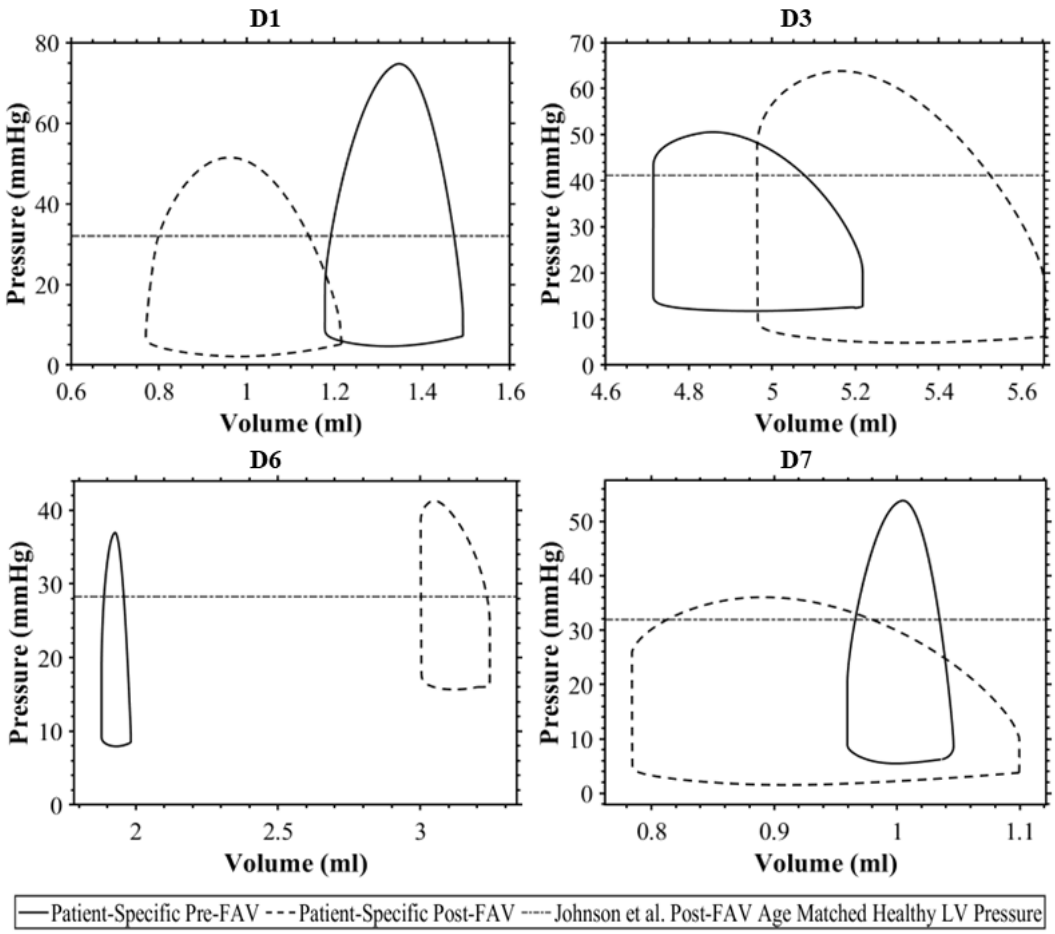

Figure 6.7. *Pre-FAV and post-FAV PV loops, extracted from patient specific modelling methods, compared to published peak systolic LV pressure measurements of age-matched (to post-FAV age) healthy fetal hearts* (Johnson et al. 2000).

Table 6.5 shows the back-computed valve dissipative coefficients for antegrade AV and MV flow, which reflected flow resistances, for the pre- and post-FAV models. These results demonstrated that FAV typically created substantial relief in AV stenosis and substantially reduced AV dissipative coefficient, but dissipative coefficients remained substantially higher than those of the age-matched healthy fetal hearts. Patient D3 was an exception, where the initial AV dissipative coefficient was not exceptionally high, and FAV intervention only decreased the AV dissipative coefficient slightly. The range of AV dissipative coefficients considered by the

virtual FAV simulations is also given in Table 6.5, and it could be observed that they encompassed the actual post-FAV dissipative coefficient, demonstrating that the virtual FAV intervention covered the appropriate stenosis relief scenarios.

Table 6.5. *Valve dissipative coefficient in the patient specific, image-based pre- and post-FAV simulations that enabled the best match between imaged and simulated SVs and valve velocities. The valve coefficient from an age-matched healthy fetal heart, determined via the scalable fetal circulatory LPM for healthy fetuses, described in Chapter 3, was included for comparison, as well as valve coefficients used in the virtual FAV intervention simulations, which ranged from the best fit pre-FAV diseased value to that of healthy LV value. Finally, the disease severity metric (as documented in Equation 6.3a) is recorded, where a higher number indicates a greater pre-FAV disease servity and the FAV improvement metric (as documented in Equation 6.3b).*

ID	Scenario	AV Dissipative Coefficient (mmHg·s²/ml²)	MV Dissipative Coefficient (mmHg·s²/ml²)	Disease Severity Metric	FAV Improvement Metric
D1	Pre-FAV	13.69	0.1168	3.346	0.5907
	Post-FAV	3.513	0.1210		
	Age-matched Healthy LV	0.006174	0.01235		
	Virtual FAV	0.006174 to 13.69	0.1168		
D3	Pre-FAV	0.2135	0.02420	1.897	0.01722
	Post-FAV	0.2052	0.03817		
	Age-matched Healthy LV	0.002705	0.005411		
	Virtual FAV	0.002705 to 0.2135	0.02420		
D6	Pre-FAV	33.07	0.2960	3.516	2.101
	Post-FAV	0.2618	0.1247		
	Age-matched Healthy LV	0.01008	0.02015		
	Virtual FAV	0.01008 to 33.07	0.2960		
D7	Pre-FAV	151.2	2.9235	4.389	1.970
	Post-FAV	1.6222	0.2030		
	Age-matched Healthy LV	0.006174	0.01235		
	Virtual FAV	0.006174 to 151.2	2.9235		

The post-FAV functional and biomechanics characteristics' compared to their corresponding pre-FAV values are shown in Figure 6.8 and documented in Table 6.6. As with Figure 6.7, it can be observed that FAV intervention resulted in an increase in SV (Figure 6.8A). Consequent to larger SV, longitudinal strain (Figure 6.8I), and circumferential strain (Figure 6.8J) increased as well for all patients, which demonstrated the ability of FAV intervention to enable greater myocardial deformations, which could be important for healthier subsequent cardiac development. For the remaining characteristics investigated, including EDV, AV velocity, MVr velocity, LV pressure, peak myofiber stress, myocardial contractility and work done (Figure 6.8B-H), pre- to post-FAV trends were not uniform across patients.

As discussed above, LV pressure (Figure 6.8E) did not always reduce, and likely depended on contractility and the extent of AV stenosis relief. For example, patient D3 experienced a substantial post-FAV increase in myocardial contractile forces (Figure 6.8G), and a consequent post-FAV elevation in LV pressure was observed. However, this elevation in LV pressure in D3 and D6 was likely responsible for the post-FAV elevation in their myocardial stresses, and in MVr velocities, as higher LV pressure induced higher wall stresses and drove stronger MVr. In the same way, despite the reduction in AV flow dissipative coefficient, AV velocity did not always reduce, and was elevated post-FAV for D3. Again, this could be attributed to its post-FAV elevation in contractility. While FAV intervention led to a reduction in AV stenosis brought about by a reduced in AV velocity towards lower healthy values, elevated contractility and increased LV outflow could then increase AV velocities, and the net effect could by an increase in AV velocity, like that observed in patient D3. As for the pre- to post-FAV trends observed for EDV, they are likely related to LV pressure, as increases in LV

pressures, could lead to LV distention, and influence the severity of AV and MVr, which would then determine the extent of diastolic filling.

Among the 4 cases, there was substantial variability, with varying extent of changes to myocardial contractility, LV pressure, AV velocities and other characteristics. The individuality of each patients' results highlighted the complex nature of CAS-eHLHS biomechanics, and the impact FAV intervention can therefore have.

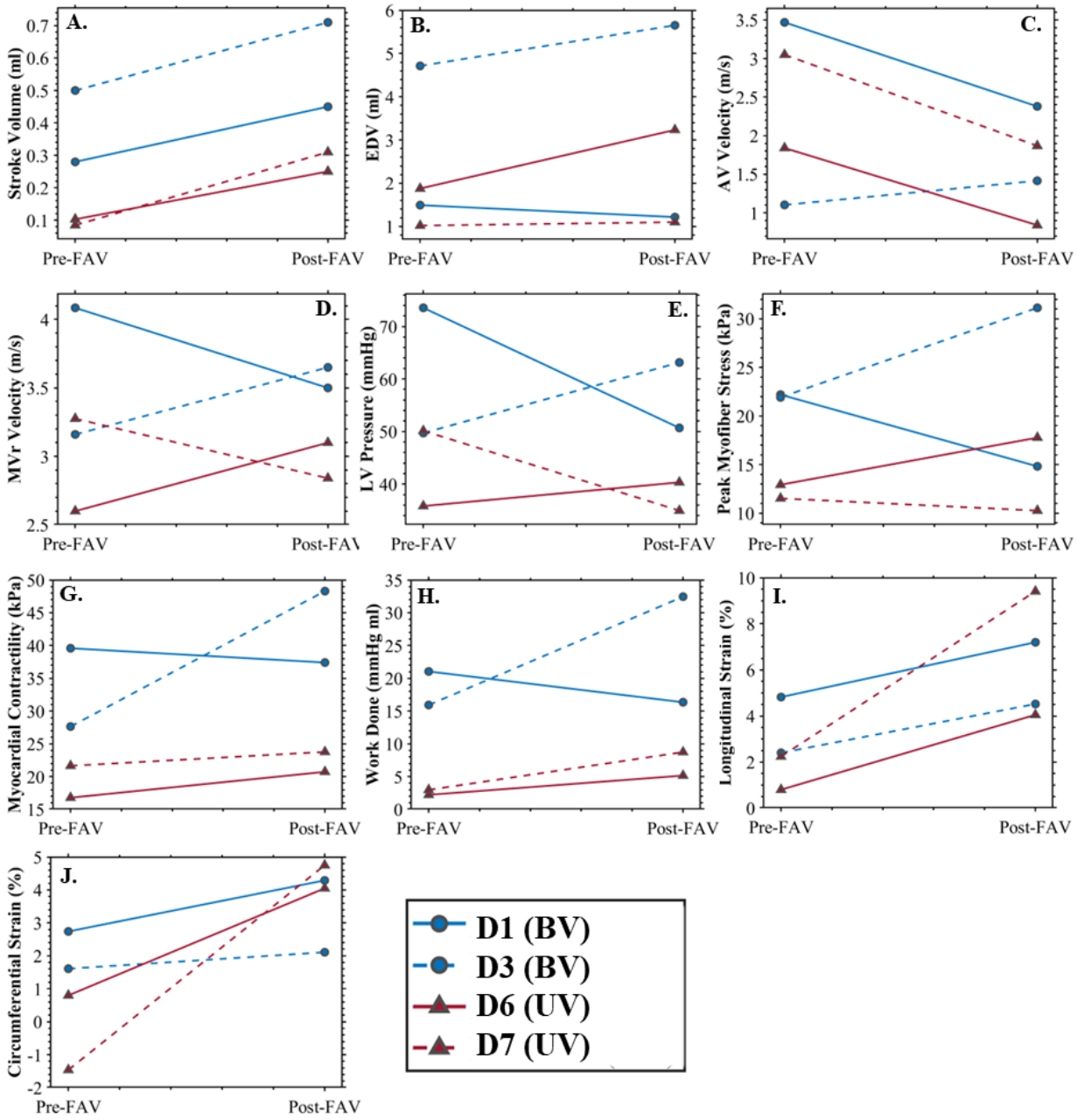

Figure 6.8. *Pre-FAV versus post-FAV fetal LV characteristics. SV, EDV, valve velocities, and strains were measured via echo, while LV pressure, myofiber stress and contractility, and work done by the LV were back computed via the iterative patient specific FE computational modelling.*

Table 6.6. *Comparison of pre- and post-FAV fetal biomechanics, extracted from the patient specific computational methods.*

	D1 (BV outcome)		**D3 (BV outcome)**		**D6 (UV outcome)**		**D7 (UV outcome)**	
	Pre-FAV	Post-FAV	Pre-FAV	Post-FAV	Pre-FAV	Post-FAV	Pre-FAV	Post-FAV
SV (ml)	0.28	0.45	0.50	0.71	0.10	0.25	0.085	0.31
EDV (ml)	1.49	1.22	4.71	5.65	1.88	3.23	1.02	1.10
LV Pressure (mmHg)	73.55	50.69	49.72	63.15	35.83	40.34	50.14	34.96
Age-Matched Healthy Heart LV Pressure (Johnson et al.)	31.71	31.96	39.67	41.17	27.73	28.23	31.71	31.96
Work Done (mmHg ml)	21.05	16.35	15.93	32.46	2.22	5.16	2.98	8.74
Peak Myofiber Stress (kPa)	22.19	14.82	21.91	31.12	12.93	17.77	11.53	10.27
Myocardial Contractility (kPa)	39.59	37.41	27.64	48.31	16.78	20.73	21.65	23.77
Longitudinal Strain (%)	4.82	7.20	2.40	4.52	-0.66	-0.48	2.25	9.41
Circumferential Strain (%)	2.74	4.29	1.61	2.11	0.80	4.05	-1.46	4.75

6.4 Discussion

In this study virtual FAV intervention was performed, to comprehend the effect of FAV intervention on the biomechanics and function of the fetal LV. This was studied with two approaches. First, the patient specific pre-FAV models optimised for in Chapter 5 had virtual FAV intervention performed on them, by imposing a reduction in AV flow and introducing AVr. This was an idealised approach, assuming that only the AV is affected by FAV intervention and that there are no other physiological responses, which served the purpose of elucidating the mechanistic effects of AV stenosis relief alone. Secondly, patient specific post-FAV intervention was performed, to compare the results to the pre-FAV simulations, to understand the overall changes.

Diseased CAS-eHLHS LVs typically had high pressures and tissue stresses, and very low myocardial strains and SV. They further had high atrial pressure and an enlarged left atrium (Pickard et al. 2020; Tulzer et al. 2022a). This unusual biomechanical environment likely

prevented normal development of the LV and LA. The virtual FAV simulations showed that by relieving AV stenosis, FAV could depressurise the LV, reduce abnormally high AV velocities, reduce MVr severity, increase SV, reduce myocardium tissue stresses, and, if AVr was not present, reduce left atrium pressure as well. All these represented partial normalisations of cardiac function and biomechanics, enabling lower stresses and increased deformational stimuli of myocardial tissue, and were thus likely beneficial for the subsequent development of the heart, to avoid progression to a UV birth outcome.

However, a complexity in this investigation was the presence of AVr, which was very common after FAV (Bradford et al. 2022). Virtual FAV intervention simulations showed that the presence of AVr could dampen the ability of the LV and left atrium to depressurise, and depending on regurgitation severity, could even increase left atrium pressure. This was because AVr brought the higher aortic pressure into the LV, through regurgitation during diastole, and the higher pressure was passed on to the LA. In a previous fluid dynamics simulation study, it was shown that AVr resulted in excessive energy losses and high cardiac workload (Wong et al. 2023), which reduced the restoration of cardiac flow function. However, AVr promoted higher SV and higher strains of myocardial tissues, and previous studies (Arzt et al. 2011; Wong et al. 2023) speculated that this higher deformational stimulus was beneficial to subsequent cardiac development. It was, however, noteworthy that the current study was limited to the acute outcomes of FAV intervention. Later in gestation, AVr improved/resolved over subsequent development, which has been observed in literature (Marshall et al. 2005), which could lead to further normalisation of function and biomechanics, as demonstrated in the virtual FAV intervention scenarios, with no AVr. It is unclear how and why this happens, but given that this

is a very positive event, further longitudinal studies are warranted, to understand the biomechanical evolution of the fetal post-FAV.

The investigations of post-FAV scans provided validation that the SV and myocardial strains indeed increased, whilst confirming that FAV indeed reduced AV valve dissipative coefficient and relieved the stenosis. However, the results suggested that stenosis was not fully relieved. This corroborated with a previous image-based fluid dynamics studies, where it was estimated that although the AV effective orifice area doubled after FAV, it remained substantially lower than (about one-fifth that of) that of a healthy fetal heart (Wong et al. 2023). The increase in circumferential and longitudinal strains agreed with previous findings by Ishii et al. which showed FAV intervention to promote increased myocardial strains (Ishii et al. 2012).

The study of post-FAV scans and simulations also revealed that some fetal LV cases did not experience a great reduction in AV velocity or LV pressure, despite relief of the stenosis and LV fluid congestion. Clinically, AV velocity and the Bernoulli's equation is often used to estimate valvular ΔP, and a failure to reduce AV velocity would have falsely implied that FAV did not relieve the stenosis. The investigations in this study, however, revealed that stenosis was indeed relieved for all cases, but there were likely other physiological responses, such as elevated myocardial contractile forces and peripheral vascular resistance, that negated the reduction of AV velocity and LV pressure. This complex interplay between various physiological features served as a reminder that simple single measures should not be used to assess stenosis severity during FAV intervention, and a complete image-based FE model might be more appropriate. It seemed reasonable to expect some LVs to have elevated contractility after FAV intervention, which could be induced by the increased deformational stimuli of the LV and an end-diastolic distension of the LV due to AVr, in line with the Frank-Starling mechanism. In this studies

results myocardial contractility increased across FAV intervention for all patients except D1, whose myocardial contractility in fact maintained a level similar to its pre-FAV state, despite a slight decrease (Figure 6.8G). The sensitivity analysis showed that contractility changes had a significant effect on cardiac function and biomechanics. Contractility changes across FAV intervention was thus an important feature to consider. In terms of peripheral vascular resistance changes, the sensitivity analysis also suggested that this could occur after FAV intervention, and this seemed reasonable, as increased overall cardiac output brought by FAV intervention could have activated higher peripheral vascular tone. However, this physiological change had a milder effect.

The modelling results demonstrated that patient specific modelling can enable a detailed investigation of the complex biomechanical and physiological effects of FAV and was useful in capturing the individuality of each patient, addressing the large patient-to-patient variability. However, it was found that the computational prediction of acute outcomes of FAV intervention remained difficult, because it was not currently possible to predict how much of the stenosis would be relieved by FAV intervention and how much (if any) the fetal heart contractility would alter, which is important as stenosis severity and contractility were shown to be very influential parameters with significant effects on simulation outcomes. However, it might be the case that with a much larger sample size, a statistical distribution can be obtained for these physiological changes after FAV intervention, to help with computational predictions.

Finally, comparing features of patients that went on to be BV (D1 and D3) or UV (D6 and D7) post-FAV, the results showed that UV patients LVs remained relatively low pressure compared to the BV cases post-FAV, and they also had lower SV, work done and myocardial contractility. This appeared to support the hypothesis developed in Chapter 5, that the

biomechanically “weaker” fetal hearts were more likely to progress to a UV outcome, but the sample size here is low and cannot provide enough evidence to test this hypothesis. However, clinical estimations of LV pressure were made by Tulzer et al. and McElhinney et al., who concluded that the higher-pressure pre-FAV LVs have a greater chance of progressing to a BV outcome post-FAV (McElhinney et al. 2009; Tulzer et al. 2022a). This corroborated the findings of this study.

There are several limitations of this study. Firstly, the biomechanics simulations required idealisations. For example, the same myocardial helix angle configuration was assumed for all LVs and applied the same myocardial stiffness across all cases. Further, the modelling of AVr and MVr was simplified, as a constant valve dissipative coefficient across diastole and systole respectively, was assumed. Thirdly, fetal echocardiography tended to have high levels of noise, which could have resulted in inaccuracies in the image-based computational modelling. This might account for some of the mismatch between virtual FAV and actual post-FAV measurements and simulations.

6.5 Conclusion

Image-based computational modelling was conducted to understand the biomechanical impact of FAV intervention. The virtual FAV simulations showed that FAV was likely to improve LV functionality, by depressurising the LV and LA, reducing AV velocity and MVr velocity, reducing myofiber stress, and increasing SV. The presence of AVr moderately inhibited LV depressurisation and could prevent left atrium depressurisation, however, it provided substantial augmentation of SV and myocardial strains, which could provide beneficial stimuli to further cardiac development. Through comparisons of virtual FAV intervention to actual post-FAV images and simulations, it was found that cardiac contractility was likely to increase after

FAV intervention, which could cause unexpected increases in AV forward velocities and LV pressure, contrary to the expectation that stenosis should decrease them. Post-FAV simulations demonstrated substantial stenosis relief, but AV dissipative coefficient remained quite different from those of healthy hearts.

Chapter 7: General Conclusions

This chapter summarises the research conducted, and key findings presented in this thesis. Finally, recommendations for future work are made, to further advance understanding of fetal heart biomechanics, particularly in CAS-eHLHS cases.

7.1 Summary of Thesis Findings

The Overall Aim of this research was to develop methods for FE modelling of fetal healthy and CAS-eHLHS LVs, to then gain understanding of the biomechanical environment of CAS-eHLHS, pre- and post-FAV intervention and determine whether pre-FAV biomechanics are indicative of post-FAV outcomes.

In previous studies, FE modelling has been a powerful tool, enabling greater insight into the functionality of a structure, such as the LV, to improve understanding of the biomechanics of the heart (Dewan et al. 2017; Ong et al. 2020; Shavik et al. 2021; Wisneski et al. 2020). To fulfil the Overall Aim, and therefore, improve understanding of fetal CAS-eHLHS pre- and post-FAV, the fetal FE methods, first, required developing. Initially the LPM was calibrated to the latest LV pressure measurements (Johnson et al. 2000) and pulse pressure measurements (Versmold et al. 1981). Then as the helix angle configuration must be defined during the FE formulation and adult FE studies have shown the helix angle configuration to impact LV functionality, due to altered contraction patterns (Palit et al. 2015; Pluijmert et al. 2012; Rijcken et al. 1999; Vendelin et al. 2002; Washio et al. 2020), the effect of helix angle configuration on fetal LV functionality was studied. Results from previous adult studies could not be relied upon, due to the many differences in morphology and physiology of the fetal and adult LV. The helix angle configuration study, described in Chapter 4, and the following publication (Green et al. 2022), found, through patient specific FE modelling of fetal LVs, that helix angle configuration substantially impacted peak systolic myofiber stress, cardiac stroke work, myocardial deformational burden and the spatial variability of myocardial strains. Literature-based helix angle configuration measurements (Garcia-Canadilla et al. 2018; Nishitani et al. 2020; Ohayon et al. 1999) resided between the optimal regions for peak systolic myofiber stress, cardiac stroke

work and myocardial deformation burden, suggesting development towards a fixed helix angle configuration in gestation is dependent on several factors rather than a single factor. The study also demonstrated how LV shape rather than size impacts the relationship between helix angle configuration and biomechanical functionality, suggesting that conclusions made in this study may also be applicable for the adult geometry. Overall, taking into consideration the existing limitations in measuring fetal LV helix angle configuration and the results of this study, it was suggested that future simulations assign a helix angle configuration of approximately $\bar{\tau} \cong 9.5^o, \tau_{diff} \cong 123^o$, based on the average of angles measured in literature (Garcia-Canadilla et al. 2018; Nishitani et al. 2020; Ohayon et al. 1999), and the generally good alignment this average helix angle configuration had with image-based strain measurements. Finally, an optimisation algorithm was developed, primarily for patient specific LPM+FE modelling of CAS-eHLHS patients. The optimisation algorithm enabled a formulised approach to modelling the patient specific disease characteristics of CAS-eHLHS patients pre- and post-FAV, providing consistency in the model generation techniques for fairer comparison, whilst also enabling the back computation of myocardial contractility.

The second specific aim sort to understand the impact of CAS-eHLHS on fetal heart biomechanics, compared to healthy hearts and evaluated whether any pre-FAV biomechanics characteristics' modelled could be indicative of post-FAV outcomes (Chapter 5). Patient specific LPM+FE models of CAS-eHLHS patients demonstrated how fetal hearts with the disease have compromised functionality, compared to age-matched healthy LVs, which included reduced myocardial strains, reduced SV, reduced myocardial contractility and elevated LV and left atrium pressure. As a substantial number of patients undergoing FAV intervention still progress to a UV outcome (Friedman et al. 2018; Gardiner et al. 2016; Mäkikallio et al. 2006; Tulzer et al.

2022a), the study also aimed analyse the predicative capabilities of pre-FAV parameters, to determine whether there is any correlation between pre-FAV function and post-FAV outcome. The computational models suggested that CAS-eHLHS cases that respond well to intervention (go on to be BV, as opposed to UV) tend to be biomechanically "stronger" and larger, with generally high myocardial contractility and larger LV size. Interestingly, peak systolic myofiber stress had a uniquely great pre-FAV ability to differentiate between the patients that would progress to a BV or UV outcome. However, peak systolic myofiber stress was a computationally expensive parameter to output, due to the time taken to construct the patient specific geometries and the computational expense of the FE methods, which in turn limits its clinical impact. Therefore, peak systolic myofiber stress was related to clinical measurements, as such:

$$\begin{aligned} Estimated\ Peak\ Systolic\ Myofiber\ Stress = {} & -24.9240 + \\ & 0.9550V_1 + 4.2687V_2 - 0.1952V_3 + 1.1530V_4 + 0.1677V_5 - \\ & 1.4611V_6 - 0.004771V_7 + 4.8968V_8, \end{aligned} \qquad \text{Equation 7.1}$$

where, the image-based parameters included are, V_1 = AV velocity, V_2 = MVr velocity, V_3 = LV longitudinal length, V_4 = RV longitudinal length, V_5 = LVID, V_6 = RWT, V_7 = EDV and V_8 = SV. This method of calculating peak systolic myofiber stress enabled quick and easy estimation of the parameter. To evaluate the robustness of estimated peak systolic myofiber stress, in predicting FAV intervention outcomes, ROC analysis was performed on a retrospective cohort of 37 pre-FAV cases. Where estimated peak systolic myofiber stress outperformed the other image-based parameters in predicting FAV intervention outcomes. The research underscored the potential advantages of estimating peak systolic myofiber stress pre-FAV. These advantages include aiding patient selection, supporting parental counselling, and facilitating

earlier preparation for longer-term surgical planning. To apply this methodology in a clinical setting, a longitudinal and multi-centre study would be imperative.

The third and final specific aim was to better understand the biomechanical effects of FAV intervention (Chapter 6), as there is limited understanding of the biomechanical impact of FAV intervention and how the LV responds to the mechanical in nature intervention. Through performing virtual FAV intervention, on pre-FAV geometries (optimised for in Chapter 5), it was found that FAV intervention can help restore some cardiac functionality, through reducing AV and MVr regurgitation velocities, depressurising the LV and LA, increasing SV, and reducing peak systolic myofiber stress. When introducing AVr into the virtual FAV intervention scenarios the LV was not able to depressurise sufficiently, with respect to the no AVr scenario. The presence of AVr also led to left atrium pressures substantially higher than the no AVr scenario and the pre-FAV state, however, the SV substantially increased when AVr was present. Sensitivity analysis showed increased myocardial contractility to improve the match between virtual FAV methods and patient specific outcomes, demonstrating how some patients may have physiological responses to FAV intervention. Finally patient specific post-FAV intervention modelling demonstrated the individuality of each patients response to FAV intervention and the need for such in depth models to quantify acute post-FAV outcomes.

In summary, in depth LPM+FE modelling of the fetal LV has enabled greater insights and improved understanding of the functionality of healthy and CAS-eHLHS fetal hearts, and gave a sense of which cases are more suitable for FAV intervention, which, with future work, could support patient selection.

7.2 Future Work

Based on the research conducted in this thesis several future studies have been identified. Such studies could contribute to further enhancing understanding of CAS-eHLHS biomechanics and provide techniques to improve computational cost.

7.2.1 Longitudinal Studies Examining the Response to FAV Intervention

This thesis has focused on healthy fetal hearts and fetal hearts immediately pre- and post-FAV intervention. Following FAV intervention, reductions, or the resolution of functional aberrations, such as AVr (occurring because of the intervention), and MVr, occur often later in gestation, as seen in Table 7.1.

Table 7.1. *Valvular velocities of CAS-eHLHS cases where follow-up data is available. Follow-up echocardiograms were taken 1-2 months after the intervention. The three cases had resolved MVr by the follow up scan, with AVr also resolved in FU1. Data extracted under the image acquisition approval described in 3.1.1.*

Case	Time	AV Velocity (m/s)	AVr Velocity (m/s)	MVr Velocity (m/s)
FU1	Pre-FAV	1.40	Not present Pre-FAV	2.50
	Post-FAV	0.80	1.95	1.40
	Follow up	1.66	Resolved	Resolved
FU2	Pre-FAV	2.13	Not present Pre-FAV	2.48
	Post-FAV	1.83	2.74	2.70
	Follow up	1.15	2.82	Resolved
FU3	Pre-FAV	2.65	Not present Pre-FAV	0.68
	Post-FAV	1.45	2.59	1.49
	Follow up	1.84	2.04	Resolved

The resolution of MVr and sometimes AVr later in gestation demonstrates how the fetal heart is continually remodelling weeks after the intervention occurred. Therefore, a valuable next step is to perform longitudinal studies, by developing patient specific models, pre- and post-FAV intervention and then at subsequent time points following the intervention. Such work may help evaluate how the natural plasticity of the fetal heart adapts, following the altered biomechanical environment, imposed by FAV intervention. Furthermore, a longer-term study would help evaluate how FAV intervention benefits cases that still progress towards a UV outcome, by quantifying how the biomechanical environment changes in those patients that do not have a technically "good" outcome, as there still may be some benefit of FAV intervention to cardiac functionality in those scenarios also.

7.2.2 FAV Intervention Timing and Early Detection of CAS-eHLHS Cases

FAV intervention is undertaken on mid-gestation fetuses, generally between 21 – 33 weeks gestation (Tulzer et al. 2022a). With respect to cardiac development in gestation, the window in which FAV intervention is undertaken is relatively large. It would be useful to analyse retrospective data to quantify whether there is a relationship between intervention outcome and gestational age and use computational models to evaluate whether there is an optimal gestational age to intervene on, to further enhance the likelihood of a BV outcome, post-FAV intervention. However, undertaking such efforts may offer limited practicality within current clinical context, as the time of intervention is limited by the detection of the fetal abnormality at the mid-gestation scan and parental logistics, as many must travel to specialist centres for the intervention. Therefore, a further study to determine whether there are any early indications of CAS-eHLHS, at the early pregnancy scan (generally taken between 11 and 14

weeks gestation), would enable more time for intervention planning and therefore, the ability to optimise for the time of intervention. So, a supplementary study is proposed to analyse the early gestation fetal scans and determine whether there are any image-based characteristics, which could indicate progression towards CAS-eHLHS and model such cases to extract biomechanically relevant data. Overall, if such biomarkers could be identified at the 11-14 weeks gestation scan, then earlier planning of FAV intervention could be initiated, and time of intervention could be optimised for.

7.2.3 Machine Learning for Real Time Biomechanical Assessment

A constraint of the work undertaken in this thesis is the simulation time, however, there is the possibility to overcome such obstacle. There is already major investment into machine learning techniques for real-time quantification of solid and fluid mechanics problems (Buoso et al. 2021; Cheng and Zhang 2021; Jin et al. 2021) and it would be recommended to extend such work to fetal heart applications. For example, developing a physics informed neural network (PINN), to accurately predict the biomechanical behaviour of the fetal LV could enable real-time estimation of patient specific biomechanics, which could also quickly expand the number of CAS-eHLHS patients studied and in turn could help evaluate and refine the estimated peak systolic myofiber stress equation developed in Chapter 5. However, the limited availability of fetal images for training such a network is a key factor hindering its success; nevertheless, efforts are already underway to overcome such an issue, as an effort it being put into augmenting current echocardiographic images, to vastly expand fetal data availability, and in turn sufficiently train a PINN. Following on from this, a study investigating the leading fetal patient specific characteristics that influence simulation accuracy could be conducted. When such leading characteristics have been identified, a parametric PINN could be developed, like that already

published for the adult LV (Buoso et al. 2021). The parametric model would remove the requirement for patient specific model reconstruction and enable clinicians to input the key patient characteristics, to scale the model and then solve such model in real-time, using the machine learning techniques. Clinicians could then have direct access to biomechanical characteristics, that are currently unavailable clinically, to support their assessment of the patient.

7.2.4 Heterogeneous Electrical Activation Model Sensitivity Analysis

Adult studies have shown LV electrical activation to originate at the sub-endocardial septal region, and then proceed sequentially to the apex, ventricle body and finally the base (Ballester-Rodés et al. 2006; Scher 1995; Sengupta et al. 2006b). Generally, electrical activation travels from the endocardium to epicardium along the fiber direction, due to the higher concentration of gap junctions in the longitudinal direction, compared to the cross-fiber direction (Saffitz et al. 1995). Upon localised electrical activation contraction occurs, which is compromised of the onset of myofiber shortening (mechanical activation) and the time to peak shortening. In adult healthy hearts regional difference in onset of shortening and time to peak tension have been measured (Zwanenburg et al. 2004) and a lag between subendocardial to subepicardial contraction has been observed (Sengupta et al. 2007). A future project could conduct a sensitivity analysis, to quantify the impact of heterogeneous electrical activation patterns on fetal LV simulation outputs. Incorporating the acknowledged limitation of the lack of consideration of spatially varying fiber patterns, as discussed in both Chapter 4 and 5, into the sensitivity analysis would further enhance understanding of the impact of a heterogeneous myocardial model on simulation outputs and serve as a useful resource for future work.

Bibliography

Di Achille P, Harouni A, Khamzin S, Solovyova O, Rice JJ, Gurev V. Gaussian process regressions for inverse problems and parameter searches in models of ventricular mechanics. Front Physiol. 2018;9(AUG):1–17.

Albers EL, Bichell DP, McLaughlin B. New approaches to neuroprotection in infant heart surgery. Pediatr Res. 2010;68(1):1–9.

Alnuaimi S, Jimaa S, Kimura Y, Apostolidis GK, Hadjileontiadis LJ, Khandoker AH. Fetal cardiac timing events estimation from doppler ultrasound signals using swarm decomposition. Front Physiol. 2019;10(JUN):1–13.

Arzt W, Wertaschnigg D, Veit I, Klement F, Gitter R, Tulzer G. Intrauterine aortic valvuloplasty in fetuses with critical aortic stenosis: Experience and results of 24 procedures. Ultrasound in Obstetrics and Gynecology. 2011;37(6):689–95.

Asner L, Hadjicharalambous M, Chabiniok R, Peresutti D, Sammut E, Wong J, et al. Estimation of passive and active properties in the human heart using 3D tagged MRI. Biomech Model Mechanobiol. Springer Berlin Heidelberg; 2016;15(5):1121–39.

Ballester-Rodés M, Flotats A, Torrent-Guasp F, Carrió-Gasset I, Ballester-Alomar M, Carreras F, et al. The sequence of regional ventricular motion. European journal of cardio-thoracic surgery. Germany; 2006 Apr;29:139–44.

Bayer JD, Blake RC, Plank G, Trayanova NA. A novel rule-based algorithm for assigning myocardial fiber orientation to computational heart models. Ann Biomed Eng. 2012;40(10):2243–54.

Beattie MJ, Friedman KG, Sleeper LA, Lu M, Drogosz M, Callahan R, et al. Late gestation predictors of a postnatal biventricular circulation after fetal aortic valvuloplasty. Prenat Diagn. 2020;41(4):479–85.

Bernardi A, Moses S, Barber B, Witte M, Seckeler M. Higher Incidence of Protein-Losing Enteropathy in Patients with Single Systemic Right Ventricle. Pediatr Cardiol. 2021;42(1):178–81.

Bradford VR, Tworetzky W, Callahan R, Wilkins-Haug LE, Benson CB, Porras D, et al. Hemodynamic and anatomic changes after fetal aortic valvuloplasty are associated with procedural success and postnatal biventricular circulation. Prenat Diagn. 2022;(July):1312–22.

Buckberg G, Hoffman JIE, Mahajan A, Saleh S, Coghlan C. Cardiac mechanics revisited: The relationship of cardiac architecture to ventricular function. Circulation. 2008;118(24):2571–87.

Buoso S, Joyce T, Kozerke S. Personalising left-ventricular biophysical models of the heart using parametric physics-informed neural networks. Med Image Anal [Internet]. Elsevier B.V.; 2021;71:1–11. Available from: https://doi.org/10.1016/j.media.2021.102066

Cavaliere TA. From Fetus to Neonate: A Sensational Journey. Newborn and Infant Nursing Reviews [Internet]. Elsevier Inc.; 2016;16(2):43–7. Available from: http://dx.doi.org/10.1053/j.nainr.2016.03.004

Chen F, Zeng S, Yi A, Chen L, Zhou D, Liu Y, et al. Z-score model of foetal ascending aorta diameter distensibility. Front Cardiovasc Med. 2022;9(August):1–7.

Cheng C, Zhang GT. Deep learning method based on physics informed neural network with Resnet block for solving fluid flow problems. Water (Switzerland). 2021;13(423):1–17.

Chrisant MRK, Naftel DC, Drummond-Webb J, Chinnock R, Canter CE, Boucek MM, et al. Fate of infants with hypoplastic left heart syndrome listed for cardiac transplantation: A multicenter study. Journal of Heart and Lung Transplantation. 2005;24(5):576–82.

Cutrì E, Meoli A, Dubini G, Migliavacca F, Hsia TY, Pennati G. Patient-specific biomechanical model of hypoplastic left heart to predict post-operative cardio-circulatory behaviour. Med Eng Phys. 2017;47:85–92.

Daimei T, Devi D, Sinam V. Difference between the left and right ventricular thickness in fetal heart. IOSR Journal of Dental and Medical Sciences. 2014;13(4):21–4.

DeVore GR, Klas B, Satou G, Sklansky M. Evaluation of the right and left ventricles: An integrated approach measuring the area, length, and width of the chambers in normal fetuses. Prenat Diagn. 2017;37(12):1203–12.

Devore GR, Klas B, Satou G, Sklansky M. Evaluation of fetal left ventricular size and function using speckle-tracking and the simpson rule. Journal of Ultrasound in Medicine. 2019;38(5):1209–21.

Dewan S, Krishnamurthy A, Kole D, Conca G, Kerckhoffs R, Puchalski MD, et al. Model of human fetal growth in hypoplastic left heart syndrome: Reduced ventricular growth due to decreased ventricular filling and altered shape. Front Pediatr. 2017;5(February):1–15.

Dipchand AI, Kirk R, Mahle WT, Tresler MA, Naftel DC, Pahl E, et al. Ten yr of pediatric heart transplantation: A report from the Pediatric Heart Transplant Study. Pediatr Transplant. 2013;17(2):99–111.

Eghtesady P, Michelfelder E, Altaye M, Ballard E, Hirsh R, Beekman RH. Revisiting Animal Models of Aortic Stenosis in the Early Gestation Fetus. Annals of Thoracic Surgery. 2007;83(2):631–9.

Ennis DB, Nguyen TC, Riboh JC, Wigström L, Harrington KB, Daughters GT, et al. Myofiber angle distributions in the ovine left ventricle do not conform to computationally optimized predictions. J Biomech. 2008;41(15):3219–24.

Finsberg H, Xi C, Tan J le, Zhong L, Genet M, Sundnes J, et al. Efficient estimation of personalized biventricular mechanical function employing gradient-based optimization. Int J Numer Method Biomed Eng. 2018;34(7):1–20.

Freud LR, McElhinney DB, Marshall AC, Marx GR, Friedman KG, del Nido PJ, et al. Fetal aortic valvuloplasty for evolving hypoplastic left heart syndrome: postnatal outcomes of the first 100 patients. Circulation. 2014;130(8):638–45.

Freud LR, Moon-Grady A, Escobar-Diaz MC, Gotteiner NL, Young LT, McElhinney DB, et al. Low Rate of Prenatal Diagnosis among Neonates with Critical Aortic Stenosis: Insight into the Natural History In Utero (Aortic Stenosis). Ultrasound in Obstetrics and Gynecology. 2015;45(3):326–32.

Friedman KG, Schidlow D, Freud L, Escobar-Diaz M, Tworetzky W. Left ventricular diastolic function and characteristics in fetal aortic stenosis. American Journal of Cardiology [Internet]. Elsevier Inc.; 2014;114(1):122–7. Available from: http://dx.doi.org/10.1016/j.amjcard.2014.04.013

Friedman KG, Sleeper LA, Freud LR, Marshall AC, Godfrey ME, Drogosz M, et al. Improved technical success, postnatal outcome and refined predictors of outcome for fetal aortic valvuloplasty. Ultrasound in Obstetrics and Gynecology. 2018;52(2):212–20.

Friedman KG, Tworetzky W. Fetal cardiac interventions: Where do we stand? Arch Cardiovasc Dis [Internet]. Elsevier Masson SAS; 2020;113(2):121–8. Available from: https://doi.org/10.1016/j.acvd.2019.06.007

Fruitman DS. Hypoplastic left heart syndrome: Prognosis and management options. Paediatr Child Health. 2000;5(4):219.

Galindo A, Gómez-Montes E, Gómez O, Bennasar M, Crispi F, Herraiz I, et al. Fetal Aortic Valvuloplasty: Experience and Results of Two Tertiary Centers in Spain. Fetal Diagn Ther. 2017;42(4):262–70.

Gao H, Carrick D, Berry C, Griffith BE, Luo X. Dynamic finite-strain modelling of the human left ventricle in health and disease using an immersed boundary-finite element method. IMA Journal of Applied Mathematics (Institute of Mathematics and Its Applications). 2014;79(5):978–1010.

Gao H, Mangion K, Carrick D, Husmeier D, Luo X, Berry C. Estimating prognosis in patients with acute myocardial infarction using personalized computational heart models. Sci Rep [Internet]. Springer US; 2017;7(1):1–14. Available from: http://dx.doi.org/10.1038/s41598-017-13635-2

Garcia-Canadilla P, Dejea H, Bonnin A, Balicevic V, Loncaric S, Zhang C, et al. Complex Congenital Heart Disease Associated With Disordered Myocardial Architecture in a Midtrimester Human Fetus. Circ Cardiovasc Imaging. 2018;11(10):1–10.

Gardiner HM, Kovacevic A, Tulzer G, Sarkola T, Herberg U, Dangel J, et al. Natural history of 107 cases of fetal aortic stenosis from a European multicenter retrospective study. Ultrasound in Obstetrics and Gynecology. 2016;48(3):373–81.

Genet M, Lee LC, Nguyen R, Haraldsson H, Acevedo-Bolton G, Zhang Z, et al. Distribution of normal human left ventricular myofiber stress at end diastole and end systole: A target for in silico design of heart failure treatments. J Appl Physiol. 2014;117(2):142–52.

Gibson PH, Becher H, Choy JB. Classification of left ventricular size: Diameter or volume with contrast echocardiography? Open Heart. 2014;1(1):1–8.

Goldberg CS, Mussatto K, Licht D, Wernovsky G. Neurodevelopment and quality of life for children with hypoplastic left heart syndrome: Current knowns and unknowns. Cardiol Young. 2011;21(SUPPL. 2):88–92.

Goldstein BH, Fifer CG, Armstrong AK, Gelehrter SK, Treadwell MC, Van De Ven C, et al. Use of a pressure guidewire in fetal cardiac intervention for critical aortic stenosis. Pediatrics. 2011;128(3):716–9.

Green L, Chan WX, Prakash I, Tulzer A, Tulzer G, Yap CH. Pre-intervention myocardial stress is a good predictor of aortic valvoluplasty outcome for fetal critical aortic stenosis and evolving HLHS. J Physiol. 2024;602(4):663–81.

Green L, Chan WX, Ren M, Mattar C, Chuan L, Choon L, et al. The dependency of fetal left ventricular biomechanics function on myocardium helix angle configuration. Biomech Model Mechanobiol [Internet]. Springer Berlin Heidelberg; 2022;22(1). Available from: https://doi.org/10.1007/s10237-022-01669-z

Greenleaf CE, Urencio JM, Salazar JD, Dodge-Khatami A. Hypoplastic left heart syndrome: Current perspectives. Transl Pediatr. 2016;5(3):142–7.

Guan D, Yao J, Luo X, Gao H. Effect of myofibre architecture on ventricular pump function by using a neonatal porcine heart model: From DT-MRI to rule-based methods. R Soc Open Sci. 2020;7(4).

Guccione JM, McCullock AD, Waldman LK. Passive material properties of intact ventricular myocardium determined from a cylindrical model. J Biomech Eng. 1991;113:42–55.

Guccione JM, Waldman LK, McCulloch AD. Mechanics of active contraction in cardiac muscle: Part II—cylindrical models of the systolic left ventricle. J Biomech Eng. 1993;115(1):82–90.

Harris IS, Black BL. Development of the endocardium. Pediatr Cardiol. 2010;31(3):391–9.

Hoffman JIE, Kaplan S. The incidence of congenital heart disease. J Am Coll Cardiol [Internet]. Elsevier Masson SAS; 2002;39(12):1890–900. Available from: http://dx.doi.org/10.1016/S0735-1097(02)01886-7

Holt JP, Rhode EA, Holt WW, Kines H. Geometric similarity of aorta, venae cavae, and certain of their branches in mammals. Am J Physiol Regul Integr Comp Physiol. 1981;10(1).

Humphrey JD, Yin FC. A new constitutive formulation for characterizing the mechanical behavior of soft tissues. Biophys J [Internet]. Elsevier; 1987;52(4):563–70. Available from: http://dx.doi.org/10.1016/S0006-3495(87)83245-9

Ishii T, McElhinney DB, Harrild DM, Marcus EN, Sahn DJ, Truong U, et al. Circumferential and longitudinal ventricular strain in the normal human fetus. Journal of the American Society of Echocardiography [Internet]. Elsevier Inc; 2012;25(1):105–11. Available from: http://dx.doi.org/10.1016/j.echo.2011.09.016

Ishii T, McElhinney DB, Harrild DM, Marcus EN, Sahn DJ, Truong U, et al. Ventricular strain in fetuses with aortic stenosis and evolving hypoplastic left heart syndrome before and after prenatal aortic valvuloplasty. Fetal Diagn Ther. 2014;35(1):18–26.

Jacot JG, Martin JC, Hunt DL. Mechanobiology of Cardiomyocyte Devlopment. J Biomech. 2010;43(1):1–13.

Jin X, Cai S, Li H, Karniadakis GE. NSFnets (Navier-Stokes flow nets): Physics-informed neural networks for the incompressible Navier-Stokes equations. J Comput Phys [Internet]. Elsevier Inc.; 2021;426(2021). Available from: https://doi.org/10.1016/j.jcp.2020.109951

Johnson P, Maxwell DJ, Tynan MJ, Allan LD. Intracardiac pressures in the human fetus. Heart. 2000;84(1):59–63.

Jopling J, Henry E, Wiedmeier SE, Christensen RD. Reference ranges for hematocrit and blood hemoglobin concentration during the neonatal period: Data from a multihospital health care system. Pediatrics. 2009;123(2).

Kanter KR, Mahle WT, Vincent RN, Berg AM, Kogon BE, Kirshbom PM. Heart transplantation in children with a Fontan procedure. Annals of Thoracic Surgery. Elsevier Inc.; 2011;91(3):823–30.

Khalafvand SS, Yin-kwee Ng E, Zhong L, Hung T. Three-dimensional diastolic blood flow in the left ventricle. J Biomech. Elsevier; 2017;50:71–6.

Kirkpatrick SE, Naliboff J, Pitlick PT, Friedman WF. Influence of poststimulation potentiation and heart rate on the fetal lamb heart. American Journal of Physiology. 1975;229(2):318–23.

Kirkpatrick SE, Pitlick PT, Naliboff J ay, Friedman WF. Frank-Starling relationship as an important determinant of fetal cardiac output. 1976;231(2):495–500.

Krishnamurthy A, Villongco C, Beck A, Omens J, McCulloch A. Left Ventricular Diastolic and Systolic Material Property Estimation from Image Data. Statistical Atlases and Computational Models of the Heart. 2015. p. 63–73.

Kwon O, Krishnamoorthy M, Cho YI, Sankovic JM, Banerjee RK. Effect of blood viscosity on oxygen transport in residual stenosed artery following angioplasty. J Biomech Eng. 2008;130(1).

Lahmers S, Wu Y, Call DR, Labeit S, Granzier H. Developmental Control of Titin Isoform Expression and Passive Stiffness in Fetal and Neonatal Myocardium. Circ Res. 2004;94(4):505–13.

Land S, Park-Holohan SJ, Smith NP, dos Remedios CG, Kentish JC, Niederer SA. A model of cardiac contraction based on novel measurements of tension development in human cardiomyocytes. J Mol Cell Cardiol [Internet]. Elsevier Ltd.; 2017;106:68–83. Available from: http://dx.doi.org/10.1016/j.yjmcc.2017.03.008

Lee LC, Sundnes J, Genet M, Wenk JF, Wall ST. An integrated electromechanical-growth heart model for simulating cardiac therapies. Biomech Model Mechanobiol. Springer Berlin Heidelberg; 2016;15(4):791–803.

Li Y, Sun J, Tang CK, Shum HY. Lazy snapping. ACM Trans Graph. 2004;303–8.

Luewan S, Yanase Y, Tongprasert F, Srisupundit K, Tongsong T. Fetal cardiac dimensions at 14-40 weeks' gestation obtained using cardio-STIC-M. Ultrasound in Obstetrics and Gynecology. 2011;37(4):416–22.

Mäkikallio K, McElhinney DB, Levine JC, Marx GR, Colan SD, Marshall AC, et al. Fetal aortic valve stenosis and the evolution of hypoplastic left heart syndrome: Patient selection for fetal intervention. Circulation. 2006;113(11):1401–5.

Marshall AC, Tworetzky W, Bergersen L, McElhinney DB, Benson CB, Jennings RW, et al. Aortic valvuloplasty in the fetus: Technical characteristics of successful balloon dilation. Journal of Pediatrics. 2005;147(4):535–9.

Marshall KH, D'udekem Y, Sholler GF, Opotowsky AR, Costa DSJ, Sharpe L, et al. Health-related quality of life in children, adolescents, and adults with a fontan circulation: A meta-analysis. J Am Heart Assoc. 2020;9(6).

Matsuda Y, Toma Y, Matsuzaki M, Moritani K, Satoh A, Shiomi K, et al. Change of left atrial systolic pressure waveform in relation to left ventricular end-diastolic pressure. Circulation. 1990;82(5):1659–67.

Maxwell D, Allan L, Tynan. Balloon dilatation of the aortic valve in the fetus: a report of two cases. Br J Heart. 1996;11(4):296–300.

McElhinney DB, Marshall AC, Wilkins-Haug LE, Brown DW, Benson CB, Silva V, et al. Predictors of technical success and postnatal biventricular outcome after in utero aortic valvuloplasty for aortic stenosis with evolving hypoplastic left heart syndrome. Circulation. 2009;120(15):1482–90.

McPherson RA, Kramer MF, Covell JW, Friedman WF. A comparison of the active stiffness of fetal and adult cardiac muscle. Pediatr Res. 1976;10(7):660–4.

Mekkaoui C, Porayette P, Jackowski MP, Kostis WJ, Dai G, Sanders S, et al. Diffusion MRI Tractography of the Developing Human Fetal Heart. PLoS One. 2013;8(8):4–9.

Metcalf MK, Rychik J. Outcomes in Hypoplastic Left Heart Syndrome. Pediatr Clin North Am [Internet]. Elsevier Inc; 2020;67(5):945–62. Available from: https://doi.org/10.1016/j.pcl.2020.06.008

Mitchell SC, Korones SB, Berendes HW. Congenital Heart Disease in 56,109 Births. Circulation. 1971;42:323–32.

Mojumder J, Choy JS, Leng S, Zhong L, Kassab GS, Lee LC. Mechanical Stimuli for Left Ventricular Growth During Pressure Overload. Exp Mech. Experimental Mechanics; 2020;

Mulieri LA, Hasenfuss G, Leavitt B, Allen PD, Alpert NR. Altered myocardial force-frequency relation in human heart failure. Circulation. 1992;85(5):1743–50.

Nauta JF, Hummel YM, Tromp J, Ouwerkerk W, van der Meer P, Jin X, et al. Concentric vs. eccentric remodelling in heart failure with reduced ejection fraction: clinical characteristics, pathophysiology and response to treatment. Eur J Heart Fail. 2020;22(7):1147–55.

NICE. Percutaneous balloon valvuloplasty for fetal critical aortic stenosis [Internet]. 2018. Available from: nice.org.uk/guidance/ipg613

Nielles-Vallespin S, Khalique Z, Ferreira PF, de Silva R, Scott AD, Kilner P, et al. Assessment of Myocardial Microstructural Dynamics by In Vivo Diffusion Tensor Cardiac Magnetic Resonance. J Am Coll Cardiol. 2017;69(6):661–76.

Nishitani S, Torii N, Imai H, Haraguchi R, Yamada S, Takakuwa T. Development of helical myofiber tracts in the human fetal heart: Analysis of myocardial fiber formation in the left ventricle from the late human embryonic period using diffusion tensor magnetic resonance imaging. J Am Heart Assoc. 2020;9(19).

Ohayon J, Usson Y, Jouk PS, Cai H. Fibre orientation in human fetal heart and ventricular mechanics: A small perturbation. Comput Methods Biomech Biomed Engin. 1999;2(2):83–105.

Ong CW, Ren M, Wiputra H, Mojumder J, Chan WX, Tulzer A, et al. Biomechanics of Human Fetal Hearts with Critical Aortic Stenosis. Ann Biomed Eng. 2020;

Palit A, Bhudia SK, Arvanitis TN, Turley GA, Williams MA. Computational modelling of left-ventricular diastolic mechanics: Effect of fibre orientation and right-ventricle topology. J Biomech. Elsevier; 2015;48(4):604–12.

Parasuraman R, Osmond C, Howe DT. Gestation-specific reference intervals for fetal cardiac Doppler indices from 12 to 40 weeks of gestation. Open J Obstet Gynecol. 2013;03(01):97–104.

Park MI, Hwang JH, Cha KJ, Park YS, Koh SK. Computerized analysis of fetal heart rate parameters by gestational age. International Journal of Gynecology and Obstetrics. 2001;74(2):157–64.

Patel ND, Nageotte S, Ing FF, Armstrong AK, Chmait R, Detterich JA, et al. Procedural, pregnancy, and short-term outcomes after fetal aortic valvuloplasty. Catheterization and Cardiovascular Interventions. 2020;96(3):626–32.

Pennati G, Bellotti M, Fumero R. Mathematical modelling of the human foetal cardiovascular system based on Doppler ultrasound data. Med Eng Phys. 1997;19(4):327–35.

Pennati. G, Fumero. R. Scaling approach to study the changes through the gestation of human fetal cardiac and circulatory behaviors. Ann Biomed Eng. 2000;28(4):442–52.

Pervolaraki E, Dachtler J, Anderson RA, Holden A v. Ventricular myocardium development and the role of connexins in the human fetal heart. Sci Rep [Internet]. Springer US; 2017;7(1):1–9. Available from: http://dx.doi.org/10.1038/s41598-017-11129-9

Pickard SS, Wong JB, Bucholz EM, Newburger JW, Tworetzky W, Lafranchi T, et al. Fetal Aortic Valvuloplasty for Evolving Hypoplastic Left Heart Syndrome: A Decision Analysis. Circ Cardiovasc Qual Outcomes. 2020;13(April):32–41.

Pluijmert M, Kroon W, Delhaas T, Bovendeerd PHM. Adaptive reorientation of cardiac myofibers: The long-term effect of initial and boundary conditions. Mech Res Commun [Internet]. Elsevier Ltd.; 2012;42:60–7. Available from: http://dx.doi.org/10.1016/j.mechrescom.2011.11.011

Prevention C for DC and. Hypoplastic Left Heart Syndrome and Normal Heart. 2013.

Prosnitz AR, Drogosz M, Marshall AC, Wilkins-Haug LE, Benson CB, Sleeper LA, et al. Early hemodynamic changes after fetal aortic stenosis valvuloplasty predict biventricular circulation at birth. Prenat Diagn. 2018;38(4):286–92.

Quijada P, Trembley MA, Small EM. The Role of the Epicardium during Heart Development and Repair. Circ Res. 2020;377–94.

Racca AW, Klaiman JM, Pioner JM, Cheng Y, Beck AE, Moussavi-Harami F, et al. Contractile properties of developing human fetal cardiac muscle. Journal of Physiology. 2016;594(2):437–52.

Ren M, Chan WX, Green L, Armstrong AK, Tulzer A, Tulzer G, et al. Contribution of Ventricular Motion and Sampling Location to Discrepancies in 2D versus 3D Fetal Ventricular Strain Measures. Journal of the American Society of Echocardiography [Internet]. American Society of Echocardiography; 2023; Available from: https://doi.org/10.1016/j.buildenv.2022.109181

Ren M, Ong CW, Buist ML, Yap CH. Biventricular biaxial mechanical testing and constitutive modelling of fetal porcine myocardium passive stiffness. J Mech Behav Biomed

Mater [Internet]. Elsevier Ltd; 2022;134(July):105383. Available from: https://doi.org/10.1016/j.jmbbm.2022.105383

Rideout VC. Cardiovascular System Simulation in Biomedical Engineering Education. Transactions on Biomedical Engineering. 1972;19(2):101–7.

Rijcken J, Bovenoeerd PHM, Schoofs AJG, Van Campen DH, Arts T. Optimization of cardiac fiber orientation for homogeneous fiber strain during ejection. Ann Biomed Eng. 1999;27(3):289–97.

Rohmer D, Sitek A, Gullberg GT. Reconstruction and visualization of fiber and laminar structure in the normal human heart from ex vivo diffusion tensor magnetic resonance imaging (DTMRI) data. Invest Radiol. 2007;42(11):777–89.

Rufaihah AJ, Chen CK, Yap CH, Mattar CNZ. Mending a broken heart: In vitro, in vivo and in silico models of congenital heart disease. Dis Model Mech. 2021;14(3).

Rugonyi S. Genetic and flow anomalies in congenital heart disease. AIMS Genet. 2016;3(3):157–66.

Saffitz JE, Davis LM, Darrow BJ, Lee Kanter H, Laing JG, Beyer EC. The Molecular Basis of Anisotropy: Role of Gap Junctions. J Cardiovasc Electrophysiol. 1995;6(6):498–510.

Sagawa K, Lie RK, Schaefer J. Translation of Otto frank's paper "Die Grundform des arteriellen Pulses" zeitschrift für biologie 37: 483-526 (1899). J Mol Cell Cardiol. 1990;22(3):253–4.

Scher AM. Studies of the electrical activity of the ventricles and the origin of the QRS complex. Acta Cardiol. England; 1995;50(6):429–65.

Schwinger RHG, Böhm M, Koch A, Schmidt U, Morano I, Eissner HJ, et al. The failing human heart is unable to use the Frank-Starling mechanism. Circ Res. 1994;74(5):959–69.

Sengupta PP, Korinek J, Belohlavek M, Narula J, Vannan MA, Jahangir A, et al. Left Ventricular Structure and Function. Basic Science for Cardiac Imaging. J Am Coll Cardiol. 2006a;48(10):1988–2001.

Sengupta PP, Korinek J, Belohlavek M, Narula J, Vannan MA, Jahangir A, et al. Left Ventricular Structure and Function. Basic Science for Cardiac Imaging. J Am Coll Cardiol. 2006b;48(10):1988–2001.

Sengupta PP, Krishnamoorthy VK, Korinek J, Narula J, Vannan MA, Lester SJ, et al. Left Ventricular Form and Function Revisited: Applied Translational Science to Cardiovascular Ultrasound Imaging. Journal of the American Society of Echocardiography. 2007;20(5):539–51.

Sewanan LR, Schwan J, Kluger J, Park J, Jacoby DL, Qyang Y, et al. Extracellular Matrix From Hypertrophic Myocardium Provokes Impaired Twitch Dynamics in Healthy Cardiomyocytes. JACC Basic Transl Sci. 2019;4(4):495–505.

Shavik SM, Jiang Z, Baek S, Lee LC. High spatial resolution multi-organ finite element modeling of ventricular-arterial coupling. Front Physiol. 2018;9(119).

Shavik SM, Wall S, Sundnes J, Guccione JM, Sengupta P, Solomon SD, et al. Computational Modeling Studies of the Roles of Left Ventricular Geometry, Afterload, and Muscle Contractility on Myocardial Strains in Heart Failure with Preserved Ejection Fraction. J Cardiovasc Transl Res. Journal of Cardiovascular Translational Research; 2021;14(6):1131–45.

Shavik SM, Wall ST, Sundnes J, Burkhoff D, Lee LC. Organ-level validation of a cross-bridge cycling descriptor in a left ventricular finite element model: Effects of ventricular loading on myocardial strains. Physiol Rep. 2017;5(21):1–14.

Sonnenblick EH, Morrow AG, Williams JF. Effects of heart rate on the dynamics of force development in the intact human ventricle. Circulation. 1966;33(6):945–51.

Tan CMJ, Lewandowski AJ. The Transitional Heart: From Early Embryonic and Fetal Development to Neonatal Life. Fetal Diagn Ther. 2019;47(5):373–86.

Teun Van Der Bom A, Zomer AC, Zwinderman AH, Meijboom FJ, Bouma BJ, Mulder BJM. The changing epidemiology of congenital heart disease. Nat Rev Cardiol. Nature Publishing Group; 2011;8(1):50–60.

Torre I, González-Tendero A, García-Cañadilla P, Crispi F, García-GarciÁa F, Bijnens B, et al. Permanent cardiac sarcomere changes in a rabbit model of intrauterine growth restriction. PLoS One. 2014;9(11):1–8.

Tulzer A, Arzt W, Gitter R, Sames-Dolzer E, Kreuzer M, Mair R, et al. Valvuloplasty in 103 fetuses with critical aortic stenosis: outcome and new predictors for postnatal circulation. Ultrasound in Obstetrics & Gynecology. 2021a;.

Tulzer A, Arzt W, Gitter R, Sames-Dolzer E, Kreuzer M, Mair R, et al. Valvuloplasty in 103 fetuses with critical aortic stenosis: outcome and new predictors for postnatal circulation. Ultrasound in Obstetrics and Gynecology. 2022a;59(5):633–41.

Tulzer A, Arzt W, Scharnreitner I, Hochpoechler J, Bauer C, Tulzer G. Complications associated with fetal cardiac interventions – prevalence and management: experience from 213 procedures. Fetal Diagn Ther. 2022b;.

Tulzer A, Arzt W, Tulzer G. Fetal aortic valvuloplasty may rescue fetuses with critical aortic stenosis and hydrops. Ultrasound in Obstetrics and Gynecology. 2021b;57(1):119–25.

Tulzer G, Arzt W. Fetal cardiac interventions: Rationale, risk and benefit. Semin Fetal Neonatal Med [Internet]. Elsevier Ltd; 2013;18(5):298–301. Available from: http://dx.doi.org/10.1016/j.siny.2013.04.002

Velagaleti RS, Gona P, Pencina MJ, Aragam J, Wang TJ, Levy D, et al. Left ventricular hypertrophy patterns and incidence of heart failure with preserved versus reduced ejection

fraction. American Journal of Cardiology [Internet]. Elsevier Inc.; 2014;113(1):117–22. Available from: http://dx.doi.org/10.1016/j.amjcard.2013.09.028

Vendelin M, Bovendeerd PHM, Engelbrecht J, Arts T. Optimizing ventricular fibers: Uniform strain or stress, but not ATP consumption, leads to high efficiency. Am J Physiol Heart Circ Physiol. 2002;283(3 52-3):1072–81.

Versmold HT, Kitterman JA, Phibbs RH, Gregory GA, Tooley WH. Aortic blood pressure during the first 12 hours of life in infants with birth weight 610 to 4,220 grams. Pediatrics. 1981;67(5):607–13.

Wang VY, Young AA, Cowan BR, Nash MP. Changes in In Vivo Myocardial Tissue Properties Due to Heart Failure. Functional Imaging and Modeling of the Heart - 7th International Conference, FIMH 2013, Proceedings. 2013. p. 216–23.

Wang Z, Bovik AC, Sheikh HR, Simoncelli EP. Image quality assessment: From error visibility to structural similarity. IEEE Transactions on Image Processing. 2004;13(4):600–12.

Wang ZJ, Wang VY, Babarenda Gamage TP, Rajagopal V, Cao JJ, Nielsen PMF, et al. Efficient estimation of load-free left ventricular geometry and passive myocardial properties using principal component analysis. Int J Numer Method Biomed Eng. 2020;36(3):1–17.

Washio T, Sugiura S, Okada JI, Hisada T. Using Systolic Local Mechanical Load to Predict Fiber Orientation in Ventricles. Front Physiol. 2020;11(June):1–14.

Wenk JF, Klepach D, Lee LC, Zhang Z, Ge L, Tseng EE, et al. First evidence of depressed contractility in the border zone of a human myocardial infarction. Annals of Thoracic Surgery. 2012;93(4):1188–93.

Widnes C, Flo K, Wilsgaard T, Kiserud T, Acharya G. Sex differences in umbilical artery Doppler indices: A longitudinal study. Biol Sex Differ. Biology of Sex Differences; 2018;9(1):1–12.

Wiputra H, Chan WX, Foo YY, Ho S, Yap CH. Cardiac motion estimation from medical images: a regularisation framework applied on pairwise image registration displacement fields. Sci Rep. 2020;10(1).

Wiputra H, Lai CQ, Lim GL, Heng JJW, Guo L, Soomar SM, et al. Fluid mechanics of human fetal right ventricles from image-based computational fluid dynamics using 4D clinical ultrasound scans. Am J Physiol Heart Circ Physiol. 2016;311(6):H1498–508.

Wisneski AD, Wang Y, Deuse T, Hill AC, Pasta S, Sack KL, et al. Impact of Aortic Stenosis on Myofiber Stress: Translational Application of Left Ventricle-Aortic Coupling Simulation. Front Physiol. 2020;11(September):1–8.

Wohlmuth C, Wertaschnigg D, Wieser I, Arzt W, Tulzer G. Tissue Doppler imaging in fetuses with aortic stenosis and evolving hypoplastic left heart syndrome before and after fetal aortic valvuloplasty. Ultrasound in Obstetrics and Gynecology. 2016;47(5):608–15.

Wong HS, Li B, Tulzer A, Tulzer G, Yap CH. Fluid Mechanical Effects of Fetal Aortic Valvuloplasty for Cases of Critical Aortic Stenosis with Evolving Hypoplastic Left Heart Syndrome. Ann Biomed Eng. 2023;

Wong HS, Wiputra H, Tulzer A, Tulzer G, Yap CH. Fluid Mechanics of Fetal Left Ventricle During Aortic Stenosis with Evolving Hypoplastic Left Heart Syndrome. Ann Biomed Eng. 2022;

Yang F, Zhu YM, Michalowicz G, Jouk PS, Fanton L, Viallon M, et al. Quantitative comparison of human myocardial fiber orientations derived from DTI and polarized light imaging. Phys Med Biol. IOP Publishing; 2018;63(21).

Yutzey KE. Cardiomyocyte proliferation. Circ Res. 2017;120(4):627–9.

Zheng Y, Chan WX, Charles CJ, Richards AM, Lee LC, Leo HL, et al. Morphological, functional, and biomechanical progression of LV remodelling in a porcine model of HFpEF. J Biomech [Internet]. Elsevier Ltd; 2022;144(October):111348. Available from: https://doi.org/10.1016/j.jbiomech.2022.111348

Zheng Y, Chan WX, Nielles-Vallespin S, Scott AD, Ferreira PF, Leo HL, et al. Effects of myocardial sheetlet sliding on left ventricular function. Biomech Model Mechanobiol [Internet]. Springer Berlin Heidelberg; 2023;22(4):1313–32. Available from: https://doi.org/10.1007/s10237-023-01721-6

Zwanenburg JJM, Götte MJW, Kuijer JPA, Heethaar RM, Van Rossum AC, Marcus JT. Timing of cardiac contraction in humans mapped by high-temporal-resolution MRI tagging: Early onset and late peak of shortening in lateral wall. Am J Physiol Heart Circ Physiol. 2004;286(5 55-5):1872–80.

Appendix

Appendix 3.1 – Baseline LPM Values

Baseline parameters from the original LPM (Pennati et al. 1997), without gestational age scaling.

Table A3.1. *Values in the original LPM by Pennati et al., for a fetus weighing 3 kg. Where the Parameter abbreviations are recorded with the second word identifying the type of parameter eg C for capacitor. The units of each parameter type are ml/mmHg for capacitors, mmHg s²/ml for inductors, mmHg s/ml for resistors and mmHg s² /ml² for the K and B relationship terms.*

	Parameter	Description	Value
Capacitors	AA C	Ascending aorta	0.05
	A01 C	Aortic arch	0.08
	A02 C	Thoracic descending aorta	0.07
	A03 C	Abdominal descending aorta	0.04
	A04 C	Femoral descending aorta	0.05
	PA1 C	Main pulmonary artery	0.08
	PA2 C	Pulmonary artery	0.08
	LUNG C	Lung	0.40
	CA C	Cerebral arteries	0.07
	BR C	Brain	0.3
	UB C	Umbilical	0.85
	INTE C	Intestinal circulation	0.25
	KID C	Kidney	0.02
	HE C	Liver	3.00
	PLAC C	Placenta	1.50
	LEG C	Leg	4.00
	UV C	Umbilical vein	0.30
	SVC C	Superior vena cava	1.00
	IVC C	Inferior vena cava	0.60
	RA C	Right atrium	1.00
	LA C	Left atrium	2.00
Inductors	DA L	Ductus arteriosus	0.006
	AO1-CA L	Aortic arch to cerebral arteries	0.08
	AA-AO1 L	Ascending aorta to aortic arch	0.002
	PA1-PA2 L	Main pulmonary artery to pulmonary artery	0.02
	RA-RAVALV L	Right atrium to tricuspid valve	0.0016
	LA-LAVALV L	Left atrium to mitral valve	0.0
e	AA-AO1 R	Ascending aorta to aortic arch	0.12

	AO1-AO2 R	Aortic arch to thoracic descending aorta	0.4
	AO2-AO3 R	Thoracic descending aorta to abdominal descending aorta	0.04
	AO3-AO4 R	Abdominal descending aorta to femoral descending aorta	0.06
	PA1-PA2 R	Main pulmonary artery to pulmonary artery	0.07
	PA2-LUNG R	Pulmonary artery to lung	13.50
	DA R	Ductus Arteriosus	0.01
	AO1-CA R	Aortic arch to cerebral arteries	0.30
	CA-BR R	Cerebral arteries to brain	3.00
	BR-SVC R	Brain to superior vena cava	8.50
	AO1-UB R	Aortic arch to umbilical cord	8.00
	UB-SVC R	Umbilical cord to superior vena cava	4.90
	AO3-HE R	Abdominal descending aorta to liver	81.00
	AO3-INTE R	Abdominal descending aorta to intestinal circulation	34.00
	INTE-HE R	Intestinal circulation to liver	7.00
	AO3-KID R	Abdominal descending aorta to kidney	3.50
	KID-IVC R	Kidney to inferior vena cava	14.00
	AO4-PLAC R	Femoral descending aorta to placenta	3.90
	PLAC-UV R	Placenta to umbilical vein	3.40
	AO4-LEG R	Femoral descending aorta to leg	3.50
	LEG-IVC R	Leg to inferior vena cava	0.60
	UV-HE R	Umbilical vein to liver	0.50
	HE-IVC R	Liver to inferior vena cava	0.16
	DV R	Ductus venosus	1.30
	SVC-RA R	Superior vena cava to right atrium	0.20
	IVC-RA R	Inferior vena cava to right atrium	0.12
	LUNG-LA R	Lung to left atrium	2.00
	RA-RAVALV R	Right atrium to tricuspid valve	0.00
	RV-RVVALV R	Right ventricle to pulmonary valve	0.08
	LV-LVVALV R	Left ventricle to aortic valve	0.00
	LA-LAVALV R	Left atrium to mitral valve	0.00
K and B Relationship Terms	FO K	Foramen ovale	0.40
	DA K	Ductus arteriosus	0.009
	DV K	Ductus venosus	0.26
	RA-RAVALV K	Right atrium to tricuspid valve	0.002
	RV-RVVALV K	Right ventricle to pulmonary valve	0.001
	LA-LAVALV K	Left atrium to mitral valve	0.002
	LV-LVVALV K	Left ventricle to aortic valve	0.001
	FO B	Foramen ovale	0.625
	DA B	Ductus arteriosus	2.00
	DV B	Ductus venosus	2.00
	RA-RAVALV B	Right atrium to tricuspid valve	2.00
	RV-RVVALV B	Right ventricle to pulmonary valve	2.00
	LA-LAVALV B	Left atrium to mitral valve	2.00
	LV-LVVALV B	Left ventricle to aortic valve	2.00

Appendix 5.1 – Images Based Measurements

Data extracted from the 4D and 2D patient images documented in Table A5.1-A5.3. Tables included retrospective data (denoted by R in case IDs) which was used later in the study to quantify the predictive capabilities of parameters.

Table A5.1. *Patient data, including gestational age in weeks (wks) and days, intervention outcome, cardiac cycle length and valvular velocity measurements. A "D" prefix in case IDs indicates a CAS-eHLHS case, while a "H" prefix indicates a healthy case. An "R" prefix in the case IDs indicates data taken from patients with 2D images available for the later retrospective receiver operator curve (ROC) analysis. Where FAV = fetal aortic valvuloplasty, BV = biventricular, UV = univentricular, AV = aortic valve and MVr = mitral valve regurgitation.*

Case ID	Age (wks+days)	FAV Outcome	Cardiac Cycle (ms)	AV Velocity (m/s)	MVr Velocity (m/s)
D1	24+6	BV	400	3.47	4.09
D2	29+0	BV	441	1.12	3.00
D3	29+3	BV	450	1.10	3.16
D4	29+6	BV	490	2.26	3.16
D5	30+1	BV	419	1.25	3.51
D6	22+4	UV	408	1.84	2.60
D7	24+6	UV	392	3.05	3.28
D8	27+2	UV	480	0.95	1.81
D9	29+1	UV	479	2.20	2.90
H1	21+2	-	400	0.61	-
H2	21+3	-	416	0.57	-
H3	21+4	-	408	0.61	-
H4	24+0	-	400	0.67	-
H5	28+0	-	400	1.03	-
H6	32+0	-	402	0.83	-
R1	24+6	UV	-	1.23	1.55
R2	30+3	UV	-	2.00	2.98
R3	29+6	UV	-	3.48	4.64
R4	24+3	UV	-	3.86	2.08
R5	24+4	UV	-	2.27	4.40
R6	27+6	UV	-	2.90	3.08
R7	23+6	UV	-	3.10	4.70
R8	26+5	UV	-	4.52	0.00
R9	26+4	UV	-	2.20	3.92
R10	23+0	UV	-	1.46	2.81

R11	27+4	UV	-	0.57	0.80
R12	22+5	BV	-	0.97	2.90
R13	30+6	BV	-	3.70	5.07
R14	23+6	BV	-	3.20	3.20
R15	32+4	BV	-	3.75	2.15
R16	32+1	BV	-	3.80	4.00
R17	25+0	BV	-	2.46	2.30
R18	29+2	BV	-	2.65	2.65
R19	30+0	BV	-	2.14	4.28
R20	30+3	BV	-	2.10	3.10
R21	22+6	BV	-	2.80	3.50
R22	24+4	BV	-	2.60	3.00
R23	31+0	BV	-	3.14	5.00
R24	25+5	BV	-	3.30	4.20
R25	31+3	BV	-	2.70	4.38
R26	29+6	BV	-	1.70	2.20
R27	24+2	BV	-	1.29	2.34
R28	30+3	BV	-	2.13	2.48

Table A5.2. *Left ventricle (LV) and right ventricle (RV) morphometrics taken from images at end diastolic volume (EDV). A "D" prefix in case IDs indicates a CAS-eHLHS case, while a "H" prefix indicates a healthy case. An "R" prefix in the case IDs indicates data taken from patients with 2D images available for the later retrospective ROC analysis. Where PWT = posterior wall thickness and LVID = LV inner diameter.*

Case ID	LV Longitudinal Length (mm)	PWT (mm)	LVID (mm)	RV Longitudinal Length (mm)	Ascending Aorta Width (mm)
D1	19.06	2.68	18.55	21.35	5.40
D2	30.80	3.95	35.14	29.26	5.80
D3	30.58	2.71	36.00	27.37	5.60
D4	30.09	4.03	31.24	26.69	5.50
D5	24.49	2.49	31.61	29.18	5.70
D6	19.03	2.40	19.00	21.00	3.90
D7	14.75	3.92	11.45	21.12	2.80
D8	19.57	2.85	26.94	21.91	4.3
D9	17.90	2.94	16.60	18.93	5.40
H1	13.47	1.65	8.59	11.91	-
H2	14.01	2.16	12.24	13.83	-
H3	15.37	1.90	12.43	15.61	-
H4	18.27	2.13	13.55	19.32	-
H5	16.66	3.70	19.33	18.95	-
H6	24.23	3.49	15.83	23.82	-
R1	17.80	1.67	9.80	20.60	-

R2	27.00	2.70	18.43	28.90	-
R3	22.00	3.77	12.43	25.10	-
R4	22.50	2.07	11.30	22.80	-
R5	15.07	3.80	10.50	19.17	-
R6	21.00	3.73	11.13	23.90	-
R7	19.00	2.27	9.67	20.90	-
R8	19.60	2.87	7.43	22.40	-
R9	24.40	3.80	13.23	20.70	-
R10	22.47	2.77	14.23	18.60	-
R11	15.70	3.17	10.57	20.00	-
R12	24.20	1.87	16.90	25.20	-
R13	23.40	2.57	12.20	27.10	-
R14	22.50	2.40	13.87	25.10	-
R15	33.00	3.37	21.83	34.50	-
R16	24.30	3.10	14.87	25.00	-
R17	27.80	3.00	17.67	27.20	-
R18	30.60	2.37	21.63	32.40	-
R19	29.40	5.77	16.57	30.00	-
R20	28.40	3.00	20.33	27.00	-
R21	18.75	1.30	8.67	21.00	-
R22	24.20	2.77	13.40	26.00	-
R23	30.90	3.10	16.13	25.70	-
R24	19.80	2.80	16.17	20.70	-
R25	26.60	3.40	18.67	26.80	-
R26	22.40	3.47	16.97	22.90	-
R27	21.17	2.80	17.47	22.37	-
R28	26.00	4.23	14.27	26.07	-

Table A5.3. *Volume data extracted from image segmentation and cardiac motion estimation methods. "D" prefix in case IDs indicates a CAS-eHLHS case, while a "H" prefix indicates a healthy case. An "R" prefix in the case IDs indicates data taken from patients with 2D images available for the later retrospective ROC analysis. Note: all R case volumes were approximated assuming a half prolate ellipsoid. LA = left atrium.*

Case ID	LV EDV (ml)	LV SV (ml)	RV EDV (ml)	RV SV (ml)	LA EDV (ml)	LA SV (ml)
D1	1.49	0.28	1.92	0.80	1.39	0.39
D2	7.20	0.30	4.03	1.44	2.58	0.44
D3	5.21	0.50	5.53	1.33	2.85	0.54
D4	6.67	0.17	4.65	1.53	2.78	0.38
D5	6.39	0.82	6.14	1.90	2.67	0.51
D6	1.98	0.10	2.91	1.09	1.04	0.13
D7	1.02	0.085	2.96	1.22	1.12	0.36
D8	3.62	0.095	4.44	0.96	1.99	0.20
D9	2.94	0.28	2.59	0.74	5.42	0.24
H1	0.41	0.22	0.65	0.29	-	-
H2	0.92	0.49	0.63	0.38	-	-
H3	0.96	0.49	0.72	0.32	-	-
H4	1.19	0.62	1.15	0.61	-	-
H5	1.36	0.82	1.48	0.63		
H6	2.17	1.32	2.90	1.50	-	-
R1	1.79	0.028	-	-	-	-
R2	9.61	0.24	-	-	-	-
R3	3.56	0.34	-	-	-	-
R4	3.01	0.19	-	-	-	-
R5	1.74	0.23	-	-	-	-
R6	2.73	0.067	-	-	-	-
R7	1.86	0.66	-	-	-	-
R8	1.13	0.56	-	-	-	-
R9	4.47	0.79	-	-	-	-
R10	4.77	0.93	-	-	-	-
R11	1.84	0.27	-	-	-	-
R12	7.24	0.74	-	-	-	-
R13	3.65	0.74	-	-	-	-
R14	4.53	0.85	-	-	-	-
R15	16.47	2.22	-	-	-	-
R16	5.62	1.90	-	-	-	-
R17	9.09	1.95	-	-	-	-
R18	15.00	2.55	-	-	-	-
R19	8.45	2.76	-	-	-	-
R20	12.30	1.05	-	-	-	-
R21	1.47	0.61	-	-	-	-

R22	4.55	1.05	-	-	-	-
R23	8.42	1.49	-	-	-	-
R24	5.42	1.83	-	-	-	-
R25	9.71	1.23	-	-	-	-
R26	6.75	1.70	-	-	-	-
R27	6.76	1.91	-	-	-	-
R28	5.53	0.67	-	-	-	-

Appendix 5.2 – Patient Specific PV Loops

Figure A5.1 documents all PV loops from patient specific biomechanics modelling, D1 to D5 are the diseased cases that went on to be BV post-FAV intervention, D6 to D9 are the diseased cases that went on to be UV post-FAV intervention and H1 to H6 are the healthy cases.

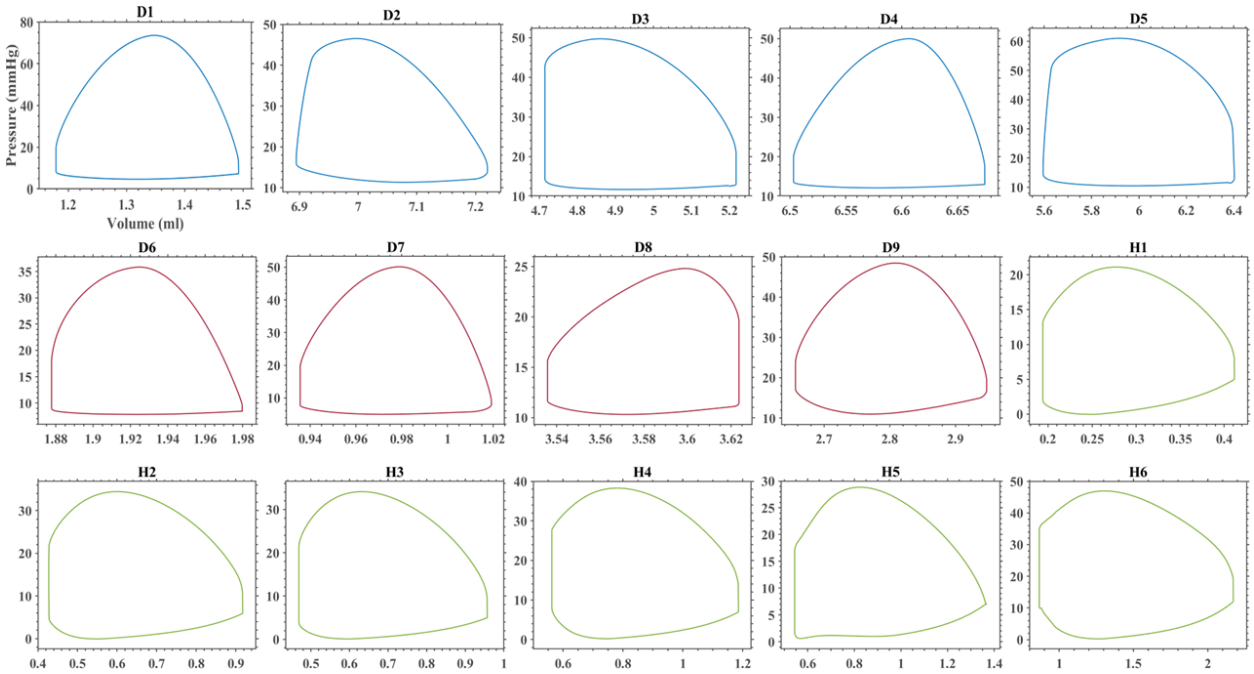

Figure A5.1. *PV loops extracted from the optimised patient specific simulations of each case; x-y axis labels documented in top left figure (D1).*